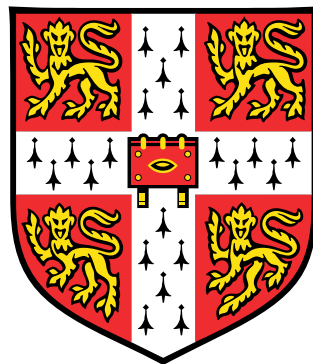


Investigating the Properties and Lattice Vibrations of Ordered and Disordered Crystalline Materials



Qi Li

Gonville and Caius College

University of Cambridge

This thesis is submitted for the degree of

Doctor of Philosophy

January 2022

Declaration

This thesis, entitled “*Investigating the properties and lattice vibrations of ordered and disordered crystalline materials*”, is the result of my own work and includes nothing which is the outcome of work done in collaboration except as declared in the Preface and specified in the text. I further state that no substantial part of my thesis has already been submitted, or, is being concurrently submitted for any such degree, diploma or other qualification at the University of Cambridge or any other University or similar institution except as declared in the Preface and specified in the text. It does not exceed the prescribed word limit for the Engineering Degree Committee.

Qi Li

Gonville and Caius College

Cambridge CB2 1TA

January 2022

Abstract

Investigating the Properties and Lattice Vibrations of Ordered and Disordered Crystalline Materials

Crystalline materials are known for their well-defined periodic structure and their properties have been widely applied in numerous fields. An ideal single crystal will exhibit a perfect ordered structure. However, in most crystalline materials defects and dislocations are commonly present and the vast majority of applications of crystalline materials concern polycrystalline materials rather than single crystals. In metals the effects of disorder and polycrystallinity have been studied extensively, but the effect on the properties of other crystals, such as organic molecular materials, are not fully understood. In this thesis the techniques of low-frequency vibrational spectroscopy by means of terahertz time-domain spectroscopy (THz-TDS) were combined with density functional theory (DFT) simulations to investigate the role and effect of disorder for small organic molecular materials including drug molecules as well as other emerging materials.

Terahertz radiation is located between the far-infrared and microwave regions on the electromagnetic spectrum. At these frequencies photons excite a complex mix of inter- and intra-molecular interactions in solid state materials, particularly low-frequency vibrational modes in molecular crystals. Due to the complexities of lattice vibrations at such low frequencies, high-accuracy computational methods are necessary to interpret the experimental results. Such simulations are usually based on ideal, defect free, structures of crystals while experiments are performed on commercial or lab-synthesised samples that will exhibit some disorder. Careful comparison between the results from the ideal calculations and the experimental observation makes it possible to study the role of defects in the crystalline systems of interest. In this context THz-TDS can be considered as a complementary method to the classical crystallographic techniques, e.g. X-ray diffraction, to aid the effective structural analysis of crystals.

The methodologies that were developed in this thesis are useful to provide more information for the design and the performance of novel materials such as metal-organic frame-

works (MOFs) in general and MOF perovskites in particular from the perspective of low-frequency vibrations. This is meaningful for the future optimisation and screening of materials. For small organic molecules, the new method is helpful to better understand the mechanism of their phase transitions and to determine the structure of polymorphs, even in the presence of disorder. This idea is explored to investigate the fundamentals of the crystallisation process where the sensitivity of terahertz spectroscopy to both crystalline structure as well as liquid dynamics is exploited to gain further insight into the transition between disorder and order.

Qi Li

Gonville and Caius College

Cambridge CB2 1TA

January 2022

Acknowledgements

There is no doubt that my PhD has been the most unforgettable and rewarding journey in my life with invaluable support from people (an endless list) along the way. I can still remember the time when I finally decided to accept the offer from Cambridge, being anxious as well as excited about the challenge. It was a brave choice back then, but now I can say it was the best decision ever. I did not only work for completing my degree and research topics, but also experienced memorable moments, met amazing people and also became a better version of myself.

I would like to pass my greatest thanks to my supervisor, Professor Axel Zeitler, the best kind of supervisor I can think of. He has not only led me into the world of science but also guided me through the ups and downs during my PhD with a smiling face all the time. At the very beginning, he was the one who offered me the chance of becoming a PhD candidate. He gave us all the freedom to explore our interests in science and tried his best to support us when we needed. I would also like to thank Dr. David Fairen-Jimenez for being my advisor, and Dr. Jonathan Evans, my college tutor, who helped me a lot for example with funding applications and minimising the impact of COVID on my time in Cambridge.

I was really lucky to join such a nice group with so many supportive people around me. I would like to thank everyone in the terahertz applications group that grew from people of six to more than ten now, as well as the visitors. Many thanks to Mike who taught me how to do experiments and simulations and offered substantial help with my first project, first report, first publication, first trip as a researcher and so forth. Also, thanks to Daniel who gave useful trainings and tutorials in my first year. Of course a big thank you to Adam as well, who spent a year as a postdoc in the group but became more like a friend to us. Dabwan (Dr. Al-Sharabi now) and Johanna (the future Dr. Kölbl), we joined the group at the same time and supported each other. You two deserve a special thank you. I also want to thank the friends I met in the past years, both in and outside of Cambridge. Life would have been so boring without you all.

It was my pleasure to meet and work with a group of amazing scientists who contributed to

my research. Dr. Andrew Bond has been helping with X-ray crystallography and discussions on crystal structures, chemical synthesis and career choices. Professor Tim Korter has been offering his help with computational work that has solved a number of problems that occurred in my projects. It was a great collaboration with Dr. Eduardo Maia Paiva and his colleagues on the project of theophylline, as well as with Dr. Terry Threlfall who contributed to the crystallisation project extensively. I appreciated Dr. Jingwei Hou and Dr. Wen Dong for introducing me to their projects, and also everyone I met and talked to at various conferences, tutorials and workshops, I was inspired and enlightened by the informative discussions. In addition, I would like to thank the China Scholarship Council for fully funding my PhD studies.

Special thanks to Axel and Johanna for proofreading this thesis.

Most importantly, thank you Mom and Dad for always being there for me and supporting my choices.

Publications and Conference Presentations

Publications in Peer-Reviewed Journals

1. **Qi Li**, Adam J. Zaczek, Timothy M. Korter, J. Axel Zeitler and Michael T. Ruggiero, Methyl-rotation dynamics in metal-organic frameworks probed with terahertz spectroscopy, *ChemComm*, 2018, 54, (45), 5776-5779.
2. **Qi Li**, Andrew D. Bond, Timothy M. Korter and J. Axel Zeitler, New insights into the crystallographic disorder in the polymorphic forms of aspirin from low-frequency vibrational analysis, *Mol. Pharm.*, 2021, 19, 1, 227-234.
3. Eduardo M. Paiva[#], **Qi Li**[#], Adam J. Zaczek, Claudete Fernandes Pereira, Jarbas José Rodrigues Rohwedder and J. Axel Zeitler, Understanding the metastability of theophylline FIII by means of low frequency vibrational spectroscopy, *Mol. Pharm.*, 2021, 18, 9, 3578-4587 (**# are co-first authors**).
4. **Qi Li**[#], Johanna Kölbl[#], Terry Threlfall and J. Axel Zeitler, Flow cell to study crystallisation processes in-situ using terahertz time-domain spectroscopy, *IEEE Trans. Terahertz Sci. Technol.*, 2021 (accepted in press; **# are co-first authors**).
5. Johanna Kölbl[#], **Qi Li**[#], Terry Threlfall and J. Axel Zeitler, Measuring solute concentration with terahertz time-domain spectroscopy in single and multiphase systems, *Analytical Chemistry*, 2022, 94, 3, 1713-1716 (**# are co-first authors**).
6. Michael T. Ruggiero, Johanna Kölbl, **Qi Li** and J. Axel Zeitler, Predicting the structures and associated phase transition mechanisms in disordered crystals via a combination of experimental and theoretical methods, *Faraday Discuss.*, 2018, 211, 425-439.
7. Jingwei Hou, Putu Sutrisna, Tiesheng Wang, Song Gao, **Qi Li**, Chao Zhou, Shijing Sun, Hao-Cheng Yang, Fengxia Wei, Michael T. Ruggiero, J. Axel Zeitler, Anthony Cheetham, Kang Liang and Vicki Chen, Unraveling the interfacial structure-performance correlation of flexible metal-organic framework membranes on polymeric

substrates, *ACS Appl. Mater. Interfaces*, 2019, 11, 5, 5570-5577.

8. **Qi Li**[#], Johanna Kölbl[#], Terry Threlfall, J. Axel Zeitler, In-situ observation of the structure of crystallising magnesium sulphate heptahydrate solutions with terahertz transmission spectroscopy, *Crystal Growth Design* (in preparation; [#] are co-first authors).
9. **Qi Li**, Wen Dong, J. Axel Zeitler, Using terahertz spectroscopy to investigate the low-frequency vibrations and magnetisation of $[\text{C}(\text{NH}_2)_3][\text{M}^{\text{II}}(\text{HCOO})_3]$ metal-organic perovskites (in preparation).

Conference Presentations

1. **Qi Li**, Michael T. Ruggiero and J. Axel Zeitler. Methyl-rotation dynamics in metal-organic frameworks probed with terahertz spectroscopy, *Multi-Scale Modelling of Flexible and Disordered Porous Materials*, CECAM, Paris, France, 2018. (Poster)
2. **Qi Li**, Adam J. Zaczek, Timothy M. Korter, J. Axel Zeitler and Michael T. Ruggiero. Methyl-rotation dynamics in metal-organic frameworks probed with terahertz spectroscopy, *12th Annual Meeting of Pharmaceutical Solid State Research Cluster*, PSSRC, Leuven, Belgium, 2018. (Oral)
3. **Qi Li** and J. Axel Zeitler. Investigating the properties of crystalline materials with terahertz spectroscopy and ab initio simulations, *THz Instrumentation and Applications*, UK-THz, Warwick, UK, 2018. (Oral)
4. **Qi Li** and J. Axel Zeitler. Investigating the properties of crystalline materials with terahertz spectroscopy and ab initio simulations, *CEB Research Conference*, Cambridge, UK, 2019. (Oral)
5. **Qi Li**, Andrew D. Bond and J. Axel Zeitler. Studying mechanical properties and phase transitions of aspirin polymorphs with terahertz spectroscopy and ab initio simulations,

- 44th International Conference on Infrared, Millimeter, and Terahertz Waves (IRMMW-THz)*, Paris, France, 2019. (Poster)
6. **Qi Li**, Andrew D. Bond and J. Axel Zeitler. Studying mechanical properties and phase transitions of aspirin polymorphs with terahertz spectroscopy and ab initio simulations, *13th Annual Meeting of Pharmaceutical Solid State Research Cluster*, PSSRC, Düsseldorf, Germany, 2019. (Oral)
 7. **Qi Li**, Andrew D. Bond and J. Axel Zeitler. Studying mechanical properties and phase transitions of aspirin polymorphs with terahertz spectroscopy and ab initio simulations, *MSSC2019-Ab initio Modelling in Solid State Chemistry*, London, UK, 2019. (Poster)
 8. **Qi Li** and J. Axel Zeitler. Molecular dynamics and magnetic properties of metal-organic perovskites $[C(NH_2)_3][M^{II}(HCOO)_3]$, *14th Annual Meeting of Pharmaceutical Solid State Research Cluster*, PSSRC, Helsinki, Finland, 2020. (Oral)
 9. **Qi Li**, Johanna Kölbl, Terry Threlfall and J. Axel Zeitler. In-situ observation of the structure of crystallising magnesium sulfate solutions, *BCA/BACG Online Joint Spring Meeting*, UK, 2021. (Oral)
 10. **Qi Li** and J. Axel Zeitler. Understanding the metastability of theophylline FIII by means of low frequency vibrational spectroscopy, *CEB Research Conference*, Cambridge, UK, 2021. (Oral)
 11. **Qi Li**, Johanna Kölbl, Terry Threlfall and J. Axel Zeitler. Crystallising magnesium sulfate solutions: observing structure with terahertz spectroscopy, *46th International Conference on Infrared, Millimeter, and Terahertz Waves (IRMMW-THz)*, Chengdu, China, 2021. (Oral)
 12. **Qi Li** and J. Axel Zeitler, Understanding the metastability of theophylline FIII by means of low frequency vibrational spectroscopy, *15th Annual Meeting of Pharmaceutical Solid State Research Cluster*, PSSRC, Glasgow, UK, 2021. (Oral)

Contents

Declaration	i
Abstract	iii
Acknowledgements	v
Publications and Conference Presentations	vi
Table of Contents	xii
List of Figures	xiii
List of Tables	xviii
1 Introduction	1
1.1 Overall Context	1
1.2 Introduction to Terahertz Spectroscopy	4
1.2.1 Terahertz Radiation	4
1.2.2 Terahertz Time-Domain Spectroscopy	12
1.2.3 Rotational and Vibrational Spectroscopy	14
1.2.4 Terahertz Spectroscopy of Liquids and Glasses	20
1.2.5 Terahertz Spectroscopy of Crystals	24
1.3 Density Functional Theory	33
1.3.1 Quantum Mechanics and Electronic Structures	33

1.3.2	Density Functional Theory	40
2	Experimental Methods	50
2.1	Experimental Setup	50
2.1.1	Room Temperature Measurements	50
2.1.2	Variable Temperature Setup	51
2.2	Sample Preparation	53
2.3	Data Acquisition	55
2.4	Data Analysis	58
3	Computational Methods	63
3.1	Introduction to Solid-State DFT	63
3.2	CRYSTAL17 Software Package	66
3.2.1	Single-Point Energy Calculations	67
3.2.2	Geometry Optimisation	68
3.2.3	Frequency Analysis	69
3.2.4	Beyond Frequency Analysis	71
4	Low-Frequency Dynamics and Physical Properties of Metal-Organic Frameworks	74
4.1	Methyl-Rotation Dynamics in Metal-Organic Frameworks: ZIF-8 and ZIF-67	75
4.1.1	Introduction	75
4.1.2	Materials and Methods	78
4.1.3	Results and Discussion	80
4.1.4	Conclusions	85
4.2	Case Study: Elasticity of MOF-5	85
4.2.1	Introduction	85
4.2.2	Materials and Methods	86
4.2.3	Results and Discussion	88
4.2.4	Conclusions	90

5	Low-Frequency Vibrations and Magnetisation of Metal-Organic Perovskites	92
5.1	Introduction	92
5.2	Materials and Methods	94
5.2.1	Materials	94
5.2.2	THz-TDS Measurements	95
5.2.3	Solid-State DFT Simulations	95
5.3	Results and Discussion	98
5.3.1	THz-TDS Measurements	98
5.3.2	Geometry Optimisation	99
5.3.3	Frequency Analysis	102
5.3.4	Magnetisation Analysis of Cu-MOF	102
5.4	Conclusions	104
6	Terahertz Spectroscopy of Small Organic Crystals	107
6.1	New Insights into the Crystallographic Disorder in the Polymorphic Forms of Aspirin from Low-Frequency Vibrational Analysis	108
6.1.1	Introduction	108
6.1.2	Experimental Section	112
6.1.3	Results and Discussion	115
6.1.4	Conclusions	125
6.2	Understanding the Metastability of Theophylline Form III by Means of Low-Frequency Vibrational Spectroscopy	126
6.2.1	Introduction	126
6.2.2	Experimental Section	132
6.2.3	Results and Discussion	136
6.2.4	Conclusions	148
7	In-situ Observation of the Structure of Crystallising Magnesium Sulphate Solutions	150

7.1	Flow Cell to Study Crystallisation Processes In-Situ Using Terahertz Time-Domain Spectroscopy	151
7.1.1	Introduction	151
7.1.2	Methods	153
7.1.3	Results and Discussion	159
7.1.4	Conclusions	163
7.2	Measuring Solute Concentration with Terahertz Time-Domain Spectroscopy in Single and Multiphase Systems	164
7.2.1	Introduction	164
7.2.2	Experimental Section	165
7.2.3	Results and Discussion	167
7.2.4	Conclusions	171
7.3	In-Situ Observation of the Structure of Crystallising Magnesium Sulphate Heptahydrate Solutions with Terahertz Transmission Spectroscopy	172
7.3.1	Introduction	172
7.3.2	Methods	174
7.3.3	Results and Discussion	177
7.3.4	Conclusions	191
8	Conclusions and Future Work	194
8.1	Porous Metal-Organic Frameworks	194
8.2	Metal-Organic Perovskites	196
8.3	Small Organic Molecules	197
8.4	In-Situ Observation of Crystallisation with THz-TDS	199
	Bibliography	201

List of Figures

1.1	Terahertz region of the electromagnetic spectrum.	4
1.2	The schematic diagram of PCA.	7
1.3	The schematic view of the design of PCA.	9
1.4	The schematic diagram of PCA detection.	10
1.5	The schematic diagram of optical rectification.	11
1.6	The schematic diagram of electrooptic sampling.	12
1.7	General arrangement of THz-TDS.	13
1.8	Terahertz time-domain signal and frequency-domain signal.	14
1.9	Demonstrations of a rigid rotor and a vibrational diatomic molecule system.	15
1.10	Illustration of the potential of harmonic oscillators.	16
1.11	An overview of the dielectric response of disordered materials.	20
1.12	The terahertz spectra of amorphous lactose and crystalline α -lactose monohydrate.	21
1.13	Terahertz spectra of five polymorphs of sulfathiazole.	28
1.14	Schematic presentation of Hohenberg-Kohn theorem.	42
1.15	Schematic presentation of solving the Kohn-Sham equation.	44
1.16	The “Jacob’s ladder” of DFT functionals.	46
1.17	The product of two Gaussian functions.	48
2.1	The TeraPulse 4000 spectrometer.	51
2.2	The optics chamber and the sample holder.	52
2.3	A photo of the Janis ST-100 cryostat system.	54
2.4	An overview of the setup for variable temperature measurements.	55

2.5	Parts for sample preparation.	56
2.6	TeraPulse 4000 settings for transmission measurement.	57
2.7	Water peaks in power spectra.	58
2.8	Schematic diagram of THz-TDS transmission measurement.	59
2.9	Using aspirin as an example to illustrate the data analysis procedure.	62
4.1	The formula unit structure and the bulk packing of ZIF-8.	76
4.2	The experimental and simulated terahertz and Raman spectra of ZIF-8 and ZIF-67.	81
4.3	Simulated methyl rotor potential energy of ZIF-8 and ZIF-67.	82
4.4	Simulated methyl rotor potential energy of ZIF-8 and ZIF-67 with vibrational levels and wavefunctions.	83
4.5	The structure of MOF-5.	87
4.6	The asymmetric unit of MOF-5.	88
4.7	The elastic properties of MOF-5.	90
5.1	The structure of $[\text{C}(\text{NH}_2)_3][\text{M}^{\text{II}}(\text{HCOO})_3]$ MOF perovskite.	95
5.2	A supercell of Cu-MOF as an example to illustrate the spin coupling.	97
5.3	The possible three types of anti-ferromagnetic spin coupling configuration.	98
5.4	Experimental terahertz spectra of all the seven MOF perovskites.	100
5.5	The comparison of the simulated and the experimental spectra of the four MOF perovskite systems.	103
5.6	The experimental and simulated spectra of Cu-MOF.	105
5.7	The experimental and simulated AFM-A spectra of Cu-MOF.	105
6.1	Projection of aspirin form I and form II viewed from a, b, and c axis.	110
6.2	Terahertz spectra of aspirin form I acquired by Laman et al.	112
6.3	PXRD patterns for the bulk samples of aspirin form I and the two measured samples of form II.	116

6.4	The maximum absorption coefficient compared with the experimental spectra for aspirin form I and form II.	116
6.5	The experimental spectra of aspirin form I, form II with high polymorphic purity, and form II with low polymorphic purity, and spectra normalised relative to the feature at 1.8 THz.	117
6.6	The simulated and experimental spectra of aspirin form I and form II.	120
6.7	The simulated spectra of aspirin form I and II when bandwidth was set to 1 cm^{-1}	121
6.8	Aspirin form I and form II experimental spectra fitted with the Lorentzian functions and the power law with fixed simulated modes.	122
6.9	The calculated energies of the structures with the atoms displaced in steps along the eigenvectors corresponding to the first spectral features of form I and form II.	123
6.10	C–H \cdots O and C–H $\cdots\pi$ intermolecular contacts within the optimised crystal structures of form I and form II.	124
6.11	The comparison between the Gibbs free energy of two aspirin polymorphs from 7 K to 300 K.	125
6.12	Molecule of theophylline.	127
6.13	Projections of the extended unit cells of theophylline polymorphs FII and FM.	128
6.14	Custom-made chamber used in dehydration process with nitrogen purge.	132
6.15	Thermogravimetric analysis of fine powder samples and large single-crystals of THEO FM before and after the dehydration at room temperature.	138
6.16	PXRD, mid-frequency Raman, and FTIR of THEO polymorphs FII, FM, and FIII.	140
6.17	Terahertz and Raman spectra of THEO FII, FM, and FIII at low frequencies.	141
6.18	Raman spectra acquired over time during dehydration of THEO FM.	142
6.19	The dehydration process of THEO FM tracked by the THz-TDS.	143
6.20	The spectra of the dehydrated THEO FM sample pellets kept after 2 days.	143
6.21	Experimental and simulated IR and Raman spectra of THEO FM.	145

6.22	The IR-active vibrations of water molecules in THEO FM at 64.4 cm^{-1} and 91.9 cm^{-1}	146
6.23	Simulated IR and Raman spectra of THEO FIII(A) and FIII(B), and experimental spectrum of THEO FIII.	148
6.24	The comparison between the terahertz spectra of THEO sample at the end of each dehydration process and the simulated spectra of FIII(A) and FIII(B).	149
7.1	Schematic setup of crystallisation measurements.	154
7.2	Three-view drawing of the cuvette.	155
7.3	Renderings of the metal sample holder with cuvette inserted.	155
7.4	Schematic of the path of the terahertz beam in the sample chamber for different cases.	160
7.5	Data processing procedure of flow cell set up measurements.	161
7.6	Spectra recorded at different times throughout the process of crystallisation, and absorption spectra of MgSO_4 heptahydrate and water at different temperatures.	162
7.7	Absorption coefficient of water from literature and measured in the crystallisation cell.	163
7.8	Solid-state terahertz spectra of crystalline $\text{MgSO}_4 \cdot 7\text{H}_2\text{O}$	167
7.9	The linear fit of temperature ($^{\circ}\text{C}$) and absorption at the example of a solution of MgSO_4 at a frequency of 0.5 THz and $c = 0.14\text{ w/w } \%$	169
7.10	The calibration curve of $\text{MgSO}_4 \cdot 7\text{H}_2\text{O}$ at 5°C	169
7.11	The absorption and calculated concentration c_l at 0.5 THz	171
7.12	Crystalline MgSO_4 hydrates measured at different temperatures.	178
7.13	Visual analysis of crystal growth.	181
7.14	Absorption extracted at $0.5, 1,$ and 1.6 THz while crystallising.	182
7.15	Analysis parameters during crystal growth plotted against concentration, time, and temperature.	184

7.16 Illustration of using the calibration method to calculate liquid phase solute concentration.	186
7.17 Relative absorption calculated and plotted against molar concentration of MgSO ₄	187
7.18 Relative changes in α when comparing the measured to the calculated purely liquid absorption before, during, and after crystallisation.	189
7.19 Crystal dissolution analysis.	192

List of Tables

4.1	The comparison of simulated and experimental structures of ZIF-8 and ZIF-67.	80
4.2	Experimental and simulated energetic components (in meV) of the methyl hindered-rotational process in ZIF-8 and ZIF-67.	84
4.3	The comparison of lattice parameter, bond lengths, and angles between experimental and simulated structures of MOF-5.	89
4.4	The MOF-5 symmetric elastic constants matrix calculated with CRYSTAL17.	89
4.5	The calculated average flexibilities properties of MOF-5.	89
4.6	The eigenvalues of the stiffness matrix.	89
5.1	Categorisation of the seven MOF perovskites based on the electronic structure and the symmetry.	96
5.2	The total energies of optimised structure of MOF perovskites in Hartree. . .	101
5.3	The comparison between the experimental lattice parameters and the optimised structures with the lowest energy (seven MOF perovskites).	102
6.1	The comparison between the simulated structures and the crystallographic data of form I at 300 K and 100 K.	118
6.2	The comparison between the simulated structures and the crystallographic data of form II at 300 K and 100 K.	118
6.3	Comparison of the properties of the two aspirin polymorphs (form I-form II).	118
6.4	The power law and Lorentzian fitting parameters of aspirin form I and form II.	124

6.5	The summary of four sets of THz-TDS measurements of the THEO FM dehydration process.	135
6.6	Main PXRD peaks in the range of 5° to 17° for THEO polymorphs FII, FM and FIII.	137
6.7	The comparison between the optimised and the published experimental structures of THEO FM, FII and FIII(B) to FM.	144
6.8	The energy difference ($10^5 \text{ kJ}\cdot\text{mol}^{-1}$) between THEO FII, FIII(A), FIII(B) and the most stable form FM.	145
7.1	Concentration overview for different solid-state samples of MgSO_4 hydrates.	175
7.2	Data for Figure 7.17.	187

Chapter 1

Introduction

1.1 Overall Context

Crystals are defined as perfectly organised periodic systems. However, other than in ideal situations, some dislocations and a certain degree of disorder are always present, even in crystalline materials. Such disorder results in deviations from the ideal crystalline properties and hence increases complexity regarding the behaviour of such materials. In some crystalline systems, such as in metals, the role of defect structures and how they influence fundamental material properties, e.g. conductivity or tensile strength, have been studied widely. However, such detailed understanding is not as advanced for many other crystalline systems, such as organic molecular materials.¹⁻³ This thesis aims to develop more insight into the disorder in ordered crystalline materials by applying the combined methodologies of terahertz time-domain spectroscopy (THz-TDS) and density functional theory (DFT) simulations. The experimental technique is used to characterise the available samples (likely to have defects), while the computational methods perform the calculations based on the structures of perfect crystals. Given the complexity of the vibrational motions that can be observed at terahertz frequencies, the computational analysis is essential to interpret the data thoroughly, and in turn, the experimental results can serve to validate the accuracy of the computational simulations. Ultimately, defects then are manually introduced into the crystal structures, and

simulations are carried out to investigate how the defects affect the properties of the crystals.

The details of these two main techniques will be discussed in Section 1.2 and Section 1.3, and the implementation will be covered in Chapters 2 and 3, respectively. The studies covered in Chapters 4-7 discuss the applications of this methodology on a range of crystalline materials that are characterised by an increasing level of disorder, including novel metal-organic frameworks (MOFs), classic small organic molecules, and a hydrate system of an inorganic salt.

In the field of materials science, a range of novel materials have been discovered and synthesised to meet the needs of potential applications, and metal organic framework (MOF) structures are a popular class of such materials. They constitute of relatively large complex metal-based organic materials and in this thesis the studies of porous MOFs (Chapter 4) and MOF perovskites (Chapter 5) focused solely on their ordered structures. MOFs combine a range of properties that traditionally only exist in either inorganic or organic materials. Due to the complexity of their structures and the numerous possible combinations of the metals and organic linkers, computational methods are very helpful to screen the most promising structures and to support the future design. In addition, the synthesis of MOFs is often not straightforward, and the products can be unstable. Therefore, computational simulations are applied to provide preliminary results to aid their design for achieving a range of application specific characteristics, such as thermodynamic and mechanical properties, their mechanical flexibility, and surface area, prior to actually carrying out the experiments.⁴⁻⁶ Porous MOFs can be applied to applications in energy storage, chemical separation, and catalysis, which means the pores in the structure are of interest.⁷⁻¹⁰ However, MOF perovskites, where a cation is occupying the centre of the structure, have been reported to exhibit slightly distorted crystals from their ideal cubic structure reflecting some natural disorder.^{11;12} They have a range of potential applications in data communications, multiferroics and solar cells.¹³⁻¹⁷

The focus of Chapter 6 turns to the investigation of small organic molecular crystals and the role defects play in their structures on their properties. This class of materials includes many molecules that are widely used as pharmaceutical drugs. In order to fully characterise active pharmaceutical ingredients (APIs), numerous methods have been utilised

to understand their structure, thermal and mechanical properties.¹⁸⁻²¹ Crystal defects are believed to greatly influence these properties but they are not easy to evaluate. Disorder can originate from impurities or the dislocation of certain atoms and molecules in the crystalline domain. They can be inherent to their structure or induced by the processing of the material, resulting in intergrowth of crystalline polymorphs and facilitate the occurrence of phase transitions that can potentially affect the performance of the drug.^{20;22;23} At the examples of the drugs aspirin and theophylline, Chapter 6 explores the implementation of the combined terahertz and computational methodology to explore this application.

Chapter 7 studies the crystallisation process from an aqueous solution of an inorganic salt, which is the most disordered system discussed in this thesis related to crystals. This system was chosen as a relatively simple model to investigate the crystallisation process that starts from the completely disordered liquid phase from which ordered crystals gradually emerge. Crystallisation is a very important but highly erratic process. In order to develop more insight from the vibrational spectroscopy point of view a versatile setup based on THz-TDS was developed that can monitor the crystal growth and potentially detect the early stage of nucleation.^{24;25} THz-TDS has not been widely applied in this field, but as it probes the vibrations in the amorphous and crystalline phases simultaneously, it has considerable potential for this area of research.²⁶ In addition, a method of measuring local concentration of solute in the liquid phase during crystallisation was also developed with the customised set up.²⁵

In general, the projects presented in this thesis cover different aspects of crystalline systems and consider the effect of disorder over a range of phenomena: For the relatively complex and large crystalline systems, the research is focused on the dynamics in ideal crystals by employing highly accurate computational techniques; for small organic molecules, the subtle defects, that play a role in the field of polymorphs and phase transitions, are studied in detail; and finally the last project investigates the transition from a completely disordered state into an ordered crystal.

1.2 Introduction to Terahertz Spectroscopy

1.2.1 Terahertz Radiation

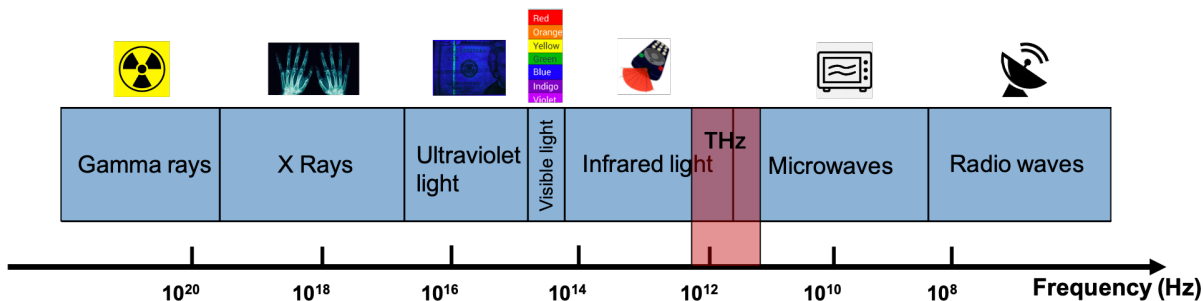


Figure 1.1. Terahertz radiation lies between the far-infrared and the microwave region in the electromagnetic spectrum.²⁷

The electromagnetic spectrum is organised based on the wavelength (frequency) of the radiation, and is categorised from high to low frequencies as gamma rays, X-rays, ultraviolet light, visible light, microwaves, and radio waves (Figure 1.1). Since the spectrum is continuous, the boundary between each type of radiation is not clearly defined. Terahertz radiation refers to the spectral region located between the far-infrared and the microwave region, and roughly covers the frequency range of 0.1 THz to 10 THz.²⁸ In the context of the low-frequency vibrational motions that can be probed using terahertz spectroscopy, the terahertz band is loosely defined as 0.3 THz to 3 THz which is also limited by the performance of the spectrometer. It has been widely applied to study solids such as organic crystals^{26;29–31}, explosives^{32;33}, pigments^{34;35}, and semiconductors^{36;37}, as well as liquids³⁸ and biomolecules^{39–41}. Terahertz radiation corresponds to the photon energies on the order of several millielectron volts (meV).

This region of the spectrum was traditionally referred to as the “terahertz gap”, due to the difficulties associated with the generation and detection of terahertz radiation. In contrast, radiation in the adjacent spectral regions to the terahertz region can be generated using a wide range of well-established approaches. At lower frequencies, the generation of microwaves and millimetre waves utilises electronic devices that are based on oscillating circuits. However, the transit time of carriers in semiconductors limit their application at frequencies exceeding a few gigahertz. In contrast, at frequencies beyond the terahertz range, photonic devices

are applied. The radiation is generated by the recombination of electrons and holes in the conduction and valence bands of semiconductors. However, this is not easily extended to the terahertz region, as no suitable semiconductors are available. In addition, the energy gap needed to generate terahertz radiation is small, which makes it harder, especially at room temperature, to control the required energy jumps. Early experiments using far-infrared gas lasers could reach the terahertz region by exciting transitions between roto-vibrational levels of gas molecules, such as via a CO₂ laser, yet the equipment was large, inefficient and poorly tuneable.^{42;43} In addition, infrared (IR) spectroscopy techniques are also applied for spectral analysis of materials in the area of 10 cm⁻¹ to 400 cm⁻¹, which is referred as the far-infrared region. However, the spectral energy density of a thermal blackbody, such as commonly used silicon carbide (GlobarTM) and Nernst glowers, is much weaker in this low-frequency range compared to the mid-IR region (400 cm⁻¹ to 4000 cm⁻¹). Therefore, far-infrared sources are often operated at high temperature and high emittance is preferred. For the very low-frequency end (~ 50 cm⁻¹), mercury arc lamps are widely applied as sources, but this approach is known to introduce additional noise to the system as well.⁴⁴ For far-infrared radiation (terahertz radiation) detection, bolometers and Golay cells are among the most extensively used choices for incoherent detection. As thermal detectors, both are based on the change of physical properties caused by the absorption of radiation, i.e. the resistance change in a bolometer and the expansion of gas in a Golay cell. Common issues are their slow response and modest noise equivalent power (NEP) value. This can be improved by operating a bolometer at low temperatures but this has the disadvantage of requiring expensive liquid helium cooling and high vacuum setups. Other detectors include the Schottky barrier diodes, pyroelectric detectors, and photoconductive detectors.^{45;46}

Terahertz Spectroscopy

In general, there are two types of terahertz radiation sources: broadband sources that convert the ultrashort optical pulses into terahertz pulses, which is the technique applied in this thesis, and continuous wave (CW) methods that result in narrow band signals. The earliest technique for the generation and detection of coherent pulses of terahertz radiation was by

utilising photoconductive switches, which were first developed by Auston et al. in 1984.⁴⁷ Another popular technique utilised electrooptic materials.⁴⁸ The breakthrough to achieve free space propagation of the generated radiation, and thus enable the spectroscopy applications in this thesis, was achieved in 1988 and 1989.^{49;50} From then on, the use of terahertz radiation for spectroscopic studies was gradually developed by characterising a range of materials. Other generation and detection techniques include large aperture antennas, air/gas induced plasmas, free electron lasers and quantum cascade lasers.⁵¹⁻⁵⁷

Femtosecond Laser Systems

The mode-locked femtosecond (fs) laser is an essential part for the generation and detection of terahertz radiation.⁵¹ The pulse produced from the lasers should follow the relation

$$\Delta\nu\Delta\tau \geq \frac{2\ln 2}{\pi} \approx 0.44 \quad (1.1)$$

where $\Delta\nu$ is the spectral bandwidth of the laser, and $\Delta\tau$ is the duration of the mode-locked pulse. To achieve very short pulses, as required to generate terahertz radiation, a material with large spectral bandwidth is needed, such as titanium-doped aluminium oxide (Ti-Sapphire).

Generation of Terahertz Radiation from Photo-Conductive Antennae

The photo-conductive antenna (PCA) is the oldest and most well-developed method of generating and detecting terahertz radiation. In 1881, Hertz first proposed the idea of using a transient electric dipole to generate broadband radiation. At the time the generated and detected electromagnetic transients were of a duration of greater than a nanosecond.⁵⁸ A hundred years later, Mourou et al. illuminated a GaAs:Cr photoconductor with sub picosecond (ps) pulses, and generated a 3 ps short pulse.⁵⁹ In 1984, Auston et al. applied photoconducting Hertzian dipoles using radiation damaged silicon-on-sapphire for both transmitting and receiving antennas.⁴⁷ This was followed by Karin et al. who observed responses of less than 1 ps and DeFonzo et al. developed the coplanar microstrip antennas.^{60;61} The group

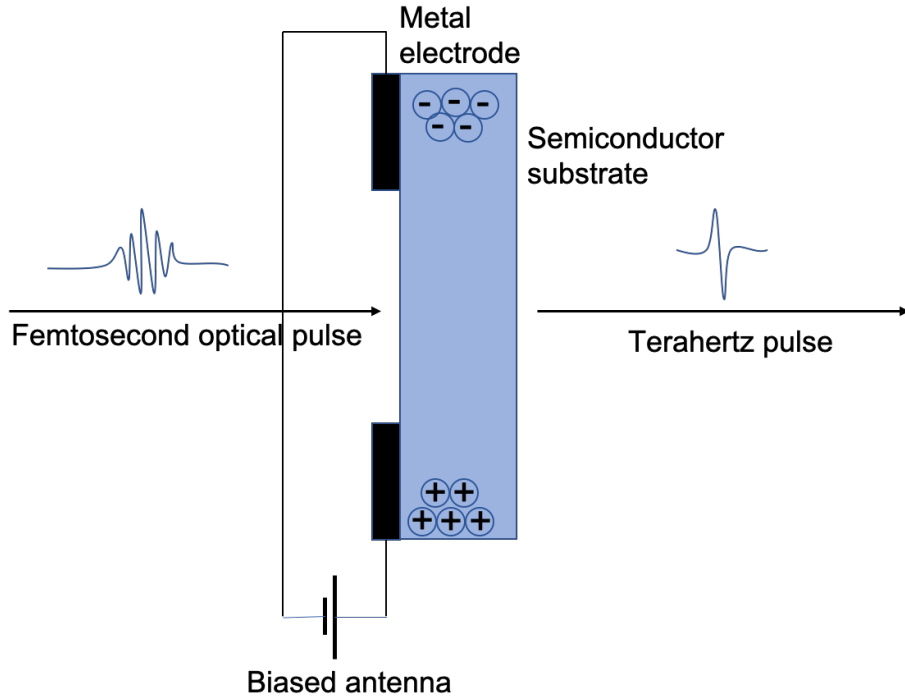


Figure 1.2. The schematic diagram of photoconductive antenna.⁶³

around Auston et al. developed microscopic antennas in 1988 and achieved free space transmission, which opened practical applications of the prior work where the terahertz field was confined within the substrate.⁴⁹ Grischkowsky extended this work by improving the optical setups using suitable spherical lenses to improve the coupling and beam forming which made useful spectrometers possible.^{50;62}

A PCA is usually composed of metal electrodes and a semiconductor substrate as shown in Figure 1.2. The femtosecond optical pulse is focused on the gap between the electrodes, and since the photon energy of the pulse is selected to exceed the band gap of the semiconductor, electron-hole pairs are generated in the substrate. The charges are accelerated by the DC field applied to the metal electrodes, and then are recaptured by the semiconductor structure on time-scales around a picosecond until the system reaches equilibrium. An electric field is generated from the oscillation of the electric dipole, and the radiated electric field is proportional to the second temporal derivative of the dipole moment or the first temporal derivative of the transient current according to Maxwell's equations. From

this procedure, each femtosecond near infrared pulse generates a single cycle electric field at terahertz frequencies (E_{THz}).⁶⁴

$$E_{\text{THz}}(t) \propto \frac{dI_{\text{PC}}(t)}{dt} \quad (1.2)$$

where I_{PC} is the photo-current generated in the gap. Important aspects that influence the performance of PCAs include:

1. The duration of the optical pulse.
2. The recapture time of the semiconductor material.
3. The design of the metal electrodes.
4. The gap between the two electrodes.
5. The power of the femtosecond pulse and the electric field applied to the gap.

The first and the second factors are based on the properties of the material for PCAs. Popular choices include Cr-doped GaAs, radiation-damaged silicon-on-sapphire (RD-SOS), low-temperature grown gallium arsenide (LT-GaAs), semi-insulating GaAs, indium phosphide (InP), and doped indium nitrides.^{47;59;65–68} The optical pulse wavelength needs to be matched with the band gap of the material. For example, the band gap of GaAs is matched by using a Ti:sapphire laser system with a wavelength centred around 800 nm. Ideally, the recapture time is minimised for achieving intense large bandwidth terahertz pulses. The larger the separation distance between the electrodes, the larger the required DC bias voltage is needed to generate the same electric field, but the higher the power of the emitted terahertz radiation. In practice, the operating value of this field is usually chosen to be as large as possible to achieve terahertz signals with higher power whilst balancing against the robustness and longevity of the devices.

Various designs of PCA were compared in the study of Tani et al., including three types of dipoles, the bow-tie, and a coplanar strip line (Figure 1.3).^{69–72} The results showed that the bow-tie antenna was the most powerful design under the same conditions, and the biased strip line resulted in the widest spectral bandwidth of the generated pulses. In addition, the

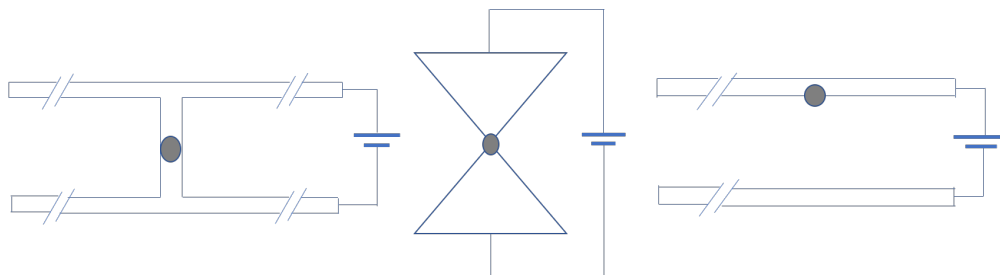


Figure 1.3. The schematic view of the design of PCA: Left: the photoconductive dipole antenna; middle: the bow-tie antenna; right: the photoconductive strip line.⁷²

carrier lifetime of the semiconductor substrate was found not to be an important factor in terms of the maximum achievable spectral bandwidth.⁷²

The detection of the terahertz pulse using a PCA is slightly different from the generation scheme described in Figure 1.2. The femtosecond pulses and the terahertz pulses illuminate the substrate front and back sides respectively. Rather than applying a biased voltage, the antenna gap is only conducting when the two pulses both arrive exactly at the same time. The electric field needed to drive the transient current is provided by the terahertz signal. The photocurrent is a convolution of incident electric field E_{THz} and the transient photoconductivity $\sigma(t)$ induced by the fs pulse.

$$J(t) = \int_{-\infty}^t E_{\text{THz}}(t')\sigma(t-t')dt' \quad (1.3)$$

The transient current is then measured by a lock-in amplifier. As a fs pulse is relatively shorter than a terahertz pulse (ps duration), the detector uses the short laser pulse to map out the terahertz pulse (Figure 1.4).

Optical Rectification and Electro-Optic Sampling

Some electrooptic materials can also be used to generate and detect broadband terahertz radiation based on their nonlinear properties as first described by Bass et al. in 1962.⁷⁴ However, the achievable signal was very weak before femtosecond lasers became more widely available. By illuminating nonlinear crystals with the fast pulses intense electrical fields can be generated (Figure 1.5). The optical rectification and electrooptic sampling that are used for

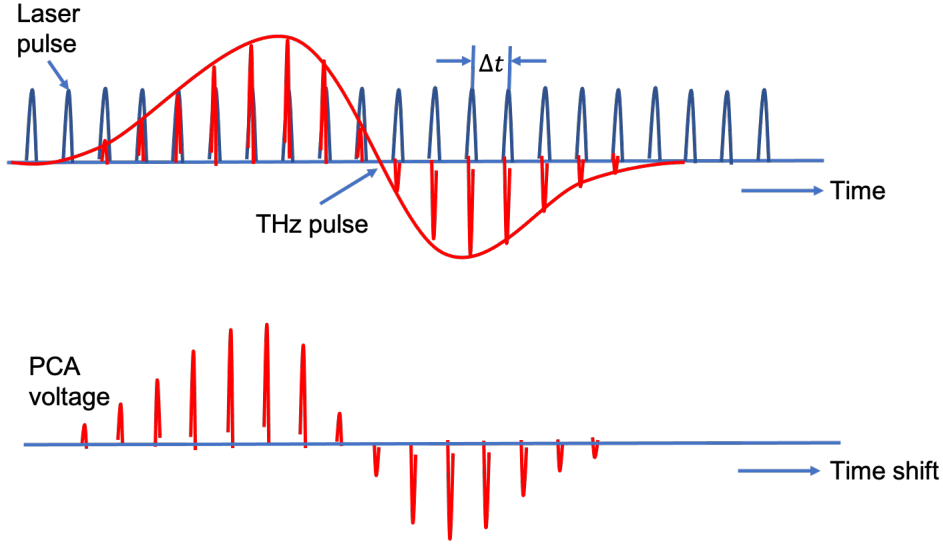


Figure 1.4. The schematic diagram of PCA detection.⁷³

the generation and detection of terahertz radiation, respectively, are based on the electrooptic Cherenkov radiation.^{48;75} The scalar relationship of polarisation P , electric susceptibility $\chi(E)$, and the electric field is

$$P = \chi(E)E \quad (1.4)$$

While in nonlinear crystals, $\chi(E)$ can be expanded in the powers of the electric field E

$$P = (\chi_1 + \chi_2 E + \chi_3 E^2 + \chi_4 E^3 + \dots)E \quad (1.5)$$

where the second order term is considered $P_2 = \chi_2 E^2$ for the optical rectification and electrooptic sampling. Considering an optical electric field $E = E_0 \cos \omega t$, P_2 equals

$$P_2 = \chi_2 E^2 = \chi_2 \frac{E_0^2}{2} (1 + \cos 2\omega t) \quad (1.6)$$

The second part of the induced polarisation is dependent on $\cos 2\omega t$ which describes second harmonic generation, which goes beyond the discussion of this thesis. While for the first part, $P \propto E_0^2$, represents the optical rectification effect, which means that when an optical field passes through a nonlinear crystal, it results in a static electric field. In the case of generating terahertz radiation with fs pulses, the optical field has a time-dependent

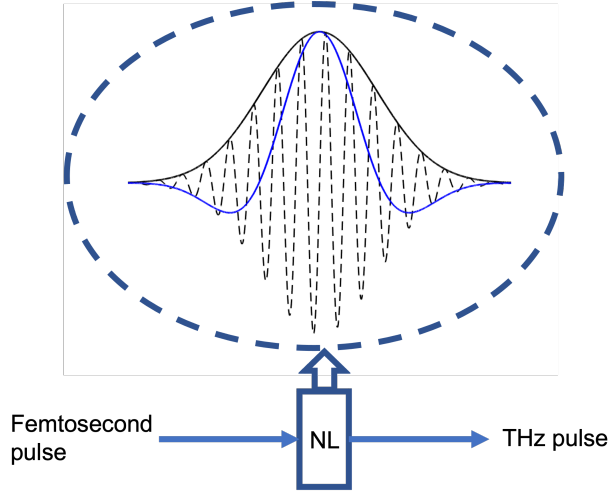


Figure 1.5. The schematic diagram of optical rectification. The fs pulse (dashed line) passes the nonlinear crystal from the left side, and induced polarisation (black solid line), which then generates the terahertz radiation (blue line) that propagates to the right.⁵¹

component $E(t) \sim E_0 e^{-at^2} e^{i\omega t}$, which induces a time-dependent polarisation

$$P \propto E_0^2 e^{-at^2} \quad (1.7)$$

The time varying polarisation generates the terahertz radiation according to Maxwell's equation. In 1988, Auston et al. used LiTaO_3 for generation and coherent detection.⁷⁵ Other commonly used nonlinear crystals are ZnTe , LiNbO_3 , GaAs , and InP .⁷⁶⁻⁷⁸ Some organic molecular crystals can produce terahertz pulses via optical rectification, such as 4-N,N-dimethylamino-4'-N'-methylstilbazolium tosylate (DAST).⁷⁹ The detection is the inverse of electro-optic sampling using Pockel's effect.^{80;81}

As shown in Figure 1.6, when a fs pulse passes through the electro-optic (EO) crystal alone, the optical pulse does not change. After passing through a $1/4$ wavelength plate, it changes to circularly polarised light and the Wollaston prism decomposes it into two components with the same intensity perpendicular to each other. Therefore, the system cannot detect any current. However, when fs and terahertz pulses pass through the EO crystal together, birefringence will convert it to an elliptical pulse that can be decomposed into two components with different intensities. Thus, the terahertz signal can be detected.

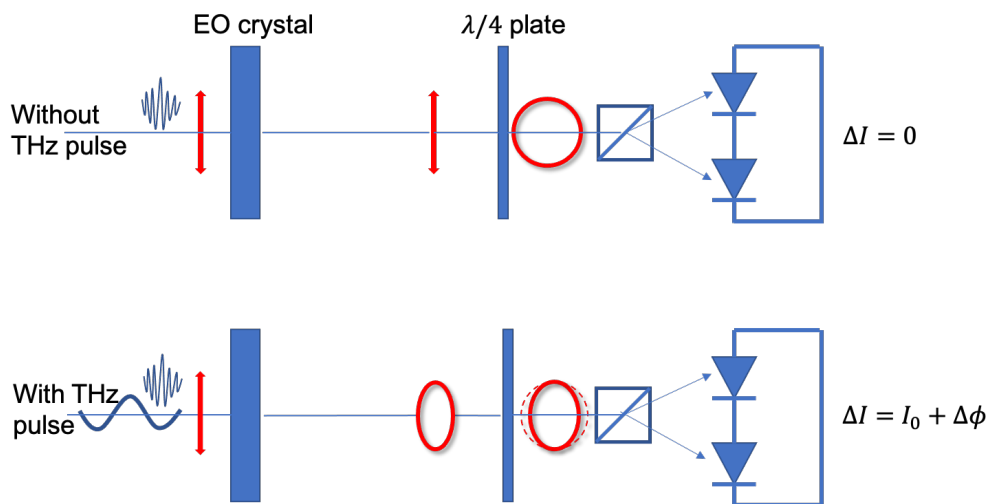


Figure 1.6. The schematic diagram of electrooptic sampling.⁸²

1.2.2 Terahertz Time-Domain Spectroscopy

Figure 1.7 shows a schematic of the general arrangement of terahertz time-domain spectroscopy (THz-TDS), which usually covers the low-frequency region of 0.3 THz to 3 THz (10 cm^{-1} to 100 cm^{-1}).⁵¹ The recent innovations to femtosecond laser systems and terahertz generation methods have made broadband THz-TDS techniques widely available, and this has resulted in a surge of interest in terahertz technology from fundamental science to industrial sectors. It has been largely applied to materials characterisation recently, from crystalline solids including explosives and small organic molecules to liquids and biomolecules.^{26;33;41;84} The pulses are generated by a femtosecond laser and divided into two identical pulses by a beam splitter.

One portion (pump) is directed to the terahertz emitter where a single-cycle of terahertz radiation is generated. This terahertz pulse is then collected and passes through and interacts with the sample, from where it is refocused on the terahertz receiver subsequently. The other portion (probe) is directed into a variable optical time delay stage, and is focused on the terahertz receiver afterwards. The detector only generates a signal if both the probe pulse and the terahertz field are present. The probe pulse is much shorter compared to the pulse of terahertz radiation. Therefore, by adjusting the optical delay, the terahertz signal can be mapped out in the time-domain, and via Fourier transform (FT) the signal is converted into

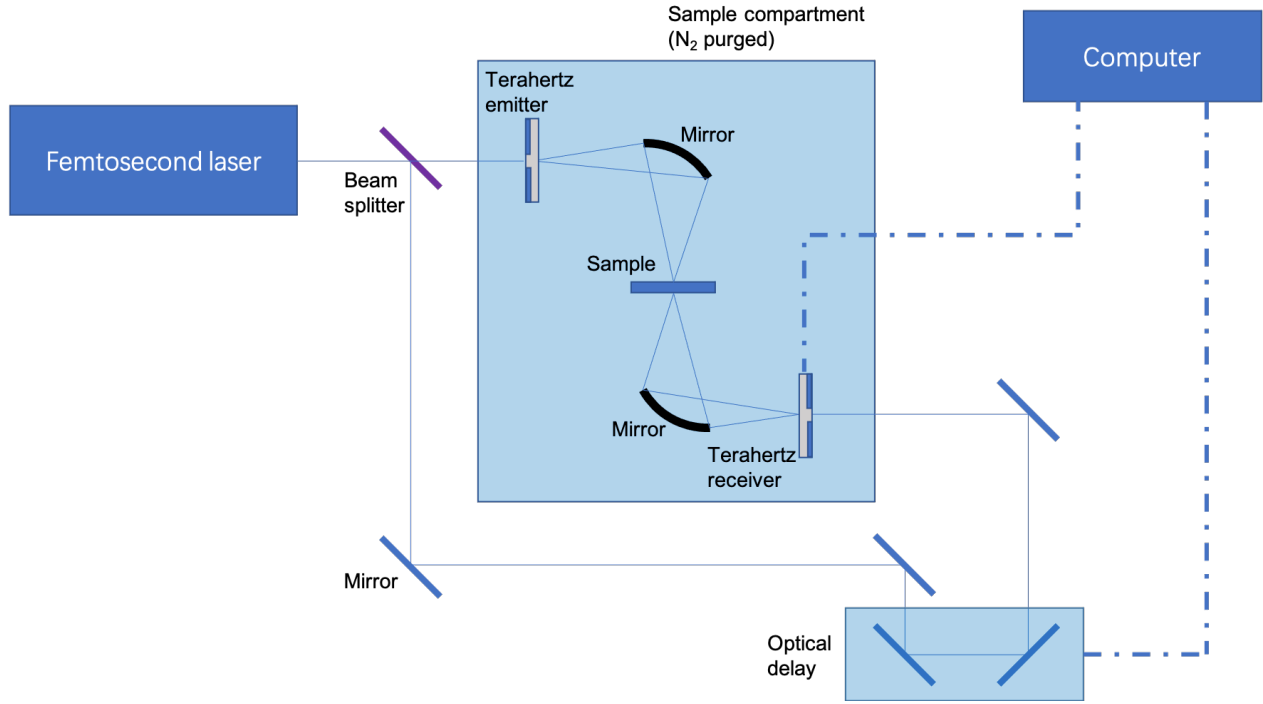


Figure 1.7. General arrangement of terahertz time-domain spectroscopy.⁸³

the frequency-domain.

The results in the frequency-domain can then be divided into phase, $\phi(\omega)$, and amplitude, $A(\omega)$ (Eqn. 1.8, 1.9, and Figure 1.8). Therefore, the complex refractive index can be directly extracted from the terahertz measurements results (details in Section 2.4) without further application of Kramers-Kronig analysis⁸⁵. While THz-TDS can be set in both transmission and reflection geometries, this thesis applies transmission measurements only.

$$E(t) \xrightarrow{\text{FT}} \frac{1}{\sqrt{2\pi}} \int_{-\infty}^{\infty} E(t)e^{-i\omega t} dt = E(\omega) \quad (1.8)$$

$$E(\omega) = A(\omega)e^{i\phi(\omega)} \quad (1.9)$$

where $E(t)$ and $E(\omega)$ are the electric field in the time- and frequency-domain, respectively. ω represents the angular frequency as a scalar, while later in Eqn 1.10 $\boldsymbol{\omega}$ is a vector representing the angular velocity.

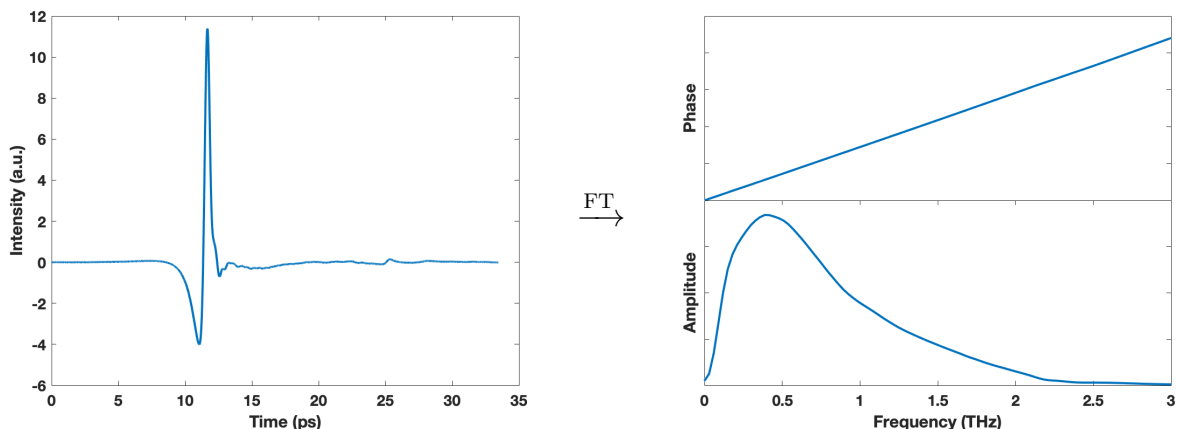


Figure 1.8. Terahertz time-domain signal (left) and frequency-domain signal (right). The upper panel shows the unwrapped phase and the lower panel shows the amplitude.

1.2.3 Rotational and Vibrational Spectroscopy

The spectral region of terahertz radiation spans from the higher frequency boundary of dielectric spectroscopy to the low-frequency side of far-infrared spectroscopy, which are the two long-established techniques and have been widely applied to study molecular vibrations and relaxation processes respectively. The development of THz-TDS offers an opportunity to investigate the interplay between dielectric relaxation and lattice vibrations in materials by probing this spectral band in detail.

The vibrational and rovibrational transitions of molecules without electronic excitations usually fall into the infrared range. The many-body molecular problem can be firstly simplified into a two-body system (i.e. a diatomic molecule). For rotations, a diatomic molecular system is composed of two atoms with the masses of M_A and M_B , respectively (Figure 1.9a).⁸⁶ Assuming they rotate around an axis with an angular velocity of ω , the rotational energy is

$$E_{\text{rot}} = \frac{1}{2}I\omega^2 = \frac{J^2}{2I} \quad (1.10)$$

where $I = M_A R_A^2 + M_B R_B^2 = MR^2$ and $M = \frac{M_A M_B}{(M_A + M_B)}$ is the reduced mass. R is the distance between A and B, and R_A and R_B are the distance from the atom to the centre, respectively.

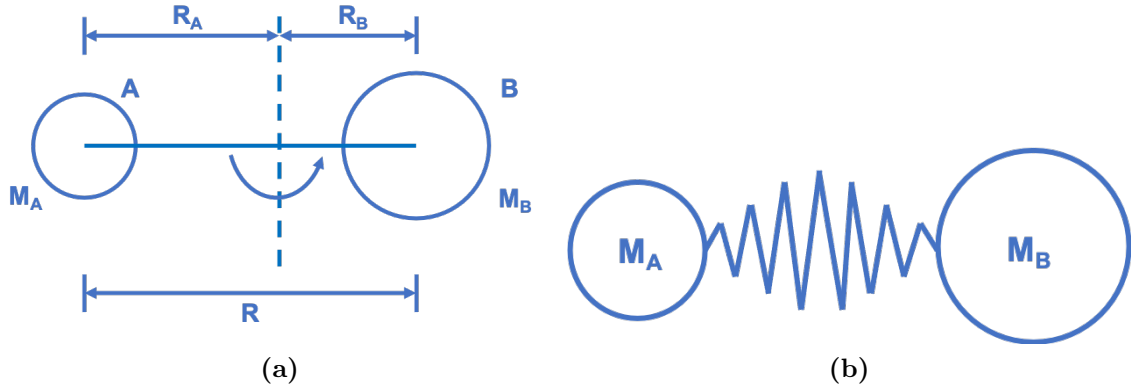


Figure 1.9. Demonstrations of (a) a rigid rotor and (b) a vibrational diatomic molecule system. Adapted from REF[86].

$|J| = I\omega$ is the rotational angular momentum. The square of the angular momentum

$$|J|^2 = J(J + 1)\hbar^2 \quad (1.11)$$

only has discrete values determined by the rotational quantum number J ($J = 0, 1, 2, \dots$), where \hbar is the Planck constant. Therefore, the possible rotational energies are

$$E_{\text{rot}} = \frac{J(J + 1)\hbar^2}{2MR^2} \quad (1.12)$$

where $\hbar = \frac{h}{2\pi}$ is the reduced Planck constant. The energy difference between the adjacent rotational levels is

$$\Delta E_{\text{rot}} = E_{\text{rot}}(J + 1) - E_{\text{rot}}(J) = \frac{(J + 1)\hbar^2}{2MR^2} \quad (1.13)$$

Figure 1.9b shows a system composed of two bonded atoms that vibrate around their equilibrium positions as an example. As the Bohr frequency rule states, the vibrations of molecules can only happen between the transitions of certain discrete energy levels.⁸⁷

$$\nu_{\gamma''\gamma'} = \nu_{\gamma'\gamma''} = \frac{E_{\gamma'} - E_{\gamma''}}{h} \quad (1.14)$$

where ν is the frequency of the radiation, E is the state energy, and γ represents vibrational levels. The fundamental illustration of such motions can start from a diatomic molecule. For

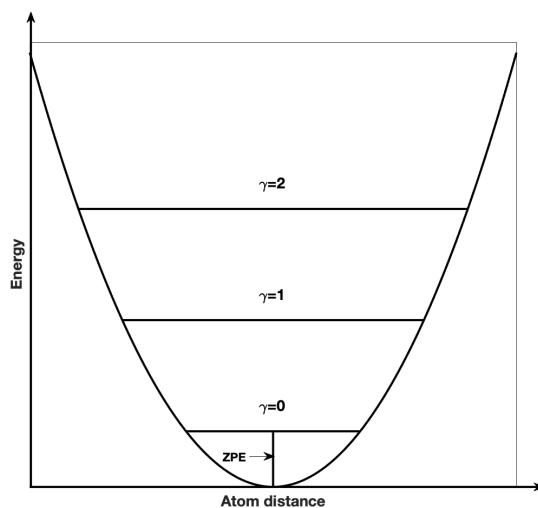


Figure 1.10. Illustration of the potential of harmonic oscillators. Adapted from REF[86].

vibrations, the frequency of such a two-body system is

$$v = \frac{1}{2\pi} \sqrt{\frac{k}{M}} \quad (1.15)$$

where k is the force constant and M is the reduced mass.

The solution of the Schrödinger equation gives the typical potential of a harmonic oscillator as shown in Eqn. 1.16. Only certain transitions are allowed between the energy levels, which correspond to the features on the spectrum. The vibrational levels are evenly spaced, and the energy at level 0 is not zero but $\frac{1}{2}hv$, which is called zero-point energy (ZPE), as shown in Figure 1.10.

$$E_\gamma = \left(\gamma + \frac{1}{2}\right)hv, \quad (\gamma = 0, 1, 2, \dots) \quad (1.16)$$

The two atoms in this model are either bonded or interacting which means they vibrate slightly away from the equilibrium positions. For a molecular crystal, which involves multiple oscillators, the displacements of all the atoms are along a particular normal mode. A system with N atoms has $3N-6$ (for a non-linear system) or $3N-5$ (for a linear system) normal modes. The mode that falls into the terahertz region either corresponds to a collective

motion (a phonon mode type of vibration) with a large mass or a torsional mode with small force constant (as shown in Eqn. 1.15), and also rather than explicitly rotational or vibrational motions, it detects combined motions. The molecular interactions that govern the lattice vibrations at terahertz frequencies can be either intermolecular interactions, such as hydrogen bonds, dipole-dipole interactions, and London dispersion forces, or intramolecular interactions, including some distortions and rotations of molecules. THz-TDS, like other infrared spectroscopic techniques, probes the IR-active normal mode that results from a dipole change between the equilibrium state and the distorted structure upon motion. In addition, compared to other mid-frequency spectroscopic techniques, THz-TDS is very sensitive to thermal effects around room temperature in weakly bonded materials such as hydrogen bonds and dispersion forces. A large population of excited states fall into the terahertz frequency region at room temperature and this broadens the spectral features significantly.²⁸ Therefore, temperature is an important factor when interpreting terahertz spectra, and spectra acquired at lower temperatures can greatly improve the quality when information about ground state transitions is of particular interest.

Two spectroscopy techniques that are frequently used to complement THz-TDS are Fourier-transform infrared spectroscopy (FTIR) and low-frequency Raman spectroscopy. For FTIR, which covers a wide frequency range, the absorption coefficient can be obtained directly from measurements while the refractive index needs to be calculated based on a Kramers-Kronig analysis. In addition, for the widely applied mid-FTIR, it probes fundamental vibrational bands related to the functional groups, and many fingerprint features of samples are also located in the mid-infrared region. However, mid-FTIR can be less powerful when characterising highly similar structures, e.g. polymorphs, as well as long-range collective motions within molecular systems. To reach the same low-frequency region as terahertz spectroscopy, FTIR requires liquid helium cooling for the bolometric detection.⁸⁸ Low-frequency Raman spectroscopy complements THz-TDS as it can probe vibrational modes that are active to the change in polarisability compared to the permanent dipole change, so all active modes within the low-frequency region can be investigated with the combination of two techniques. In addition, Raman spectroscopy is based on scattering effect compared to absorption spectroscopy

like THz-TDS and FTIR.

On the low-frequency side, terahertz spectroscopy covers the extended part of traditional dielectric spectroscopy. Dielectric spectroscopy measures the response of a sample to an external electric field in a wide frequency range from 10^{-6} to 10^{10} Hz (i.e. microwave), which is represented by the complex dielectric function $\hat{\epsilon}(\omega)$. The results provide information of the polarisation of electrons, the movements of ions, and the reorientation motions of dipolar species. This is found to be extremely helpful to study the dielectric relaxation in solvation, liquids, as well as amorphous solids that occurs on a time scale of nanoseconds to femtoseconds.⁸⁹ The dielectric losses can be linked to the complex refractive index $\hat{n}(\omega)$, $\hat{n}(\omega) = n(\omega) + i\kappa(\omega)$, shown in Eqn. 1.17, which can be directly calculated from the experimental results acquired by THz-TDS.²⁸

$$\begin{aligned}\hat{\epsilon}(\omega) &= \epsilon'(\omega) - i\epsilon''(\omega) = \hat{n}(\omega)^2 \\ \epsilon'(\omega) &= n(\omega)^2 - \kappa(\omega)^2 \\ \epsilon''(\omega) &= 2n(\omega)\kappa(\omega) = \frac{n(\omega)\alpha(\omega)c}{\omega}\end{aligned}\tag{1.17}$$

where ω represents the angular frequency, c is the speed of light in vacuum, $\kappa(\omega)$ is the extinction coefficient, and ϵ' and ϵ'' are the real and imaginary part of the dielectric losses, respectively.

The relaxation processes can be resolved into different regions based on the time scales: the slow primary α relaxation and the secondary Johari-Goldstein β (JG- β) relaxation.⁸⁴ The former is related to the global mobility in a frequency range of 10^{-6} to 10^3 Hz. The latter refers to local mobility (i.e. small-scale motions). These relaxation processes can be described with Debye models, e.g. a two-component model

$$\hat{\epsilon}(\omega) = \epsilon_\infty + \frac{\Delta\epsilon_1}{1 + i\omega\tau_1} + \frac{\Delta\epsilon_2}{1 + i\omega\tau_2}\tag{1.18}$$

where $\Delta\epsilon_1$ and $\Delta\epsilon_2$ are the strength of the corresponding relaxation processes, and τ_1 and τ_2 are the relaxation times. Extra Debye terms and oscillators are also applied in addition to Eqn. 1.18 to take other effects into account, such as intermolecular stretching vibrations.

In 1955, Poley studied microwave dispersion of polar liquids and revealed discrepancies between the dielectric constant measured in the microwave region and the square of the complex refractive index extrapolated from the visible and infrared experimental data. Therefore, it was hypothesised that an additional region of dipolar absorption existed in the neighbourhood of a wavelength of 1 mm (i.e. terahertz frequencies). This is mainly caused by the reorientational motions of polar molecules that are triggered by an external electric field, such as terahertz radiation.^{90–92}

In 1965, it was firstly proposed by Chantry and Gebbie that the broad absorption behaviour of liquids in the terahertz region, which is beyond the description of Debye theory, is resulted from the nature of the pseudo-lattice.⁹³ This broad microscopical peak spanning over most of the terahertz region was later referred to as vibrational density of states (VDOS). Strom et al. reported the first terahertz absorption spectra of inorganic glasses using FTIR in 1974.⁹⁴ The study proposed that the temperature-independent absorption of amorphous materials at terahertz frequencies rises with frequency as ν^β ($\beta \lesssim 2$) that resembles the density of states predicted by Debye theory, so it is assumed as an effect of the disorder-induced coupling of the optical radiation to a density of low-frequency Debye mode. In addition, Reid and Evans discovered the γ process in 1982, which corresponds to the same region as mentioned above, by studying decalin solutions of halogenated benzenes and methylene chloride over a broad frequency range from below 100 Hz to 10 THz with dielectric and FTIR spectroscopy.⁹⁵ However, the γ process appears as a defined peak, while the Debye mode only becomes obvious when absorption is plotted against the square of frequency. Additionally, the γ process is temperature dependent. The excess of density of states above the Debye model is defined as the Boson peak (i.e. the Boson peak is the part of the VDOS that is above the Debye level.), which is usually observed around 0.5 THz to 1.2 THz, while the full range of the VDOS can extend to much higher frequencies.²⁸ A recent study of sorbitol identified the Boson peak at 1.1 THz, and its intensity decreases while cooling but the feature does not shift in frequency.⁹⁶

Parrott and Zeitler argued that spectral data covering a broadband are necessary for determining an appropriate fitting of Debye model. As the terahertz region only covers the

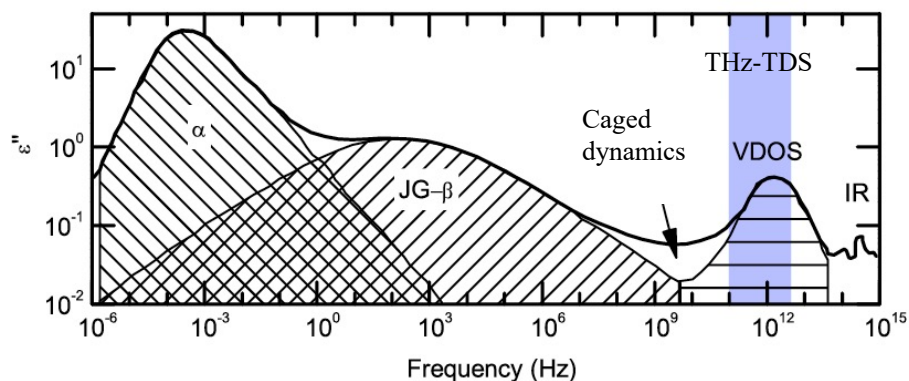


Figure 1.11. An overview of the dielectric response of disordered materials. Adapted from Sibik et al.⁹⁷

high frequency end of the main relaxation process, all the models will fit the terahertz data alone.²⁸

1.2.4 Terahertz Spectroscopy of Liquids and Glasses

The high frequency wing of the dielectric spectra extends to the terahertz region, which represents the reorientational/rotational dynamics of disordered materials and THz-TDS has the potential to grow further insight into this area. The disordered materials discussed here are liquids and glasses, and they lack long-range order compared to crystalline materials. Therefore, their terahertz spectra show an increase of absorption against frequencies but the spectra remain featureless otherwise. It is also important to note that spectra from different disordered materials are hardly distinguishable from each other based on structural factors. While liquids can transform to the crystalline state via cooling, under certain conditions instead of crystallising, they may reach a metastable state called supercooled liquid. When the temperature decreases below a certain point, where the viscosity increases by orders of magnitude and the system seems to not flow anymore on experimental time scales, the glass transition occurs.⁹⁸ The critical temperature point is referred as the glass transition point T_g . The glassy state and all the disordered systems mentioned above are treated as an amorphous phase in this thesis.

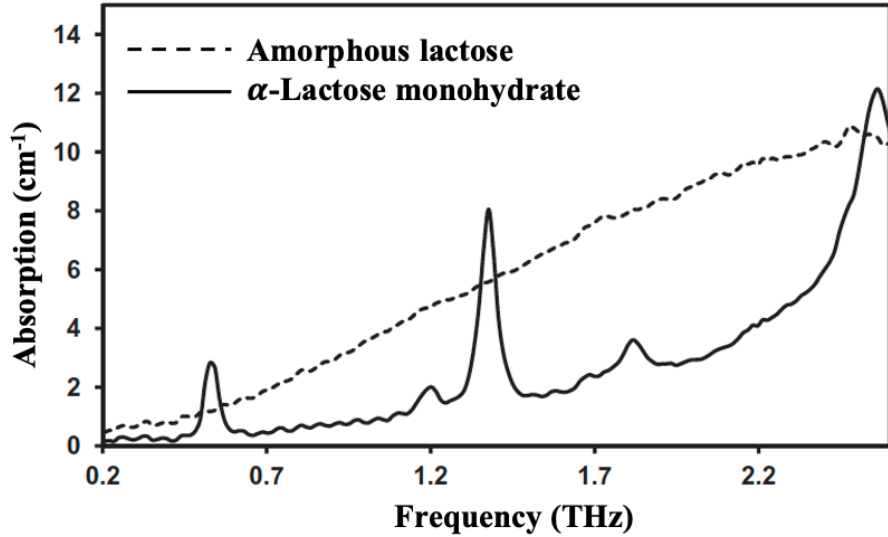


Figure 1.12. The terahertz spectra of amorphous lactose and crystalline α -lactose monohydrate. Adapted from McIntosh et al.⁹⁹

Taraskin et al. demonstrated that, in disordered materials, the frequency-dependent absorption coupling coefficient between the far-infrared photons and atomic vibrations has a universal form of $C(\omega) = A + B\omega^2$, and the study used THz-TDS data of two inorganic glassy systems, SiO_2 and As_2O_3 .¹⁰⁰ Later, Zeitler et al. demonstrated the possibility of studying relaxation and crystallisation by investigating the state transition process of carbamazepine using variable temperature THz-TDS.¹⁰¹ Followed by a systematic study of a series of polyhydric alcohols with temperature resolved terahertz transmission measurements, Sibik et al. observed three universal features in the dielectric losses $\epsilon''(\omega)$ in three temperature regions: At temperatures well below the glass transition temperature (T_g), $\epsilon''(\omega)$ comprises a temperature-independent microscopic peak due to librational motions; a secondary β transition is spotted at $0.65 T_g$; above T_g , α relaxation dominates the losses.⁸⁴ The two key transition points were introduced as $T_{g\alpha}$ and $T_{g\beta}$ with $T_{g\alpha} \sim T_g$ and $T_{g\beta} \ll T_g$. The subscripts corresponded to the relaxation process that the authors originally thought they were linked to. The results support that three absorption mechanisms influence the terahertz response in the organic amorphous materials: VDOS, caged dynamics, and dielectric relaxation (Figure 1.11).⁹⁷ The principal mechanism that applies to terahertz radiation is

the VDOS that governs the frequency region from 0.1 THz upwards. Secondly, the caged dynamics contribute to the terahertz spectra at very low frequencies (<0.5 THz) before the onset of the VDOS, and is also called fast β -relaxation. This region corresponds to the fast rattling process in the molecular systems that happens in the cage formed by the neighbouring molecules, explained by the mode-coupling theory (MCT).¹⁰² Lastly, the primary and secondary dielectric relaxations are too slow from THz-TDS to detect below T_g , while they might contribute to terahertz spectra at higher temperature.

Amorphous solids are of great interest in pharmaceuticals as they offer a solution to overcome the challenge of low solubility that 40 % of drugs on the market and 90 % in development are facing.¹⁰³ However, crystallisation and instability of amorphous drugs are the resultant problems that need to be overcome in order to be able to exploit the advantages of higher dissolution rates in amorphous materials. Dielectric spectroscopy has been widely applied to measure the global mobility in amorphous materials, which is found to play an important role to the crystallisation at temperatures above T_g (and also below T_g). The crystallisation of amorphous drugs well below T_g was found to be related to the JG- β relaxation. As THz-TDS can probe both global and local mobility, it is a promising method to reveal a more complete picture of crystallisation in amorphous solids.

A series of amorphous drugs were measured with terahertz spectroscopy while heating from a low temperature to above $T_{g\alpha}$. The results showed that the larger the gradient of absorption between $T_{g\beta}$ and $T_{g\alpha}$, the local mobility plays a more important role in the crystallisation process (i.e. the more unstable the system is).¹⁰⁴ The authors also acquired terahertz spectra of partially crystallised naproxen in a temperature range of 100 K to 310 K, and crystal growth was reflected by the drop of absorption while heating up. The results revealed that at the temperature above $T_{g\beta}$ the change of terahertz absorption is 3.5 times larger than at lower temperatures.¹⁰⁴

In the field of water studies, terahertz spectroscopy also has additional advantages compared to other commonly used vibrational spectroscopic techniques, namely FTIR and Raman spectroscopy. Water is transparent to the Raman signal, which is useful to some extent, but not if the solution as a whole is of interest. For FTIR, in the mid-frequency region, the

absorption from water is much higher compared to the terahertz region and often results in a noisy background that adds difficulty to measurements and data processing. From this aspect, the advent of terahertz spectroscopy offers a new way of combining vibrational and dielectric spectroscopy.

A number of studies applied the combination of terahertz spectroscopy and molecular dynamics (MD) simulations to investigate the dielectric relaxation processes of liquid water, as well as other liquid systems and mixtures. Ronne and coworkers studied the temperature dependence of dielectric relaxation in liquid water with terahertz reflection spectroscopy and MD, and Venables and Schmuttenmaer studied binary mixtures of water with acetone, acetonitrile, and methanol.^{105;106} Yada et al. applied terahertz time-domain attenuated total reflection spectroscopy and decomposed the dielectric constants of water and heavy water into four components: slow relaxation, fast relaxation, intermolecular stretching vibration, and intermolecular libration.¹⁰⁷ Followed by their work in 2009 the same group studied the intermolecular stretching vibration mode in water isotopes (H_2O , D_2O , and H_2^{18}O) with broadband THz-TDS from 0.2 THz to 7 THz. The results indicate that H_2O is the most structurally disordered.¹⁰⁸ Tielrooij and co-workers controlled the number of water molecules per lipid molecule in the model membrane, and revealed different water dynamics.¹⁰⁹ Also, via various temperature measurements, they determined three different types of water molecules in the system. In addition, Tielrooij et al. investigated the hydrophobic hydration shell of tetramethylurea.¹¹⁰ By studying mixtures at various concentrations and temperatures, the results clearly showed that the reorientation dynamics of water molecules were slower in the hydration shell, but the effect was short-ranged to 8-12 water molecules. Additionally, the number of water molecules in the hydrophobic hydration shell decreased with increasing temperature.

Alcohol-water mixtures have been well-studied with THz-TDS and pulsed field gradient nuclear magnetic resonance (NMR).⁸⁹ From the results of methanol/water, ethanol/water, 1-propanol water, and 2-propanol/water mixtures, three key concentrations were identified for the alcohol-water mixtures (from low to high): (a) Above this concentration, the interaction between water and -OH in alcohol becomes dominant, while below the value the hydration

shells around the alcohols are the main effect; (b) At a higher concentration, the highest level of hydrogen bonding network forms, which is also the point where the system reaches the minimum diffusivity; (c) Above the third concentration, water and alcohol molecules become independent. Following this study, Tan et al. extended the method to a wider range of mixtures: diol-alcohol, diol-water, aprotic solvent-water, and acetone-chloroform.¹¹¹ The concept of characterising mixtures of solutions can be applied to many other systems, such as carbohydrates, peptides, proteins, and salt solutions, to investigate the influence of solutes on the water networks, hydration shells, and solvation dynamics.¹¹²⁻¹¹⁵

1.2.5 Terahertz Spectroscopy of Crystals

Usually, crystallographic methods, such as X-ray diffraction (XRD), are used to detect the arrangement of atoms in crystalline solids. However those techniques, providing a time-averaged structure by their very nature, exclude vibrational motions in molecules that have been proven of great importance of many physical properties of crystals.^{37;116;117} Low-frequency vibrational spectroscopy is a very attractive method to complement the structural investigations, and terahertz spectroscopy is a relatively recent technique that is now readily available along with Raman spectroscopy to investigate the vibrational dynamics.

Amorphous solids and liquids, discussed in the last section, are strongly disordered which results in featureless spectra at terahertz frequencies and lack of any distinctive bands. In contrast, crystals are periodic and well-organised in the long range, so well-defined peaks can be detected in the terahertz absorption spectra. The direct comparison between the amorphous lactose and crystalline α -lactose monohydrate is shown as an example in Figure 1.12. As it is very sensitive to the intermolecular interactions, THz-TDS is useful to identify and distinguish crystalline systems. For example, one early application of THz-TDS is to identify materials for security checks, as many of explosives and illicit drugs have fingerprint features falling into the terahertz region.^{33;118}

Since THz-TDS is very sensitive to the intermolecular interactions of molecular systems, particularly hydrogen bonds in organic materials, it is found to be effective to investigate

the polymorphs in pharmaceuticals. Polymorphism refers to the crystallographic studies of crystalline materials composed of the same molecules while packed in different ways. As polymorphs are chemically identical, mid-IR and conventional Raman spectroscopy at higher frequencies rely on detecting subtle differences in the interaction between (intermolecular) functional groups, while their terahertz spectra are distinct for each polymorphic form. Even though the structural differences between polymorphs can be subtle, their performance can be different in applications, such as solubility and mechanical stability.^{119;120} For example, the well-known drug paracetamol has three polymorphs reported. Other than the unstable form III, the mechanical properties of form I and form II influence the strength of the compacted tablets in manufacturing.¹²⁰

Walther et al. applied THz-TDS to distinguish the three isomers of retinal, and managed to assign the feature at 54 cm^{-1} to an intramolecular vibration of the carbon ring, a pioneering early work on the assignment of terahertz spectra.¹²¹ Further studies of conformers of saccharides in both crystalline and amorphous forms observed that the absorption increased with frequency in the amorphous state, which resulted from the lack of long-range order. It was also concluded that the spectral features in the crystalline phase were due to intermolecular vibrations.¹²²

Taday et al. first applied terahertz pulsed spectroscopy (TPS, now referred to as THz-TDS) to distinguish the two polymorphs of ranitidine hydrochloride.¹²³ It demonstrated the ability of THz-TDS to differentiate the two forms not only in the form of pure samples, but also when formulated as commercial tablets. Furthermore, Taday demonstrated a method of quantifying crystallinity by applying THz-TDS spectra with a partial-least-squares (PLS) calibration model, using aspirin and paracetamol in lactose as examples.¹²⁴ This area was continued by the study of Strachan et al. on carbamazepine, enalapril maleate, indomethacin, and fenoprofen.¹²⁵ Distinct modes were observed in the different crystalline samples, while these features were absent in the spectra of amorphous and liquid samples, supporting the results of Walther's earlier work.¹²² The results strengthened the hypothesis that terahertz spectroscopy can easily differentiate different crystalline polymorphs, and also distinguish crystalline forms from amorphous and liquid forms. The four compounds have also been ap-

plied as model systems to illustrate the method of quantifying polymorphism and crystallinity using THz-TDS and the PLS algorithm. In addition, early studies showed that the hydrate and anhydrate forms of lactose, carbamazepine, piroxicam, theophylline, and D-glucose also exhibit distinct features in the terahertz spectra, and the last two were also used as examples to investigate the dehydration process using terahertz spectroscopy.^{30;126}

Furthermore, THz-TDS was demonstrated to be able to distinguish between different hydrates of metal sulphates, such as $\text{CuSO}_4 \cdot x\text{H}_2\text{O}$ and $\text{FeSO}_4 \cdot x\text{H}_2\text{O}$. By combining the experimental spectra with solid-state simulations, the distinct vibrations can be identified.^{127;128} Similar studies have been performed on alkali halides. Recently, Chen et al. systematically studied 20 alkali halides and their solid hydrates formed from their frozen aqueous solutions.¹²⁹ By comparing the terahertz spectra of sample pellets and frozen solution, new spectral features were identified, which were attributed to the crystallised salts in ice. It was also reported that the cooling rate did influence the formation process but did not change the form obtained, and also a threshold of 1.0 mol l^{-1} of NaCl solution was determined, above which THz-TDS can probe the crystallised hydrates in the frozen solution.

By applying temperature-variable terahertz measurements, it is possible to investigate the phase transition between polymorphs, and to determine the transition temperature and kinetics. Zeitler et al. had the first attempt to study the solid-solid transformation of carbamazepine form III to I in 2005, and following that Upadhyaya et al. reported the phase transitions between two anhydrous and monohydrate forms of theophylline.^{130;131} Subsequently, the five existing polymorphs of sulfathiazole were investigated in 2006, and their terahertz spectra were found to be clearly distinguishable (Figure 1.13). The study also suggested polymorphic impurities in the sample based on the analysis of the terahertz spectra.²⁹ Further studies of carbamazepine extended the polymorphic phase transitions to include the glass transformation as well. Following the work, McIntosh studied crystallisation of amorphous lactose to the monohydrate form, and the sample was kept at 295 K and high humidity. The terahertz spectra were nicely fitted with a Lorentzian function for the spectral peak and a power law for the baseline, and the crystallisation was found to follow the Avrami kinetics.⁹⁹ Sibik et al. used THz-TDS to fully characterise the solid and liquid phase transitions of parac-

etamol while heating up, from the supercooled amorphous phase, crystallising to form III, transforming to form II, then to form I, until melting at 455 K. The kinetics were determined with similar methods as by McIntosh et al.²⁶ Pallipurath and co-workers studied solid-solid phase transformations between the four polymorphs of diflunisal using variable temperature terahertz transmission measurements, as well as Raman spectroscopy, differential scanning calorimetry (DSC), and X-ray powder diffraction (XRPD).³¹

Other than processes with a sharp transition point, Ruggiero et al. reported a continuous phase transition process of N-methyl-4-carboxypyridinium chloride (Me4CP·Cl), which was demonstrated as a model to study concomitant polymorphism using THz-TDS. The authors also quantified the population of each form with both experimental and computational methods.¹³² The combination of THz-TDS, Raman, and ab initio computational methods also challenged the historic belief that the γ form indomethacin is the stable form at ambient conditions, while results showed that the “meta-stable” α form is actually thermodynamically more stable.¹³³ A recent study of camphor applied the combined methods and characterised low-frequency vibrations of disordered materials at an atomic level for the first time. The phase transition points between the ordered structure at low temperature and a disordered structure at high temperature were also predicted at various temperatures and pressures, as well as the key modes at 0.57 THz and 1.91 THz that correspond to the phase-transition pathway.¹³⁴

Even though crystals are by their very nature well-organised and periodic systems, actual crystals are rarely free from defects and disorder can be present. This disorder affects their physiochemical properties and the thermodynamic and kinetic barriers for phase transitions between its polymorphic forms. Terahertz spectroscopy can be used to probe subtle disorder in materials. For example in benzoic acid, there are two possible hydrogen bond configurations between the carboxylic acid groups of the dimers in the crystal structure that can introduce disorder, and it was found to have a big effect on the vibrational spectra, particularly on certain inter-molecular motions.¹³⁵ Delaney et al. investigated two polymorphs of irbesartan (Form A and Form B), which exhibited distinct spectral features at terahertz frequencies, while conformational disorder was also spotted within the n-butyl hydrocarbon

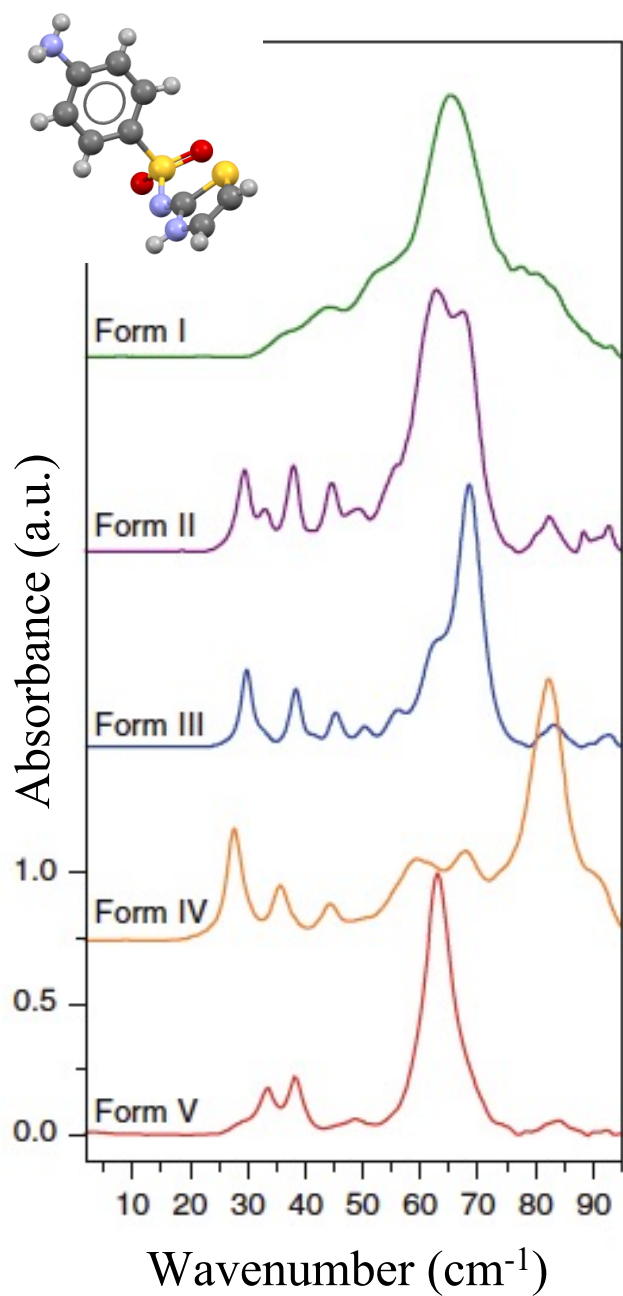


Figure 1.13. Terahertz spectra of five polymorphs of sulfathiazole ($100 \text{ cm}^{-1} = 3 \text{ THz}$). Adapted from Zeitler et al.²⁹

chain in Form B. Combined with solid-state DFT simulations, the disorder was determined to originate from a competition between internal conformational strain and external cohesive binding.¹³⁶ For succinonitrile, orientational disorder was observed in the plastic crystal phase, which arises from the rotation of its central carbon-carbon bond.¹³⁷ This motion is frozen out when cooling and that also results in the phase transition to a rigid crystal. The homochiral and racemic plastic-crystal camphor undergoes a different phase transition upon cooling, as the former forms an ordered crystal while the latter transforms to a glassy state. This phenomenon was assigned to the orientational disorder of the molecules. The broad feature is consistent in the terahertz spectra of the plastic and glassy phases, which was correlated to rotation/libration of the molecules with a relaxation time of 0.2 ps to 0.3 ps.¹³⁸ Simvastatin is an example where three polymorphs are due to the disorder in the ester tail. A recent study investigated the occupational disorder at two ortho sites on one phenyl ring of diflunisal, occupied by hydrogen and fluorine. Combining THz-TDS with computational methods, the authors proposed that four possible configurations of the dimer are in an arrangement showing a short-range correlation, which is represented by fingerprint peaks in the frequency region of 1.5 THz to 5 THz.¹³⁹

Two studies have been published thus far utilising THz-TDS to investigate the crystallisation process from aqueous solution. May and Taday employed terahertz spectroscopy in attenuated total reflectance configuration and monitored the crystallisation of sucrose in confectionary products.¹⁴⁰ The results clearly showed the transition from sugar solution to a solid glassy and then into the crystalline state. Soltani et al. refined this method and successfully proved the existence of intermediate hydrate states in the crystallisation of L-(+)-tartaric acid during the evaporation of water from aqueous solutions of tartaric acid solutions.¹⁴¹ Terahertz spectra were acquired over a period of 60 h while water evaporated and three stages of crystallisation were discernible. At the beginning, the spectra of the solution phase were featureless. During the nucleation stage, the absorption decreased as a result of the reduction in water concentration due to evaporation. In some experiments a discontinuous increase in absorption was observed which was attributed to water being released when the hydrated states transformed to the final crystals. A feature was spotted at approximately 750 GHz

that was hypothesised to result from the vibration of water molecules surrounding the fragments of solvent molecules. The final observed stage was the crystalline phase displaying a dominant absorption feature at 1.1 THz. These three stages were assumed to be happening inhomogeneously throughout the probed volume.

Beyond the characterisation of crystalline and amorphous systems comprising of a single component, there has also been increasing interest of characterising co-crystalline and co-amorphous materials with THz-TDS. Particularly in pharmaceuticals, both strategies offer potential routes to design new drug combinations or formulations to achieve better bioavailability and stability, as well as the potential to combine pharmacological effects. As co-crystals are highly dependent on the non-covalent bonding between the co-crystal formers, and THz-TDS is highly sensitive to probe weak interactions in molecular materials compared to more established solid-state analytical tools, it is not surprising that the technique has been applied to understand the fundamental properties of co-crystals.

The formation of a co-crystal by grinding phenazine and mesaconic acid together was monitored with THz-TDS. As the two formers do not exhibit distinct features in the terahertz spectra, while the co-crystal does, the intensity of the feature at 1.2 THz was used to identify the formation of the co-crystal.¹⁴² Following this study, Parrott et al. compared two pairs of co-crystals in 2009 to test the sensitivity of terahertz spectroscopy.¹⁴³ One pair were composed of theophylline with chiral and racemic forms of malic acid, and the other one were formed from theophylline and the two forms of tartaric acid. The results proved that THz-TDS can distinguish between chiral and racemic co-crystals with similar molecular and supramolecular structures. The study also attempted to use computational methods for feature assignment, while the analysis was limited by the non-ideal agreement between the simulated and experimental spectra. However, a later study of Delaney and Korter successfully reproduced the experimental terahertz spectrum of the flufenamic acid/nicotinamide co-crystal via solid-state simulations, as well as energetic information that is of great importance to the formation of the co-crystal.¹⁴⁴ Recently, Davis et al. reported a study on the polymorphs of the co-crystal enalapril maleate (EM-I and EM-II), which are large and flexible systems.¹⁴⁵ Given the good agreement between the terahertz and computational spectra,

the heterodimer energies, solid cohesion energies, and Gibbs free energies were determined quantitatively from the simulations, which are important information for the further understanding of polymorphs and co-crystals formation mechanisms, as well as their relative stabilities.

While amorphous drugs are expected to help overcome the formulation challenges of low solubility, they tend to be physically unstable and co-amorphous drugs have the potential of better stability and bioavailability compared to single amorphous drugs. Based on the previous studies of using terahertz spectroscopy to study amorphous systems, it has also been found useful to characterise co-amorphous materials, along with other solid-state characterisation methods.^{146;147}

Other than the classical small molecular systems, THz-TDS is also useful to investigate more complicated and emerging materials, such as metal-organic frameworks (MOFs). MOFs, as a class of newly developed hybrid materials, are versatile in structures due to the countless combination of metals and organic linkers. MOFs also have unique properties and large surface area that are suitable for many applications, while realising these technologies require the fundamental understanding of MOFs, including their physical properties, structural stability and thermo-mechanical behaviours. Zeolitic imidazolate frameworks (ZIFs), as a subclass of MOFs, are relatively stable in their thermal and chemical properties compared to other MOF structures. They have been widely studied for potential applications in energy storage and chemical separations, and the performance of these materials for the applications is thought to be closely related to their lattice dynamics. Ryder et al. presented the low-frequency vibrations of ZIF-4, ZIF-7, and ZIF-8 using inelastic neutron scattering (INS) and IR spectroscopy combined with computational methods.¹¹⁶ Interesting motions, such as pore breathing, gate-opening and shearing, were proposed to fall in the terahertz frequency range, but when such dynamics were probed with INS the lack of sufficient spectral resolution limited the analysis. Later, Tan et al. applied THz-TDS to acquire well-resolved spectra of ZIF-8 and ZIF-90, and the results were further compared with computed spectra via ab initio simulations.¹¹⁷ Subsequent XRPD experiments and temperature resolved terahertz transmission measurements suggested water adsorption in ZIF-90 under ambient conditions. Tanno

et al. also observed gas adsorption onto ZIF-8 using terahertz spectroscopy, by monitoring the intensity of the feature at 2 THz.¹⁴⁸ The dynamics of the methyl group in the pores of ZIF-8 and ZIF-67 were closely investigated, as it is believed to be important for the adsorption process.¹⁰ The mechanochemical response of ZIF-8 at various pressures was reported to be connected with gate-opening motions of the imidazolate linkers, which can then be linked to the change of pressure- and temperature-dependent terahertz spectra.¹⁴⁹ THz-TDS has also been applied to MOFs beyond the ZIFs family. For example, Schröck et al. characterised the absorbed interfacial water in MOF-5 with THz-TDS and MD simulations.¹⁵⁰ A coupling of the intermolecular interactions of the absorbed water molecules to the collective motions of the framework was observed at 4 wt% hydration, and MOF-5 decomposed when the water content reached 8 wt%. The very first studies have also started to apply terahertz spectroscopy to investigate the conductivity of MOFs.¹⁵¹ In addition, the technique has also been applied to many other emerging materials, including perovskite solar absorbers, metal oxide photoelectrodes, and 2D materials.¹⁵²

Many of the studies mentioned above applied computational methods along with terahertz spectroscopy to fully characterise the solid-state material of interest. Due to the complexities of the phonon modes at terahertz frequencies, it is much more challenging to assign the experimentally measured peaks to specific vibrational motions compared to the motion of characteristic functional groups that can be observed in the mid-infrared by FTIR spectroscopy for example. Therefore, the application of highly accurate computational techniques that have been developed for periodic solid structures are necessary for the interpretation of the experimental low-frequency spectra.

The spectra are calculated based on the crystal structure as determined by crystallography methods and the resultant spectra can then be compared to the experimental terahertz or low-frequency Raman spectroscopy results. A good agreement between the experimental spectra and the computational output serves to validate the simulation and further analysis of the simulation results can be performed quite confidently. Recently, it has been shown that by combining computational methods with low-frequency vibrational spectroscopy it is possible to go beyond feature assignment and that this approach can facilitate fundamen-

tal understanding of non-covalent interactions. It has been shown to be a powerful method with potential for a wide range of research, such as polymorphism in pharmaceuticals and the properties of well-known as well as emerging materials. Many computational methods have been developed to simulate molecular systems, such as density functional theory (DFT), molecular dynamics (MD), and Monte Carlo simulations.^{153;154} A number of popular software packages have been developed, namely CASTEP, VASP, Gaussian, CP2K, and CRYSTAL17 amongst others that readily perform the task provided sufficient computational resource is available.¹⁵⁵⁻¹⁵⁹ This thesis mainly applies the DFT method as implemented by the CRYSTAL17 software package that will be discussed in detail in the following section and Chapter 3.

1.3 Density Functional Theory

1.3.1 Quantum Mechanics and Electronic Structures

At the beginning of the 20th century, it became apparent that some experimentally observed phenomena could no longer be explained by classical physics, such as atomic spectra, the stability of atoms, radioactivity, blackbody radiation, and the photo electric effect.¹⁶⁰ This highlighted that the existing theory of mechanics was not adequate to understand the physical phenomena that could be measured. In 1923 Louis de Broglie postulated that not just light but that electrons and potentially all matter exhibit wave properties.¹⁶¹ The De Broglie relation represents the relation of wavelength λ and the momentum p , $\lambda = \frac{h}{p}$, where h is the Planck constant. The following year, Werner Heisenberg established a matrix formulation of quantum mechanics, and in 1927 he established the famous Heisenberg uncertainty principle.¹⁶² In 1926, Erwin Schrödinger derived the equation that now bears his name that offers a wave-based explanation of the quantum behaviour.¹⁶³ This equation is at the heart of quantum chemistry and is used to describe the electronic structure and molecular dynamics, as well as for the quantum Monte Carlo method.

In order to solve electronic problems in chemistry, quantum chemists are aiming to find

approximate solutions of the time-independent Schrödinger equation.

$$\hat{H}\psi = E\psi \quad (1.19)$$

where \hat{H} is the Hamilton operator, and ψ is the wavefunction. An operator, in general, transforms one wavefunction into another.

In a molecular system, the Hamiltonian \hat{H} includes the kinetic energy of the electrons (\hat{T}_e) and the nuclei (\hat{T}_N), the Coulomb attraction between nuclei and electrons (\hat{Z}), and the repulsion between electrons (\hat{U}) and between nuclei (\hat{N}) energies.¹⁶⁴

$$\hat{H} = \hat{T}_e + \hat{T}_N + \hat{Z} + \hat{U} + \hat{N} \quad (1.20)$$

By expanding each energy term, the \hat{H} operator can be expressed as:

$$\hat{H} = \sum_i^N -\frac{\hbar}{2m_i} \nabla_i^2 + \sum_I^M -\frac{\hbar}{2m_I} \nabla_I^2 + \xi \left(\sum_{i,I}^N \frac{Z_I}{|r_i - R_I|} + \frac{1}{2} \sum_i^N \sum_{j \neq i}^N \frac{1}{|r_i - r_j|} + \sum_I^M \sum_{J \neq I}^M \frac{Z_I Z_J}{|R_I - R_J|} \right) \quad (1.21)$$

$$\xi = \frac{e^2}{4\pi\epsilon_0} \quad (1.22)$$

where \hbar is the Planck constant, m_i and m_I are the mass of electrons and nucleus, r and R are the radii of electrons and nucleus, and Z is the positive charge of the nucleus. The following subsections will cover how the equation is solved approximately.

The Born-Oppenheimer Approximation

The Born-Oppenheimer approximation divides the electronic problem into two parts: the electronic and the nuclear Schrödinger equation.^{165;166} Since the nuclei are much heavier than the electrons, they move relatively much more slowly. The kinetic energy of the nuclei can be neglected, and the repulsion between the nuclei can be treated as a constant. After

this approximation, the sum of the rest terms is the electronic Hamiltonian \hat{H}_{elec} :

$$\hat{H}_{\text{elec}} = - \sum_{i=1}^N \frac{1}{2} \nabla_i^2 - \sum_{i=1}^N \sum_{A=1}^M \frac{Z_A}{r_{iA}} + \sum_{i=1}^N \sum_{j>i}^N \frac{1}{r_{ij}} \quad (1.23)$$

Therefore, the electronic Schrödinger equation is:

$$\hat{H}_{\text{elec}} \psi_{\text{elec}} = E_{\text{elec}} \psi_{\text{elec}} \quad (1.24)$$

and φ_{elec} is the electronic wavefunction. $\varphi_{\text{elec}} = \varphi_{\text{elec}}(\mathbf{r}_i; \mathbf{R}_A)$ means that the electronic wavefunction not only depends on the electronic coordinates, but also it varies with the coordinates differently when the nuclear coordinates change. The total energy for stagnant nuclei is the electronic energy plus the repulsion between nuclei:

$$E_{\text{tot}} = E_{\text{elec}} + \sum_{A=1}^M \sum_{B>A}^M \frac{Z_A Z_B}{R_{AB}} \quad (1.25)$$

Variational Principle

The variational principle states that the expectation value of the Hamiltonian is the ground-state energy and also the lowest energy that can be found.^{167;168}

$$E_{GS} \leq \langle \Psi | \hat{H} | \Psi \rangle \quad (1.26)$$

where E_{GS} is the ground-state energy, and Ψ is the normalised wavefunction. If $\Psi = \sum_n C_n \Psi_n$ (n is the number of particles, and C_n is the corresponding coefficient of the wavefunction), then

$$\langle \Psi | H | \Psi \rangle = \sum_n |C_n|^2 \langle \Psi_n | H | \Psi_n \rangle = \sum_n |C_n|^2 E_n \geq E_0 \sum_n |C_n|^2 = E_0 \quad (1.27)$$

The equal sign is only valid for the ground state. This is an important principle that is applied to the Hartree-Fock approximation and density functional theory.

Slater Determinants

The electronic Hamiltonian in Eqn. 1.23 is only related to the spatial coordinates, but to fully describe the state of an electron, the spin status must be specified. Thus, two spin functions $\alpha(\omega)$ and $\alpha(\beta)$ are introduced to the theory representing spin up and down, respectively. The electrons should be described in four coordinates (\mathbf{x}): three spatial coordinates and one spin coordinate, so the wavefunction of a system with N electrons is $\chi(\mathbf{x}_1, \mathbf{x}_1, \dots, \mathbf{x}_N)$. Because the Hamiltonian operator does not reflect the effect of spin, an additional requirement of the wavefunction theory is needed. The antisymmetry principle states that “*A many-electron wavefunction must be antisymmetric with respect to the interchange of the coordinate \mathbf{x} of any two electrons.*”¹⁶² The formulation is:

$$\chi(\mathbf{x}_1, \dots, \mathbf{x}_i, \dots, \mathbf{x}_j, \dots, \mathbf{x}_i, \dots, \mathbf{x}_j, \dots, \mathbf{x}_N) = -\chi(\mathbf{x}_1, \dots, \mathbf{x}_j, \dots, \mathbf{x}_i, \dots, \mathbf{x}_i, \dots, \mathbf{x}_j, \dots, \mathbf{x}_N) \quad (1.28)$$

To be more specific, as illustrated in the Pauli exclusion principle, “*Two or more identical fermions cannot occupy the same quantum state within a quantum system simultaneously.*”¹⁶⁹ Therefore, a satisfied wavefunction must satisfy the Schrödinger equation while being anti-symmetric. For a single electron, the spatial orbital ($\psi_i(\mathbf{r})$) only describes the spatial distribution of the electron, while the spin orbital $\chi(\mathbf{x})$ also describes its spin

$$\chi(\mathbf{x}) = \begin{cases} \psi(\mathbf{r})\alpha(\omega) \\ \psi(\mathbf{r})\alpha(\beta) \end{cases}$$

For a system with N -electrons, the interactions between the electrons make things much more complicated, so the electron-electron interactions are neglected as a start. Then, the Hamiltonian for the whole system is

$$\hat{H} = \sum_{i=1}^N h(i) \quad (1.29)$$

where $h(i)$ is the kinetic energy and the potential energy of a single electron i . The

wavefunction is the product of the spin orbital wavefunctions of each electron.

$$\chi^{\text{HP}}(\mathbf{x}_1, \mathbf{x}_2, \dots, \mathbf{x}_N) = \chi_i(\mathbf{x}_1)\chi_i(\mathbf{x}_2)\dots\chi_i(\mathbf{x}_N) \quad (1.30)$$

where χ^{HP} is termed as a Hartree product, and the electrons are described by their own orbitals exclusively. The main discrepancies of the Hartree product are the distinguishability between electrons and the dissatisfaction of the antisymmetry principle. Both can be resolved by the Slater determinant.^{166;168}

If we consider a system with two electrons with electron 1 in χ_i and electron 2 in χ_j , the Hartree product is

$$\chi_{12}^{\text{HP}}(\mathbf{x}_1, \mathbf{x}_2) = \chi_i(\mathbf{x}_1)\chi_j(\mathbf{x}_2) \quad (1.31)$$

Alternatively, if one is in χ_j and two is in χ_i , then

$$\chi_{21}^{\text{HP}}(\mathbf{x}_1, \mathbf{x}_2) = \chi_i(\mathbf{x}_2)\chi_j(\mathbf{x}_1) \quad (1.32)$$

The Slater determinant solves the two problems via introducing a linear combination of the two Hartree products. The wavefunction can thus be represented as:

$$\chi(\mathbf{x}_1, \mathbf{x}_2) = 2^{-\frac{1}{2}} \begin{vmatrix} \chi_i(\mathbf{x}_1) & \chi_j(\mathbf{x}_1) \\ \chi_i(\mathbf{x}_2) & \chi_j(\mathbf{x}_2) \end{vmatrix} \quad (1.33)$$

In Eqn. 1.33, the two electrons are indistinguishable, and the sign of the wavefunction will change if the coordinates are interchanged. In addition, the determinant becomes zero if the two columns are equal, which means two electrons cannot be at the exact same quantum state. For an N -electron system, the Slater equation is

$$\chi(\mathbf{x}_1, \mathbf{x}_2, \dots, \mathbf{x}_N) = \frac{1}{\sqrt{N!}} \begin{vmatrix} \chi_1(\mathbf{x}_1) & \chi_2(\mathbf{x}_1) & \dots & \chi_n(\mathbf{x}_1) \\ \chi_1(\mathbf{x}_2) & \chi_2(\mathbf{x}_2) & \dots & \chi_n(\mathbf{x}_2) \\ \dots & \dots & \dots & \dots \\ \chi_1(\mathbf{x}_n) & \chi_2(\mathbf{x}_n) & \dots & \chi_n(\mathbf{x}_n) \end{vmatrix} \quad (1.34)$$

Hartree-Fock Approximation

In the late 1920s, Hartree and Fock were the first trying to tackle the many-body system, and their method was to alternate the complex many-electron problem into a one-electron problem, also referred to as the Hartree-Fock approximation.^{166;170-173} This was achieved by treating the electron-electron repulsion with an average potential. The simplest wavefunction available that can describe an N -electron system at ground state is the Slater determinant. All other states are referred to as excited. Therefore, Eqn. 1.34 can also be written as

$$|\chi_0\rangle = |\chi_1\chi_2\cdots\chi_N\rangle \quad (1.35)$$

The choice of the spin orbitals is flexible, while according to the variational principle, the best choice should result in the lowest energy E_0 .

$$E_0 = \langle \chi_0 | \hat{H} | \chi_0 \rangle \quad (1.36)$$

For two electrons, Eqn. 1.36 can be extended as

$$\hat{h}(1)\chi_a(1) + \sum_{b \neq a} \left[\int d\mathbf{x}_2 |\chi_b(2)|^2 r_{12}^{-1} \right] \chi_a(1) - \sum_{b \neq a} \left[\int d\mathbf{x}_2 \chi_b^*(2) \chi_a(2) r_{12}^{-1} \right] \chi_b(1) = \varepsilon_a \chi_a(1) \quad (1.37)$$

where $\hat{h}(1) = -\frac{1}{2}\nabla_1^2 - \sum_A \frac{Z_A}{r_{1A}}$ includes the kinetic energy and the attractive energy between the chosen electron 1 to the nuclei. The first term involving electron 2 is the Coulomb interactions represented by the Hartree product, while the second term is the exchange term arising from the antisymmetric effect. The spin orbitals χ_a and χ_b can vary until the electronic energy reaches the minimum, and the two orbitals are chosen orthonormal to each other, $\langle \chi_a | \chi_b \rangle = \delta_{ab}$. The Coulomb operator and the exchange operator for electron 1 are defined by $J_b(1)$ and $H_b(2)$, respectively.

$$J_b(1) = \int d\mathbf{x}_2 |\chi_b(2)|^2 r_{12}^{-1} \quad (1.38)$$

$$H_b(1) = \int d\mathbf{x}_2 \chi_b^*(2) r_{12}^{-1} \chi_a(2) \quad (1.39)$$

where r_{12}^{-1} is the average interaction of electron 1 and 2. Therefore, Eqn. 1.37 can be rewritten as

$$\left[h(1) + \sum_{b \neq a} J_b(1) - \sum_{b \neq a} H_b(1) \right] \chi_a(1) = \varepsilon_a \chi_a(1) \quad (1.40)$$

Removing the summation, the Fock operator is equal to

$$f(1) = h(1) + \sum_b J_b(1) - H_b(1) \quad (1.41)$$

where $h(1)$ is the core-Hamiltonian operator, and the other parts compose the Hartree-Fock potential $v^{\text{HF}}(1)$.

$$v^{\text{HF}}(1) = \sum_b J_b(1) - H_b(1) \quad (1.42)$$

Then, the Hartree-Fock equation becomes

$$f(i)\chi(\mathbf{x}_i) = \varepsilon\chi(\mathbf{x}_i) \quad (1.43)$$

or without the consideration of spin

$$f(i)\psi(\mathbf{r}_i) = \varepsilon\psi(\mathbf{r}_i) \quad (1.44)$$

where $f(i)$ ¹ is the effective one-electron operator, and the $v^{\text{HF}}(i)$ is the average potential that one electron experiences when other electrons exist. As $v^{\text{HF}}(i)$, the average potential experienced by the i th electron, depends on the spin orbitals of the other electrons, Eqn. 1.43 must be solved iteratively. This procedure is the self-consistent-field (SCF) method that starts with an initial guess and calculates the average field to solve Eqn. 1.43 for a new set of spin orbitals. It then repeats the calculation with the new set of spin orbitals until the self-consistency is reached.

For a set of known basis functions $\varphi_\mu (\mu = 1, 2, \dots, K)$, the molecular orbitals can be

¹ $f(i) = -\frac{1}{2}\nabla_i^2 - \sum_{A=1}^M \frac{Z_A}{r_{iA}} + v^{\text{HF}}(i)$

expanded as a linear expansion

$$\psi_i = \sum_{\mu=1}^K C_{\mu i} \varphi_{\mu}, i = 1, 2, \dots, K \quad (1.45)$$

Since the set can only perfectly describe the molecular orbitals when it is complete, the choice of basis functions offers a reasonable description due to the restriction of computational resources. Plugging Eqn. 1.45 into Eqn. 1.44 and using v to illustrate every possible combination:

$$f(1) \sum_v C_{vi} \varphi_v(1) = \varepsilon_i \sum_v C_{vi} \varphi_v(1) \quad (1.46)$$

Multiplying φ_{μ}^* on both sides and integrating over \mathbf{r}_1 , the equations turns into a matrix equation

$$\sum_v C_{vi} \int d\mathbf{r}_1 \varphi_{\mu}^*(1) f(1) \varphi_v(1) = \varepsilon_i \sum_v C_{vi} \int d\mathbf{r}_1 \varphi_{\mu}^*(1) \varphi_v(1) \quad (1.47)$$

where $S_{\mu\nu} = \int d\mathbf{r}_1 \varphi_{\mu}^*(1) \varphi_{\nu}(1)$ is the overlap matrix, and $F_{\mu\nu} = \int d\mathbf{r}_1 \varphi_{\mu}^*(1) f(1) \varphi_{\nu}(1)$ is the Fock matrix. The Hartree Fock equation can now be rewritten in an integrated form, called the Roothaan's equation

$$\sum_v F_{\mu\nu} C_{vi} = \varepsilon_i \sum_v S_{\mu\nu} C_{vi} \quad (1.48)$$

or for the simplest $\mathbf{FC}=\mathbf{SC}\varepsilon$, where \mathbf{C} is a $K \times K$ coefficients matrix, and ε is diagonal matrix with the value of orbital energies.

1.3.2 Density Functional Theory

The Hartree-Fock theory was a breakthrough, and provided a way to handle the many-body problem. There are still some limitations: First, for a N -electron system, the full wavefunction is a $3N$ -dimensional function (and could be even larger if spin is considered); Second, the HF theory treated electrons individually without interactions with others, which was obviously not ideal. An alternative choice is to use the density of electrons at a certain position $n(\mathbf{r})$. This led to the development of density functional theory (DFT). For an N -

electron system, the density is

$$n(\mathbf{r}) = N \int \psi^*(\mathbf{r}, \mathbf{r}_2, \dots, \mathbf{r}_N) \psi(\mathbf{r}, \mathbf{r}_2, \dots, \mathbf{r}_N) d\mathbf{r} d\mathbf{r}_2 \dots d\mathbf{r}_N \quad (1.49)$$

where ψ^* is the complex conjugate of ψ . One attractive aspect of using the electron density is that it is a function of only three coordinates, while for the full wavefunction the dimension is $3N$ coordinates, increasing with the number of electrons. The idea of DFT was first proposed by Thomas and Fermi in 1927.^{174;175} They treated the system of electrons as non-interacting electrons in a homogeneous gas, therefore the density was equal to the local density at a given point. Dirac in 1930 extended the theory and was the first one who introduced a local approximation of exchange.¹⁷⁶ This exchange correlation is still the key topic of the DFT today. The full energy equation of the Thomas-Fermi-Dirac approximation is

$$E_{\text{TF}}[n] = C_1 \int d^3r n(\mathbf{r})^{(5/3)} + \int d^3r V_{\text{ext}}(\mathbf{r}) n(\mathbf{r}) + C_2 \int d^3r n(\mathbf{r})^{4/3} + \frac{1}{2} \int d^3r d^3r' \frac{n(\mathbf{r})n(\mathbf{r}')}{|\mathbf{r} - \mathbf{r}'|} \quad (1.50)$$

where $V_{\text{ext}}(\mathbf{r})$ is an external potential, and for electrons in materials, it is the Coulomb potential due to the existence of nuclei.² The first term is the local kinetic energy, the third term is the local exchange between electrons, and the last term is the electrostatic Hartree energy. The ground state density, $n_0(\mathbf{r})$, is the solution that gives the lowest energy in Eqn. 1.50, and also the answer is constrained by

$$\int d^3r n(\mathbf{r}) = N \quad (1.51)$$

where N is the total number of electrons. While the local approximation in the Thomas-Fermi-Dirac theory is too crude, it is not meaningful in physics and chemistry.¹⁷⁷

² $C_1 = \frac{3}{10} (3\pi^2)^{2/3}$; $C_2 = -\frac{3}{4} (\frac{3}{\pi})^{1/3}$

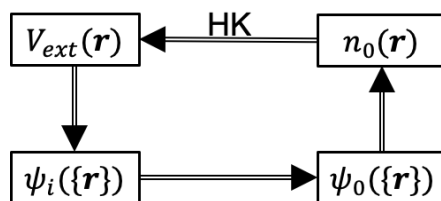


Figure 1.14. Schematic presentation of Hohenberg-Kohn theorem.¹⁶⁴

Hohenberg-Kohn Theorem

A big step towards the modern density functional theory was made P. Hohenberg and W. Kohn in 1964 (as shown in Figure 1.14).¹⁷⁸ The famous paper illustrated two important theorems:

1. The ground state energy from the Schrödinger equation is a unique functional of the electron density.
2. The electron density that minimises the energy of the overall functional is the true electron density corresponding to the full solution of the Schrödinger equation.

The importance of the two theorems is in the aspects that the ground state energy determines all the properties of the system at the state, and also that if we know the “true” functional, we can vary the electron density until the energy is minimised. Based on the Hohenberg-Kohn theory, the Hamiltonian of a system of electrons and fixed nuclei can be written as:

$$\hat{H} = -\frac{\hbar^2}{2m_e} \sum_i \nabla_i^2 + \sum_i V_{\text{ext}}(\mathbf{r}_i) + \frac{1}{2} \sum_{i \neq j} \frac{e^2}{|\mathbf{r}_i - \mathbf{r}_j|} \quad (1.52)$$

Kohn-Sham Theory

The Kohn-Sham theory (KS) replaces the many-body problem with a chosen non-interacting independent particle system that is relatively easier to solve.¹⁷⁹ In general, the energy of a system can be simply divided into two parts: E_{known} covers all the known terms and E_{XC} is

the exchange-correlation functional which includes everything else.

$$E[\{\psi_i\}] = E_{\text{known}}[\{\psi_i\}] + E_{\text{XC}}[\{\psi_i\}] \quad (1.53)$$

$$E_{\text{known}}[\{\psi_i\}] = \frac{\hbar^2}{m} \sum_i \int \psi_i^* \nabla^2 \psi_i d^3r + \int V(\mathbf{r}) n(\mathbf{r}) d^3r + \frac{e^2}{2} \int \int \frac{n(\mathbf{r}) n(\mathbf{r}')}{|\mathbf{r} - \mathbf{r}'|} d^3r d^3r' + E_{\text{ion}} \quad (1.54)$$

From the left to the right side, the terms are the kinetic energies of the electrons, the Coulomb interactions between the electrons and the nuclei, the Coulomb interactions between the electrons, and the Coulomb interactions between the nuclei. The above theory proposed the idea of finding an electronic density to minimise the energy, but did not show a practical way. Kohn and Sham solved this problem. What they suggested was to solve a set of equations, one for each electron, instead of solving a full Schrödinger equation for the whole system. The form of the Kohn-Sham equation is

$$\left[\frac{\hbar^2}{2m} \nabla^2 + V(\mathbf{r}) + V_{\text{H}}(\mathbf{r}) + V_{\text{XC}}(\mathbf{r}) \right] \psi_r(\mathbf{r}) = \varepsilon_i \psi_i(\mathbf{r}) \quad (1.55)$$

This simplifies Eqn. 1.21 by removing the summation over the terms. What we are looking for now in Eqn. 1.55 is the wavefunction of a single electron $\psi_i(\mathbf{r})$. The three potentials on the left side are: $V(\mathbf{r})$ that corresponds to the known term of the interactions between the electrons and the nuclei; $V_{\text{H}}(\mathbf{r})$ that is a Hartree potential including the Coulomb interactions between electrons and also a single electron to itself; V_{XC} that covers the exchange and correlation contributions, which is defined as a functional derivative of the exchange-correlation energy (E_{XC}), whereas the E_{XC} can be estimated as a functional of the density around point \mathbf{r} .

$$V_{\text{H}}(\mathbf{r}) = e^2 \int \frac{n(\mathbf{r}')}{|\mathbf{r} - \mathbf{r}'|} d^3r' \quad (1.56)$$

$$V_{\text{XC}}(\mathbf{r}) = \frac{\delta E_{\text{XC}}(\mathbf{r})}{\delta n(\mathbf{r})} \quad (1.57)$$

The Kohn-Sham equation offered a way to find the “true” electron density that can minimise the energy, while introducing a practical iterative solving procedure. Even though

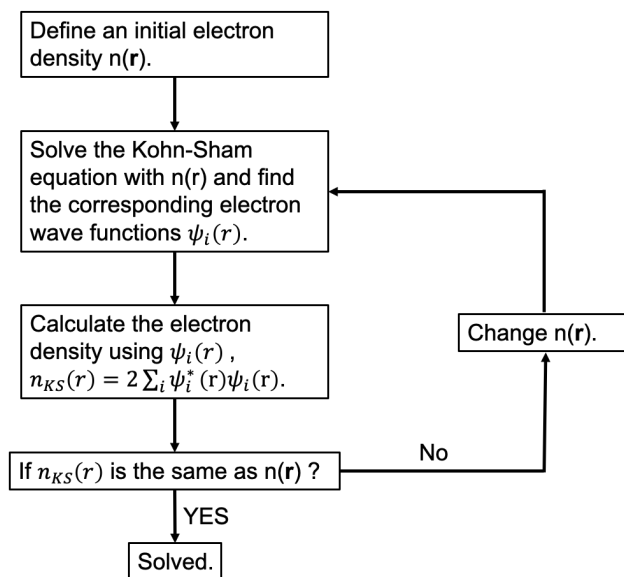


Figure 1.15. Schematic presentation of solving the Kohn-Sham equation.¹⁶⁴

we have to define all the terms in Eqn. 1.55 reasonably to solve the equation following the scheme as shown in Figure 1.15. However, this is not the case for V_{XC} . Based on the Kohn-Sham theory, various density functionals were developed to accurately describe the $E_{XC}[\{\psi_i\}]$.

Density Functionals

Similar to a function taking variables, a functional takes a function and defines a single value from the function. The functionals that are used in the DFT are developed to exactly describe the exchange-correlation interaction, while due to the complexity of the electron density within materials, such as chemical bonds, it is hard to find something that is practically useful for the Kohn-Sham equation. Based on different approximations, a hierarchy of functionals were constructed, including the local density approximation (LDA), the generalised gradient approximation (GGA), Meta-GGA, Hyper-GGA and so on (Figure 1.16).¹⁶⁸

Local Density Approximation The functional of the uniform electron gas can be derived, as the electron gas density is a constant at any point, $n(\mathbf{r}) = \text{constant}$. The local density approximation (LDA) sets exchange-correlation potential as the known exchange-correlation

potential at that point of the uniform electron gas. It is named after the fact that it only uses the local density to define the approximate functional.

$$V_{\text{XC}}(\mathbf{r}) = V_{\text{XC}}^{\text{electron gas}}[n(\mathbf{r})] \quad (1.58)$$

Generalised Gradient Approximation Functionals Extended from LDA, GGA describes the exchange-correlation contribution including the local electron density and the local gradient in the electron density. The Perdew-Wang functional (PW91) and the Perdew-Burke-Ernzerhof functional (PBE) are the two widely used functionals at GGA level in DFT calculations.^{180;181}

$$V_{\text{XC}}^{\text{GGA}}(\mathbf{r}) = V_{\text{XC}}[n(\mathbf{r}), \nabla n(\mathbf{r})] \quad (1.59)$$

Meta-Generalised Gradient Approximation Functionals Including the information of $n(\mathbf{r})$, $\nabla n(\mathbf{r})$, and $\nabla^2 n(\mathbf{r})$. Practically, the kinetic energy density $\tau(\mathbf{r})$ may be used instead of $\nabla^2 n(\mathbf{r})$. Examples of meta-GGA functionals are Tao-Perdew-Staroverov-Scuseria (TPSS) and M06-2X.^{182;183}

$$\tau(\mathbf{r}) = \frac{1}{2} \sum_{\text{occupied states}} |\nabla \psi_i(\mathbf{r})|^2 \quad (1.60)$$

Hyper-Generalised Gradient Approximation Functionals At this level, the functionals include the contribution of both GGA and the exact exchange energy, called hyper-GGAs.

$$E^{\text{exchange}}(\mathbf{r}) = \frac{1}{2n(\mathbf{r})} \int d^3 r' \frac{|\sum_{\text{occupied states}} \psi_i^*(\mathbf{r}') \psi_i(\mathbf{r})|^2}{|\mathbf{r} - \mathbf{r}'|} \quad (1.61)$$

The most widely used hyper-GGA functional is the B3LYP density functional while the acronym refers to the developers and the mathematical method applied.

$$V_{\text{XC}}^{\text{B3LYP}} = V_{\text{XC}}^{\text{LDA}} + \alpha_1(E^{\text{exchange}} - V_X^{\text{LDA}}) + \alpha_2(V_X^{\text{GGA}} - V_X^{\text{LDA}}) + \alpha_3(V_c^{\text{GGA}} - V_c^{\text{LDA}}) \quad (1.62)$$

where V_X^{GGA} is the Becke 88 exchange functional, V_c^{GGA} is the Lee-Yang-Parr correlation functional, and α_1 , α_2 , and α_3 are coefficients.¹⁸⁴⁻¹⁸⁶

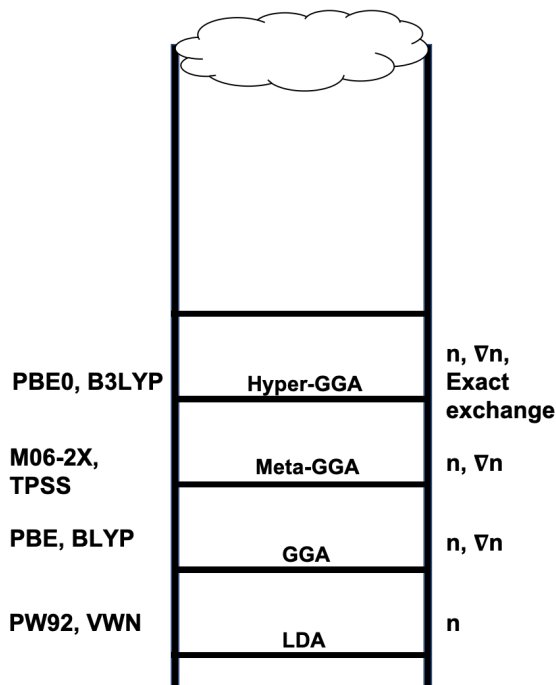


Figure 1.16. The “Jacob’s ladder” of DFT functionals.¹⁸⁷

Additional Functionals Any functionals that incorporate exact exchange are called hybrid functionals. Therefore, the hyper-GGA functionals are also hybrid functionals. Hybrid-meta-GGA functionals combine the exact exchange with meta-GGA functionals.

London Dispersion Corrections

The long-range correlation between electrons is missing in classic DFT simulations, among which the weak London interactions that are very important to many phenomena in molecular materials in particular in the solid state, such as crystal structures. Considering the dispersion energy in DFT,

$$E^{\text{DFT-D}} = E^{\text{DFT}} + E_{\text{Disp}} \quad (1.63)$$

the dispersion energy is corrected by a pairwise method

$$E^{\text{Disp}} = - \sum_{AB} \sum_{n=6,8,10} \left(\frac{C_n^{AB}}{R_{AB}^n} \right) \quad (1.64)$$

while for D3 correction,^{188;189} an extra damping term is added

$$E_{\text{DFT-D}} = E_{\text{DFT}} - S \sum_{i \neq j} \frac{C_{ij}}{r_{ij}^6} f_{\text{damp}}(r_{ij}) \quad (1.65)$$

where C_{ij} is a dispersion coefficient for atoms i and j , r_{ij} is the distance between atoms i and j , $f_{\text{damp}}(r_{ij})$ is a damping function, and S is a scaling factor applied to each pair of atoms uniformly.

Basis Sets

One essential step of solving the molecular problem with the Hartree Fock approximation is to describe the molecular orbitals with a linear combination of a set of basis functions φ . The various sets of basis functions are called the basis sets.¹⁶⁶ Even though the ideal basis functions would be complete, the possible size of a set of basis functions is limited by the practical resources. Also, the choice of appropriate basis sets is an important part of the computational work. The molecular orbitals can be separated into two main regions: The atomic region including the part with rapid oscillations, and the valence (bonding) region which is very flexible. The orbitals can be described with basis functions that are similar to the atomic orbitals (which is the method applied throughout this thesis), or periodic plane wavefunctions can be used instead (as implemented in other codes such as VASP or CASTEP).

Atomic Centred Basis Sets As implied by its name, this type of basis sets are centred at the atomic nuclei. The two most widely used are the Slater-type orbitals (STOs; $e^{-\zeta r}$) and the Gaussian-type orbitals (GTOs; $e^{-\alpha r^2}$). ζ and α are the Slater and Gaussian orbital exponent, respectively. The smaller the exponents are, the more diffuse the functions are. The main differences between the two types are at $r = 0$ and when r is large. At $r = 0$, the slope of the Gaussian function is zero, while for the Slater function it is not. On the other hand, the Gaussian function decays much faster than the Slater function. Describing the molecular orbitals, ψ_i , via the Slater function is more accurate and less functions are required compared

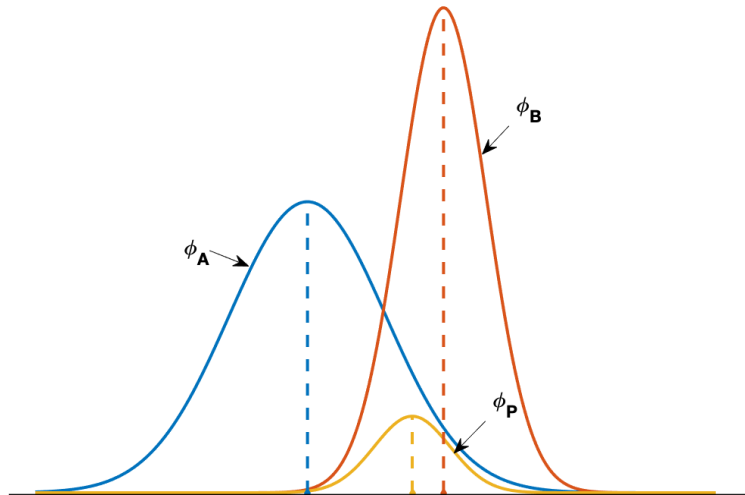


Figure 1.17. The product of two Gaussian functions. ϕ_P centred at point P is the product of ϕ_A and ϕ_B that centred at A and B, respectively.

to the Gaussian functions. While when the interactions between electrons are considered, the Gaussian-type orbitals are more efficient since the product of two Gaussian orbitals is also a Gaussian orbital with the shift of the centre (Figure 1.17). This advantage avoids using the Slater basis functions to deal with four integrals at different centres that improves the efficiency of computations.

The nature of Gaussian functions does not perfectly fit the the behaviour of molecular orbitals. To optimise the Gaussian functions, linear combinations of the primitive Gaussian functions Φ_p^{GF} are applied, called contracted Gaussian functions (CGF).

$$\Phi_\mu^{\text{CGF}}(\mathbf{r} - \mathbf{R}_A) = \sum_{n=1}^L d_{p\mu} \Phi_p^{\text{GF}}(\alpha_{n\mu}, \mathbf{r} - \mathbf{R}_A) \quad (1.66)$$

where L is the length of the contraction, and $d_{p\mu}$ and $\alpha_{p\mu}$ are the contraction coefficients and exponents. Φ_n^{GF} is a normalised Gaussian function. The procedure is to fit a STO to a linear combination of the primitive Gaussian functions, STO-1G, STO-2G, STO-3G and so on.¹⁹⁰ It can also reduce the number of basis functions required for a reasonable approximation. STG-3G is widely used in polyatomic calculations that fit the Slater function with three

primitive GTOs.

A minimal basis set, such as STO-3G, that uses the least number of functions to describe the occupied atomic orbitals can be effective for a single-atom calculation, while it is not ideal and flexible enough for most systems. Therefore, more GTOs are used to describe the atomic orbitals that results in double-zeta, triple-zeta basis sets and so forth. For example, if each function of the minimal basis sets is split into two GTOs, the new set is a double-zeta basis set like 4-31G and 6-31G.^{191;192} The acronym 4-31G means that the valence shell functions are contractions of three primitive GTOs and one primitive GTO, and the inner shell functions are the contractions of four primitive GTOs. Same as 4-31G, the only difference of 6-31G is that the inner shell functions are contractions of six primitive GTOs. The next step of improving the performance of the basis sets is to add polarisation functions, for instance by adding d-type functions for the first row elements and p-type functions for hydrogen. These are called polarised basis sets. Only isolated hydrogen atoms obey the s-symmetry. Any charge distribution of the H atoms, which are placed in a uniform electric field, is attracted to the direction of the electric field and becomes polarised. 6-31G* adds an uncontracted set of d-type functions to the heavy metals, and 6-31G** adds another set of uncontracted p-type functions to hydrogen atoms.¹⁹³⁻¹⁹⁵ For triple- and quadruple-zeta basis sets, more than one polarisation function are added, such as adding f-type functions to the heavy atoms and d-type functions to hydrogen. Other split valence and triple zeta basis sets, such as the ones developed by Ahlrichs and co-workers in 1993 and the later modified basis sets (i.e. def2SVP and def2TZVP), were also well-developed and robust.¹⁹⁶⁻¹⁹⁹ For sure the larger the basis sets, the more expensive the computations are. However, larger basis sets do not necessarily give better results. The choice of basis sets depends on the specific system, and also the compromise between accuracy and the computational cost.

Chapter 2

Experimental Methods

2.1 Experimental Setup

2.1.1 Room Temperature Measurements

A commercial THz-TDS spectrometer TeraPulse 4000 (TeraView LTd., Cambridge, UK) was used for all experiments (Figure 2.1). For room temperature measurements, as shown in Figure 2.2, the sample holder is positioned at the centre of the measurement chamber and is perpendicular to the beam propagation direction between two mirrors. The beam width is ~ 2 mm when it hits the sample. To eliminate the influence of water vapour in the atmosphere surrounding the sample that strongly absorbs the terahertz radiation, the chamber was purged with dry nitrogen gas during the measurements.

Due to the high absorption at the peak frequencies of vibrational features of pure crystals, the transmission measurements are usually carried out using pellets that are compacted from a powder mixture of transparent diluent and sample material, along with a blank reference pellet made from diluent alone to compare with. The reference is usually air or polycrystalline substances that are transparent to terahertz radiation, such as polyethylene (PE) and polytetrafluoroethylene (PTFE). For the projects in Chapter 4, 5 and 6, the room temperature set up was usually used for a quick check to assure that the sample pellet is well-prepared at an appropriate concentration. While for Chapter 7, all the terahertz spectra were acquired



Figure 2.1. The TeraPulse 4000 spectrometer.

at room temperature.

2.1.2 Variable Temperature Setup

The effect of temperature on the spectral features is significant due to the relatively close energy spacing of the vibrational levels relative to the thermal energy at terahertz frequencies. At low temperatures, the peaks are sharper and more well-defined as less of the higher vibrational states are populated and the dielectric relaxations are coherent for crystalline materials. Also, the shift of the peaks with temperature can provide additional insight into the properties of the materials. For example, a discontinuous shift in peak frequency with temperature for a specific feature could indicate underlying anharmonicity of the vibrational mode. Therefore, low-temperature measurements are usually performed to acquire a spectrum of crystalline systems. An additional advantage is such low temperature spectra are more comparable with the simulated spectrum that can be obtained from the computational techniques at a temperature of 0 K. A series of variable temperature measurements are useful to study the temperature-dependent lattice vibrations of the targeted systems, and also possible structural changes triggered by the change of temperature, such as phase transitions.

For all the measurements discussed in Chapter 4-6, low-temperature transmission measurements were carried out to acquire terahertz spectra for the studied materials. A modified

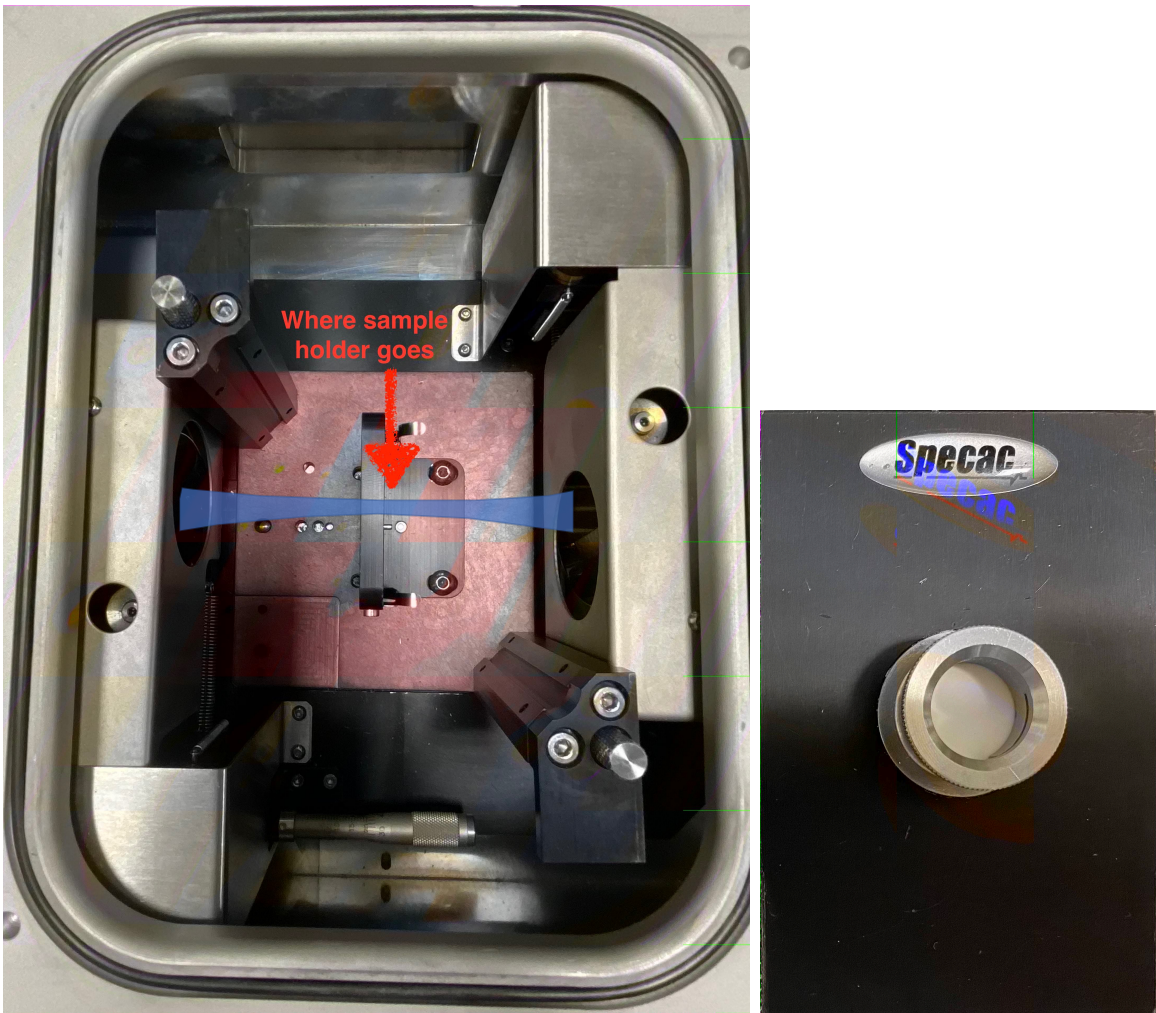


Figure 2.2. The optics chamber on the left and the sample holder on the right. The blue shade indicates the terahertz beam.

Janis ST-100 cryostat system (Janis, Wilmington, USA) was used as shown in Figure 2.3. The cryostat is attached to the optics sample compartment from above and is fixed in place using a set of mechanical steel bolts. The sample compartment outside the cryostat is continuously purged with dry nitrogen gas similar to the room temperature setup, and the cryostat sample chamber was evacuated using a vacuum pump to a pressure of 1.2 mbar. A Lakeshore 331 temperature controller (Lakeshore, Westerville, USA) is attached to the cryostat to monitor the temperature, and the temperature is measured using a thermocouple (suitable for high temperatures up to 700 K) and a silicon diode (for low temperatures and up to 500 K) that are attached to the very end of the cold finger.

For low temperature measurements, the cryostat is cooled with liquid nitrogen that is pumped into the system via a transfer tube, while heating was achieved using a cartridge heater in the cold finger that is connected to the temperature controller. For the temperature range between 80 K to room temperature, temperature stabilisation is achieved by regulating the flow rate of liquid nitrogen and the power of heater. The motor on the cryostat is used to switch the position of the sample holder relative to the signal, so reference and sample can be measured alternatively for variable temperature measurements. An overview of the variable temperature set up is shown in Figure 2.4. The temperature range used to acquire spectra for this work is between 80 K to 500 K.

2.2 Sample Preparation

For crystalline materials, the samples were usually in the form of commercially sourced high purity polycrystalline powder particles or lab-synthesised single crystals. For terahertz transmission measurements the samples were firstly deagglomerated into a uniform powder using an agate mortar with a pestle, and then mixed with fine particles of high density polyethylene as the diluent (PE, Induchem, Volketswil, Switzerland) to the desired concentration.

The well-mixed powder was compressed using a manual hydraulic press (Specac Ltd., Kent, UK) at a load of ~ 2 t into a pellet, and the thickness was measured with a micrometer. The parts for sample preparation are shown in Figure 2.5. The diameter of the pellets was



Figure 2.3. A photo of the Janis ST-100 cryostat system.

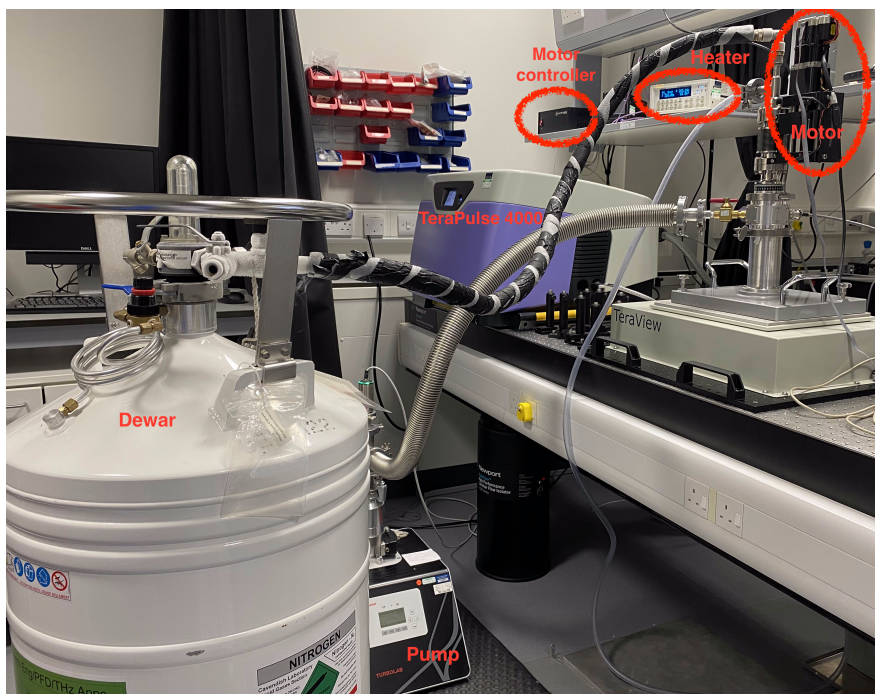


Figure 2.4. An overview of the setup for variable temperature measurements.

13 mm, while the thickness was in the range of around 2 mm to 3 mm. A blank pellet of PE was usually used as a reference. The optimal concentration was dependent on the absorption of the material and was limited by the maximum absorption coefficient that can be measured, which will be discussed in Section 2.4.

2.3 Data Acquisition

The software interface of the TeraPulse 4000 is shown in Figure 2.6. The parameters shown in this Figure are the standard settings that were used for all experiments (unless specified explicitly). Each transmission spectrum was acquired with an average of 1,000 waveforms and the resolution was set at 0.94 cm^{-1} , while the optical delay offset was adjusted slightly based on the sample. The waveforms of reference and sample were acquired alternatively.

The high absorption of the rotational transitions in water vapour can influence the results of measurements significantly, and hence it was necessary to carefully check whether the sample chamber was purged sufficiently before starting a measurement. One practical way



Figure 2.5. Parts for sample preparation: scale, mortar and pestle, pellet die, hydraulic press, and micrometer.

Scan Settings ▼ 🔒

Measurement mode: CoreTransmission ▼

Scanner type: SpectraSeries ▼

Measurement config: ▼

Config id: 11149 Undo View Load...

Save Batch Add

Config name: Measurement name

Config description: Measurement description ...

No. of repeats: 0

Start delay: 0.000 s

Time delay: 0.000 s

Sample averages: 1000

Waveform rate: 15.000 Hz

Resolution: 0.94 cm-1

Optical delay offset: 0.000 ps

Split directions:

Oversamples: 1 ▼

Figure 2.6. TeraPulse 4000 settings for transmission measurement.

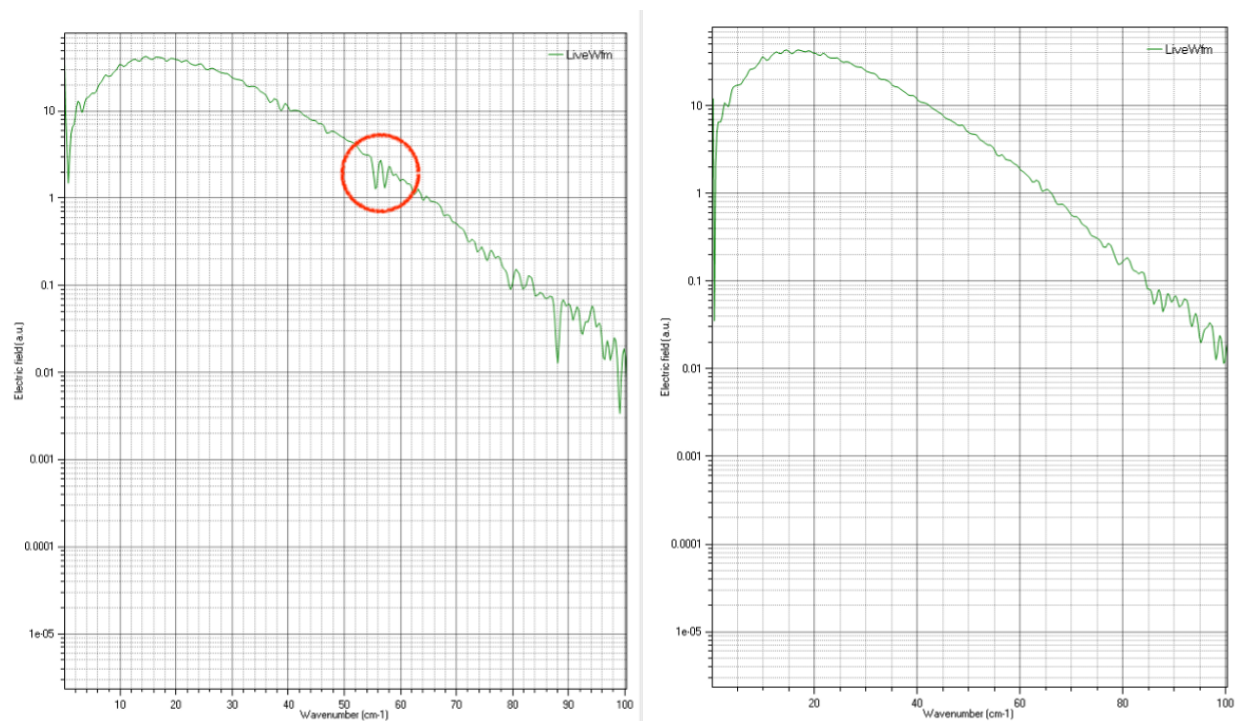


Figure 2.7. Power spectrum of the transmitted terahertz pulse through the empty sample compartment. Left: before purging; right: after the water vapour was displaced by dry nitrogen gas during purging. The red circle highlights the feature of water vapour at 1.7 THz.

is to check the feature around 1.7 THz with an empty chamber, as that spectral feature represents the absorption of water vapour (Figure 2.7).²⁰⁰

2.4 Data Analysis

THz-TDS measures the amplitude and phase of the time-varying electric field of a terahertz pulse and then the time-domain information is transformed into the frequency-domain using the fast Fourier transform method. After the operation, the optical constants, usually the real part of the complex refractive index (n) and the absorption coefficient (α), were derived using the Fresnel coefficients and the Beer-Lambert law. The whole process of data analysis was performed on Matlab.

As shown in Figure 1.7 for the terahertz transmission measurement, one probe pulse is propagating through the sample, and Figure 2.8 illustrates the details of the process.⁶⁴ The

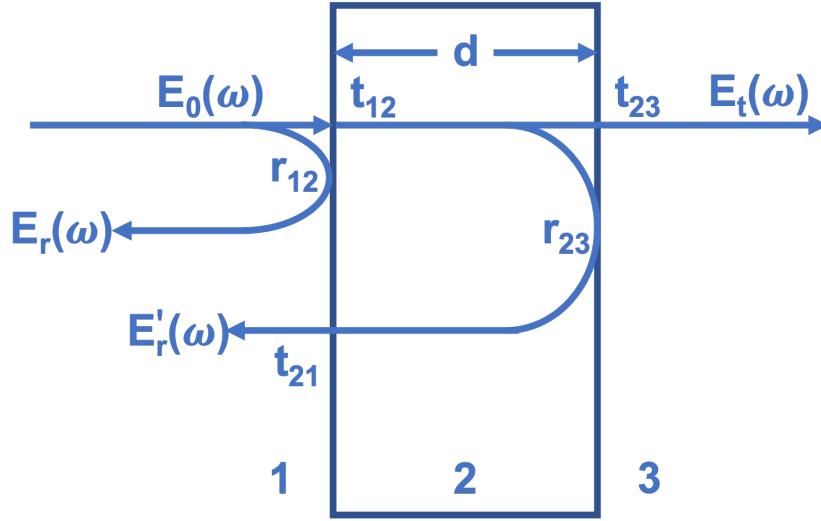


Figure 2.8. Schematic diagram of THz-TDS transmission measurement. $E_0(\omega)$ is the incident electric field, $E_t(\omega)$ is the transmitted field, $E_r(\omega)$ and $E'_r(\omega)$ are the reflected fields from the front and back interfaces, respectively. t and r represent the corresponding Fresnel transmission and reflection coefficients.⁶⁴

numbers 1, 2, and 3 refer to different media. Media 1 and 3 are typically air and medium 2 is the sample. When the terahertz pulse is incident on the sample, part of it reflects from the front face $E_r(\omega)$ due to the change in refractive indices between the media. When the transmitted part reaches the back interface another reflection occurs $E'_r(\omega)$ and finally the transmitted field $E_t(\omega)$ emerges from the back face of the sample pellet. The Fresnel transmission and reflection coefficients at each interface are denoted as t_{12} , t_{23} , t_{21} , r_{12} , and r_{23} . For the measurements covered in this thesis, the reference and sample pellets are relatively thick ($d = 2\text{ mm to }3\text{ mm}$), and hence the multiple internal reflections are neglected as they are separated in the time-domain from the main pulse. Therefore, the transmitted and reflected electric fields of interest are

$$\begin{aligned}
 E_t(\omega) &= E_0(\omega)t_{12}t_{23}e^{-\alpha d/2}e^{i\omega d/c} \\
 E_r(\omega) &= E_0r_{12} \\
 E'_r(\omega) &= E_0t_{12}r_{23}t_{21}e^{-\alpha d/2}e^{i\omega d/c}
 \end{aligned} \tag{2.1}$$

The complex refractive index $\hat{n}(\omega) = n(\omega) + i\kappa(\omega)$ is extracted from the transmission measurements, where $\kappa(\omega) = \alpha(\omega)c/2\omega$, and $\kappa(\omega)$ and $\alpha(\omega)$ are the extinction coefficient

and absorption coefficient, respectively. When both reference and sample are measured, the refractive index and the absorption coefficient are calculated via the following equations

$$\frac{E_{\text{sam}}(\omega)}{E_{\text{ref}}(\omega)} = T(\omega)e^{i\varphi(\omega)} = t_{12}t_{23}e^{-\alpha d/2}e^{i(n-1)\omega d/c} \quad (2.2)$$

$$n(\omega) = 1 + \frac{\varphi(\omega)c}{\omega d} \quad (2.3)$$

$$\alpha(\omega) = -\frac{2}{d} \ln \left(\frac{(n+1)^2}{4n} T(\omega) \right) \quad (2.4)$$

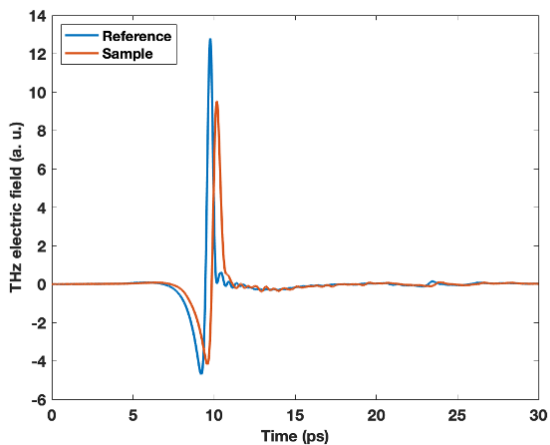
Due to the limit of the equipment, the valid range is usually 0.3 THz to 3 THz, and for a good measurement it may extend to 3.5 THz, before the signal reaches the noise level. However, this also depends the maximum measurable absorption coefficient α_{max} in the dynamic range, which depends on each measurement. The method to define this was introduced by Jepsen and Fischer in 2004.²⁰¹

$$\alpha_{\text{max}}d = 2 \ln \left[\text{DR} \frac{4n}{(n+1)^2} \right] \quad (2.5)$$

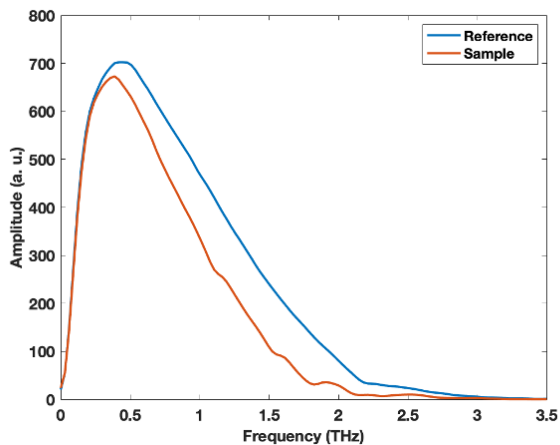
where DR refers to the dynamic range, n is the refractive index, and d is the sample thickness in centimetres. As the black curve shows in Figure 2.9(d), the dynamic range drops rapidly with increasing frequency. Therefore, the data analysis at the high frequency wing of the spectrum has to be performed with caution in case the signal drops below the noise level.

Figure 2.9 uses the measurement of a pellet of aspirin as an example to illustrate the data analysis process. The time-domain data are acquired directly for both reference and sample (Figure 2.9(a)), and the waveforms are converted to the power spectra presented in the frequency-domain (Figure 2.9(b)). Afterwards, using the method described above, the absorption spectrum of the sample is acquired (Figure 2.9(c)). As mentioned before, the refractive index can also be extracted at the same time, but that will not be discussed in this thesis. Figure 2.9(d) shows that the peaks did not reach the upper limit up to 3 THz, which is the low-frequency region that is of interest. Therefore, the experimental results can

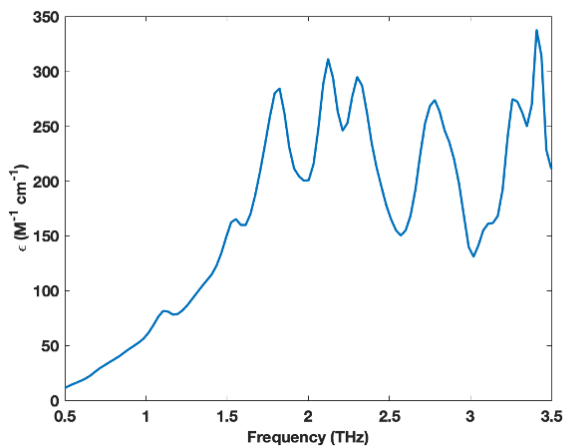
be used for further analysis. All the spectra of the crystals covered in this thesis were double checked with this method, but these figures were not included in the following chapters for brevity.



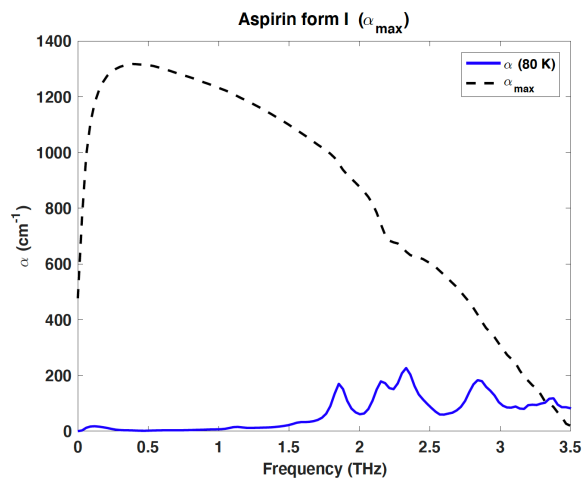
(a) The acquired time-domain waveforms.



(b) The frequency-domain power spectrum after fourier transform.



(c) the terahertz absorption spectrum after the comparison between the reference and the sample.



(d) The absorption spectrum of aspirin form I (solid) and the upper limit of the maximum detectable absorption coefficient (dashed).

Figure 2.9. Using aspirin as an example to illustrate the data analysis procedure.

Chapter 3

Computational Methods

This thesis focuses on crystalline materials and solid-state DFT (ss-DFT) was used for all the calculations. In general, DFT studies the electronic structure by considering the quantum mechanical states of electrons in the field of fixed nuclei, while ss-DFT in addition utilises the periodic structure of crystals to simplify the complex many-body calculations. All the simulation work was performed using the CRYSTAL17 software package that applies the periodic ss-DFT and atom-centered basis sets.¹⁵⁹

3.1 Introduction to Solid-State DFT

Due the nature of periodicity, a crystalline system is usually described by a unit cell, which, if reproduced, can generate the whole structure of the solid.²⁰² The Bravais lattice specifies the periodic array of how the repeated units of a crystal are arranged. However, the Bravais lattice only shows the periodic patterns, but not the actual unit. It includes all points with the form of

$$\mathbf{R} = n_1\mathbf{a}_1 + n_2\mathbf{a}_2 + n_3\mathbf{a}_3 \quad (3.1)$$

where n_1 , n_2 , and n_3 are integers, and \mathbf{a}_1 , \mathbf{a}_2 , and \mathbf{a}_3 are three primitive vectors. Since crystalline materials are well-organised, there are only certain ways they can be packed. Based on the parameters of the Bravais lattice, crystalline systems are divided into seven different groups: triclinic, monoclinic, orthorhombic, tetrahedral trigonal, hexagonal, and

cubic. By further considering the symmetry of the atoms, crystals can be categorised into a total of 230 so-called space groups.

The unit cell can be variable in length as long as the repetition of the unit cell can cover the whole crystal space without overlapping. Additionally, the smallest unit that can produce a unit cell is called the asymmetric unit, and this concept is exploited in the ss-DFT simulations. The cell that fits in the group with the smallest volume is called a primitive cell; other valid choices are conventional cells that have a relatively larger volume but likely include more symmetry information. A primitive cell with all the symmetry information of a crystal is called the Wigner-Seitz cell. In a unit cell, all points \mathbf{r} can be expressed by the three lattice vectors \mathbf{a}_1 , \mathbf{a}_2 , and \mathbf{a}_3 .

$$\mathbf{r} = x_1\mathbf{a}_1 + x_2\mathbf{a}_2 + x_3\mathbf{a}_3 \quad (3.2)$$

where x_1 , x_2 , and x_3 can be any value between 0 and 1. For an ideal crystal, its packing pattern is perfectly periodic, so the external potential for the electrons is periodic as well. Therefore,

$$V(\mathbf{r} + \mathbf{R}) = V(\mathbf{r}) \quad (3.3)$$

The periodicity of the potential determines that for any translation operators that follow the rule

$$\hat{T}_{\mathbf{R}}\varphi(\mathbf{r}) = \varphi(\mathbf{r} + \mathbf{R}) \quad (3.4)$$

the Hamiltonian stays invariant.

The Wigner-Seitz primitive cell of the reciprocal space is called the first Brillouin zone (BZ), and the centre of BZ is the Γ point. All the calculations are performed within the BZ. As in the real space, the vectors (\mathbf{k}) in the reciprocal space can be represented by a linear combination of three basic vectors.

$$\mathbf{k} = n_1\mathbf{b}_1 + n_2\mathbf{b}_2 + n_3\mathbf{b}_3 \quad (3.5)$$

The relationship between the lattice vectors of the reciprocal space and the real space is that

$$\mathbf{a}_i \cdot \mathbf{b}_j = 2\pi\delta_{ij} \begin{cases} = 2\pi, i = j, \\ = 0, i \neq j, \end{cases} \quad (i, j = 1, 2, 3) \quad (3.6)$$

where δ_{ij} is the Kronecker delta that equals one if $i = j$ and otherwise is zero. Therefore,

$$\mathbf{b}_1 = 2\pi \frac{\mathbf{a}_2 \times \mathbf{a}_3}{\mathbf{a}_1 \cdot (\mathbf{a}_2 \times \mathbf{a}_3)} \quad (3.7)$$

$$\mathbf{b}_2 = 2\pi \frac{\mathbf{a}_3 \times \mathbf{a}_1}{\mathbf{a}_1 \cdot (\mathbf{a}_2 \times \mathbf{a}_3)} \quad (3.8)$$

$$\mathbf{b}_3 = 2\pi \frac{\mathbf{a}_1 \times \mathbf{a}_2}{\mathbf{a}_1 \cdot (\mathbf{a}_2 \times \mathbf{a}_3)} \quad (3.9)$$

The larger the vectors are in the real space, the smaller they are in the reciprocal space. That is one advantage of solving the Schrödinger equation in reciprocal space, especially more efficient for a large crystalline system.

In CRYSTAL17, atom centred basis sets are applied to describe the electronic structure at each point in the crystals. The method considers the neighbouring interactions and chemical properties, but an infinite number of parameters will be required for accurate ss-DFT simulations due to the lack of periodicity. This problem can be solved by transforming the original atom centred basis sets to periodic Bloch functions via Fourier transformation. Bloch functions satisfy Bloch's theorem which states that if a Bloch function has the same periodicity as the studied crystalline system, it has the same value at the corresponding k points (as shown in Eqn. 3.10).^{203;204}

$$\psi(\mathbf{r} + \mathbf{R}; \mathbf{k}) = e^{i\mathbf{k}\mathbf{R}}\psi(\mathbf{r}; \mathbf{k}) \quad (3.10)$$

The atomic orbitals $\varphi_\mu(\mathbf{r})$ need to be converted into Bloch functions $\phi_\mu(\mathbf{r}; \mathbf{k})$, so that Bloch's theorem can be applied to simplify the calculations. The crystalline orbital $\psi_i(\mathbf{r}; \mathbf{k})$ is then

composed of a linear combination of Bloch functions.

$$\phi_{\mu}(\mathbf{r}; \mathbf{k}) = \sum_{\mathbf{R}} \varphi_{\mu}(\mathbf{r} - \mathbf{A}_{\mu} - \mathbf{R}) e^{i\mathbf{k} \cdot \mathbf{R}} \quad (3.11)$$

$$\psi_i(\mathbf{r}; \mathbf{k}) = \sum_{\mu} a_{\mu,i}(\mathbf{k}) \phi_{\mu}(\mathbf{r}; \mathbf{k}) \quad (3.12)$$

where A_{μ} is the position of the nucleus that φ_{μ} is centred at. By converting the calculation from the real space to the reciprocal space, the method reduces the complexity from infinite to the certain k values that obey Bloch's theorem, and each k value can be treated individually. In addition, the Born-von Karman boundary condition states that

$$\psi(\mathbf{r} + N_i \mathbf{a}_i) = \psi(\mathbf{r}) \quad (3.13)$$

where $N_1, N_2,$ and N_3 are the number of cells along each primitive direction.²⁰² This suggests that it is possible to study a periodic crystalline system with translational invariance and without the disturbance of boundaries.

3.2 CRYSTAL17 Software Package

All the ss-DFT calculations in this thesis were performed using the CRYSTAL17 software package.¹⁵⁹ The routine on the computational work was: i, start from the published crystallographic structure, usually from Cambridge Structural Database (CSD)²⁰⁵, try to identify possible combinations of density functionals and basis sets, and then use a series of single-point energy calculations to determine the appropriate \mathbf{k} -points in the reciprocal space; ii, set the parameters and the convergence criteria to optimise the geometry; iii, use the optimised geometry for the further frequency analysis, from which the simulated spectrum is acquired. Further analyses, such as Gibbs free energy, quasi-harmonic frequency calculations, and elastic properties, are also possible depending on the specific requirements in each project. The details of each step will be discussed in the following subsections.

3.2.1 Single-Point Energy Calculations

CRYSTAL17 calculates the electronic energy from a single-point energy calculation, which was also the first step to determine the choice of density functionals, basis sets, and the values of computational settings. The method is called self-consistent field (SCF).^{179;206} The initial electron density was estimated from the atomic positions and geometries imported in the input file. The Hamiltonian was calculated in direct space and converted to reciprocal space via Fourier transform for each \mathbf{k} point. Following that, the matrix was diagonalised, which yielded the total energy of the system. This information was then used to guess the new density for the next round of calculation. SCF continued until there was no noticeable difference (as specified by a parameter before the calculation) between the results of two rounds, i.e. when convergence was reached.

The number of \mathbf{k} points was specified by two factors activated by the keyword SHRINK in CRYSTAL17. The first one determined the grid of \mathbf{k} points in the reciprocal space based on the Pack-Monkhorst method²⁰⁷, while the second one was important for the calculations of the density matrix and Fermi energy of conductors. Since the projects presented in this thesis did not cover conductors, the second factor will not be discussed and was set the same as the first factor for the calculations in the following chapters. The shrinking factor was tested by running the single point energy calculation on a series of integers from small to large until the energy stopped changing.

The truncation criteria of the Coulombic and Hartree-Fock exchange integrals were determined for each calculation based on the system. The values are in the form of 10^{-X} , 10^{-X} , 10^{-X} , 10^{-X} , and 10^{-Y} , while Y was usually set to a value twice of X (TOLINTEG). This can also be adjusted according to the shrinking factor testing calculations, or if problems occur in the calculations of SCF cycle at the later stage of geometry optimisation.

For a spin polarised system, an open shell Hamiltonian needed to be activated with the keyword SPIN, and a spin polarised solution can be calculated after the $(\alpha - \beta)$ electron occupancy was specified by SPINLOCK. ATOMSPIN can be used to specify the atomic spin of certain atoms, while this may reduce the symmetry of the studied system that makes the

calculations more computationally expensive. This method was applied in Chapters 4.1 and 5 when metal-based MOFs were investigated.

3.2.2 Geometry Optimisation

The crystalline structure was optimised after proper parameters were determined via several runs of single-point energy calculations. Geometry optimisation was performed via an iteration process with a full set of SCF calculation in each cycle. The calculated electron density was used to change the atomic positions slightly for the next cycle. The process continued until the structure with the minimum energy was found that met the set convergence criteria. For the calculations discussed later, the energy convergence was set at $\Delta E < 1 \times 10^{-8} E_h$ (TOLDEE). The root-mean-square (RMS) of the gradient of the potential energy curve (TOLDEG) and the RMS of the displacement (TOLDEX) are set to 1×10^{-5} a.u. and 4×10^{-5} a.u., respectively.

While geometry optimisation of a system is a step of the routine, there are some keywords in CRYSTAL17 that can be used to adjust the crystal structure or change the procedure of geometry optimisation in order to provide results of interest according to the specific projects. In Section 4.1, LNGSFROZEN, ANGSFROZEN, and FREEZINT were used to freeze bond lengths, bond angles and dihedral angles, respectively, which enables to study the motion of methyl groups explicitly. In Section 6.2, ATOMONLY was applied to perform geometry optimisation with cell parameters fixed.

It is also possible to calculate the cohesive energy of a crystalline system in order to offer more insight for certain cases, such as comparing the stability of polymorphs (Section 6.1). The cohesive energies were calculated using the following equation:

$$E_{\text{cohesive}} = \frac{E_{\text{total}} - N \times E_{\text{molecule}}}{N} \quad (3.14)$$

E_{total} is the total electronic energy of a unit cell, N is the number of molecules within a unit cell, and E_{molecule} is the energy of an isolated molecule that can be estimated by inserting the keyword MOLECULE. However, the effect of the basis-set superposition error (BSSE)

also needs to be considered, which is caused by the incompleteness of the basis set, and that can be corrected with the Boys-Bernardi counterpoise correction (BB-CP) method in CRYSTAL17.²⁰⁸ BSSE is estimated by the keyword MOLEBSSE, and the corrected cohesive energy becomes $E_{\text{cohesive}}(\text{BB-CP})$ (3.15).

$$E_{\text{cohesive}}(\text{BB-CP}) = E_{\text{cohesive}} + \text{BSSE} \quad (3.15)$$

3.2.3 Frequency Analysis

The optimised structure can then be used to calculate the frequencies and intensities of IR and Raman active vibrational modes (FREQCALC and INTENS/INTRAMAN). The energy convergence is set to $\Delta E < 1 \times 10^{-10} E_h$, as the frequency calculations are more sensitive to slight differences in atomic positions compared to the geometry optimisation. It is noted that the frequency analysis here applies the harmonic approximation (HA). While quasi-harmonic calculations are also possible with CRYSTAL17, it is beyond the content of this thesis. The molecular vibrations at each frequency obtained from the simulated results were visualised with Jmol programme.²⁰⁹

The method of calculating vibrational frequencies used by the CRYSTAL17 code is explained in detail in Pascale et al.²¹⁰ Starting from a molecular system, the Born-Oppenheimer potential energy surface with N atoms, $V(\mathbf{x})$, is defined by $3N$ coordinates. Based on the harmonic approximation,

$$V(0) = \frac{1}{2} \sum_{ij} u_i H_{ij} u_j = \frac{1}{2} \langle u | H | u \rangle \quad (3.16)$$

where u_i is the displacement along the i -th cartesian coordinate relative to its equilibrium position, and H is the Hessian matrix of the second derivatives of $V(\mathbf{x})$ at equilibrium compared to when atoms are displaced.

$$H_{ij} = \frac{1}{2} \left[\frac{\partial^2 V(\mathbf{x})}{\partial u_i \partial u_j} \right]_0 \quad (3.17)$$

The weighted displacement coordinates can be represented as $q_i = \sqrt{M_i}u_i$, where M_i is the atomic mass associated with i -th coordinate. The vibrational potential can be rewritten as

$$V(0) = \frac{1}{2} \langle q | W | q \rangle \quad (3.18)$$

where W is the mass-weighted Hessian matrix, i.e. Hermitian matrix.

$$W_{ij} = \frac{H_{ij}}{\sqrt{M_i M_j}} \quad (3.19)$$

By diagonalising W , the force constants can be determined from the eigenvalues, as well as the vibration frequencies $\omega = \frac{\sqrt{\kappa_j}}{2\pi}$. In CRYSTAL, the first derivatives are solved analytically, but numerically for the second derivatives.

For periodic solid-state materials, the symmetric properties are used to reduce the calculations to a minimal set. Translational invariance is introduced to describe the infinite crystalline system with finite matrices. The generalised coordinates $q_i(\mathbf{k})$ are defined to solve the problem for each \mathbf{k} point in the BZ. In this case, the Hermitian matrix W becomes

$$W_{ij}(\mathbf{k}) = \sum_{\mathbf{G}} \exp[i\mathbf{k} \cdot \mathbf{G}] \frac{H_{ij}^{0\mathbf{G}}}{\sqrt{M_i M_j}} \quad (3.20)$$

where $H_{ij}^{0\mathbf{G}}$ represents the Hessian matrix with respect to atom i in the cell $\mathbf{0}$ and atom j in the cell \mathbf{G} . When considering these calculations for the special point Γ , the Hermitian matrix can be simplified to the following form.

$$W_{ij}(0) = \sum_{\mathbf{G}} \frac{H_{ij}^{0\mathbf{G}}}{\sqrt{M_i M_j}} \quad (3.21)$$

The frequencies can be calculated the same way as for single molecules. Each atom is displaced along the three Cartesian coordinates and the energy derivatives are calculated by $(3N + 1)$ SCF cycles. The vibrational frequencies can then be determined via the diagonalisation of the Hermitian matrix. This method applies to the frequency analysis for both IR and Raman spectroscopy.

The IR intensities are calculated from the Born charge tensor, which represents the change of dipole moment relative to the atomic displacements. The Berry phase method with the default Direct Inversion of Invariant Subspace (DIIS) convergence accelerator is used to perform these calculations, as the polarisation changes between the neutral and the distorted geometries.²¹¹ The IR-intensities at each p -th mode are computed with the formula:

$$I_p = \frac{\pi N_A}{3} \frac{d_p}{c^2} |\mathbf{Z}_p|^2 \quad (3.22)$$

where N_A is the Avogadro's number, c is the speed of light, d_p is the degeneracy of the mode, and \mathbf{Z}_p is the mass-weighted Born effective charge vector.

Raman intensities are calculated by first computing the Raman tensor with a coupled-perturbed Hartree-Fock/Kohn-Sham approach with accelerated convergence by mixing Fock/KS matrix second derivatives (ANDERSON2).²¹²⁻²¹⁴ The method calculates the Raman polarisability tensors along all Cartesian directions (X, Y, Z, XX, XY, XZ, YY, YZ, ZZ) based on an applied electric field. Experimental temperatures and laser excitation wavelength are also considered.

The frequency analysis provides the peak positions and intensities, while the peak width depends on the experimental results. For the best comparison, the simulated spectra are fitted to Lorentzian line shapes with the same full-width value at half maximum as the experimental spectra.

3.2.4 Beyond Frequency Analysis

Elastic Properties

Elasticity is an important aspect of the mechanical properties of materials. The second-order elastic constants C of a crystalline system relate the stress and strain as the following equation shows.

$$\sigma_{ij} = C_{ijkl} \epsilon_{kl} \quad (3.23)$$

where i, j, k and $l = 1, 2, 3$, σ_{ij} is the stress, and ϵ_{kl} is the strain. The elastic constants

C_{ijkl} are usually expressed in a simplified format $C_{\alpha\beta}$ with Voigt's notation, as $\alpha = ij, \beta = kl$, and $\alpha, \beta = 1, 2, \dots, 6$ (i.e. $xx = 1, yy = 2, zz = 3, yz = 4, xz = 5$, and $xy = 6$). $C_{\alpha\beta}$ is defined as the strain second derivative of the total energy:

$$C_{\alpha\beta} = \frac{1}{V} \frac{\partial^2 E}{\partial \varepsilon_\alpha \partial \varepsilon_\beta} \quad (3.24)$$

where V is the volume of the unit cell.^{215;216}

A calculation of second-order elastic constants can be activated by the keyword ELASTCON, and the input structure needs to be well-optimised. The symmetry of crystals is applied to reduce the number of independent components which in turn accelerates the calculation. The symmetry determines how many deformations (up to 6) are actually needed to compute the $C_{\alpha\beta}$ matrix. For each deformation, the number of points and the size of displacement can be defined by NUMDERIV and STEPSIZE, and a geometry optimisation is performed at each point resulting in the strain matrix. After the elastic constants matrix is achieved, elastic properties such as shear modulus, Young's modulus, Poisson's ratio and bulk modulus can be obtained from the Voigt-Reuss-Hill approximation.²¹⁶ In Section 4.2, a case study of MOF-5 is an example of computing the elastic constants using the automated procedure implemented in CRYSTAL17.

Thermodynamic Properties

When the phonon modes are accurately calculated for the crystals, the thermodynamic properties within a defined temperature range in steps (TEMPERAT) can also be predicted (based on the HA) with nearly zero additional computational time. For each \mathbf{k} point in the BZ, there are $3N$ harmonic oscillators labelled by i ($i = 1, \dots, 3N$; N is the number of atoms in a unit cell). Therefore, the energy can be expressed as:

$$\varepsilon_m^{i,\mathbf{k}} = \left(m + \frac{1}{2} \right) \omega_{\mathbf{k}i} \quad (3.25)$$

where m is an integer referring to the vibrational level and $\omega_{\mathbf{k}i} = 2\pi\nu_{\mathbf{k}i}$. The vibrational canonical partition function of the crystalline system at a defined temperature is

$$Q_{\text{vib}}(T) = \prod_{\mathbf{k}} \prod_{i=1}^{3N} \sum_{m=0}^{\infty} \exp \left[-\frac{\varepsilon_m^{p,\mathbf{k}}}{k_{\text{B}}T} \right] \quad (3.26)$$

where k_{B} is the Boltzmann's constant. The entropy $S(T)$ and the internal energy $U(T)$ can be calculated from Q_{vib} as

$$S(T) = k_{\text{B}}T \left(\frac{\partial \log(Q_{\text{vib}})}{\partial T} \right) + k_{\text{B}} \log(Q_{\text{vib}}) \quad (3.27)$$

$$U(T) = k_{\text{B}}T^2 \left(\frac{\partial \log(Q_{\text{vib}})}{\partial T} \right) \quad (3.28)$$

and the constant-volume specific heat $C_v(T)$ can also be calculated via $C_v(T) = \partial \varepsilon(T) / \partial T$.²¹⁷ From the available thermodynamic data, the Gibbs free energy curve (at atmospheric pressure and constant volume) can be calculated that is very helpful to determine the possible phase transitions and relative stability between polymorphs (Section 6.1).

Chapter 4

Low-Frequency Dynamics and Physical Properties of Metal-Organic Frameworks

The first system discussed here is a class of large ordered crystalline systems, metal-organic frameworks (MOFs), usually porous materials. The nature of the interatomic interactions present within the pores and its flexibility can affect the adsorption process, and is also critical to design and utilise these advanced materials with desirable applications. The work outlined in Section 4.1 has been published in the journal *Chemical Communications* and is reproduced from Li et al. (doi.org/10.1039/C8CC02650E)¹⁰ with permission from the Royal Society of Chemistry. It was a collaboration with Prof. Timothy Korter and Dr. Adam J. Zaczek at the University of Syracuse, who performed the Raman spectroscopy measurements for the project. The author of this thesis performed THz-TDS measurements and all the computational work.

Section 4.2 is an extension of this work following on MOFs. At the example of MOF-5, the work shows the possibility of applying the developed methodologies to study the flexibilities of MOFs. However, due to the unstable nature of MOF-5, it only contains computational results. All the results presented in this section were achieved by the author of this thesis.

4.1 Methyl-Rotation Dynamics in Metal-Organic Frameworks: ZIF-8 and ZIF-67

4.1.1 Introduction

Metal-organic frameworks (MOFs) are a class of solid materials that have exciting physical properties with numerous applications including gas storage, chemical separation, drug delivery, and catalysis.^{5;7-9;218} The basis of the diverse utility of MOFs partly lies in their rich topological possibilities.^{219;220} A wide range of three dimensional structures can be realised, with many of these containing large spatial voids that are related to their applicability.²²¹⁻²²³ Unquestionably, the molecular and bulk structures of MOFs play a major role in defining their performance for such applications.^{224;225} It has however become clear in recent years that the vibrational dynamics of the solids are also of critical importance in dictating the efficacy of such materials.^{226;227} Previous work has demonstrated that in particular, the low-frequency (sub 200 cm^{-1}) vibrational motions are clearly critical for many properties, such as mechanochemical and gas adsorption phenomena.^{148;149} It is therefore highly desirable to develop a complete understanding of the interplay between the structural and dynamical aspects of MOFs in order to optimise their design, and ultimately, their function. In one of the most well-studied MOF systems, ZIF-8, it has been shown that the solid is capable of adsorbing a large variety of molecules, ranging from gaseous nitrogen to active pharmaceutical ingredients.^{228;229} Zeolitic imidazolate frameworks (ZIFs) are composed of transition metal ions connected by imidazolate linkers with a tetrahedral coordination. The “zeolitic” term refers to the similarity between the metal-imidazole-metal angle and the Si-O-Si angle in zeolites. Figure 4.1 shows the structure of ZIF-8 where the big blue sphere in the middle on the right side represents the large pore within the material that can potentially accommodate adsorbed molecules. ZIF-8 is regarded as a prototype of ZIFs, and has been investigated both experimentally and computationally in much greater detail compared to other ZIFs.^{116;117;230} ZIF-67^{231;232} is the cobalt-substituted structural analogue of ZIF-8. It is less well-studied, yet the similarity between the two makes it readily possible to extend the

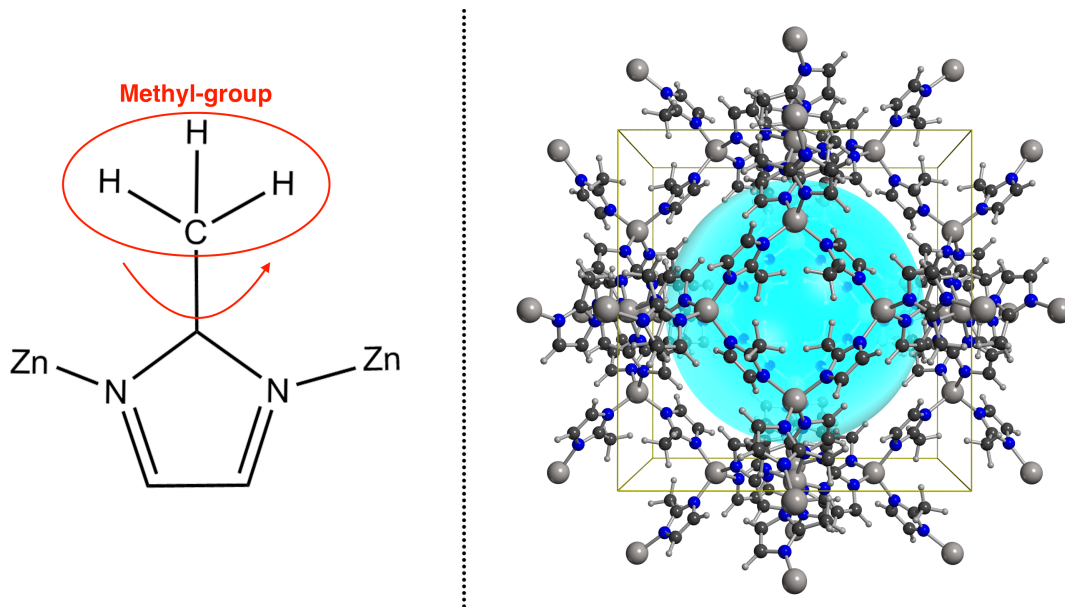


Figure 4.1. The formula unit structure of ZIF-8 is shown on the left and with the bulk packing on the right. The grey atoms represent the zinc atoms which are connected by the imidazolate linkers. The blue sphere displays the void volume within the material.

computational method used for ZIF-8 to ZIF-67, and also the straight-forward comparison of the two sets of results.

Low-frequency vibrational spectroscopy (10 cm^{-1} to 200 cm^{-1} or 1 meV to 25 meV) provides unique insight into the weak forces that are present within molecular solids.^{233–236} Since the vibrations often involve large amplitude motions of entire molecules, it is possible to experimentally explore a large portion of both the intra- and inter-molecular potential energy hypersurface.²³⁷ By combining the experimental data with quantum mechanical simulations, it is possible to fully characterise the atomic-level structure, dynamics, and forces that are present within the solid. The accurate simulation of the low-frequency vibrational spectra inherently depends on the description of the weak forces that supports the investigation of the mentioned properties of solids using a theoretical approach.^{153;238} A good match between the experimental vibrational spectrum and the simulated spectrum can be used as a method to experimentally validate the ab initio simulations. The simulations in turn also yield additional data that would be difficult to obtain experimentally (e.g. band structures) to be extracted with a high degree of confidence. In this work, THz-TDS and low-frequency

Raman spectroscopy are combined with ss-DFT simulations in order to probe the quantum mechanical origin and atomic dynamics of the quasi-free methyl rotation in crystals of ZIF-8 and ZIF-67.

Previous research on the gate-opening and pore-breathing mechanisms in ZIF-4, ZIF-7, and ZIF-8 demonstrates that DFT calculations, along with THz-TDS, offer new opportunities to study the fundamental lattice dynamics of ZIFs. In that study, the simulated results of ZIF-4 and ZIF-7 matched well with measurements, however the agreement was not attained for ZIF-8 when it reached low-frequency range.¹¹⁶ A recent study by Tan et al. successfully investigated the mechanical dynamics of ZIF-8 and ZIF-90 with the combination of THz-TDS and DFT simulations, and the simulated results showed excellent agreement with the experimental data, even at frequencies below 3 THz. Critically, the authors shared that it was possible to get a far more accurate result for this sample when using the M06-2X density functional¹⁸³ instead of the functional developed by Perdew, Burke and Ernzerhof (PBE)^{239;240}.¹¹⁷ This work also makes the case for the importance of low-frequency motions in the applications of ZIFs, such as gas storing.

For both materials, the methyl-groups (at the top of left side Figure 4.1) on the imidazolate linkers that point into the pore exhibit free (or nearly-free) rotation even at cryogenic temperature without discernible methyl-methyl coupling, giving rise to very low energy transitions on the order of μeV .²³⁰ This class of quasi hindered-rotational motions have long been used as a probe of the weak forces within materials, and thus the investigation of the interactions within the pores and the methyl-rotation dynamics is important to fully understand the adsorption process for further practical applications. However, even though methyl quantum rotors have been studied in other materials, such as 4-methylpyridine, and the topic has drawn attention of scientists for a long time,²⁴¹ the methyl-rotation dynamics in MOFs have not been well investigated. Previous research of Zhou et al. gives an estimated value of the barrier height of ZIF-8 as 7 meV probed by inelastic neutron scattering without any detailed explanation.²³⁰ By building on the existing understanding of the fundamental quantum mechanical processes underpinning these motions, this project aims to develop better insight into the properties of ZIF-8 and ZIF-67.

In this work, the methyl-rotation energy barriers of ZIF-8 and ZIF-67 were calculated explicitly. The 1-D Schrödinger equation was solved and used to compute the vibrational levels and wavefunctions for both materials, leading to an explanation of the origin of quasi-free methyl group rotation within ZIFs. In addition, the transition energies were computed to investigate the rotational tunnelling phenomena by comparing with previously published results.

4.1.2 Materials and Methods

Terahertz Time-Domain Spectroscopy

For THz-TDS transmission measurements, the samples were mixed with polyethylene (PE) to a 5% w/w concentration and mixed using a mortar and a pestle. The well-mixed powder was subsequently pressed by a hydraulic press at 2 tons of pressure into a pellet with a 13 mm in diameter and ~ 2 mm of thickness. A blank PE pellet was prepared with the same method and used as a reference. Cryogenic temperature measurements were performed via the set up described in Chapter 2.

Low-Frequency Raman Spectroscopy

The low-frequency Raman spectra were acquired with an Ondax (Monrovia, California, United States) THz-Raman system with a 784.7 nm centered laser excitation fibre coupled to an Andor (Belfast, United Kingdom) Shamrock 750 nm spectrograph equipped with an Andor iDus 416 CCD. Pure ZIF samples were placed in a 1 cm capillary, and an empty capillary was used as a reference.

DFT Simulations

Both MOFs were studied using fully-periodic DFT calculations with the CRYSTAL17 software package.¹⁵⁹ The M06-2X meta-global gradient approximation (meta-GGA) density functional¹⁸³ (including the gradient of electron density and the kinetic energy density) was used for correlation and exchange (with 54% explicit Hartree-Fock exchange), and was combined

with the split-valance double-zeta 6-31G (d,p) basis set.²⁴² The initial geometries of ZIF-8 and ZIF-67 were obtained from the published crystallography database (CSD)²⁰⁵. A SHRINK of 4 was set corresponding to 8 k-points in the reciprocal space, and the energy convergence was set at 10^{-8} Hartree. The tolerance of bielectronic coulomb and Hartree-Fock (HF) exchange integrals were set to 10^{-8} , 10^{-8} , 10^{-8} , 10^{-8} and 10^{-16} (TOLINTEG). For the geometry optimisations, atomic positions and lattice parameters were fully relaxed except for the space group symmetry. Based on the electronic structure of cobalt, spin-unrestricted calculations were applied to ZIF-67 with three electrons initially unpaired in a ferromagnetic arrangement for the first five self-consistent field cycles. The optimised structures were then used to calculate harmonic vibrational frequencies. The PBE density functional²³⁹ was tested at first, while this resulted in the undesired generation of negative modes in the frequency output. Thus, the M06-2X density functional¹⁸³ was chosen as it proved to be effective in previous studies on ZIFs.¹¹⁷ The energy convergence was set to 10^{-10} Hartree for frequency analysis, as the accuracy of the electrons' positions highly influences the intensities. Two displacements for each atoms were performed along the three directions in Cartesian coordinates to compute the first-derivatives of the gradient $g(x) = dE(x)/dx$, where $g(x)$ is the derivative of energy change against displacement (NUMDERIV=2).

In order to explore the methyl rotation dynamics within the ZIFs, the optimised crystal structures were locked except the methyl group which was rotated in steps of 10° corresponding to the carbon-carbon bond (as shown in Figure 4.1). To calculate the new position of the three hydrogen atoms, the Cartesian coordinates were first extracted from the optimised geometry output, and the origin was changed to the carbon within the methyl group. The new coordinates of hydrogen atoms were then calculated by a 3×3 rotation matrix as a function of \hat{n} and θ , where \hat{n} is a real vector of unit length passing through the origin, and θ is the rotation angle (Eqn 4.1).

$$R(\hat{n}, \theta) = \begin{pmatrix} \cos\theta + n_1^2(1 - \cos\theta) & n_1n_2(1 - \cos\theta) - n_3\sin\theta & n_1n_3(1 - \cos\theta) + n_2\sin\theta \\ n_1n_2(1 - \cos\theta) + n_3\sin\theta & \cos\theta + n_2^2(1 - \cos\theta) & n_2n_3(1 - \cos\theta) - n_1\sin\theta \\ n_1n_3(1 - \cos\theta) - n_2\sin\theta & n_2n_3(1 - \cos\theta) + n_1\sin\theta & \cos\theta + n_3^2(1 - \cos\theta) \end{pmatrix} \quad (4.1)$$

Table 4.1. The comparison of simulated and experimental structures.

	Relative error	RMSDs	
	Cell length	Bonds length	Angles
ZIF-8	0.3 %	0.04 Å	3.20 °
ZIF-67	0.6 %	0.02 Å	1.12 °

Once the new coordinates were obtained, the origins were altered back to the initial one, and divided by the cell length to obtain the fractional coordinates. For each new structure, the geometry optimisation calculation was performed resulting in the respective potential energies. Further calculations were done on an expanded (+1.5 %) and a compressed (-1.5 %) volume relative to the optimised structure of ZIF-8 to study the volume dependence of the methyl-rotation energy barriers, as upon comparison ZIF-67 was found to be 1.5 % smaller than ZIF-8 in volume.

4.1.3 Results and Discussion

Geometry Optimisation

The optimised structures acquired from the simulations were compared with the experimental data in terms of the cell length difference, the root-mean-square deviations (RMSDs) of bond lengths and angles without hydrogen atoms. The differences between dihedrals were not looked at in detail, as the molecule lies generally in a plane. Both simulated structures for ZIF-8 and ZIF-67 are in excellent agreement with the crystallographic data. The details are shown in Table 4.1. In order to validate the simulated results, THz-TDS and low-frequency Raman spectroscopy measurements were performed, and the results are compared with the simulated harmonic frequencies analysis shown in the following section.

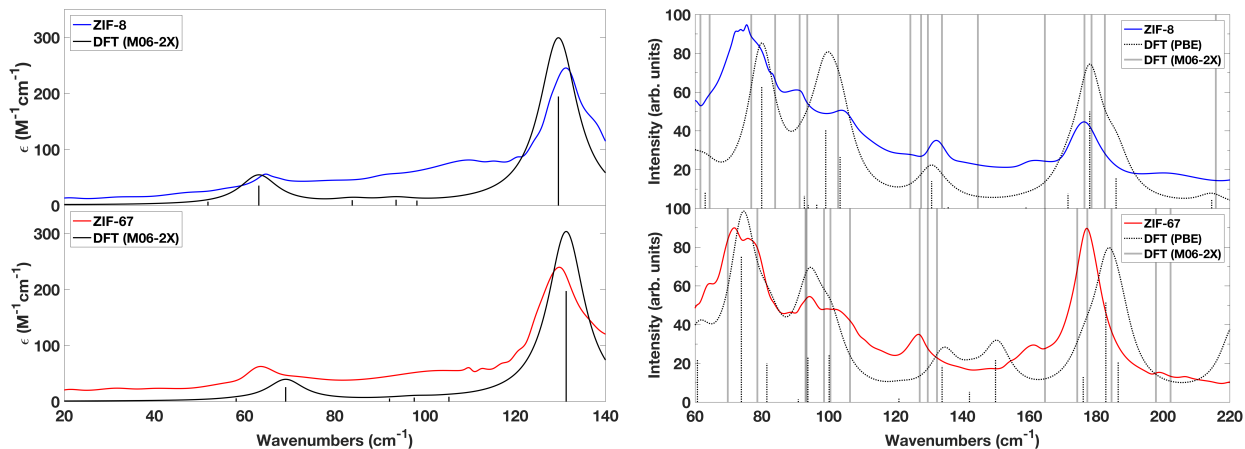


Figure 4.2. The experimental low-frequency vibrational spectra of ZIF-8 (blue) and ZIF-67 (red). The left panel shows the 78 K THz-TDS spectra, as well as the simulated IR-spectra (black) convolved with Lorentzian line-shapes based on the experimental full-width at half-maxima (FWHM), and corresponding vibrational transitions (black sticks). The right panel shows the experimental 298 K low-frequency Raman spectra, with the M06-2X-predicted Raman-active modes and PBE-predicted spectra shown as solid and dashed lines, respectively.

Low-Frequency Vibrational Spectra

Figure 4.2 shows the THz-TDS spectra of ZIF-8 and ZIF-67 on the left side and Raman spectra on the right. The high similarities correspond to the isomorphic structures of both materials, and only minor shifting is observed for a few adsorption features. With respect to THz-TDS spectra, the black curve represents the simulated spectra with the short vertical black ticks displaying the intensities. The results are in great agreement with the experimental measurements except for the intensities which are a little bit overestimated near 130 cm^{-1} in both solids. The spectra of low-frequency Raman spectroscopy are shown in the right figures. Unfortunately, CRYSTAL17 software package¹⁵⁹ cannot provide the intensities for Raman spectroscopy with the M06-2X density functional¹⁸³, but the active modes are marked by vertical solid lines, and fit well with experimental results except missing those modes at 70 cm^{-1} and 103 cm^{-1} in the ZIF-8. The Raman intensities are acquired using PBE density functional²³⁹, but it does not match with the experimental spectra as well as M06-2X¹⁸³. The modes for hindered-rotational motion are 129.6 cm^{-1} (Raman active) and 176 cm^{-1} (neither Raman nor IR active) in ZIF-8 and ZIF-67, respectively. Within the range of 120 cm^{-1} to 140 cm^{-1} in ZIF-8, there is another IR-active mode which is more likely a gate-opening

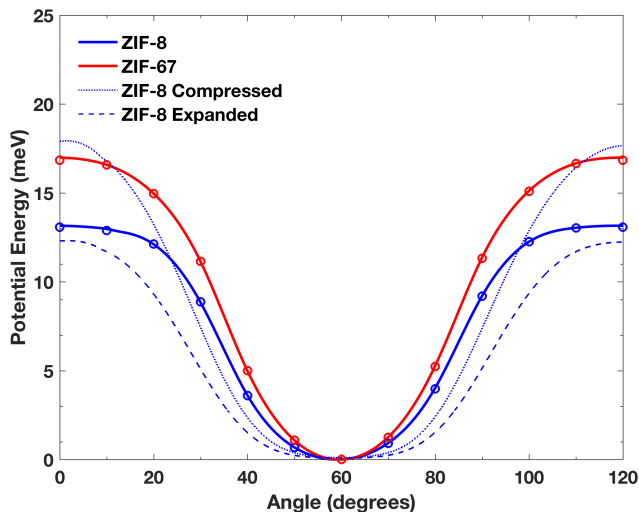


Figure 4.3. Simulated methyl rotor potential energy of ZIF-8 (blue) and ZIF-67 (red) with a step of 10° from 0° to 120° with the 60° minimum representing the equilibrium staggered conformation of the methyl-hydrogens with respect to the plane of the imidazolate ring. The blue dotted and dashed lines represent a contracted and expanded ZIF-8 structure, respectively.

motion as visualised with Jmol²⁰⁹. The combination of THz-TDS and Raman spectroscopy enables the full investigation of all the active modes within the terahertz radiation region, and the perfect match validates the simulated outputs. Therefore, the optimised structures can be used for further calculations such as the study of methyl-rotation dynamics.

Simulations of Methyl-Rotation Potential Energy

The potential energies were acquired in steps of 10° both for ZIF-8 and ZIF-67 as shown in Figure 4.3 with the blue/red circles marked at each point. The figure only displays the potential energies from 0° to 120° as the rotation has a three-fold symmetry, so the phenomenon repeats after every 120° . The results show that ZIF-67 has a higher energy barrier than ZIF-8, and this can be explained by the relative smaller volume (-1.5%) of ZIF-67. To understand the volume-dependence of energy barriers, calculations were performed on an expanded ($+1.5\%$) and a compressed (-1.5%) structure of ZIF-8. Comparing the three blue curves, the barrier heights increase when the volume shrinks, which supports the explanation. Also the comparison between compressed ZIF-8 with ZIF-67 proves that volume influences the energy barrier, while the slight difference can be explained by the metal atoms within

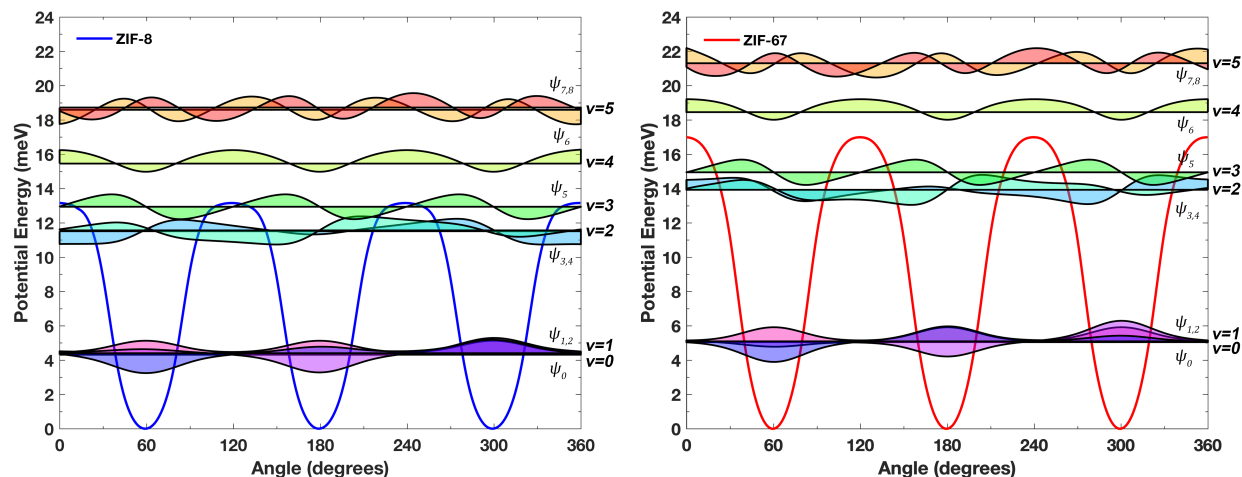


Figure 4.4. Simulated methyl rotor potential energy of ZIF-8 (left, blue) and ZIF-67 (right, red) with the torsional vibrational curves drawn as black lines, and the scaled-normalized ($\times 3$) vibrational wavefunctions drawn as shaded curves.

the materials that result in a change of angles from 0.15° to 0.25° . The effect of volume is intuitively understandable, as when the pore size decreases, it becomes more difficult for methyl groups to rotate within the structures. This can be used to explain the importance of the methyl-rotation dynamics as well. When MOFs are applied to adsorb gases or other molecules, the pores will be occupied by the adsorbents which may inhibit the rotation process of methyl groups. Therefore, the detailed understanding of methyl rotors could be a new method of probing the adsorption process in MOFs and the amount of molecules adsorbed. In addition, the potential energies were calculated explicitly with reduced symmetry groups, and the simulated outputs show the same results as the calculations with the original symmetry groups. Therefore, no obvious change occurs when the symmetry is altered. It can be concluded that there is only one type of methyl groups in the structure. Combined with Figure 4.2, as there are no split peaks on the experimental spectra, the assumption of no methyl-methyl coupling was proved both experimentally and computationally.

Insight into Methyl-Rotation Dynamics

In order to explain the existence of methyl rotation even at low temperature (below 80 K), the method proposed by Lewis et al. was applied that obtained the vibrational levels and the

Table 4.2. Experimental and simulated energetic components (in meV) of the methyl hindered-rotational process in ZIF-8 and ZIF-67.

		Experimental	ZIF-8	ZIF-67
Potential Max (meV)		–	13.16	16.99
Zero-Point (meV)		–	4.31	5.04
Barrier Height (meV)		~ 7	8.85	11.95
	$0 \rightarrow 1$	334×10^{-3}	225×10^{-3}	466×10^{-3}
Transition Energies (meV)	$1 \rightarrow 2$	2.7	6.97	8.83
	$2 \rightarrow 3$	–	1.43	1.02

wavefunctions by solving the 1-D Schrödinger equation, which provided the potential energies up to level 6.²⁴³ The wavefunction describes the quantum state of a particle. Figure 4.4 shows that at some levels there are more than one wavefunction because of degenerate levels that also correspond to the existence of methyl-rotation. The square of the wavefunction corresponds to the possibility of the population of electrons within a specific region. Here, even when the temperature is low that the energy can only reach one of the lowest level, the population of electrons still expands over a wide range of angles that means the methyl groups are still rotating. Thus, this result offers a fundamental explanation of methyl-rotation dynamics. The maximum potential and the zero-point energy (ZPE) can be read from the figure directly, while the actual energy barrier was calculated by subtracting the maximum value from the ZPE. The final results are shown in the Table 4.2. The maximum barrier height is 13.16 meV and 16.99 meV of ZIF-8 and ZIF-67, respectively. Considering the ZPE, the predicted values of ZIF-8 and ZIF-67 are 8.85 meV and 11.95 meV. The transition energies were also calculated from the vibrational levels. All these energies corresponding calculations were performed with fully crystalline symmetry and periodic boundary conditions, and are given in units of meV mol⁻¹methyl⁻¹.

Comparison with Inelastic Neutron Scattering Results

In Table 4.2, the results from this study are compared with the previous study of methyl-rotation in ZIF-8 by Zhou et al. with the inelastic neutron scattering (INS).²³⁰ The values in the “experimental” column were obtained from the study by Zhou et al.²³⁰ The predicted value for the barrier height matched well with the experimental data except for the big difference at the transition energy from $1 \rightarrow 2$. In this context, it is useful to note that in the chemistry community the simulated result will be regarded as good if the difference between the predicted value and the experimental data is below 1 kcal/mol (43 meV).^{188;189} In this project, the relative difference are three orders of magnitude lower than this requirement. The difference for the transition energy $1 \rightarrow 2$ can be explained properly when we looked into the two methods in detail. As the predicted value for $1 \rightarrow 2$ were 6.97 meV and 8.83 meV that are both out of the range shown in the previous paper of ZIF-8 which reached 4 meV at maximum, the value measured by the INS of $1 \rightarrow 2$ could be the transition energy of $2 \rightarrow 3$.

4.1.4 Conclusions

In ZIF-8, one of the most well-studied MOFs to date, and its cobalt analogue ZIF-67, the imidazolate methyl-groups, which point directly into the void space, have been shown to freely rotate even down to cryogenic temperatures. Using a combination of experimental terahertz time-domain spectroscopy, low-frequency Raman spectroscopy, and state-of-the-art ab initio simulations, the methyl-rotor dynamics in ZIF-8 and ZIF-67 are fully characterised within the context of a quantum-mechanical hindered-rotor model. The study successfully predicts the rotational energy barriers of ZIF-8 and ZIF-67 as 8.85 meV and 11.95 meV. Closer analysis of the vibrational levels and the wavefunctions lends insight into the fundamental origins of the experimentally observed methyl-rotor dynamics, and provides valuable information into the nature of the weak interactions present within this important class of materials.

4.2 Case Study: Elasticity of MOF-5

4.2.1 Introduction

The mechanical properties of porous MOFs are very important for potential utilisations. The elastic constants of MOF-5 have been studied via experimental and computational methods, and the reported results show that MOF-5 is a non-flexible cubic material but highly anisotropic. Bahr et al. used two different nanoindentation techniques, the continuous stiffness measurement (CSM) and the quasistatic indentation, to measure the Young's modulus as 2.7 ± 1.0 GPa and 2.5 ± 1.0 GPa respectively. There are three factors that were proposed might influence the experimental results: surface roughness, atmospheric interactions, and plastic deformation.²⁴⁴ While the result was corrected by the method studied by Vlassak and Nix, the final estimated value was 7.9 GPa when considering the anisotropic effect.²⁴⁵ However, the Young's modulus predicted by computational methods had an average around 21.6 ± 0.3 GPa, which is much higher than the experimental results. Even by applying the correction factors, the simulated result is still three times higher than that of experiments. In addition, the lattice parameters were not well reproduced by the LDA and GGA simulations.^{4;246} Herein, M06-2X density functional¹⁸³ is applied to carry out geometry optimisation and to calculate elastic constants of MOF-5 (the structure is shown in the Figure 4.5) in order to get better insights of its flexibilities from computational perspective. The method has been proved to be effective to enhance the accuracy of computational work based on the previous studies on MOFs.^{10;247} Unfortunately, due to the instability of MOF-5, there was no sample available for experiments, so this case study only covers the computational work and results.

4.2.2 Materials and Methods

The optimised geometry, the harmonic frequencies, and the elastic tensors were calculated by ss-DFT simulations performed using CRYSTAL17 software package¹⁵⁹ (the details of the calculations were discussed in Section 3.2). The crystallographic published data (MIBQAR²⁴⁹)

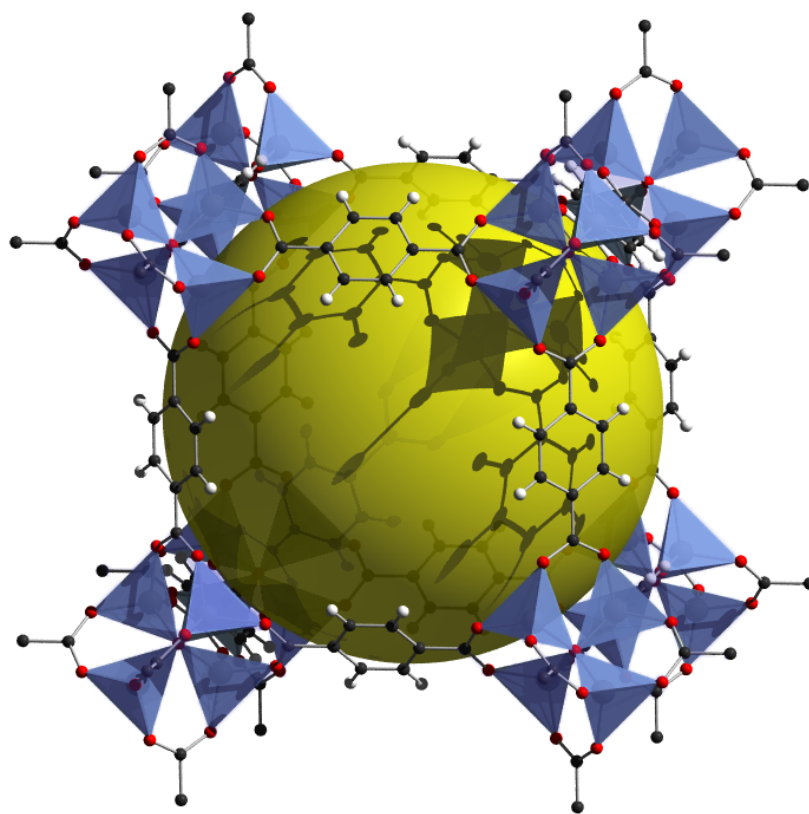


Figure 4.5. The structure of MOF-5. Adapted from Rosi et al.²⁴⁸

was used as the initial geometry input. The M06-2X meta-global gradient approximation (meta-GGA) density functional¹⁸³ was combined with the split-valence double-zeta 6-31G(d,p) basis set²⁴². The geometry optimisation was carried out without any restriction on lattice parameters and atomic coordinates except for the geometry symmetry. A SHRINK of 4 was set corresponding to 8 k-points in the reciprocal space, and the tolerance of bielectronic coulomb and Hartree-Fock (HF) exchange integrals were set to 10^{-8} , 10^{-8} , 10^{-8} , 10^{-8} and 10^{-16} (TOLINTEG). The energy convergence criteria was set at 10^{-8} Hartree, and the criterion was more strict for the frequency and the elastic constants calculations which was set to 10^{-10} Hartree.

4.2.3 Results and Discussion

The simulated structure of MOF-5 was in great agreement with the experimental result measured by neutron diffraction from deuterated MOF-5 at 3.5 K²⁵⁰, with an 0.04 % relative error of the lattice parameters. This was more promising than all the slightly lower values obtained from previous LDA and GGA methods.⁴ Civalleri et al. published a case study on MOF-5 with B3LYP density functional, and the output was comparable with the experimental data. It also found the lowest IR active mode was at 52 cm^{-1} , and our result showed a terahertz active mode at 50.8 cm^{-1} .⁴ However, when it comes to the lattice parameter, bond lengths and angles, the results from our method are much closer to the values in the database. The close comparison is shown in the Table 4.3, and the labels are denoted as shown in Figure 4.6. The various elastic constants were calculated including bulk modulus, Young’s modulus, shear modulus and Poisson’s ratio. The Voigt, Reuss, and Hill averages are shown in Table 4.5. Compared with the experimental results, the predicted Young’s modulus from this study is 8.24 GPa, which is very close to the corrected value of 7.9 GPa.

The symmetric matrix of elastic constants calculated from CRYSTAL17 (Table 4.4) was imported to the elastic tensor analysis, ELATE, to fully process the elastic tensor which gave out detailed information.²⁵¹ The results are shown in Table 4.6 and Figure 4.7.

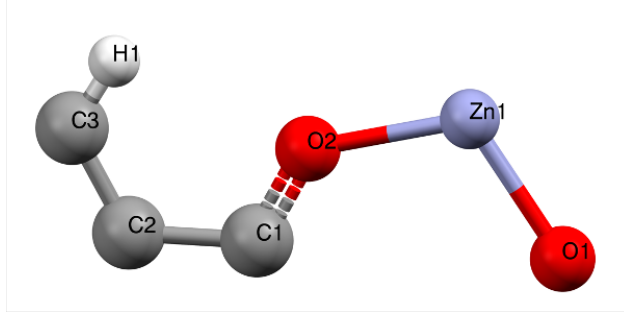


Figure 4.6. The asymmetric unit of MOF-5.

Table 4.3. The comparison of lattice parameter (Å), bond lengths (Å), and angles (°).

	B3YLP	M06-2X	Exp. (165 K)	Exp. (3.5 K)
a	26.088	25.903	25.856	25.909
O1-Zn	1.972	1.945	1.947	1.968
Zn-O2	1.961	1.948	1.936	1.947
O2-C1	1.270	1.262	1.261	1.254
C1-C2	1.499	1.498	1.489	1.515
C2-C3	1.402	1.396	1.382	1.381
C3-C4	1.932	1.396	1.374	1.381
C3-H	1.084	1.084	-	1.108
Zn-O2-C1	131.7	131	131.4	130.7
O2-C1-O2	125.2	125.69	125.2	127.2
O2-C1-C2	117.4	117.16	117.4	116.4
C1-C2-C3	120.1	119.79	120.7	120.1
C2-C3-H	119.2	118.98	118.8	119.5

Table 4.4. The MOF-5 symmetric elastic constants matrix calculated with CRYSTAL17.

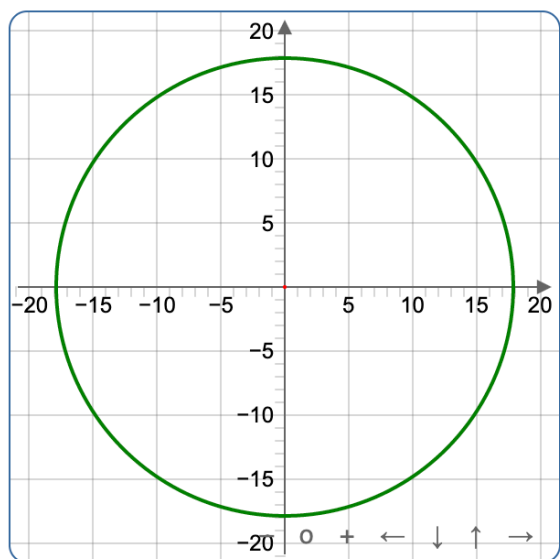
$$\begin{vmatrix}
 29.939 & 12.948 & 12.948 & 0.000 & 0.000 & 0.000 \\
 & 29.939 & 12.948 & 0.000 & 0.000 & 0.000 \\
 & & 29.939 & 0.000 & 0.000 & 0.000 \\
 & & & 1.116 & 0.000 & 0.000 \\
 & & & & 1.116 & 0.000 \\
 & & & & & 1.116
 \end{vmatrix}$$

Table 4.5. The average properties are based on the calculated elastic matrix, and the CRYSTAL17 picked the Hill average as the final value of Young's modulus.

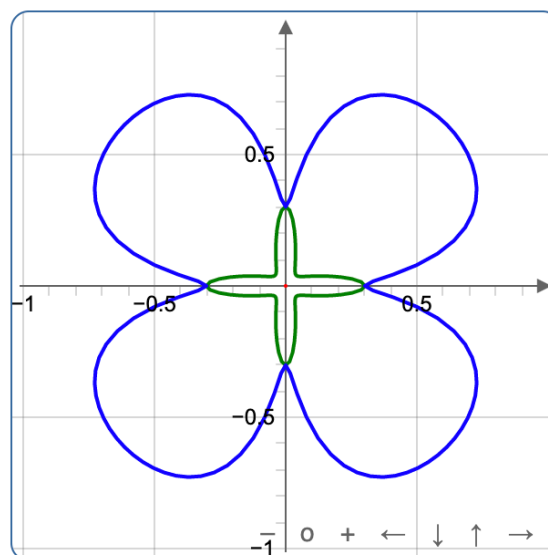
Averaging scheme	Bulk modulus	Young's modulus	Shear modulus	Poisson's ratio
Voigt	$K_v = 18.612$ GPa	$E_v = 11.375$ GPa	$G_v = 4.0678$ GPa	$\nu_v = 0.39814$ GPa
Reuss	$K_R = 18.612$ GPa	$E_R = 4.9782$ GPa	$G_R = 1.7102$ GPa	$\nu_R = 0.45542$ GPa
Hill	$K_H = 18.612$ GPa	$E_H = 8.2407$ GPa	$G_H = 2.889$ GPa	$\nu_H = 0.42621$ GPa

Table 4.6. The eigenvalues of the stiffness matrix.

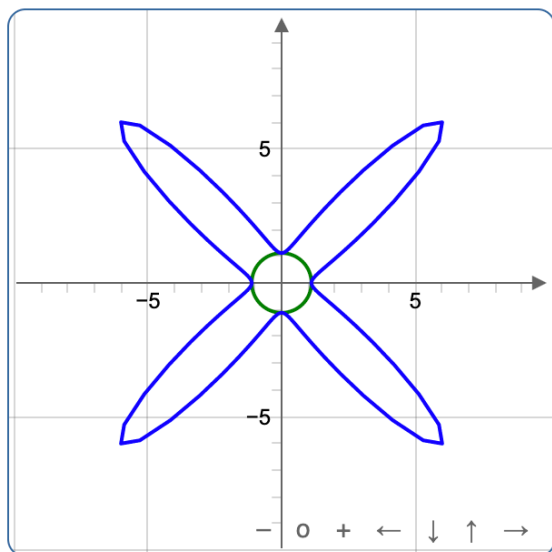
λ_1	λ_2	λ_3	λ_4	λ_5	λ_6
1.116 GPa	1.116 GPa	1.116 GPa	16.991 GPa	16.991 GPa	55.835 GPa



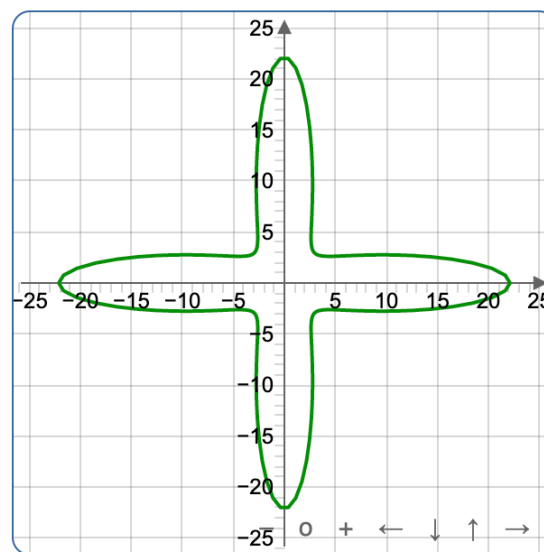
(a) Spatial dependence of linear compressibility.



(b) Spatial dependence of Poisson's ratio.



(c) Spatial dependence of shear modulus.



(d) Spatial dependence of Young's modulus.

Figure 4.7. The elastic properties of MOF-5.

4.2.4 Conclusions

The optimised geometry has a high agreement with the published crystallographic structure and the relative error for lattice parameters is 0.04%. The predicted Young's modulus is 8.24 GPa that is very close to the corrected experimental value. From both aspects, the results show that applying the M06-2X density functional can highly improve the accuracy of computational results and can also help with further studies of the flexibility of MOFs. However, it turns out that the synthesis of MOF-5 is too complicated and the structure is not very stable, thus no further experimental measurements are currently available to validate the computational results. As the case study showing here, the method can be extended to other MOF systems.

Chapter 5

Low-Frequency Vibrations and Magnetisation of Metal-Organic Perovskites

5.1 Introduction

Multiferroics are regarded as the materials that possess more than one ferroic property such as ferromagnetism, ferroelectricity, and ferroelasticity.²⁵² The materials with the combined properties of the first two have attracted more attention recently, as they are potential promising candidates for data storage.²⁵³ After TbMnO_3 was found to have magnetic coupling polarisation with a very low ordering temperature, and BiFeO_3 was discovered to possess strong polarisation without clear magnetoelectric coupling, researches were stimulated in this field looking for ideal candidates of multiferroic materials.^{254;255} As both structures fall into the perovskite category, many studies have been carried out aiming to search for or synthesise ideal perovskite multiferroics.²⁵⁶ At the beginning, more studies are focused on inorganic transition-metal oxides, and then the screening expanded to organic compounds such as perovskite metal-organic frameworks (MOFs). MOFs are composed of metal ions and organic linkers and attract a lot of attentions recently partially because of the highly porous materials

that are achieved with such structures, and therefore can be potentially applied to energy and gas storage, chemical separations, and catalysis.^{7;257} Metal-organic perovskites are a subclass of MOFs with similar structures as perovskite (ABX_3). The metal atoms are at the B site and are linked by the organic linkers denoted as X, and the organic cations occupy the A site in the centre. The composition and the inorganic-organic duality of these materials by nature lead to the possibility of exhibiting both magnetism and strong polarisation. One advantage from the nature of perovskite MOFs is that the multiferroic properties of the systems can be controlled by tuning the magnetic ordering of the metal ions or by adjusting the combination of the metals and the cations. Therefore, more fundamental studies on such materials will offer useful information for future design of new materials. Our interest of this project is the $[C(NH_2)_3][M^{II}(HCOO)_3]$ series that was first synthesised by Hu et al. in 2009. Their experimental work extensively studied and characterised the structures of the series, and showed the spin-canted anti-ferromagnetic (AFM) characteristics of such materials.¹¹ While ferromagnetism (FM) is more favourable for the potential applications, the study of magnetism and the possible magneto-electric coupling become more important in the field.²⁵⁶ Later on, Stroppa et al. and Svane and Aaron have also studied magnetic and ferroelectric properties of perovskite MOFs with computational approaches. However, the computational work was performed on certain MOF perovskites to investigate their magnetism and polarisation, but there was no systematic comparison between the same systems with different metals or the various spin configurations.^{12;258;259} In addition, the available vibrational spectroscopy studies on these systems were mainly at mid-IR range performed with classic FTIR and Raman spectroscopy.^{11;260} This study aims to combine the terahertz time-domain spectroscopy and the ab initio simulations to study the series of $[C(NH_2)_3][M^{II}(HCOO)_3]$ perovskite MOFs with various metal atoms from the low-frequency vibrational spectroscopy perspective, which is expected to be useful for this study to investigate the lattice vibrations at low-frequencies and the magnetisation of the targeting series of MOF perovskites with the only substitutions of metal atoms.

Seven such MOF perovskites (M=Mg, Mn, Co, Ni, Cu, Zn, and Cd) were investigated (M-MOF will be used to refer them individually). THz-TDS effectively probes weak interactions

within molecular systems e.g. hydrogen bonds. In addition, at such frequencies between 0.3 - 3 THz (10cm^{-1} - 100cm^{-1}), the spectral features show the contribution of long range vibrations of the whole structures, which makes the technique very sensitive to the slight structural differences. THz-TDS has been applied to a wide range of classic and emerging materials, such as small organic molecules^{23;26;101}, metal-halide perovskites^{152;261;262}, and MOFs^{10;117}, and promising results have been achieved, while there were no earlier studies using THz-TDS to study MOF perovskites. Same as the importance of molecular structures and bulk properties, previous work illustrates that vibrational dynamics are a major factor to the performance of materials as well.^{10;152;263} Therefore, the application of THz-TDS in this project is expected to provide some information that can complement the results acquired *via* other techniques. Due to the complexity of the collective motions falling in the terahertz range, ss-DFT simulations are applied to fully interpret the experimental results. With the proper tuning of the computational settings, comparable computational results for all the structures are achieved which offers the opportunity to study the effect of the slight change in spin configurations. Even though some materials may not be necessarily stable in nature, or have been hard to synthesise experimentally, simulations can still provide results based on reasonable assumptions. Thus, it will be helpful to guide the future design and synthesis process and to screen potential materials for desired applications.

5.2 Materials and Methods

5.2.1 Materials

The structure of the $[\text{C}(\text{NH}_2)_3][\text{M}^{\text{II}}(\text{HCOO})_3]$ series, with the guanidinium cation $[\text{C}(\text{NH}_2)_3]^+$ named as Gua^+ , is shown in Figure 5.1. The framework is composed of the metal atoms (M^{2+}) and the formate groups as the linkers. The Gua^+ cation in the centre is connected to the framework by six hydrogen bonds that makes this series more stable than similar structures with other cations.¹¹ Among the seven systems, the Cd-MOF is the only trigonal system and the other six are orthorhombic. The Cu-MOF perovskite, due to the John-Teller (J-T) effect

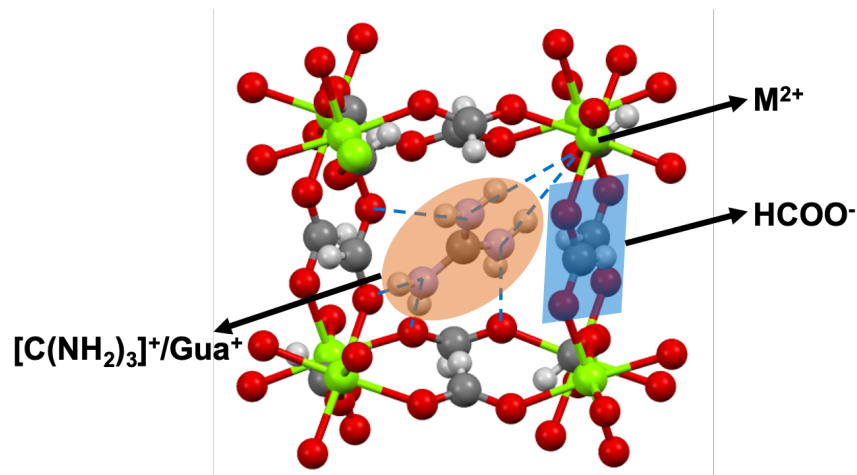


Figure 5.1. The structure of $[\text{C}(\text{NH}_2)_3][\text{M}^{\text{II}}(\text{HCOO})_3]$ MOF perovskite. The orange shaded area marks the Gua^+ cation, and the blue shaded area highlights the formate group linker. The blue dashed lines represent the six hydrogen bonds.

of the Cu atoms, results in a $\text{Pna}2_1$ symmetry, and all the other five are belonged to the Pnna space group.¹¹

5.2.2 THz-TDS Measurements

The THz-TDS transmission measurements were performed on a commercial spectrometer TeraPulse 4000 (TeraView Ltd., Cambridge, UK) with a cryostat (Janis, Massachusetts, USA) attached to cool the measurement chamber down to 80 K. The temperature was monitored and controlled by a coupled heater (Lakeshore 330, Ohio, USA). The perovskites single crystals were gently grounded with an agate mortar and a pestle and were then mixed with polyethylene (PE) to a 2% w/w concentration. The powder mixture was then compressed into a pellet with a hydraulic press at 2 tons, and a blank PE pellet was used as a reference. The spectrum of each sample was acquired from an average of 1000 waveforms with a spectral resolution of 0.94 cm^{-1} .

5.2.3 Solid-State DFT Simulations

All the calculations were performed using the CRYSTAL17 software package.¹⁵⁹ The same settings and parameters were applied to all the structures whenever possible to keep the

Table 5.1. Categorisation of the seven structures based on the electronic structure and the symmetry respectively.

Electrons	Unpaired	Ni, Co, Mn, Cu
	All-paired	Mg, Zn, Cd
Symmetry	Orthorhombic	Mg, Mn, Ni, Co, Zn
		Cu (J-T effect)
	Trigonal	Cd

results comparable. The 6-31G(d,p) basis set²⁴² and the B3LYP density functional with Grimme-D3 dispersion correction^{188;189} were used for the six systems, except for Cd-MOF. Since 6-31G(d,p)²⁴² was not available for Cd, def2SVP was chosen as an alternative and all the parameters were kept the same as the others.^{198;199} The energy convergence criterion for the geometry optimisation was set at 10^{-8} Hartree and 10^{-10} Hartree for the frequency analysis. The IR intensities were calculated based on the Berry phase method^{211;264} with the default Direct Inversion of Invariant Subspace (DIIS) convergence accelerator.

The seven structures were categorised based on two different criteria for the convenience of further computational work: First, they were divided into two groups depending on whether the metal atoms have or have not unpaired electrons; Second, they were grouped into two different symmetry groups (Table 5.1).

To closely study the magnetisation of the series materials, the spin configuration within a unit cell is considered specifically. For each metal atoms in the series of $[\text{C}(\text{NH}_2)_3][\text{M}^{\text{II}}(\text{HCOO})_3]$, there are six nearest metal atoms as shown in Figure 5.2. Four (M=Mn, Co, Ni, and Cu) out of the seven structures were composed of metal atoms with unpaired electrons, and the spin coupling was specified within one unit cell considering the computational resources.

Ferromagnetic (FM) spin coupling means all the unpaired electrons spin in the same direction, while the anti-ferromagnetic (AFM) coupling describes the electrons spinning oppositely and some effects may therefore cancel out. The spin configuration of each metal atom was set arbitrarily using the keyword SPIN and SPINLOCK available in CRYSTAL17 code. There were in total four metal atoms within one unit cell, therefore three AFM configurations were possible depending on how to set the spinning of each metal atom in a unit cell as shown in Figure 5.3 as well as the FM configuration. The relative energies and simulated spectra

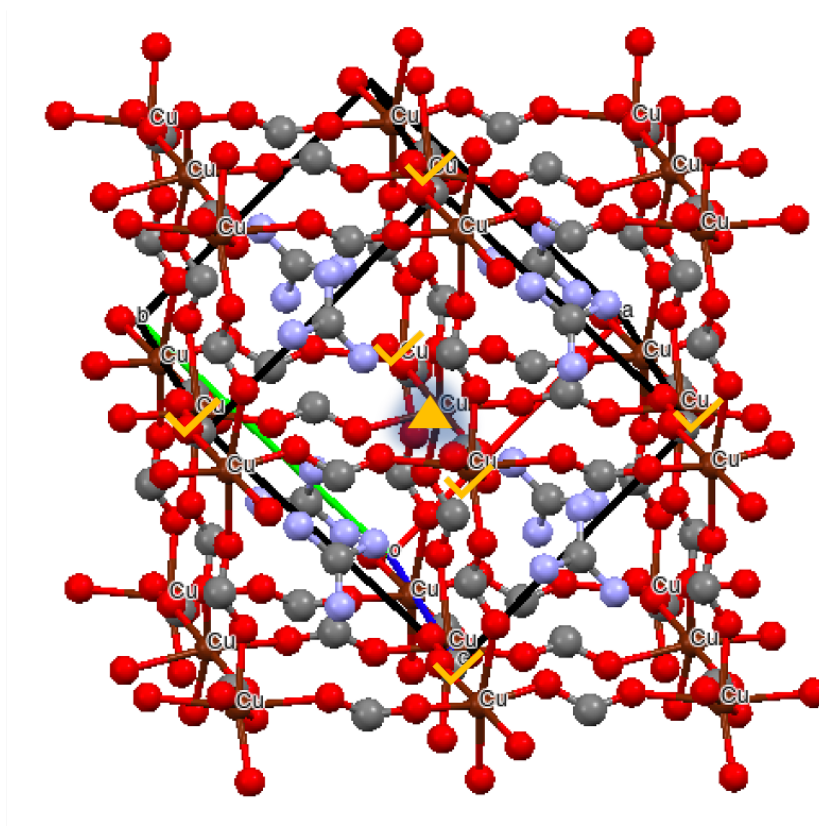


Figure 5.2. A supercell of Cu-MOF as an example to illustrate the spin coupling. The triangle marks the Cu atom in the centre, and the check marks highlight the six nearest Cu atoms to the centred one.

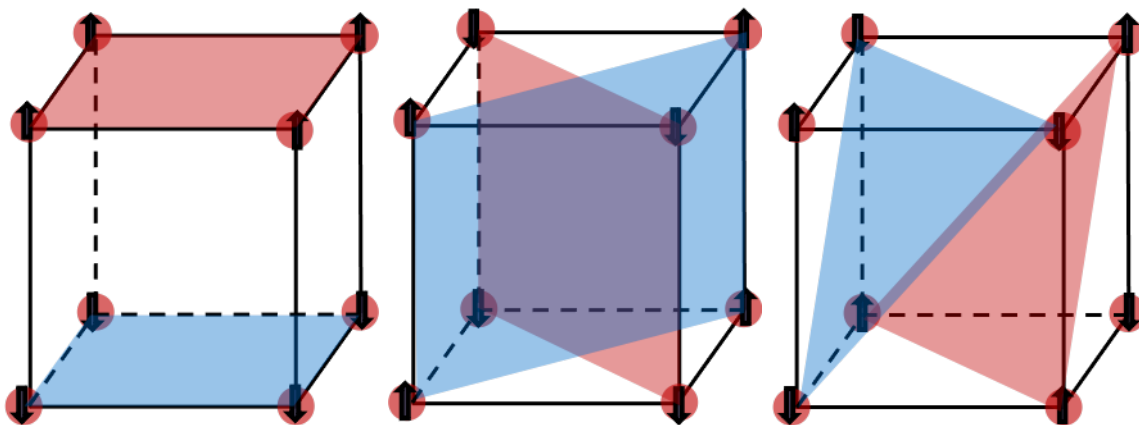


Figure 5.3. The possible three types of anti-ferromagnetic spin coupling with the restriction that the calculation was performed within one unit cell (AFM-A, AFM-B, and AFM-C, respectively). The arrows represent the spin direction of the unpaired electron of the specified atoms, and the atoms on the same coloured plane have the same spin setting.

were then compared between the structures with different metals and also the same metal but with different spin configurations.

The geometry for the systems was firstly optimised with the only restriction of space group. However, when the optimised structure was used for further frequency analysis, negative modes were predicted. The problem was fixed by moving all the atoms along the eigenvector of the negative mode with the highest intensity, and the unit cell was then fully re-optimised with the symmetry removed.¹² The optimised structures acquired after removing the symmetry led to good frequency analysis results without negative modes, yet this method also caused great amount of computational resources expenditure.

5.3 Results and Discussion

5.3.1 THz-TDS Measurements

Terahertz transmission measurements were performed on the seven MOF perovskites samples. Figure 5.4 shows the summary of the experimental spectra of all the systems. Cd-MOF, which is the only trigonal crystal, shows a clearly different spectrum compared to the other six. All six orthorhombic systems have comparable spectral features with two intense peaks at around

1.6 THz and 2.3 THz and one broad weak peak at around 2 THz. It is also observed that for the Mn-MOF spectrum the spectral features shift to lower frequencies compared to the other structures. In addition, the electron configuration of the high spin state Mn^{2+} , which has 5 unpaired electrons, just has one unpaired electron going into each 3d orbital. From the available crystallographic data, Mn-MOF is also the one with an obviously larger volume than the others, which can be another explanation of the features being located at relative lower frequencies.

5.3.2 Geometry Optimisation

All the finalised optimised structures were slightly distorted from the original lattice, which reflected the nature of disorders within their structures and also the sensitivities of the computational method. Mg-, Zn-, and Cd-based perovskites had all electrons in pair, therefore the simulated spectra were calculated directly from the frequency analysis calculations. For the structures with unpaired electrons (M=Mn, Co, Ni, and Cu), the energies for the systems with different spin configurations are summarised in Table 5.2, and the ones underlined are the configuration with the lowest energy among the structures with the same metal atoms. For all the structures, FM configuration had the highest energy among all the possibilities, which suggested clear AFM characteristics of the materials. Mn-, Co-, and Ni-MOF had the lowest energy with AFM-C configuration, while Cu-MOF reached the lowest with AFM-A that reflected its FM characteristics. The calculation of the AFM-C configuration of Ni-MOF did not fully converge to the set convergence criteria, so the energy was chosen as the average value of the several structures that were very close to meet the convergence criteria. The lattice parameters of the lowest energy structures were compared with the experimental data as shown in Table 5.3. Since the experimental data were acquired at room temperature (expect for Ni-MOF which was acquired at 173 K), the volume of all optimised systems shrank compared to the experimental data (while Ni-MOF shrank the least) which is due to the thermal effect, as the DFT calculations are calculated at 0 K. The relatively small differences and the consistent value for all the structures showed the accuracy of simulations. Neither the change

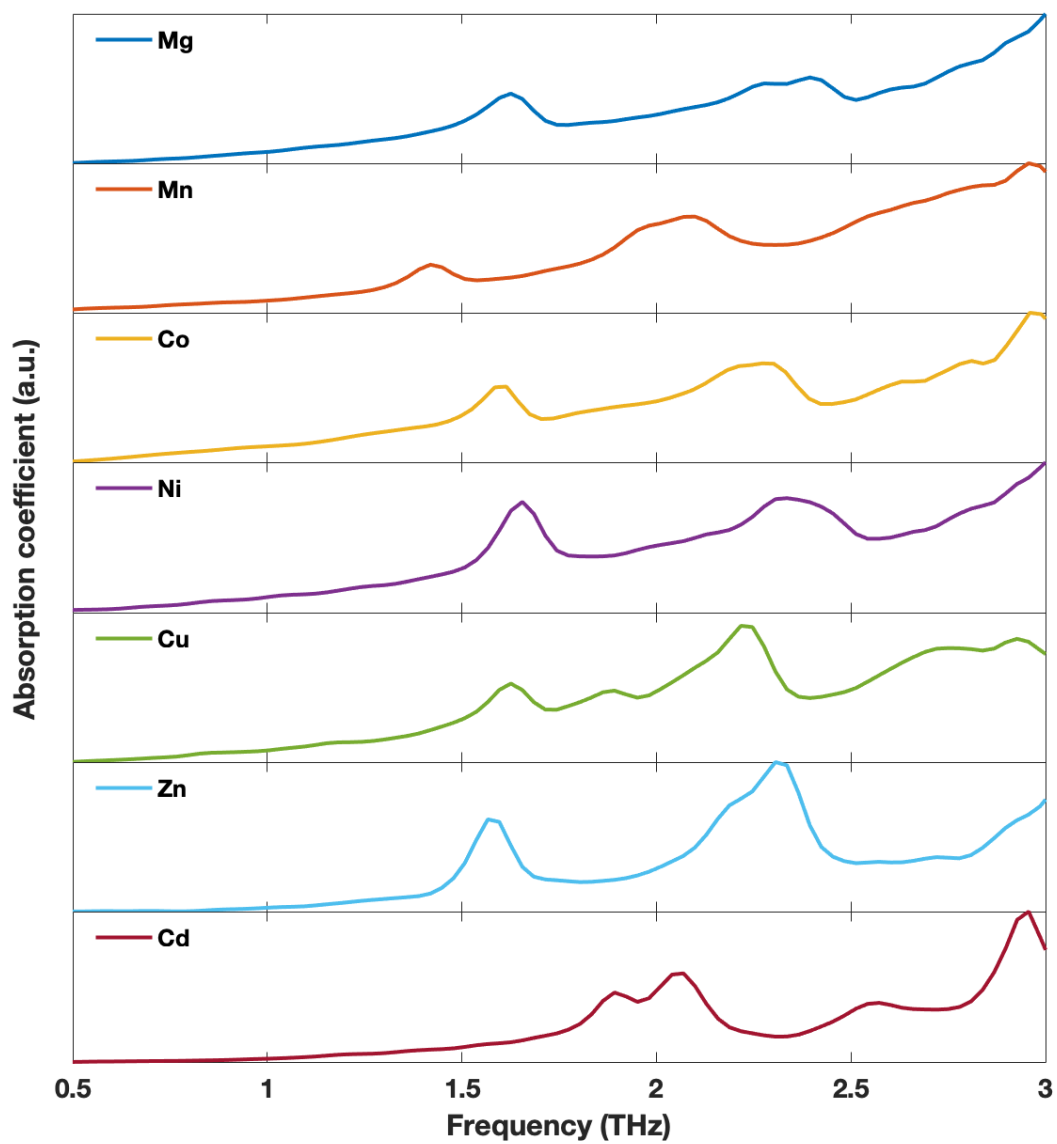


Figure 5.4. Experimental spectra of all the seven systems: Mg-MOF (blue), Mn-MOF (red), Co-MOF (yellow), Ni-MOF (purple), Cu-MOF (green), Zn-MOF (light blue), and Cd-MOF (brown).

Table 5.2. The energies of optimised structure in Hartree. The first row represents M in the corresponding structures, and the electron configurations are shown in the brackets. The first column shows the spin configuration, and in the brackets is the number of nearest metal atoms having the electrons spinning in the opposite way. The underlined ones are the ones with the lowest energy among the structures with the same metal but different spin configurations.

	Mn ²⁺ ([Ar]3d ⁵)	Co ²⁺ ([Ar]3d ⁷)	Ni ²⁺ ([Ar]3d ⁸)	Cu ²⁺ ([Ar]3d ⁹)
FM (0)	-7697.1144	-8623.8171	-9125.8604	-9654.2576
AFM-A (2)	-7697.1146	-8623.8174	-9125.8607	<u>-9654.2582</u>
AFM-B (4)	-7697.1149	-8623.8175	-9125.8612	-9654.2576
AFM-C (6)	<u>-7697.1150</u>	<u>-8623.8179</u>	<u>-9125.8615</u>	-9654.2581

of metal atoms nor the spin configurations had an obvious effect on the O-M-O' angles or on the hydrogen bonds that link the formate groups and the framework. The six M-O bond lengths connected to the same metal atoms were measured. When the symmetry was kept for simulations, the six bonds were restricted to have the same lengths. However, when the symmetry was removed, the six M-O bond lengths changed slightly and could be categorised in three pairs: the middle lengths pair were generally aligned and the short and long pairs settled on each side, yet for Cu-MOF the six bond lengths were all slightly different from each other. Both arithmetic and geometric means were calculated for the six orthorhombic structures (M = Mg, Mn, Co, Ni, Cu and Zn). While the other five systems had a relatively comparable value of around 2.09 Å, the Mn-MOF had an average value of 2.17 Å that was clearly larger than any of the other systems. This reflected on the larger volume of Mn-MOF and can also be an explanation for the red shift for the spectral features observed in the experimental spectrum in Figure 5.4. The three O-M-O' angles were also influenced by the distorted cell from the ideal orthorhombic. Even though the differences were subtle, a trend was observed for the structures composed of the metals from the first row of the transition region: Mn, Co, Ni, Cu and Zn. Mn-MOF had the largest angle of 179.7° between the two bonds of the middle length, while that angle of Zn-MOF was with 177.08° the smallest among the series.

Table 5.3. The comparison between the experimental lattice parameters and the optimised structures with the lowest energy (in percentage): (Exp.-Cal.)/Exp.*100.

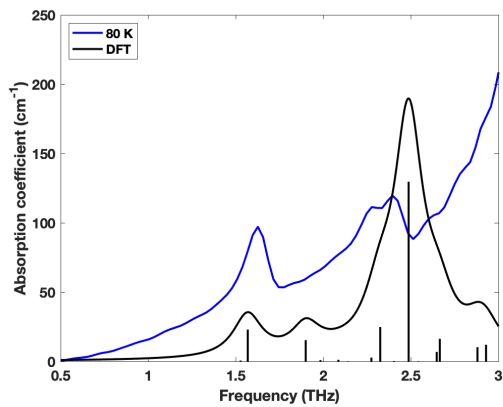
	Mg	Mn	Co	Ni	Cu	Zn	Cd
a	2.17 %	3.70 %	3.39 %	1.92 %	2.62 %	3.30 %	3.65 %
b	1.45 %	2.43 %	2.83 %	1.44 %	0.27 %	2.46 %	3.72 %
c	-0.15 %	-0.70 %	-0.79 %	-1.28 %	2.24 %	-0.31 %	3.65 %
Volume	3.46 %	5.38 %	5.39 %	2.10 %	5.06 %	5.38 %	4.72 %

5.3.3 Frequency Analysis

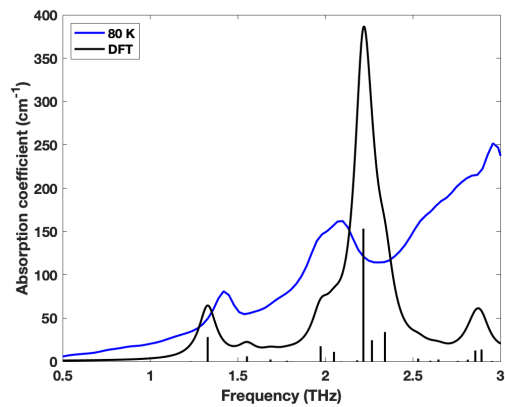
Frequency analysis was done for all the seven structures on its optimised structure with the lowest energy, and the four different spin configurations were performed on Cu-MOF to investigate the influence of magnetisation on lattice dynamics. The detailed comparison between the experimental and the simulated spectra are shown in Figure 5.5, except for the spectra of Cu-MOF that will be discussed in the following section. The frequency analysis results of Ni- and Co-MOF generated negative modes even after removing the symmetry, so they are not included in the discussion of this section. For the other four orthorhombic structures, the simulated spectra matched very well with the experimental spectra, but the intensity of the peak at around or below 2.5 THz was over predicted for all the systems. The phonon mode was visualised using Jmol that corresponded to a shift of the formate groups along the b-axis while the framework was barely involved. This can explain why the overestimation was spotted in the frequency simulations for all the structures since the motion of the Gua⁺ cations would be quite similar in all the studied structures. The first feature showing in the experimental spectrum of Zn-MOF was replaced by separated peaks at two frequencies around it. The spectrum of Cd-MOF, which was calculated using the def2SVP basis set, generally showed similar shape as the experimental results, while it was clearly less accurate than the results calculated with the 6-31G(d,p) basis set.

5.3.4 Magnetisation Analysis of Cu-MOF

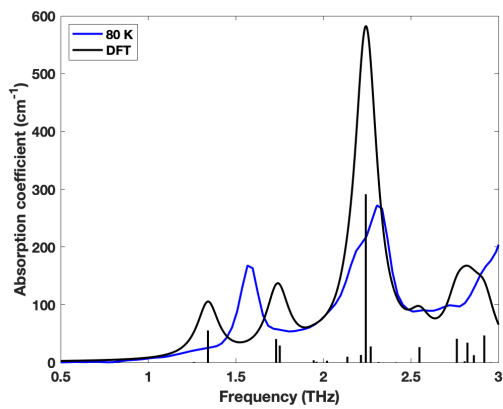
The spin configuration affected the structures and also the lattice dynamics of the perovskites. Other than comparing the energies to predict the relatively stable structure, it was more



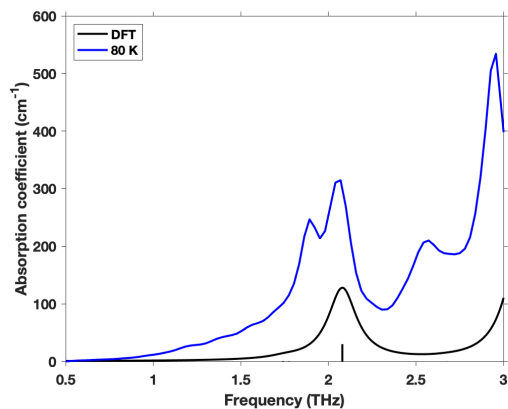
(a) Mg-MOF.



(b) Mn-MOF.



(c) Zn-MOF.



(d) Cd-MOF.

Figure 5.5. The comparison of the simulated (black) and the experimental (blue) spectra of the four systems: (a) Mg-MOF, (b) Mn-MOF, (c) Zn-MOF and (d) Cd-MOF. The black ticks correspond to the active modes predicted by the frequency analysis calculations and the height marks the intensity of each mode.

reliable to validate the hypothesis by the results of frequency analysis. The Cu-MOF was used as an example, and a spectrum was calculated for all four possible spin coupling structures. As shown in Figure 5.6, the calculations resulted in a distinguishable spectrum of the FM structure compared to other spectra predicted with AFM configurations. This is a clear evidence of the magnetism effect on the molecular dynamics. For the details of the spectral features, there is a clear peak at 1.6 THz showing in the experimental spectrum that is only predicted in the AFM simulated spectra. It proves that the Cu-MOF has anti-ferromagnetic characteristics. The calculated spectra of AFM-B and AFM-C are very similar to each other. Both compared to the spectrum of AFM-A, there is an extra peak at 1.9 THz and another one after the very intense feature at 2.3 THz. However, for the experimental spectrum the peak at 2.4 THz is very sharp without a shoulder afterwards. Therefore, it is concluded that the simulated spectrum with AFM-A configuration matches the experimental results best. Figure 5.7 shows a closer comparison between the experimental and the AFM-A simulated spectra. The peaks match very well between the two, and several weak features on the left side of the intense feature at 2.3 THz also match perfectly with the left shoulder of the anharmonic feature at 2.2 THz in the experimental spectrum.

5.4 Conclusions

The combination of THz-TDS and DFT simulations offered a new way of characterising the series of $[\text{C}(\text{NH}_2)_3][\text{M}^{\text{II}}(\text{HCOO})_3]$ and also complemented the techniques previously applied. THz-TDS provided information of molecular vibrations at low frequencies that showed very high similarities of the structures of the same crystal systems. However, the shifting of the peaks and the difference between the relative intensities also reflects the differences of the metal atoms. DFT simulations not only helped with interpretations of the experimental spectra, but also investigated the series of materials in depth, such as the slight distortions, the different spin configurations and the comparison between various metals, which otherwise would be hard to approach experimentally. The results suggested that the systems distorted from the perfect defined crystal space group and all the systems exhibited AFM character-

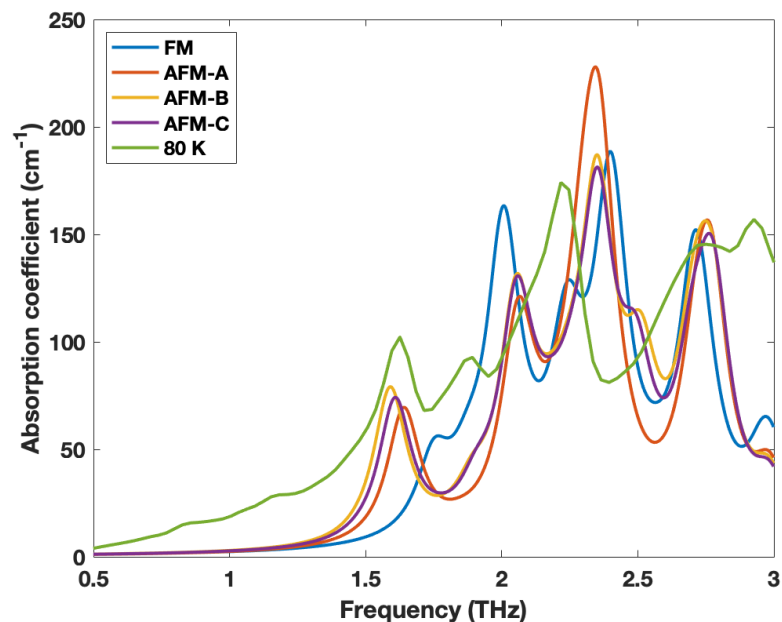


Figure 5.6. The Cu-MOF experimental spectrum acquired at 80 K (green) and simulated spectra with difference spin configurations: FM (blue), AFM-A (red), AFM-B (yellow) and AFM-C (purple) are shown above. The active modes predicted are not plotted here to simplify the figure for clarification.

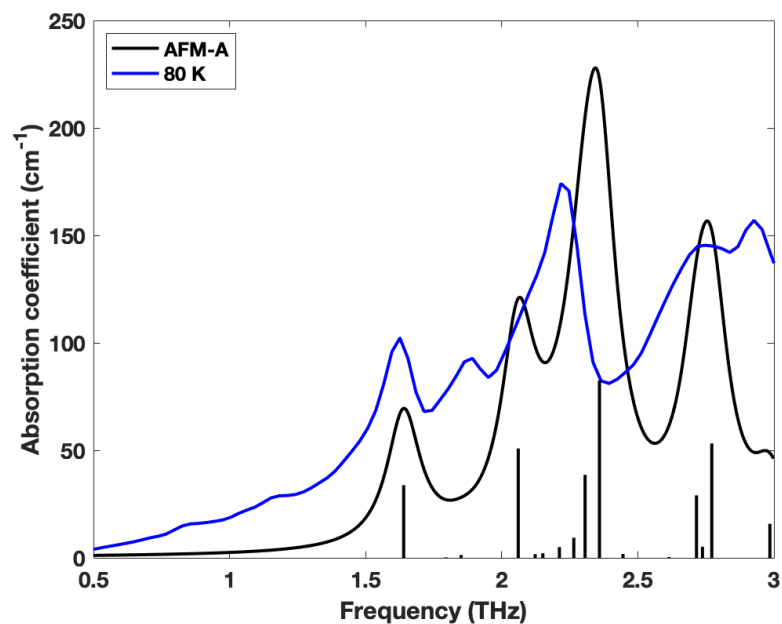


Figure 5.7. The experimental spectrum of Cu-MOF (80 K) and the simulated spectra of Cu-MOF (AFM-A). The black ticks represent the intensities of the modes predicted in the simulation.

istics. Also, the different spin configurations did not result in obvious structural changes, while they did influence the energy which in turn would affect the relative stabilities of the materials.

Chapter 6

Terahertz Spectroscopy of Small Organic Crystals

This chapter covers two studies of small organic crystals: aspirin and theophylline. Both studies have been recently published in the journal *Molecular Pharmaceutics*, entitled “New insights into the crystallographic disorder in the polymorphic forms of aspirin from low-frequency vibrational analysis” and “Understanding the metastability of theophylline FIII by means of low-frequency vibrational spectroscopy”, respectively.^{22;23}

Section 6.1 focuses on two quite similar polymorphs of aspirin. THz-TDS was combined with DFT simulations to investigate the intergrowth/polymorphic impurities in the systems. The computational work was discussed with Prof. Timothy Korter at the University of Syracuse. Dr. Andrew Bond in the Chemistry Department at the University of Cambridge contributed to the X-ray diffraction measurements and aspirin synthesis. The author of this thesis performed THz-TDS measurements, DFT simulations, and data analysis of the work.

Section 6.2 presents a study of the polymorphs of theophylline that unveiled the dehydration process and phase transitions between monohydrate and anhydrous forms, as well as the structure of the metastable form III. This was a collaboration with Dr. Eduardo M. Paiva, Prof. Claudete F. Pereira, and Prof. Jarbas J. R. Rohwedder at the State University of Campinas-Unicamp, who performed the majority of the experimental work including

X-ray diffraction, thermogravimetric analysis, mid- and low-frequency infrared and Raman spectroscopy. Dr. Adam J. Zaczek contributed to the ss-DFT simulations, and I would like to thank Prof. Timothy Korter (Syracuse University) for helpful discussions concerning the simulations and crystal symmetry. The author of this thesis characterised the different forms of theophylline as well as the dehydration process of the monohydrate form with THz-TDS, and also performed all the computational work.

6.1 New Insights into the Crystallographic Disorder in the Polymorphic Forms of Aspirin from Low-Frequency Vibrational Analysis

6.1.1 Introduction

The crystal structure of one of the most well-known analgesics, acetylsalicylic acid, commonly referred to under its trade name aspirin, was first characterised by Wheatley in 1964.²⁶⁵ After the initial crystal structure was determined, it was widely discussed whether other crystal forms of aspirin may exist, but it was not until 2005 that Vishweshwar et al. reported the crystal structure of aspirin form II.²⁶⁶ The form II structure had been identified as an energy minimum by Ouvrard and Price²⁶⁷ in a crystal-structure prediction exercise, but sub-optimal features of the experimental structure determination left doubts over the validity of the crystal structure and the existence of form II as a discrete polymorph.²⁶⁸ The origin of these difficulties was explained by Bond et al., who showed that aspirin forms I and II exist as intergrown single crystals, comprising domains of both structure types.²⁶⁹ Reproducible crystallisation of form II remained challenging, but it was shown in 2010 that domains of the second polymorph of aspirin are introduced reliably in the presence of aspirin anhydride during the crystallisation process.²⁷⁰ More polymorphs of aspirin have since been discovered. A high-pressure polymorph form III has been observed from changes in Raman spectra on compression of form I above 2 GPa.²⁷¹ A further polymorph (form IV), obtained from the

melt, has been structurally characterised at ambient conditions, but it transforms to form I within a couple of minutes at room temperature.²⁷² Given their limited stability, these additional forms are not considered in this study.

In this paper, we focus on the closely-related aspirin polymorphs, form I and form II. There are considerable similarities in their respective crystal structures, which permit the observed intergrowth behaviour. Figure 6.1 shows the projections of the two polymorphs along the a, b, and c axis. The structures are polytypes²⁷³, having consistent layers lying in the bc planes. For the two forms, the difference is seen in the arrangement of these layers along the a axis. The relationship between the structures can be viewed as a shift of neighbouring layers by half a unit-cell length along the c axis (as can be seen in the a axis projection), or alternatively as a reflection of every second layer perpendicular to the b axis. Given the observed intergrowth behaviour, it is evident that the two arrangements must have closely comparable energies. Computational work using density functional theory (DFT) has indicated that the two forms exhibit only a subtle energetic difference, and it was suggested that the two polymorphs were virtually degenerate.²⁷⁴ Later on, Reilly and Tkatchenko applied a many-body dispersion approach with DFT to investigate their energetic differences at room temperature, which inferred that the stability of form I was due to the coupling of low-frequency phonon modes and collective electronic fluctuations.²⁷⁵ A recent work of Vaksler et al. proposed a new method to study the mechanical properties using quantum chemical calculations constituted of two steps: analysis of the pairwise interactions between molecules and modelling displacement between strongly bound fragments.²⁷⁶ The results identified the crystallographic c axis, within the region between the common planes of the polytypes, as the most likely direction for shear deformation to occur.

Even though crystals are defined as well-organised and ordered systems, defects and dislocations are commonly encountered in crystalline materials. The influence of defects, for example on the properties of metals, has been widely studied. It is well known that defects can also affect the performance of molecular materials such as their mechanical stability.²⁷⁷ The subtle differences in crystal structure between the two aspirin forms and the comparable energetic stabilities challenge the view of distinct polymorphs and make this an interesting

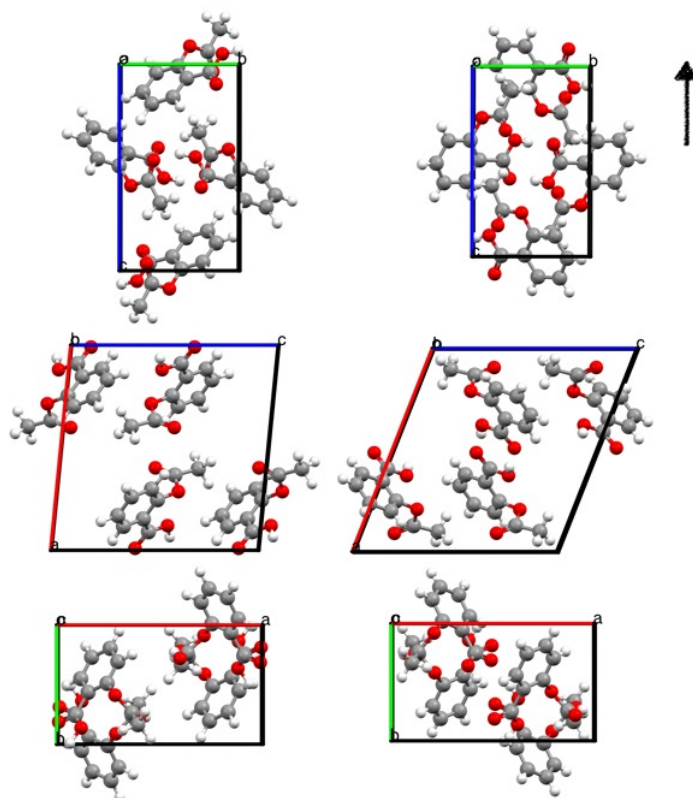


Figure 6.1. Projection of aspirin form I (left) and form II (right), viewed from a, b, and c axis (from top to bottom). The arrow next to the a-axis points in the direction of the c-axis. It emphasises the relationship between the two polymorphs by shifting neighbouring layers by half a unit-cell length in this direction.

model system for investigating the effect of disorder and the structural dynamics in organic molecular crystals beyond their perfect structures. Chan et al. have reported a detailed structural study of aspirin crystals, with disorder models fitted to diffuse X-ray scattering data.²⁷⁸ These results confirm that crystals of form I are well ordered, but that form II crystals contain stacking faults corresponding to the form I interlayer arrangement, which aggregate to form included regions of the form I structure. Hence, “pure” form II is generally not encountered, and may not be experimentally attainable.

Well-established solid-state analytical techniques can probe a wide range of molecular, particulate, and bulk properties. For example, by combining information from spectroscopic techniques (i.e. Raman and Fourier transform infrared spectroscopy), X-ray diffraction, differential scanning calorimetry, as well as thermogravimetric analysis,²⁷⁹ a thorough characterisation of the sample of interest can be achieved. The method proposed in this study augments this approach by combining vibrational spectroscopy in the far-infrared region, measured by terahertz time-domain spectroscopy (THz-TDS), and ab initio DFT simulations under periodic boundary conditions. The unique perspective this adds is to explicitly take into account the influence of the low-frequency vibrational dynamics. These motions typically exhibit large amplitude and are very soft and complex motions dictated by the weak dispersion and hydrogen bonding interactions in organic molecular crystals. We show here how this information can reveal further insight regarding the nature of the polymorphism at the example of aspirin forms I and II. These low-frequency dynamics are of universal importance for crystal polymorphism, and the approach described in this work can be applied directly to many other pharmaceutical systems of interest. The measurement of vibrational dynamics complements the structural characterisation from crystallographic techniques, while the solid-state DFT methods provide a powerful route for interpretation of the terahertz spectra. These methodologies have previously been applied to study a wide range of organic molecular crystals, including polymorphs of pharmaceutical drug molecules.^{29;235;280;281} THz-TDS probes weak interactions within molecular crystals, but due to the complexity of the motions at terahertz frequencies, not least given the strong coupling between large amplitude external and internal motions, the spectra are difficult to interpret without the complementary DFT

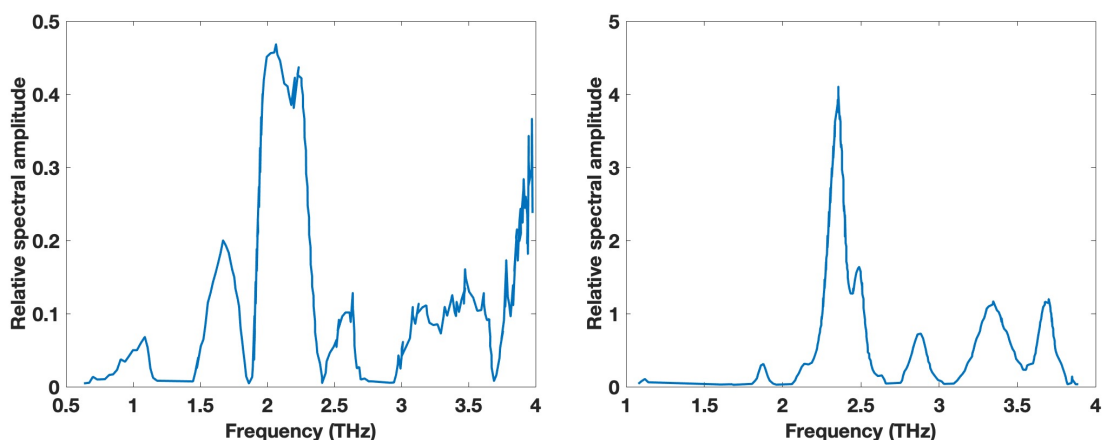


Figure 6.2. Terahertz spectra of aspirin form I acquired by Laman et al.²⁸² Left: Aspirin pellet; Right: Aspirin film.

method. The terahertz spectrum of aspirin form I has previously been measured by Laman, Harsha and Grischkowsky using a bespoke THz-TDS setup, where thin films of crystals were grown directly onto the surface of an aluminium parallel plate waveguide structure.²⁸² This method has the advantage that no scattering occurs when the terahertz electric field propagates along the surface of the waveguide and the effervescent field can interact very efficiently with the crystalline film. As a result, the line width of the vibrational modes is dramatically sharpened compared to conventional transmission spectroscopy of a polycrystalline sample (Figure 6.2). However, the requirement to crystallise the sample directly onto the flat aluminium plate waveguides in the form of a thin film restricts the application of the method for detailed investigation of complex polymorphism where such constraints in crystallisation conditions limit the accessible solid-state forms. Therefore, we apply transmission measurements on pellets containing polycrystalline particles of the two polymorphic forms of aspirin using a commercial terahertz spectrometer.

6.1.2 Experimental Section

Materials

Commercial aspirin form I of USP grade was acquired from Sigma-Aldrich (Gillingham, UK) and used as received. Form II was prepared following the procedure described by Bond et

al. through crystallisation from the organic solution of form I in the presence of aspirin anhydride.²⁷⁰ A bulk solid mixture of 9 g aspirin and 1 g aspirin anhydride was prepared, and divided into 10×1 g portions in separate vials. The solid in each vial was dissolved in 3 ml tetrahydrofuran (THF) with shaking, then left to evaporate under ambient conditions. X-ray powder diffraction (XRPD) was used to confirm the crystalline structure of all samples prior to any subsequent terahertz spectroscopy experiments.

X-Ray Powder Diffraction (XRPD)

X-ray powder diffraction measurements were carried out on a Panalytical XPert Pro diffractometer in Bragg-Brentano geometry, using non-monochromated $\text{CuK}\alpha$ radiation ($\lambda_{\text{ave}} = 1.5418 \text{ \AA}$). Samples were prepared on glass flat-plate sample holders and data were measured over the range $2\theta = 3^\circ$ to 40° . Due to the polytypic relationship between the crystal structures, the diffraction patterns of aspirin form I and II are closely comparable (50% of the reflections are identical). Form II domains are indicated by signature peaks at $2\theta \approx 16.0$, 19.2 and 26.0° .²⁶⁹

Terahertz Time-Domain Spectroscopy (THz-TDS)

The THz-TDS measurements were performed in transmission using a commercial spectrometer (TeraPulse 4000, TeraView Ltd., Cambridge, UK) equipped with a cryostat (Janis, Massachusetts, USA) and an attached temperature controller (Lakeshore 330, Ohio, USA). The set up was used to acquire measurements in the temperature range between 80 and 400 K.

Due to the strong absorption from pure crystals, polycrystalline aspirin powder was diluted in polyethylene (PE) powder (Induchem, Volketswil, Switzerland) to a 5% w/w concentration using an agate mortar and a pestle by gentle mixing. The powder mixture was then compressed into a pellet of 13 mm diameter using a hydraulic press (Specac Ltd., Kent, UK) at a load of 2 tons, and a blank PE pellet was prepared in the same way to be used as a reference. For each sample, 1000 waveforms were acquired and averaged with a spectral resolution of 0.94 cm^{-1} . A spectrum was first acquired at room temperature to check

if the sample pellet was at the proper concentration. The whole system was then cooled to 80 K with liquid nitrogen to acquire a spectrum at low temperature that would be more comparable with the simulated spectrum from the DFT calculations.

Density Functional Theory Calculations

The DFT simulations were performed using the CRYSTAL17 software package.¹⁵⁹ The published crystallographic data from the Cambridge Structural Database (CSD) (ACSALA07; ACSALA17) were used to set the initial atomic positions and lattice parameters.^{205;278;283} The subtle differences between the two polymorphs required very strict parameters for the best differentiation. The “extra extra large” grid (XXLGRID) was used to generate 100 k-points in reciprocal space (SHRINK=7) and the tolerance of bielectronic coulomb and Hartree-Fock (HF) exchange integrals were set to 10^{-12} , 10^{-12} , 10^{-12} , 10^{-12} and 10^{-24} (TOLINTEG). The atomic centered triple- ζ Ahlrichs VTZ basis set (with polarisation)¹⁹⁶ and the PBE density functional¹⁸¹ with Grimme-D3 London dispersion correction^{188;189} were applied with a three body Axilrod-Teller-Muto repulsion term (ABC)²⁸⁴. The energy convergence criterion for the geometry optimisation was set at 10^{-8} Hartree, and 10^{-10} Hartree for the frequency analysis. The default DIIS convergence accelerator was applied. In addition, two displacements for each atom along each Cartesian direction were calculated for the phonon modes (NUMDERIV=2) and the IR intensities were calculated based on the Berry phase method.^{210;211} The cohesive energies of both forms were calculated by subtracting the isolated molecular energy from the total solid-state energy considering the basis set superposition error (BSSE), which originates from the finite basis sets.²⁰⁸ Certain normal modes were selected and the corresponding geometries were scanned along the eigenvectors to obtain more information on these modes (SCANMODE). The Gibbs free energy as well as other thermodynamic properties were calculated from 7 K to 300 K for each structure.

6.1.3 Results and Discussion

X-Ray Powder Diffraction (XRPD)

The bulk solids from the crystallisation trials contained differing degrees of form II domains, as indicated by the relative intensities of the signature form II peaks in the XRPD patterns (Figure 6.3). Trace aspirin anhydride was also detected in most samples. The variability in the crystallisation outcome is attributed principally to (deliberate) inhomogenous mixing of the initial aspirin/aspirin anhydride solid sample. Three samples were selected for further analysis, which contained minimum quantities of aspirin anhydride and a range of form II peak intensities. The sample referred to as “form I” shows no evidence of form II peaks in the XRPD, “low purity form II” shows form II peaks of intermediate intensity, and “high purity form II” shows the most intense form II peaks. Here, “purity” refers to the polymorphic composition. Hence, the form I sample straightforwardly represents the aspirin form I structure, the high purity form II sample is the best available representative of the form II structure, and the low purity form II sample comprises the form II structure with a more substantial fraction of form I domains.

Terahertz Time-Domain Spectroscopy (THz-TDS)

The maximum absorption coefficient (α_{\max}) was determined by the dynamic range of the terahertz signal.²⁰¹ It was checked qualitatively for the experimental results to make sure that the absorption was within the accessible range. Figure 6.4 shows that the absorption did not exceed the dynamic range of the instrument for frequencies up to 3 THz. Therefore, the spectra obtained for the two polymorphs were valid for further analysis.

Figure 6.5 shows the experimental spectra of form I and the two form II samples at 80 K. The overall resemblance of all parts of the spectra reflects the close structural similarity between the two forms, which is not generally common in other polymorphic systems. In order to facilitate comparison, the spectra were normalised relative to the peak at 1.8 THz, which is a pronounced feature in both forms (Figure 6.5). The reason for choosing this feature will be explained in the following section of computational results. In general, the peaks of

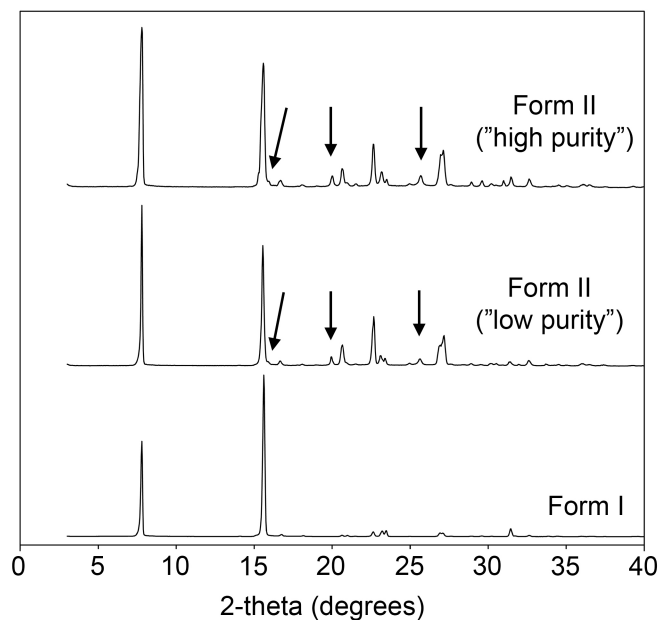


Figure 6.3. PXR D patterns for the bulk samples of aspirin form I and the two measured samples of form II. The arrows highlight signature peaks for form II that are absent from form I.

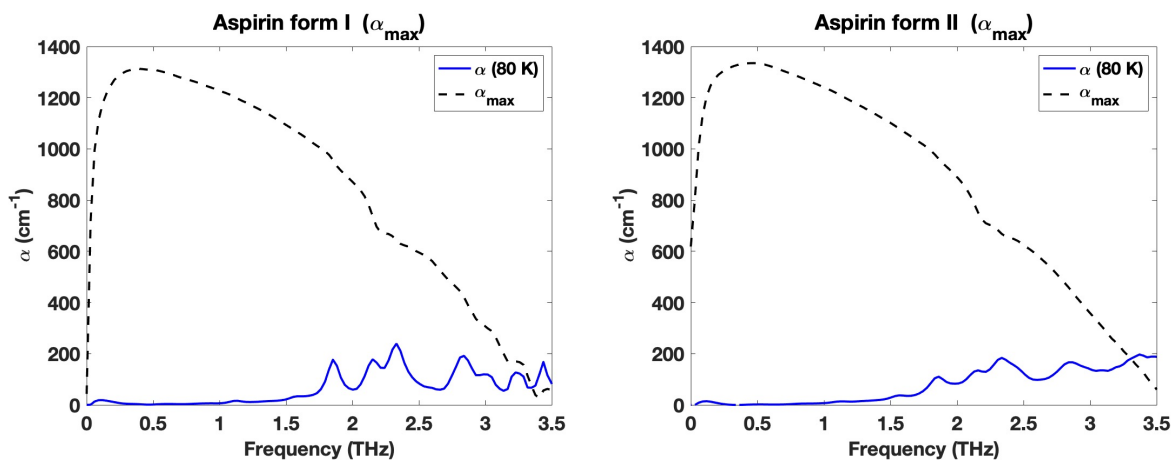


Figure 6.4. The maximum absorption coefficient compared with the experimental spectra for form I (left) and form II (right).

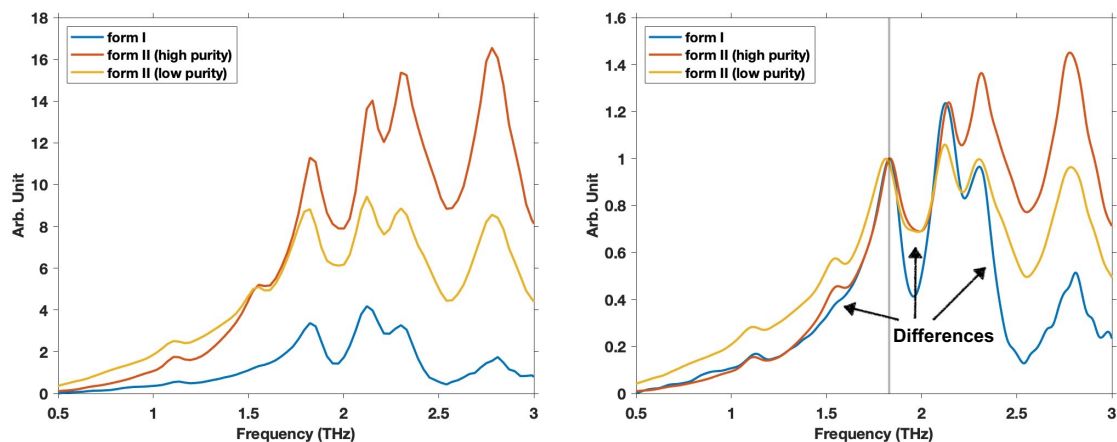


Figure 6.5. The experimental spectra (left) of aspirin form I (blue), form II with high polymorphic purity (red), and form II with low polymorphic purity (yellow). The spectra (right) are normalised relative to the feature at 1.8 THz (highlighted by the grey vertical line). The arrows highlight the three main noticeable differences between the two forms.

form II appeared relatively broader than those of form I, which may reflect the inherent disorder expected for form II. The three main differences are pointed out in Figure 6.5: (i) the feature at around 1.5 THz is considerably more intense in the form II samples than in form I; (ii) around 2.0 THz, the spectra of the form II samples clearly show peak broadening and merging; (iii) the form II samples show a shoulder on the high frequency flank of the peak just before 2.5 THz.

Optimisation of the Crystal Structures

The experimental crystal structures of both polymorphic forms were optimised using the settings described in the Experimental Section and compared with their published experimental data at 100 K and 300 K respectively (as shown in Table 6.1 and 6.2). The relative errors between experimental and optimised structure are small, demonstrating the accuracy of the calculations. As expected, the calculated physical properties of the two polymorphs (Table 6.3) show only marginal differences. The total lattice energy of form II is calculated to be $0.293 \text{ kJ mol}^{-1}$ higher than form I, which implies that form I is marginally the more energetically stable state. The energy difference increases to $1.609 \text{ kJ mol}^{-1}$ when considering also the zero-point energies. The cohesive energy (E_{cohesive} per molecule) of form I

Table 6.1. The comparison between the simulated structures and the crystallographic data of form I at 300 K and 100 K. Difference in percentage (%)=(Exp.-Calc.)/Exp. \times 100.

				Difference	
	300 K	100 K	Optimised	300 K	100 K
a	11.416	11.233	11.28884893	1.114 %	-0.497 %
b	6.598	6.544	6.64371589	-0.693 %	-1.524 %
c	11.483	11.231	11.18437958	2.600 %	0.514 %
β	95.6	95.89	95.614354	-0.015 %	0.287 %
Volume (\AA^3)	860.803	821.218	834.803486	3.020 %	-1.654 %

Table 6.2. The comparison between the simulated structures and the crystallographic data of form II at 300 K and 100 K. Difference in percentage (%)=(Exp.-Calc.)/Exp. \times 100.

				Difference	
	300 K	100 K	Optimised	300 K	100 K
a	12.2696	12.095	12.10525594	1.339 %	-0.085 %
b	6.5575	6.491	6.51259457	0.685 %	-0.333 %
c	11.496	11.323	11.30727436	1.642 %	0.139 %
β	68.163	68.491	69.046117	-1.296 %	-0.810 %
Volume (\AA^3)	858.575	827.047	832.475974	3.040 %	-0.656 %

is predicted to be 0.560 kJ mol⁻¹ lower than form II prior to any correction for BSSE, but rises to 0.035 kJ mol⁻¹ higher than form II after BSSE correction. A noticeable difference is that the entropy of form I is predicted to be smaller than that of form II. It should be noted that this refers to vibrational entropy, calculated for the idealised form I and form II crystal structures. The calculations do not quantify configurational entropy associated with the structural disorder described for form II single crystals.

Table 6.3. Comparison of the properties of the two polymorph (form I-form II). The entropy and heat capacity listed in the table are values predicted at 298.15 K and atmospheric pressure.

	Form I	Form II	Difference
Energy ($\times 10^6$ kJ mol⁻¹)	-6.80803637	-6.80803608	-0.293
Volume (\AA^3)	834.803	832.476	2.328
Density (g cm⁻³)	1.433	1.437	-0.004
E_{cohesive} (kJ mol⁻¹)	205.092	205.652	-0.560
E_{cohesive} with BSSE (kJ mol⁻¹)	10.285	10.250	0.035
Zero-point energy (kJ mol⁻¹)	1617.261	1615.945	1.316
Entropy (J mol⁻¹ K⁻¹)	862.097	875.594	-13.497
Heat capacity (J mol⁻¹ K⁻¹)	785.492	785.638	-0.146

Frequency Analysis

The simulated vibrational spectra were calculated for the optimised crystal structures, and are compared with the experimental results in Figure 6.6 (the experimental results of the high purity form II are used onwards for further analysis). Figure 6.7 shows the simulated spectra of both forms with the bandwidth set to 1 cm^{-1} in order to display each feature for a clearer comparison. As shown, the peak at around 1.8 THz is predicted for both forms with comparable intensities, hence the decision to normalise the experimental spectra relative to that feature in Figure 6.5. The three circled areas correspond to the differences identified between the experimental spectra: (i) the feature at 1.53 THz is predicted only for form II, which explains why the peak is more pronounced in the spectra of the form II samples; (ii) the merging of the peaks just below 2.0 THz in form II can be explained by the extra feature predicted on the high frequency side of the intense peak at 1.82 THz; (iii) the broad shoulder at 2.5 THz in the experimental spectra of the form II samples matches well with the two less intense peaks at 2.37 THz and 2.58 THz predicted for form II. Overall, the simulated spectra show a greater degree of difference between the two polymorphs compared to that observed in the experimental spectra. One way to explain this could be the expectation that the form II samples are intergrown with form I domains. To explore this possibility further, a small amount of the “high purity” form II sample was used to spike the bulk form I sample and vice versa. This resulted in even closer similarity between the experimental spectra. As a final observation, the anticipated structural disorder in the form II samples would be expected to result in non-coherent and less pronounced vibrational motions, which are suggested by the increase of the baseline in the terahertz spectra.⁹⁷

To quantify the comparison, the experimental spectra were fitted in Matlab with the spectral features constrained to the frequencies predicted by the simulations, where the peaks were fitted to Lorentzian functions and the baseline was fitted to a power law Eqn. 6.1.

$$y = \sum_n \frac{A_n}{\left(1 + \left(\frac{x - f_{c_n} - d}{g_n}\right)^2\right)} + Bx^a + c \quad (6.1)$$

where A_n is the amplitude of the peak, g_n is the peak width, f_{c_n} is the predicted frequency

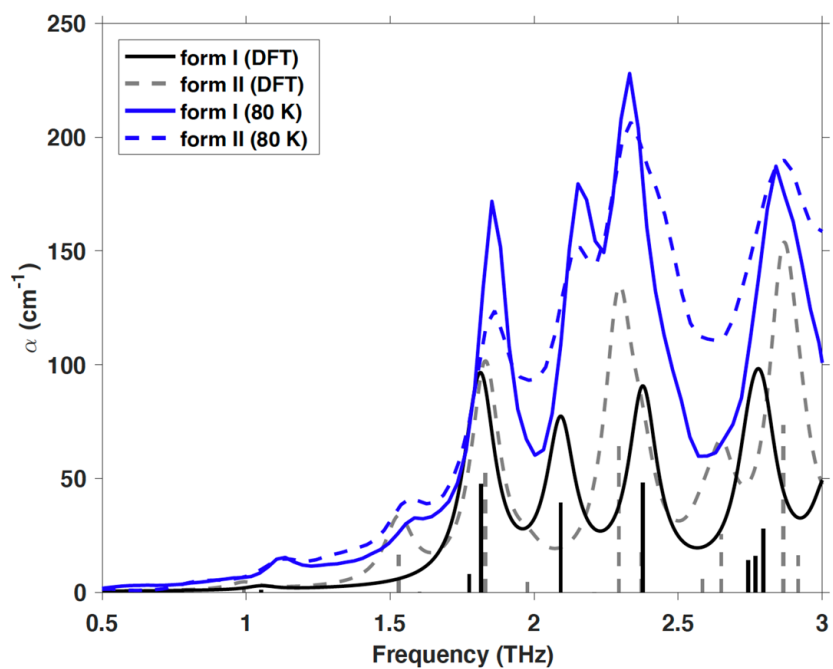


Figure 6.6. The simulated (black or grey) and experimental (blue) spectra of aspirin form I (solid) and form II (dashed). The vertical bars represent the precise frequencies and intensities for active modes that were predicted by the DFT method for each form. A bandwidth of 1 cm^{-1} was used for the simulated spectra in each case.

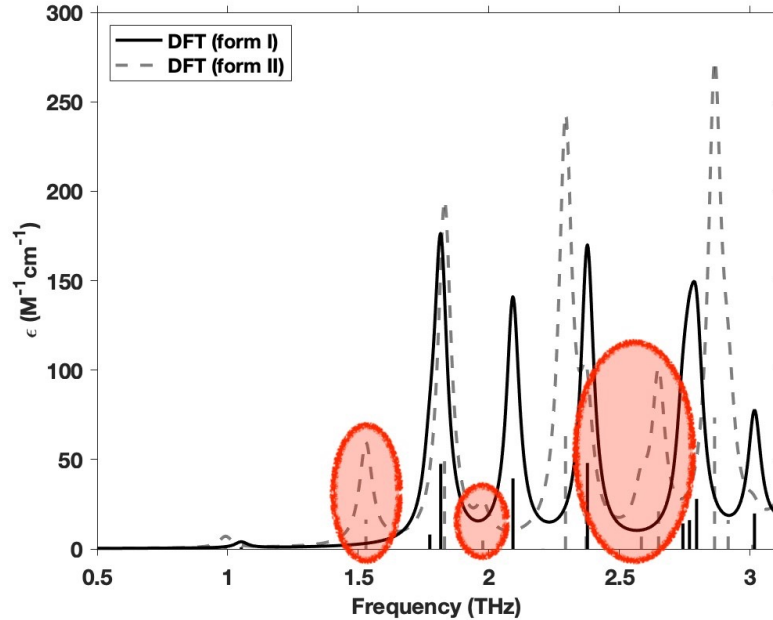


Figure 6.7. The simulated spectra of form I and II when bandwidth was set to 1 cm^{-1} . The red circles highlight the three simulated features predicted in form II that were assigned to the differences of experimental spectra of form II from form I.

of the peak, d is the relative shift between the simulated active modes, and $Bx^a + c$ was used to fit the baseline. Application of the shift d is common practice and is mainly due to the difference in temperature between the experimental (80 K) and simulated (0 K) results as well as additional effects of anharmonicity. The fits are shown in Figure 6.8, and the resulting parameters are shown in Table 6.4. The highlighted features in both samples are not predicted in the corresponding form, but rather in the other polymorph. The fact that it is possible to fit the experimental spectra very closely using this methodology, but that both spectra contain residual features indicative of the other polymorphic form, substantiates the hypothesis that the two polymorphs are intergrown in the samples analysed, and furthermore demonstrates that this feature can be detected by the terahertz measurements. It is also notable that the baseline fitting parameters of form II in Table 6.4 are larger than those required for form I, consistent with the expectation that the form II sample is more disordered. This can also be reflected from the wider peak width in form II on average, as peak broadening is a significant effect to the terahertz absorption spectra caused by disorder in crystalline materials.^{138;285}

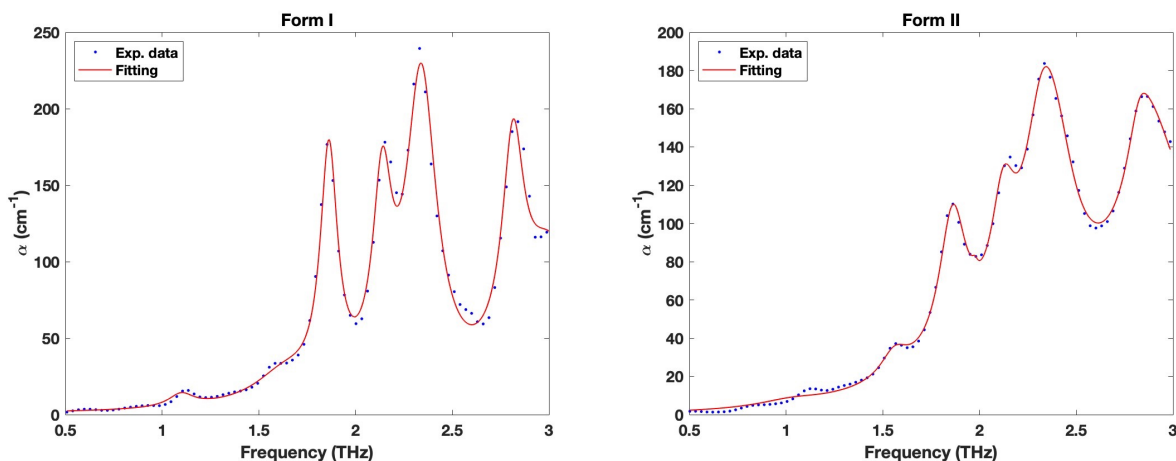


Figure 6.8. Aspirin form I (left) and form II (right) experimental spectra fitted with the Lorentzian functions and the power law with fixed simulated modes. The blue dots represent the raw data from the experimental data points, while the red curves result from the fitting process.

It is evident in Figure 6.8 that the first peak of form II at 1.0 THz is not fitted as well as the other features. Therefore, further calculations were performed to examine the energies of the structures with the atoms displaced in steps along the eigenvectors corresponding to the first spectral features of each form. Figure 6.9 shows that the difference between the energy calculated with the harmonic approximation and the real total energy of form II, along the displacement, was much larger than that of form I. This implies that the influence of anharmonicity is much larger for the first peak of form II than for form I, which can account for the less effective fitting that is observed. In addition, it was found that the methyl groups ($-\text{CH}_3$) in form II were much more active than in form I within the whole low-frequency range (0.5 THz to 3 THz), showing both rotation around the $\text{C}-\text{CH}_3$ bond and greater motion of the entire acetyl group. This can be related to differences in the local environments of the CH_3 groups, which include $\text{C}-\text{H}\cdots\text{O}$ and $\text{C}-\text{H}\cdots\pi$ intermolecular contacts (Figure 6.10). Two out of three such contacts (within the layers common to the polytypes) are directly comparable in the two polymorphs, but the “interlayer” $\text{C}-\text{H}\cdots\text{O}$ contact in form I is shorter and closer to linear than that in form II. Hence, the CH_3 groups in form I adopt an approximately symmetrical position between two neighbouring O atoms in form I, compared to an asymmetrical arrangement in form II. The results confirm the

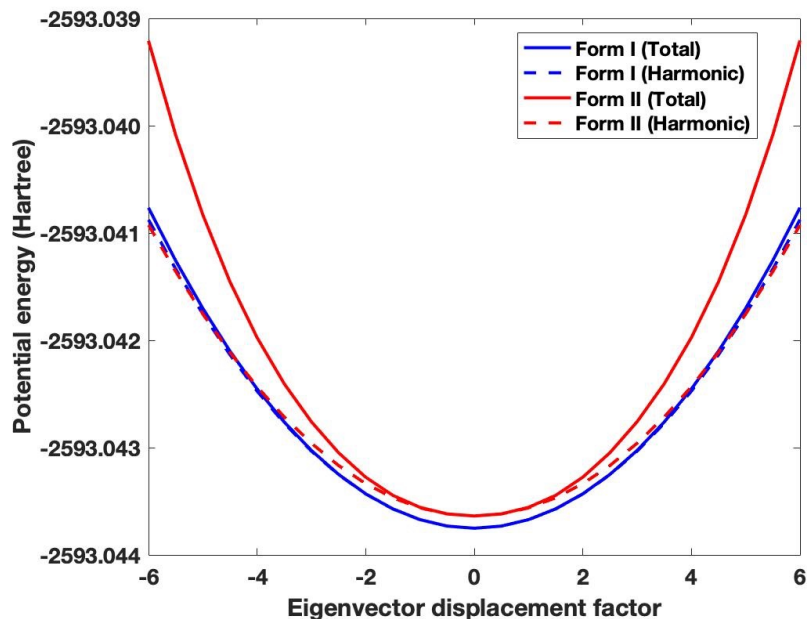


Figure 6.9. The calculated energies of the structures with the atoms displaced in steps along the eigenvectors corresponding to the first spectral features of form I (blue) and form II (red). The solid lines represent the total energies of the geometry at each position, and the dashed ones are for the energies calculated based on harmonic approximation.

observations reported in the early work of Reilly and Tkatchenko.²⁷⁵

Free Energies of the Polymorphs

In Section 3.3 (Table 6.3), it was shown that the total lattice energy of form I is calculated to be marginally lower than that of form II at absolute zero. To further investigate the relative stability of the polymorphs at real temperatures, the Gibbs free energy curves of both forms were calculated from 7 K to 300 K (shown in Figure 6.11 and the lower bound being limited by the CRYSTAL17 software package¹⁵⁹). A turning point is predicted at 75 K, where the Gibbs free energy of form I becomes larger than that of form II, which infers that form II is more stable at ambient temperature. The dynamic calculations show specifically that the stability of form II arises as a result of its greater vibrational entropy. However, two caveats apply: (1) the free energy calculation is based on the harmonic approximation, which would be expected to influence the predicted value of the transition point; (2) the calculations refer to the idealised form I and form II crystal structures, and do not consider structural disorder

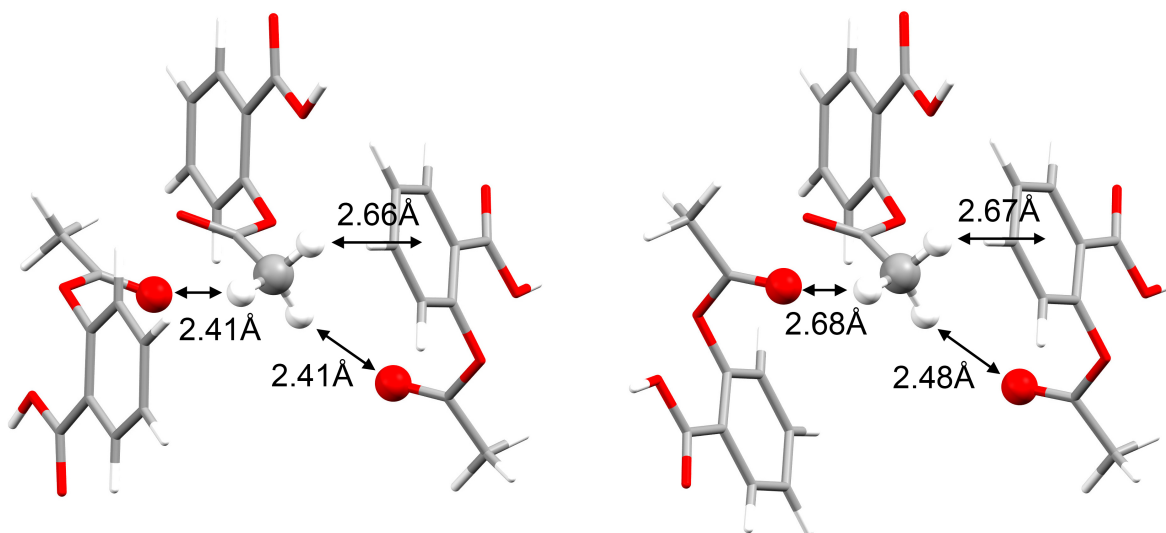


Figure 6.10. C–H···O and C–H··· π intermolecular contacts within the optimised crystal structures of form I (left) and form II (right). The central and right-hand molecule in each diagram lie within the consistent 2–D layers of the polytypes, while the different C–H···O contact is formed between layers.

Table 6.4. The power law fitting parameters for aspirin form I and form II (top). The Lorentzian fitting parameters of form I (bottom left) and form II (bottom right). Features highlighted with an asterisk are not predicted in the corresponding form but rather in the other polymorph.

	B	a	c	d (THz)	d (cm^{-1})	R ²
Form I	0.0164	0.364	0.00285	0.0476	1.59	0.991
Form II	1.04	4.14	0.150	0.0329	1.10	0.999

f_{c_n} (THz)	A_n (cm^{-1})	g_n	f_{c_n} (THz)	A_n (cm^{-1})	g_n
1.05	8.82	0.0772	1.00	3.67	0.209
1.53*	18.2	0.164	1.53	14.5	0.115
1.81	157	0.0564	1.83	75.9	0.0876
2.10	123	0.0600	1.98	3.58	0.0823
2.29	206	0.0959	2.09*	60.3	0.118
2.38	0.285	0.274	2.29	91.5	0.0848
2.77	134	0.0675	2.37	50.0	0.128
3.02	99.5	0.198	2.79*	45.4	0.538
			2.86	40.3	0.134

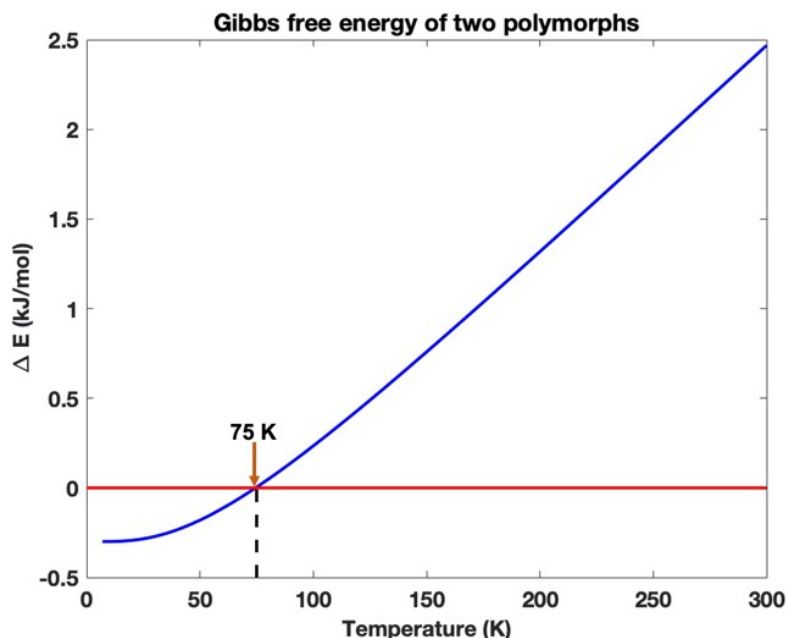


Figure 6.11. The comparison between the Gibbs free energy of two polymorphs from 7 K to 300 K ($\Delta E = \text{form I} - \text{form II}$).

associated with the intergrown nature of form I/form II single crystals.

6.1.4 Conclusions

This work applies THz-TDS and ab initio simulations to explore the two highly similar polymorphs of aspirin. The results show that, even for these two nearly identical crystal structures, THz-TDS can reveal spectral differences based on its sensitivity to inter- and intra-molecular forces. With the help of DFT simulations, slight differences observed for the aspirin polymorphs and the spectra provide further solid evidence of the intergrown nature of the two forms. A number of calculated physical properties are compared for the two forms and most of them are found to be quite similar, reflecting the high degree of structural similarity. However, form II shows a relatively larger vibrational entropy, which yields a lower free energy than form I at temperatures above 75 K. Larger parameters for the baseline fitting of the THz-TDS spectra also indicate a higher degree of structural disorder for form II, consistent with established expectations for this polymorph. The methodology

introduced here for aspirin complements existing physicochemical techniques and adds a new perspective to rationalise the crystallography of polymorphic systems and their structural and thermodynamics analysis. Further computational work on a supercell structure incorporating defects would be very valuable to investigate the influence of structural imperfections in the system and could also add insight into possible phase transitions between the aspirin polymorphs. However, a highly efficient computational plan will be required as well as a large amount of computational resources to pursue this work further.

6.2 Understanding the Metastability of Theophylline Form III by Means of Low-Frequency Vibrational Spectroscopy

6.2.1 Introduction

Theophylline (THEO) (Figure 6.12), a compound with bronchodilator properties, has five known anhydrous polymorphs (I, II, III, IV, V) and one known monohydrate polymorph (M) which is a typical channel type hydrate.²⁸⁶⁻²⁸⁸ In industry, the anhydrous form II (FII) and monohydrate form M (FM) are the two most relevant THEO derivatives because FII is easier to be crystallised and they readily interconvert depending on the ambient temperature and relative humidity (RH).²⁸⁹ Because of the tendency of solvates to have poor solubility in the same solvent that they contain within their packed structure, FII is preferred over FM for medicinal production.²⁹⁰ However, during the production of dosage forms containing FII, FM can inadvertently form when techniques such as wet granulation are used.²⁹¹ The polymorphic form of a drug can greatly impact its pharmaceutical efficacy and it is therefore of great importance to intimately know the chemical nature of these solids and the physical-chemical transformation mechanisms between the solid phases.

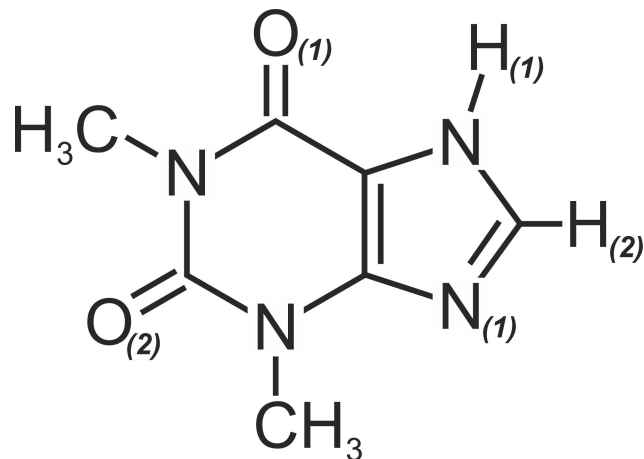


Figure 6.12. Molecule of theophylline.

The existence of a THEO metastable state was first reported by Phadnis and Suryanarayanan in 1997, where its formation was described rather than the expected FII following an experiment of the dehydration of FM.²⁹² It was found that extended heating yielded a different pattern in the powder X-ray diffractogram (PXRD), which was attributed to a metastable state initially referred to as FI* and later named form III (FIII).²⁹³ The diffraction peaks that were supposed to be characteristic of this metastable state started to appear at 40 °C and disappeared at 130 °C upon continuous heating. In a second PXRD experiment, FIII was characterised and found to persist until 140 °C. The authors synthesised this metastable state by exposing FM to reduced pressure (< 0.6 kPa) at room temperature for 12 h. According to the authors, this crystalline form is an intermediate product of the solid-solid transformation during dehydration of FM to FII following a general pathway of FM→FIII→FII. In contrast, this intermediate product does not appear in the hydration process from FII to FM, which occurs in a single step.²⁹⁴

Airaksinen et al. also studied FM dehydration in order to investigate the efficiency of drying techniques with multichambered microscale fluid bed drying and variable temperature powder X-ray diffractometry.²⁹¹ In addition to the PXRD patterns of FII and FM, a third pattern attributed to a metastable state was observed during the process. Its distinctive main peaks at 9.4°, 11.3°, 12.5°, 13.5° and 15.4° 2θ , corresponded to the pattern that was found previously by Phadnis and Suryanarayanan. This further indicated that FIII was involved

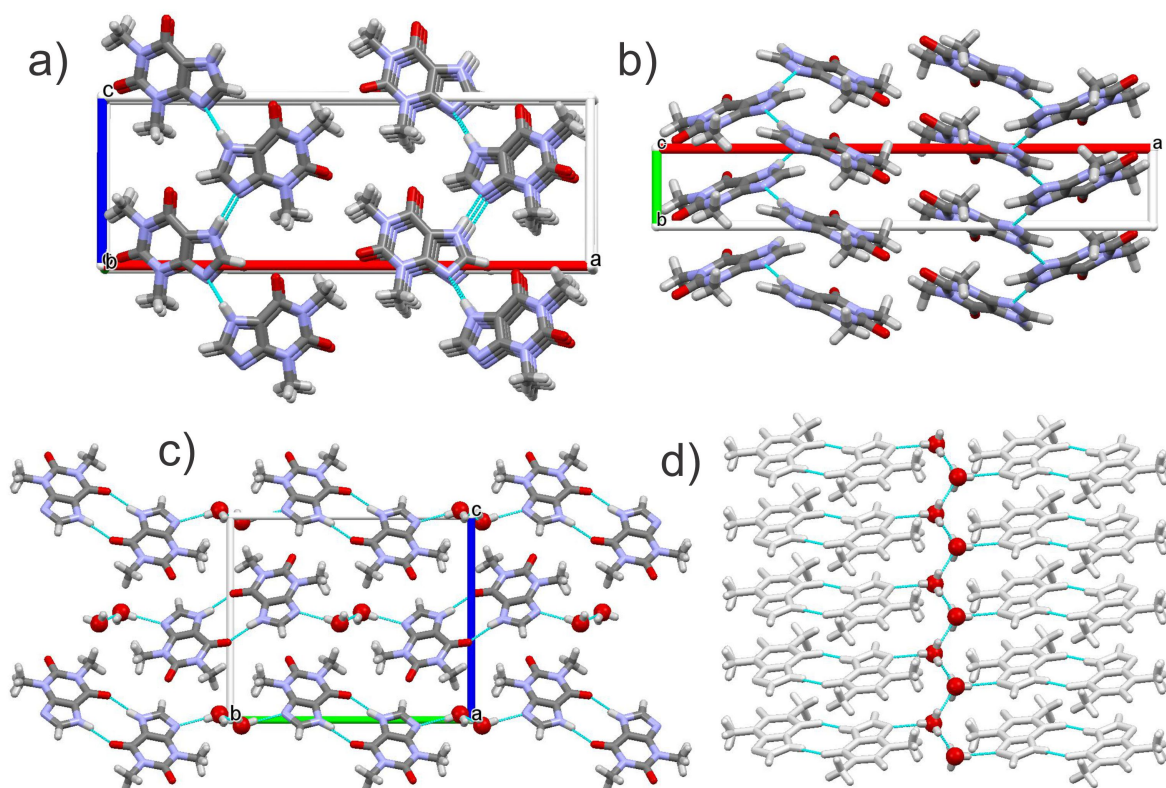


Figure 6.13. Projections of the extended unit cells of theophylline polymorphs FII (a-b) and FM (c-d). d) highlights the channel formed by the water molecules in the “a” direction of FM. CSD code: a-b) BAPLOT01 and c-d) THEOPH01.

in THEO dehydration.

Other studies also pointed to the existence of this same FIII metastable state (sometimes also referred to as I* or A*) during the dehydration of FM based on PXRD measures.^{286;293;295} As described by Sun et al., the crystalline structure of FM is created by dimers of theophylline containing an inversion center.²⁸⁸ This structure exposes the N(1), which is a strong acceptor of hydrogen, and therefore the water molecule binds with this site of the THEO molecule (Figure 6.13).

According to Fucke et al., the dehydration mechanism of FM proceeds in two steps: the first step starts with the release of entire columns of water molecules from the channel hydrate by breaking the HOH—N(1) hydrogen bonds that are weaker than the homomeric hydrogen bonds between water molecules.²⁹⁶ This step should result in a FIII structure that is quite similar to the structure of FM, characterised by signature stacked dimers but with empty

channels remaining where the water molecules in the hydrate were located. However, the FIII structure has not been conclusively determined. In the second step of the dehydration mechanism, the dimer structure collapses, resulting in greater mobility for THEO molecules to rotate and allowing for the conversion to the FII structure. It is worth noting that the above-described mechanism is expected to occur during dehydration when heating is introduced to the system.

Zeitler et al. studied the transformation of FM to produce FII by heating and measuring the low-frequency vibrational spectra with in situ terahertz time-domain spectroscopy (THz-TDS).³⁰ The transformation to FII occurred but the presence of a distinct metastable state during the phase transition was not observed. The authors proposed that during the transition process, the concentration of the metastable state was too low to be observed by terahertz spectroscopy. It is important to note in this context that rather than a free-flowing powder for the THz-TDS measurements the samples of FM were embedded in a porous PTFE matrix that was formed by compressing PTFE and polycrystalline FM particles. In addition to observing the solid-state transformation, intense, narrow peaks were observed in terahertz spectrum during the heating process despite continuous purging of the sample chamber with dry nitrogen. The peaks are characteristic of the rotational spectrum of water vapor and it was therefore possible to measure the hydrate water emerging from the FM crystals before, during and after the solid-state phase transition.

In a recent paper, Robert et al. realised isothermal dehydration of THEO FM at 50, 60, 70, and 80 °C monitoring the mid- and low-frequency Raman spectra evolution with time.²⁹⁷ The results showed complete transformation from FM to FII in all experiments within 90 min as evident from tracking the concentration of solid-state forms by using principal component analysis (PCA) and multivariate curve resolution (MCR) chemometric methods. Although a clear signal of metastate FIII was not observed in these experiments, the authors state that at 50 °C, the dehydration was a multicomponent system based on the concentration profile recovered by MCR. The authors highlighted the advantages of including the low-frequency vibrational spectral range in studies of polymorphs of pharmaceuticals products.

The FII THEO polymorph has an orthorhombic²⁹⁶ unit cell while FM is monoclinic (shown

in Figure 6.13). These polymorphs exhibit plane stacking of theophylline molecules in the “b” direction for FII and in the “a” direction for FM (Figure 6.13a and 6.13c). The distances of these layers are 3.37 Å and 3.26 Å for FII and FM, respectively, indicating π - π stacking but with parallel displacements. FII has infinite H-bonds in the “c” direction involving N(1) and H(1). FM is formed by dimers of theophylline molecules, bounded by H-bonds between O(1) and H(1) interspersed by water molecules that bind via H-bonds with the N(1) of theophylline. The water molecules form a channel perpendicular to the plane “b-c”.

The optical phonon modes that disturb the polarisability of the π - π stacking structures found in the THEO crystal structures result in strong signals in low-frequency Raman spectroscopy.²⁹⁸ The infrared active modes in the same frequency range also exhibit intense bands that can be measured using terahertz spectroscopy (typical spectral range of 0.3 to 6 THz or 10 to 200 cm^{-1}).^{299;300} Thus far, the low-frequency Raman spectra of FIII (metastable state) still have not been reported and its THz-TDS spectrum suggests a low-quality crystal because of the absence of sharp, high intensity bands despite the PXRD data confirming that it is a crystalline solid.^{301;302}

Phadnis and Suryanarayanan stated that FIII is a very unstable solid phase of THEO, and for this reason its structure had not been reported prior to their publication.²⁹² Vora et al. suggested that a mixed structure between amorphous and crystalline phases might exist for this metastable state during the transformation from FM to FII.³⁰³ It is clear that the nature of this metastable FIII polymorph is complex and highly dependent on temperature and RH conditions, so additional studies are required in order to gather more insight into the FIII structure.

Larsen et al. conducted molecular dynamics simulations to provide a mechanism for FM dehydration and to compare the theoretical results with PXRD and solid-state nuclear magnetic resonance experimental data.³⁰⁴ The phase transformation results showed several defects occurring in the crystalline structure until the formation of FIII which presented disorder. Additionally, they found evidence for the different stages of the dehydration process, beginning with FM undergoing a transition state before turning to FIII which finally reaches FII at room temperature. Refinements were made to propose the crystalline structure of FIII.

This structure has stacked hydrogen bond dimers such as in FM but with layers tilted by approximately 60° in its “c” direction (CSD code: KOJNIJ³⁰⁴). The reason for this torsion can be understood as a way to minimize the energy of the system due to the exposure of the group N(1) after water leaving, since in this new structure N(1) has short connections with three hydrogens from CH₃ group of neighboring molecules.

As terahertz radiation is located at the low-frequency end of the far-infrared region, terahertz and low-frequency Raman spectroscopy are very sensitive to inter- and intra-molecular vibrations in the system where interaction energies are low and the masses of the vibrating oscillators are large. This makes the techniques very useful to detect the role of water within the theophylline structure while also to distinguish the different polymorphs that can be present while the sample is kept at various conditions. While THz-TDS is similar to conventional IR spectroscopy and can only detect molecular vibrations that result from changing dipole moments, the remaining vibrations that result from a change in polarisability can be detected with Raman spectroscopy. Therefore, the two techniques will be used to complement each other in this study in tandem with PXRD to fully characterise the structure and observe all low-frequency modes of the various forms of theophylline.

In the low-frequency region ($10\text{-}200\text{ cm}^{-1}$), the vibrations are relatively complex collective motions related to the whole structure rather than to specific functional groups observed in the mid-IR region ($400\text{-}4000\text{ cm}^{-1}$). Therefore, computational methods are necessary to fully interpret the vibrational motions corresponding to the observed modes by low-frequency Raman and terahertz spectroscopy. This combined methodology has been applied to a wide range of materials and has been shown to provide much deeper insight into the nature and behavior of a chemical system.^{10;233;238;305} In this study, solid-state density functional theory (ss-DFT) simulations were used to simulate the experimentally obtained structures and vibrational spectra of the theophylline forms. Thereby, an uniquely conclusive evidence to the dehydration process has been provided while offering a novel proposal for the anhydrous metastable state.

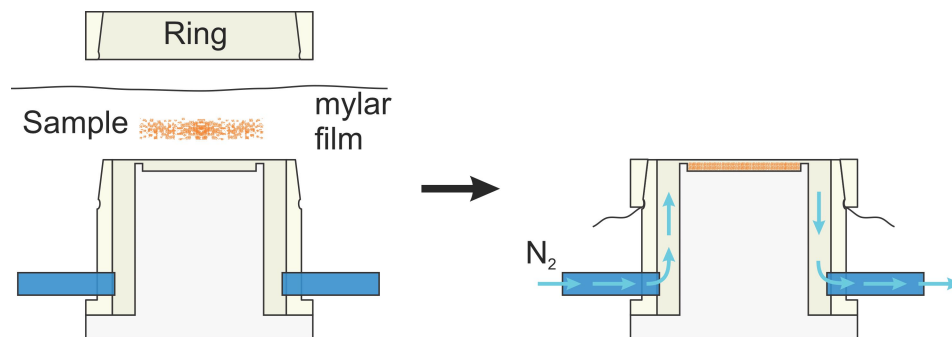


Figure 6.14. Custom-made chamber used in dehydration process with nitrogen purge.

6.2.2 Experimental Section

Sample Syntheses

Theophylline FII was purchased from Sigma-Aldrich (theophylline anhydrous $\geq 90\%$, powder-T1633) and used as received. Theophylline FM was synthesised in the laboratory according to the method described in the work of Pinon et al. by dissolving FII (1 g) in ultrapure water (50 mL) at approximately $60\text{ }^{\circ}\text{C}$ under vigorous stirring.²⁸⁹ When fully dissolved, the system was allowed to cool slowly to room temperature ($\sim 20\text{ }^{\circ}\text{C}$) under continuous stirring for a period of 24 h. The precipitate was filtered and allowed to dry at room temperature for 2 days. FM single crystals (large single crystals with 3 mm length) were made by dissolving 100 mg of FII in 5 ml of ultrapure water and the solution was allowed to evaporate at room temperature until dry long needle shape crystals formed. To obtain FIII, a dehydration procedure was followed by exposing FM powder (fine particles) or single-crystal (large particles) samples to a continuous dry nitrogen purge of at a minimum flowrate of $10\text{ L}\cdot\text{min}^{-1}$ for 24 h at room temperature ($\sim 20\text{ }^{\circ}\text{C}$). Heating was not used in order not to induce FIII \rightarrow FII transformation, as observed in previous works described in the Introduction to this article. Throughout this process the sample was confined in a closed chamber to measure the Raman spectrum in real-time (Figure 6.14).

Experimental Characterisation and Analyses

Thermogravimetric analysis (TGA) was performed to confirm the non-heating dehydration process efficiency from FM to FIII. All the theophylline polymorphs were characterized using powder and single crystal X-ray diffraction (PXRD and SC-XRD), mid-infrared absorption with attenuated total reflectance (FT-IR-ATR), mid- and low-frequency Raman spectroscopy, and THz-TDS.

Thermogravimetric Analysis Four samples were analysed using TGA (TA Instruments model TGA2950): fine powder of FM (sample P1), dehydrated product of P1 (sample P2), large crystals of FM (sample S1), and dehydrated product of S1 (sample S2). A heating rate of $1\text{ }^{\circ}\text{C min}^{-1}$ was used over the range of 30 to $95\text{ }^{\circ}\text{C}$ with argon gas with the samples placed in an aluminum pan.

Powder and Single Crystal X-Ray Diffraction The powder X-ray diffractometer was a Shimadzu, model XRD7000, with $\text{Cu K}\alpha$ $\lambda = 1.54180\text{ \AA}$ source, voltage of 40 kV, current of 30 mA and a range of 5° to $50^{\circ} 2\theta$.

To determine the structures of the THEO forms, single-crystal X-ray diffraction (SC-XRD) experiments were performed at 296 K on a Bruker model Apex with a CCD camera with a $\text{Mo K}\alpha$ ($\lambda = 0.71073\text{ \AA}$) radiation source and a resolution of 8.33 pixels per mm^2 .

Fourier Transform Mid-Infrared Spectroscopy The FT-IR-ATR spectrophotometer was an Agilent model Cary 630, with 4 cm^{-1} of spectral resolution in the range from 400 to 4000 cm^{-1} . Spectra were acquired with 64 scans per sample, using a diamond crystal ATR.

Mid- and Low-Frequency Raman Spectroscopy For the Raman spectrophotometer measurements, FM powder was supported on a lab-made chamber that allowed Raman measurements to be acquired while the sample was subjected to a continuous flow of nitrogen that promotes dehydration. The lab-made Raman spectrophotometer was described in detail in previously published work.³⁰⁶ The instrument used a single-mode 785 nm laser with

500 mW of power as an excitation source with a power of 20 mW detected on the sample surface. The Raman spectra had a spectral resolution of 2 cm^{-1} acquired with an integration time of 4 s per spectrum in the range from 10 to 1800 cm^{-1} . The low temperature (77 K) measurements were performed using a temperature control stage (model THMS600, Linkam Scientific Instruments, UK).

Terahertz Time-Domain Spectroscopy The terahertz measurements were divided in two parts. The first aimed to investigate the spectra of the THEO polymorphs as well as the dehydration product. A terahertz spectrophotometer based on Asynchronous Optical Sampling (ASOPS) technology and electro-optical detection (HASSP-THZ, Quantum Laser) was used. For each time-domain waveform the data was averaged using 500 measurements. The spectral range was analysed from 10 to 200 cm^{-1} (0.3 to 6 THz) and the spectra in the frequency-domain were obtained by the fast Fourier transform method. The sample chamber of the terahertz spectrometer was purged with nitrogen at room temperature ($\sim 20^\circ\text{C}$). The sample was positioned out of focus in the propagation direction of the terahertz pulse to increase the spot of radiation in the sample and allow for monitoring of a larger region of the pellet.^{307;308} The pellet weighed 200 mg in total and consisted of 30% m/m THEO FM and 70% m/m polyethylene.

The second portion of terahertz work aimed to further examine THEO dehydration behavior and to support the solid-state DFT simulations. Here, the room temperature transmission THz-TDS experiments were used to track the entire dehydration process of FM by placing the sample pellet under vacuum or by purging the sample chamber that contained the sample with dry nitrogen gas overnight, both of which achieved the same results. In these cases, the terahertz transmission spectra were acquired with the TeraPulse 4000 spectrometer (TeraView Ltd., UK) at a continuous measurement interval of 10 sec per spectrum for measurements acquired during dehydration under vacuum and 5 mins per spectrum for the overnight sets under dry nitrogen flow (Table 6.5). For these measurements, the FM sample was gently ground with an agate mortar and a pestle and mixed with polyethylene (PE) to 5% w/w concentration. The homogeneous powder was then compressed into a pellet of

Table 6.5. The summary of four sets of THz-TDS measurements of the THEO FM dehydration process.

Set	Sample	Conc.	Method	Waveforms	Rate/spectrum	Time
1	FM	5 %	Vacuum	150	8 sec	30 mins
2	FM	4 %	Purging N ₂ overnight	1000	5 min	15 hrs
3	FM	5 %	Vacuum	200	10 sec	50 mins
4	FM	10 %	Purging N ₂ overnight	1000	2 min	17 hrs

13 mm diameter and 2-3 mm thickness with a hydraulic press at 2 tons. A blank PE pellet was used as the reference. After dehydration, the sample was cooled to 80 K with liquid nitrogen using a cryostat (Janis, Massachusetts, USA) and an attached heater (Lakeshore 330, Ohio, USA) to acquire a terahertz transmission spectrum of the final THEO state. The experimental spectra acquired at low temperature have better resolved peaks and are more comparable with simulated spectra that are calculated at 0 K. The low temperature measurement was performed on FII using the same method.

Solid-State Density Functional Theory Calculations

All ss-DFT simulations were performed using the CRYSTAL17 software package.¹⁵⁹ Geometry optimisation and frequency analysis of both IR and Raman spectra were calculated for FII, FM and potential metastable dehydrated state FIII. The FIII structure was suspected to be very similar to FM as guided by the preliminary XRD and mid-frequency vibrational spectroscopy results showing very similar lattice parameters. Two possible structures of FIII were proposed in this project: FIII(A) with the fixed lattice parameters of FM but where the water molecules were removed; FIII(B) with water molecules removed as well but with the unit cell fully optimised. The initial atomic positions and lattice parameters were acquired from the published crystallographic data from the Cambridge Structural Database (CSD)²⁰⁵ (THEOPH01²⁸⁸ for FM; BAPLOT01²⁹⁶ for FII). All calculations applied the atomic centred triple-zeta 6-311G(d,p) basis set and the PBE¹⁸¹ density functional with Grimme-D3 London dispersion correction.^{188;211} A shrink of 9 was determined corresponding to 205 k-points in the reciprocal space. The Hartree-Fock (HF) exchange integrals were set to 10^{-9} , 10^{-9} , 10^{-9} , 10^{-9} , and 10^{-18} (TOLINTEG). All the structures were optimised with the

only restriction of symmetry, while the FIII(A) was optimised with the restricted space group and fixed cell length (ATOMONLY). The energy convergence criterion for the geometry optimisation was set at 10^{-8} Hartree and a stricter 10^{-10} Hartree for the frequency analysis. The IR intensities were calculated based on the Berry phase method^{210;211} with the default DIIS convergence accelerator, and the Raman spectra were calculated by first computing the Raman tensor with a coupled-perturbed Hartree-Fock/Kohn-Sham approach with accelerated convergence by mixing Fock/KS matrix 2nd derivatives (ANDERSON2).^{213;214} The experimental temperatures and laser excitation wavelength were also taken into account in the Raman spectra calculations. While the 6-311G (d,p) basis set gave reliable energy and optimisation results, it generated imaginary modes in frequency calculations for only form III structures, despite very accurate spectral results for all other theophylline forms. To mitigate this problem, simulations were additionally re-analyzed for all structures with the triple-zeta Ahlrichs VTZ basis set (with optimisation)¹⁹⁶ which solved this issue. All the frequency results presented are devoid of imaginary frequencies.

6.2.3 Results and Discussion

Samples and Dehydration Process Characterisation

Most previous THEO studies realised that the rate of THEO FM dehydration increases with temperature and results in FII as the final solid state, i.e. FM→FIII→FII. In this dehydration study the FIII to FII transition was not reached. Room temperature dehydration was enhanced by applying a high flow rate N₂ purge (10 L·min⁻¹) for 12 h over FM samples in a closed custom-made chamber. Two different sets of FM samples were used as the starting material of dehydration: two fine powder samples and two large single-crystal samples. To evaluate the efficiency of the non-heating dehydration process on these samples, TGA was employed on the start and final materials using a heat flow rate of 1 °C min⁻¹ shown in Figure 6.15.

Upon heating the samples up to 54 °C, the observed weight loss was gradual. This behavior is consistent with the first step of dehydration, which corresponds to the removal of the

Table 6.6. Main PXRD peaks in the range of 5° to 17° for THEO polymorphs FII, FM and FIII of theophylline.

Form II (°)	Form M (°)	Form III (°)
7.38	8.88	9.66
12.86	11.52	11.50
14.62	13.36	22.64
	14.70	13.84
		15.50
		16.50

hydrate water from the molecular columns closer to the sample surface resulting in voids between the dimer structures of THEO molecules in the FM configuration. This behavior is in line with the transition state described by Larsen et al.³⁰⁴ In addition, the gradual weight loss was more pronounced in the powder sample which has a higher surface area than large single crystals. At 55 °C the rate of weight loss suddenly accelerated, indicating the rapid expulsion of the remaining hydrate water molecules. This second stage resulted in the formation of form FIII that was characterised by a cracked morphology (small crystallites) in random directions. The particles appeared opaque after dehydration compared with the transparent crystals of the FM starting material (see images S1 and S2 in Figure 6.15). The macroscopic cracking is known to result in a larger number of defects and dislocations in the dehydrated material and a more disordered crystal. This was confirmed by the loss of high-quality diffraction spots in the single-crystal X-ray diffraction analysis (Figure 6.15). The TGA analyses were also performed on dehydrated samples and are shown by the red curves in Figures 6.15a and 6.15b. The data shows that dehydration was efficient at removing all of the water from the FM starting material before being subjected to TGA analysis.

In Figure 6.16a the PXRD patterns of FII and FM are shown. It is clear that the dehydrated material exhibits a distinctly different pattern, corresponding to FIII, in agreement with previously reported measurements.^{293;302} We will refer to the dehydration product as FIII from here onwards. Table 6.6 summarises the main peaks that were observed of each polymorph in the range from 5° to 17° 2θ , corresponding to a distinct pattern in their crystal packing.

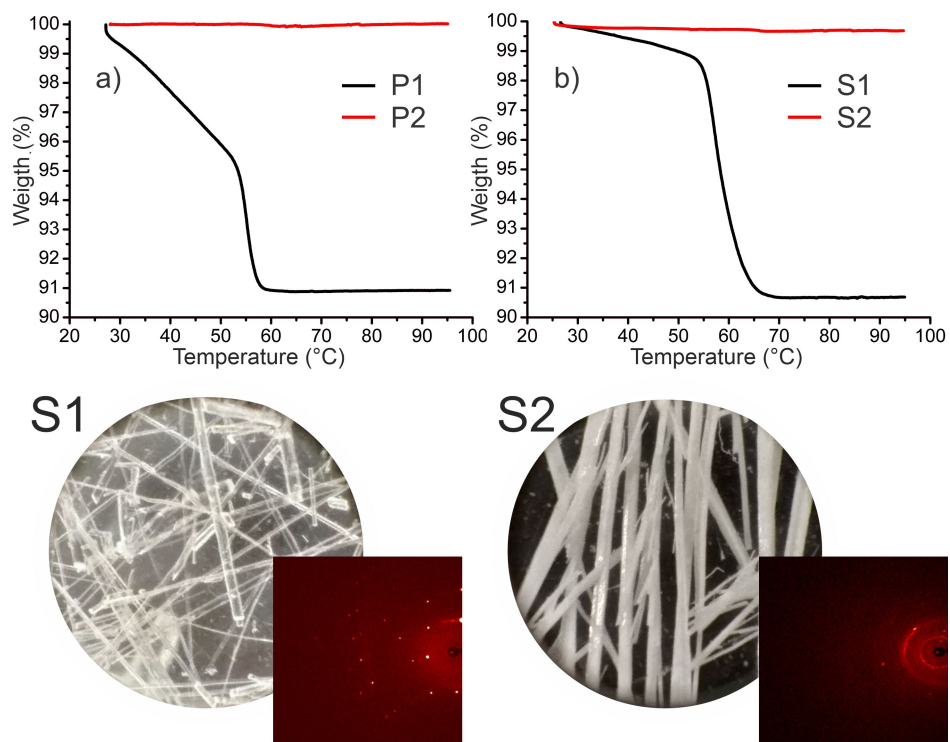


Figure 6.15. Thermogravimetric analysis of fine powder samples (a: P1 and P2) and large single-crystals (b: S1 and S2) of THEO FM before (P1 and S1) and after (P2 and S2) the dehydration at room temperature. The images at the bottom are of the large single crystals before and after dehydration with an inset image of their X-ray diffraction spots.

FTIR (400 - 4000 cm^{-1}) and Raman spectra at mid-frequencies (400 - 1800 cm^{-1}) are shown in Figure 6.16b and 6.16c, respectively, for THEO polymorphs FII, FM, and FIII. This spectral range can be used to differentiate the polymorphs by careful analysis of the vibrational features that are involved in intermolecular H-bonds. Based on the spectral analysis, we can infer that the crystalline structures of FM and FIII exhibit high similarity. In addition, the FIII FTIR spectrum shows a clear absence of the O-H water stretching band at 3350 cm^{-1} (Figure 6.16c) which is present in FM FTIR spectrum. In the mid-frequency Raman spectra, the most notable differences are for the bands at 1238 and 1475 cm^{-1} where only a change in intensity was observed (highlighted in Figure 6.16b).

Low-Frequency Vibrational Spectroscopy of THEO Polymorphs

The terahertz and Raman spectra for THEO polymorphs FII, FM, and FIII obtained in the low-frequency spectral region (10 to 200 cm^{-1}) are shown in Figures 6.17a-b and 6.17c-d, respectively. As expected, the Raman and terahertz spectra are quite different for the theophylline polymorphs FII and FM, since this spectral range captures a direct fingerprint related to phonon vibrations. The number of phonon modes (only optically active ones) is calculated according to $6Z-3$, where Z is the number of molecules into the unit cell.²⁹⁸ Thus, since FII and FM have 4 molecules of theophylline within their unit cell, the number of optically active phonon modes for each polymorph should be 21. Due to the high symmetry of the crystals and selection rules, the phonon vibrational modes that are active in Raman happen to be inactive in terahertz spectroscopy. In addition, it is known that the spectral bands in the terahertz range overlap considerably when measured at room temperature, due to the significant anharmonicity and the contribution of excited states in the vibrational modes.^{238;309} Therefore, given the limited spectral range from 10 to 200 cm^{-1} , the spectral resolution, and the temperature of the measurement, the number of observed bands were less than calculated. In the THz-TDS spectra, FII and FM exhibited 6 and 5 bands, respectively and in the Raman spectra FII and FM showed 7 and 6 bands, respectively.

Based on the structure suggested by Larsen et al., FIII also has $Z = 4$ which results in 21 optical phonon vibrational modes.³⁰⁴ The terahertz and Raman spectra of FIII in

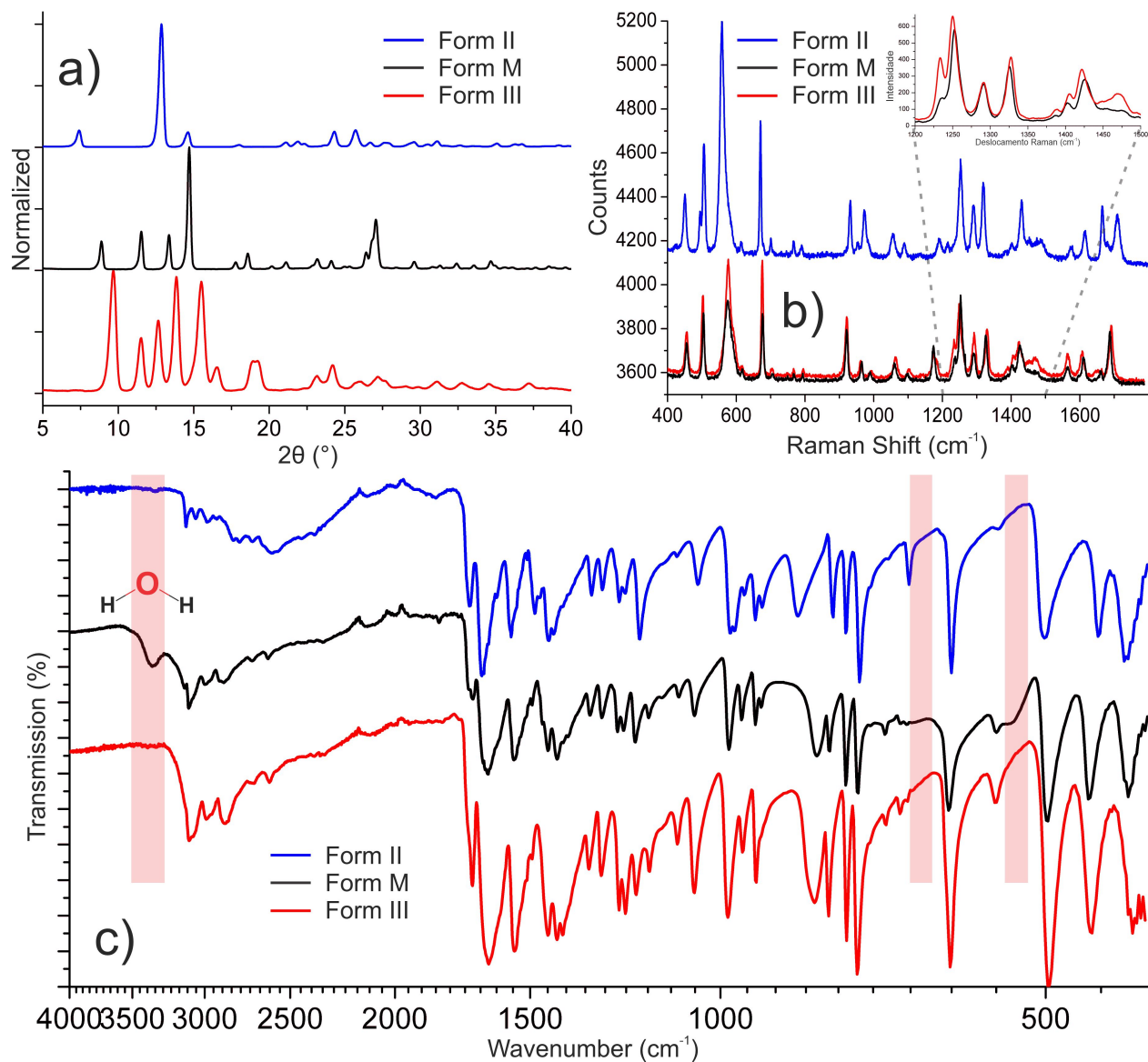


Figure 6.16. a) PXR D, b) mid-frequency Raman, and c) FTIR of THEO polymorphs FII, FM, and FIII. The present and absent vibrational bands of water in FM and FIII, respectively, are highlighted in the FTIR spectra.

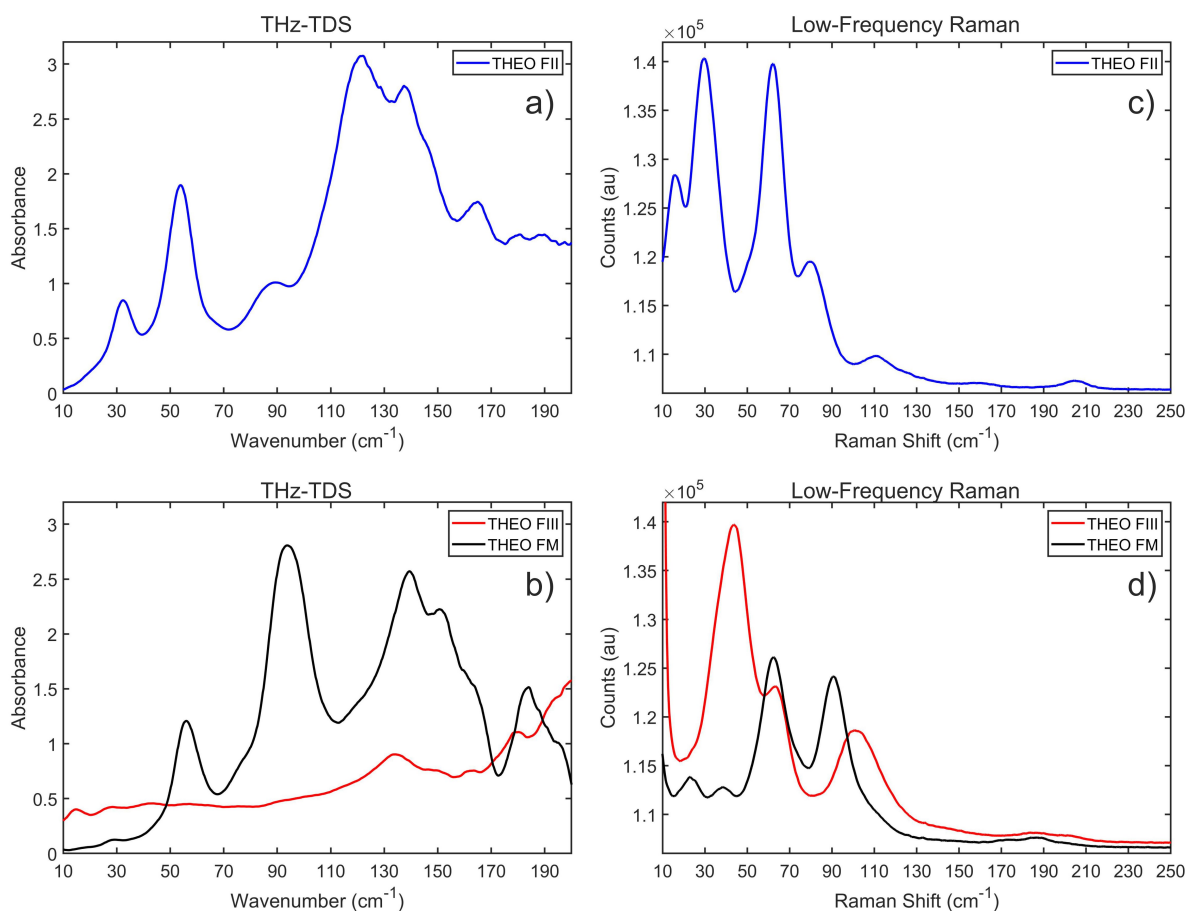


Figure 6.17. a-b) Terahertz and c-d) Raman spectra of theophylline polymorphs FII, FM, and FIII at low frequencies.

Figure 6.17 showed about 3 and 5 bands, respectively. In the low-frequency Raman spectrum, the band at 43 cm^{-1} increased in intensity and the bands at 62 and 90 cm^{-1} appeared to only shift in frequency during dehydration from FM to FIII (see Figure 6.18), indicating, within the context, that they are similar phonon vibrational modes in a new environment. After dehydration, the closed chamber was purged with air at 90% relative humidity and the spectrum of FM polymorph was recovered, as can be observed by the spectrum recorded at 240 min.

In addition, the dehydration process was tracked in situ with THz-TDS as shown in Figure 6.19. The spectra, continuously acquired over time, clearly showed that the spectral features both at 60 and 90 cm^{-1} were decreasing, indicating a structure change. The last spectrum lacked any obvious crystalline features. This result suggests that the structure

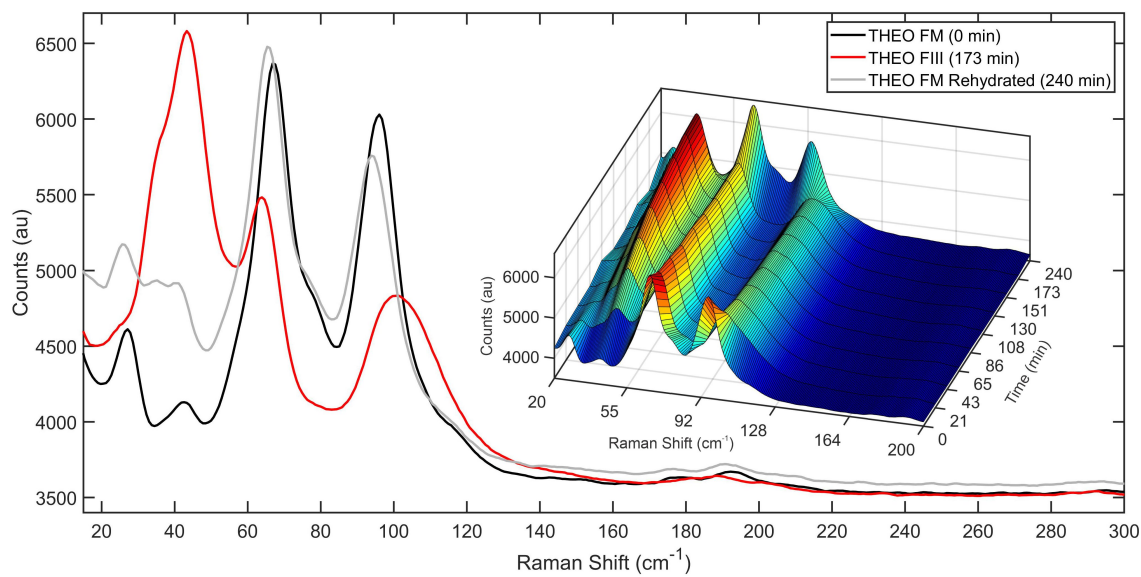


Figure 6.18. Raman spectra were acquired over time during dehydration of theophylline FM showing the solid transformation to FIII. The curve at 240 min shows the recovered FM spectrum after submitted to rehydration with 90 % humidity air.

became successively disordered, which is expected as water leaves the system. It was also observed that after leaving a sample pellet at 20 °C and 40% RH for 2 days, it was converted from FIII to FII. (Figure 6.20).

All these vibrational spectroscopic and PXRD results indicated that FM and FIII are distinct polymorphs. However, they should present similar structures at a molecular level since their infrared and Raman vibrational characteristics at mid-infrared frequencies (400 to 1800 cm^{-1}) are quite similar. This similarity should be most likely due to the stacked dimers of theophylline keeping the water binding site, N(1), exposed and allowing re-entry of the water and thereby reconstituting the monohydrate (FM). In addition, the dehydration process causes a loss of crystal structural quality by forming a cracked short structure due to the collapse of the dimers (microcrystalline environment).

The resultant reduction in crystal quality makes experimental structural determination extremely difficult and simulations of THEO FIII are an elegant alternative to conclusively determine possible structures and complement the characterisation work that already performed. By accurately simulating the low-frequency vibrational spectra of a structure and comparing it to the terahertz and Raman results obtained experimentally, it ensures that the

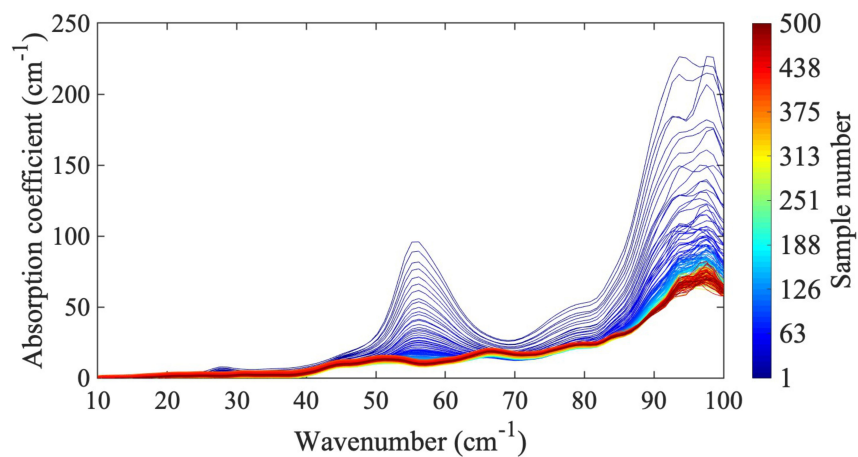


Figure 6.19. 5% w/w FM pellet was kept under the purge of N_2 overnight for 17 hrs. The dehydration process was tracked by the THz-TDS and a spectrum was acquired every 5 mins.

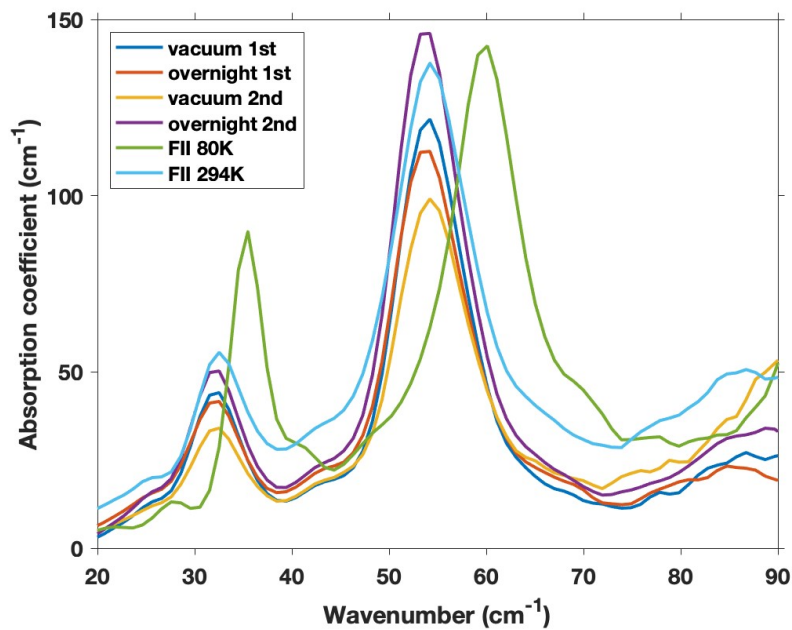


Figure 6.20. The spectra of the dehydrated FM sample pellets kept after 2 days, and the spectra of FII at 80 K and 294 K.

intermolecular forces are correctly modeled, and therefore validates the proposed structure.

Computational Results of THEO Polymorphs

Geometry optimisations were performed for all the structures of interest with relative errors in volume and unit cell dimensions of less than 3% (Table 6.7). The energies of the optimised structures are in the trend of FM < FII < FIII(B) < FIII(A) (Table 6.8). The relative energies are in good agreement with the observations that FM forms at specific temperatures and humidity, as well as the observed transition of FIII to FII after FM is dehydrated. However, the widely reported P21/n space group for FM resulted in energetically unfavourable positions of water molecule pairs that oriented toward each other and frequency simulations that showed negative modes around 500 cm^{-1} , indicating an incorrect structure. The only way to resolve this issue is by reducing the symmetry to the Pc space group, showing that the correct space group for FM is not P21/n, but Pc. The simulated and experimental IR and Raman spectra of FM are well matched as shown in Figure 6.21. For the IR spectra, the experimental features are accurately predicted in the computational results with pronounced peaks at 60.2 , 64.4 and 91.9 cm^{-1} . It was impossible to acquire a spectrum of FM at 80 K due to the limitations of the experimental setup as cooling the sample to 80 K requires evacuation of the sample chamber which would unavoidably cause dehydration under vacuum. The first two modes at around 60 cm^{-1} , shown in Figure 6.21 as one broad peak in the experimental spectra, correspond largely to water molecule translational motions in the channel along the a-axis. The mode at 90 cm^{-1} corresponds to a vibrational motion of the water dimer along the c-axis (Figure 6.22). The visualisation of these modes nicely explains the collapse of the peaks shown in Figure 6.19. As water leaves the system over time, these motions disappear and the modes they correspond to diminish.

However, the intense peaks that are observed in the infrared correspond to the vibrations of water molecules. They are infrared active due to the strong dipole coupling and are predicted to exhibit relatively low intensities in the Raman spectra. Intense Raman-active modes, such as those at 25.6 , 79.9 and 105.8 cm^{-1} mainly involve intermolecular vibrations of THEO molecules. Overall, the Raman spectra appear to provide a highly accurate probe of

Table 6.7. The comparison between the optimised and the published experimental structures of FM, FII and FIII(B) to FM. Difference (%) = (Exp.-Calc.)/Exp.*100 %.

	FM (Pc)	FII	FIII(B)
a	2.509 %	2.393 %	-0.342 %
b	2.072 %	1.471 %	9.980 %
c	-0.921 %	0.724 %	3.099 %
β	-0.266 %	N/A	0.417 %
Volume	3.745 %	4.525 %	12.388 %

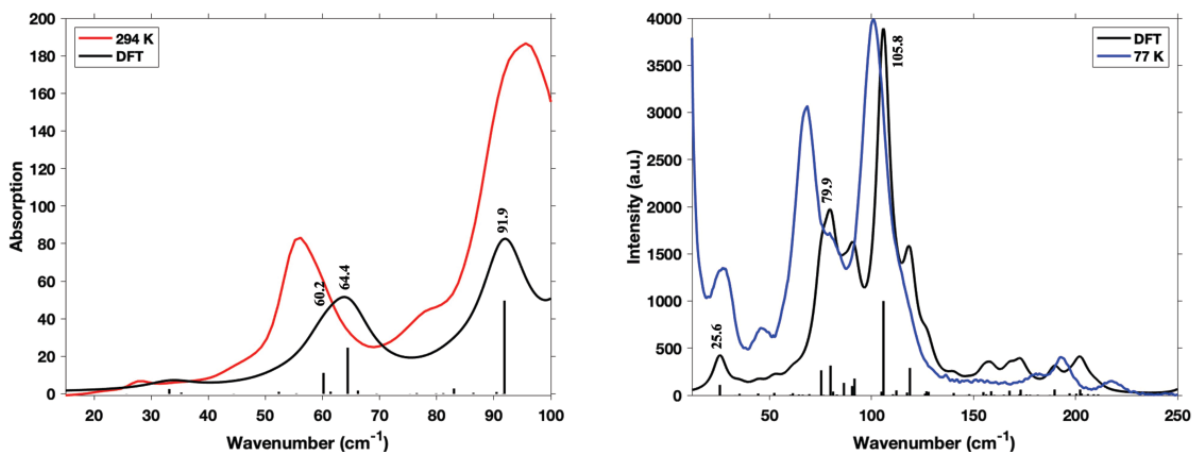


Figure 6.21. Experimental and simulated IR (left) and Raman (right) spectra of FM.

Table 6.8. The energy difference (10^5 kJ·mol⁻¹) between FII, FIII(A), FIII(B) and the most stable form FM. Both sets of data were calculated using the PBE density functional, while the first column applied the 6-311G(d,p) basis set which worked better for the FM and FII system, and the second column used Ahlrichs VTZ basis set that was more suitable for the FIII structure.

	6-311G(d,p)	Ahlrichs VTZ
FM	0	0
FII	7.72098	7.72170
FIII(B)	7.72110	7.72173
FIII(A)	7.72231	7.72205

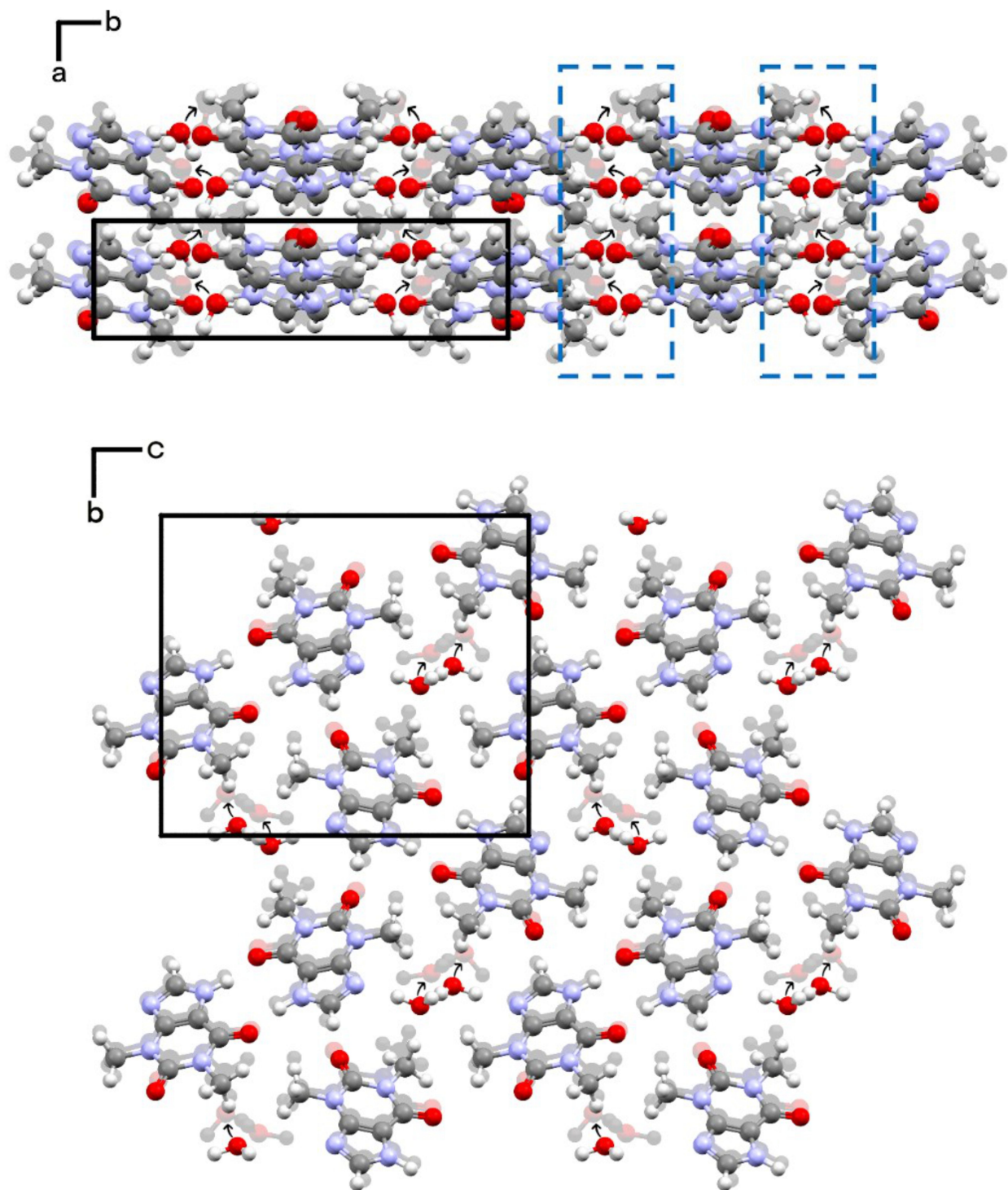


Figure 6.22. The IR-active vibrations of water molecules along the a-axis in FM at 64.4 cm^{-1} (above with channels highlighted in dashed blue boxes for clarity) and along the c-axis at 91.9 cm^{-1} (below). The faded atoms represent positions at the peak of a vibration. Arrows indicate the direction of water molecules in the channels.

the vibrational dynamics related to the crystal structure formed by the theophylline molecules in FIII while the spectral features observed in the terahertz spectrum are uniquely sensitive to the role of water molecules as they are removed from the hydrate channels. Together, the two methods allow for a detailed investigation of the mechanism of the dehydration process.

The predicted IR and Raman spectra for FIII(A) and FIII(B) are similar, but their features appear shifted (Figure 6.23), which can be explained by the fact that the structures differ by a 12.4% reduction in the cell volume for FIII(B) compared to FIII(A). For the Raman spectra, the simulated FIII(B) spectrum with three main intense bands matches the experimental results very well, while only two high-intensity features were predicted in the simulation of FIII(A). The third of the broad features that can be resolved in the experimental spectrum at around 120 cm^{-1} nicely matches with the several closely spaced predicted modes in FIII(B). In addition, the simulated IR spectra of the two hypothetical structures are compared with the experimental spectra that were acquired at the end of dehydration processes using THz-TDS. As shown in Figure 6.24, the intensities of the two main features highly depend on how thoroughly the system is dehydrated. For the two extended dehydration experiments that were run overnight, the spectra lose any clear crystalline features, which can be reflected from the simulated results showing only very weak features in terms of intensities in the low-frequency range. However, for the two dehydration experiments under vacuum, the intensities of the spectral features at 60 and 90 cm^{-1} remain, but their shape are not as defined as at the beginning of the experiments. The increasing disorder is also evident from the broad spectral features that are characteristic of all the FIII spectra that were recorded. From both the experimental and computational results, it can be concluded that FIII is a highly disordered meta-stable state following the dehydration of FM. In addition, due to the fact that FIII has a relatively higher predicted energy compared with other polymorphs, it is easily able to transform to other more stable forms depending on the surrounding conditions. However, despite being disordered, the structure corresponds to the proposal of an FM structure with water molecules removed. It matches better to the proposed FIII(B) structure, as no intense features are predicted for FIII(B) below 100 cm^{-1} and has an energy comparably lower to FIII(A).

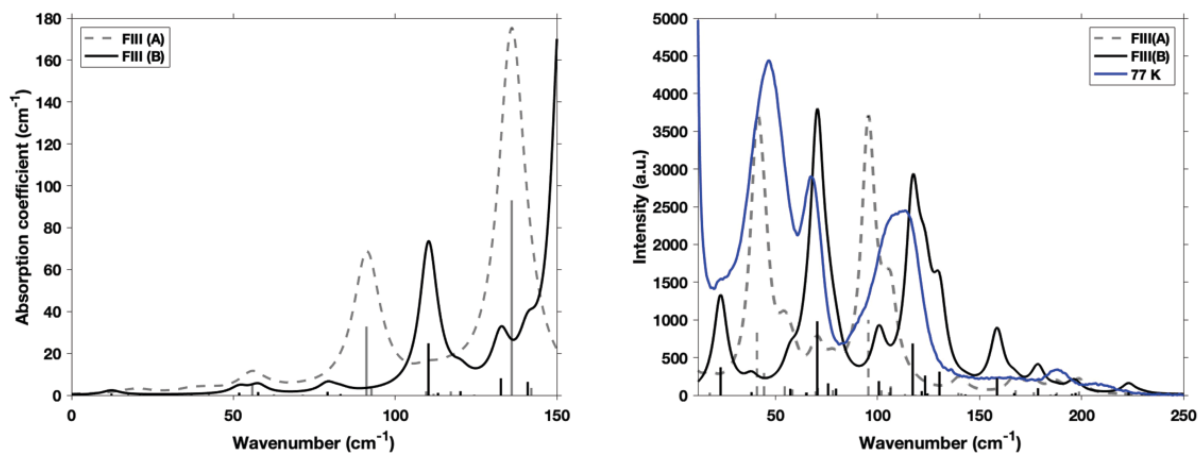


Figure 6.23. Left: Simulated IR spectra of FIII(A) and FIII(B); Right: Simulated and experimental Raman spectra of FIII.

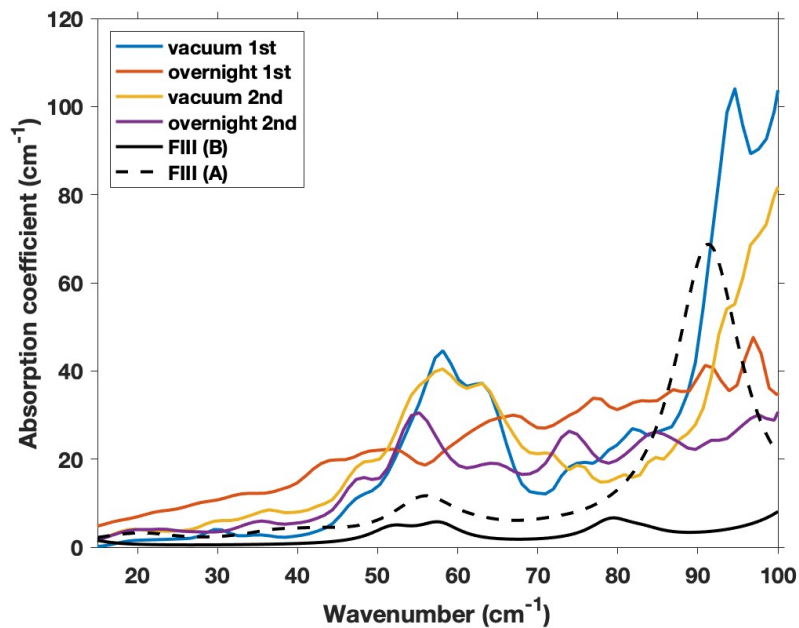


Figure 6.24. The comparison between the terahertz spectra at the end of each dehydration process and the simulated spectra of FIII(A) and FIII(B).

6.2.4 Conclusions

The disordered structure and the metastability of theophylline FIII have been extensively studied based on a novel combination of X-ray diffraction, Raman and terahertz spectroscopy, as well as computational simulations. The molecular arrangement of FIII is similar to that in the FM structure, but in the Pc space group and with no water molecules present (here referred to as FIII(B), i.e., following full unconstrained geometry optimisation of the structure THEOPH01 along with the removal of all water molecules). This was further corroborated by simulating FM and determining that the main experimentally observed peaks at 64.4 and 91.9 cm^{-1} corresponded largely to water molecule motions within the theophylline FM lattice. Upon dehydration, these peaks disappear while the experimental spectrum comes to match the simulated spectrum for FIII. The structural similarities of FM and FIII result in comparable vibrational spectra in the mid-frequency region, another indication of their structural similarities. Therefore, low-frequency spectroscopy techniques that are more sensitive to inter- and intra-molecular interactions within the crystals were necessary to deduce its structure by resolving its vibrational modes, while simulated structures were necessary to gain the required insight into the dynamics occurring during dehydration. Those additionally offered more definitive evidence to the partially crystalline and highly disordered structure of FIII. This work shows the significant impact that combining low-frequency spectroscopy with more commonly used analytical techniques can have in determining the subtle dynamics in a sample, as well as how computational simulations can provide necessary and conclusive insight to experimental results.

Chapter 7

In-situ Observation of the Structure of Crystallising Magnesium Sulphate Solutions

This chapter contains extensive discussion of utilising terahertz spectroscopy to investigate the crystallisation process. Magnesium sulphate heptahydrate is used as an example here to demonstrate the newly developed experimental setup, as well as data processing and concentration measurements methods, while the concept can be directly applied to other systems of interest. The results are presented focusing on three aspects: the experimental set up, the solute concentration measuring method, and the crystallisation process of $\text{MgSO}_4 \cdot 7\text{H}_2\text{O}$.

Sections 7.1 and 7.2 outline the work that has been accepted (in press) in the journal *IEEE Transactions on Terahertz Science and Technology* (doi: 10.1109/TTHZ.2021.3132800) and published in *Analytical Chemistry* (doi: 10.1021/acs.analchem.1c04279), respectively, while a manuscript corresponding to the third section is still in preparation.^{24;25}

All experimental work was carried out jointly with my colleague Johanna Kölbl, a Ph.D. student in our group. The study was a collaboration with Dr. Terry Threlfall from the University of Southampton, who contributed his expertise on the topic of crystallisation in general and the fascinating crystallography of magnesium sulphate hydrates in particular.

7.1 Flow Cell to Study Crystallisation Processes In-Situ Using Terahertz Time-Domain Spectroscopy

7.1.1 Introduction

Crystallisation has been an intriguing topic in both crystallography and chemistry for decades, yet resolving its fundamental nature at the molecular level is still not straightforward. This is due to the complexity of the seemingly simple process which can give the impression of a highly erratic process. Nucleation and crystal growth are widely understood to constitute the two main steps.^{310;311}

A number of techniques have been applied to study the crystallisation process. X-ray techniques, such as small-angle and wide-angle X-ray scattering, X-ray spectroscopy, and X-ray diffraction, are of great importance in providing information on the molecular level. In addition, spectroscopic methods can be used to probe the chemical interactions in the system of interest, including NMR, FTIR, Raman, and UV/Vis spectroscopy.³¹¹ Typically, a combination of selected techniques is necessary to fully characterise a system, and in recent years computational methods have been used increasingly great effect to complement the experimental investigations.

In aqueous systems, the high absorption of water in the infrared results in a noisy background signal, which complicates FTIR measurements and limits their application largely to measurements near surfaces in attenuated total reflectance (ATR). Raman spectroscopy is therefore commonly used as an alternative to investigate the vibrational modes in the infrared given the lack of contribution from water molecules to the Raman spectra due to the different selection rules. In recent years, terahertz time-domain spectroscopy (THz-TDS), has emerged as a new tool that can be used, similar to FTIR, to probe the molecular vibrations due to permanent dipole changes but it has the advantage that it can also be applied in transmission when water is present in the sample given the slightly lower absorption of water at terahertz frequencies compared with the mid-infrared. THz-TDS has been proved to be a useful technique to study both amorphous and crystalline materials in the solid state, as

it is sensitive to inter- and intra-molecular interactions within such systems.²⁶ It has been successfully applied to investigate the properties of pure amorphous materials and crystals, and also phase transitions of polymorphs and crystallisation from the amorphous to crystalline phase.^{26;28;29} Additionally, the dielectric relaxation phenomena on picosecond time scales have been investigated with terahertz spectroscopy in polar liquids, such as alcohol, water, and their mixtures.⁸⁹

However, there are not yet many studies utilising THz-TDS to investigate the crystallisation process in solutions. May and Taday employed terahertz spectroscopy in ATR configuration and monitored the crystallisation of sucrose in confectionary products.¹⁴⁰ The results clearly showed the transition from sugar solution to a solid glassy and then crystalline state. Soltani et al. refined this method and successfully proved the existence of intermediate hydrate states in the crystallisation of L-(+)-tartaric acid during the evaporation of water from aqueous solutions of tartaric acid solutions.¹⁴¹ Terahertz spectra were acquired over a period of 60 h while water evaporated and three stages of crystallisation were discernible. At the beginning of the measurement, the spectra of the solution phase were featureless. In the nucleation stage, the absorption decreased as a result of the reduction in water concentration due to evaporation. In some experiments discontinuous increases in absorption were observed which were attributed to water being released when the hydrated states transformed to the final crystals. A feature was spotted at approximately 750 GHz that was hypothesised to result from the vibration of water molecules surrounding the fragments of solvent molecules. The final observed stage was the crystalline phase displaying a dominant absorption feature at 1.1 THz. These three stages were assumed to be happening inhomogeneously throughout the probed volume.

Even though the absorption of terahertz radiation from water is approximately two orders of magnitude weaker than in the mid-infrared it is still around 200 cm^{-1} at 1 THz, which limits the path length of the cuvette that can be used for transmission measurements to around $100\text{ }\mu\text{m}$ in terms of trading off dynamic range and spectral bandwidth for the measurement. However, such a path length is sufficient for crystallisation experiments and terahertz spectroscopy combined with microfluidics offers the opportunity to measure samples containing

water with high sensitivity and over a wide frequency range. Similar approaches using thin cuvettes in transmission were previously found to be useful to investigate biomaterials such as proteins and DNA^{312;313}. While in the current set-up, a crystallisation cell with a fixed path length was used, it would be entirely feasible to replace this with a variable thickness cell, which opens up other avenues for data processing and extraction of optical constants as for example used in Venables et al.³¹⁴

In the newly developed set up, a closed microfluidics platform made of z-cut quartz was utilised, enabling investigation of both the solvent and solute at frequencies from 0.35 THz to 2 THz whilst allowing for optical observations in the visible range of the spectrum during crystallisation and for cleaning of the cell between experiments. Magnesium sulphate hydrates were chosen as a model system, as different hydrates are known to form under specific conditions. Between 2 °C to 47 °C, $\text{MgSO}_4 \cdot 7\text{H}_2\text{O}$ is the predominant form that can be crystallised at reasonable experimental time scales.³¹⁵. Therefore, $\text{MgSO}_4 \cdot 7\text{H}_2\text{O}$ is used as an example to demonstrate the setup designed based on transmission THz-TDS that can observe the crystallisation and characterise the structure before, during, and after crystal formation in situ.

7.1.2 Methods

Up to now, all published studies using terahertz spectroscopy to study crystallisation from solution have relied on solvent evaporation to trigger nucleation. These studies were performed by ATR sampling, which restricts the observations to the evanescent field near the surface of the ATR crystal rather than in the bulk of the liquid.^{140;141} The goal of this project was hence to build a versatile setup that would be capable to study crystallisation mechanisms from supersaturated solutions with THz-TDS in transmission geometry. Main design criteria were intended to cover operation over wide temperature and concentration ranges, assure stability at high temperature, control temperature gradients during crystallisation, and enable measurements under stagnant and flowing conditions.

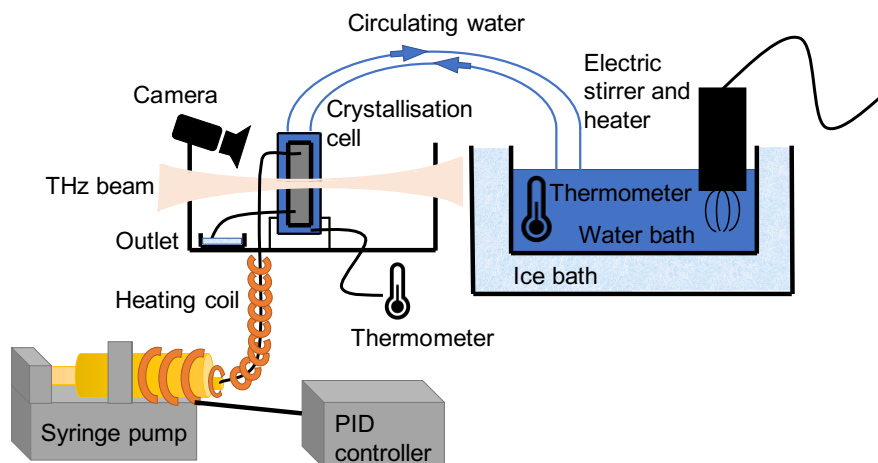


Figure 7.1. Schematic setup.

Description of the Setup

The setup comprised a temperature controlled crystallisation cell that was designed such that it fits into a standard transmission chamber of a commercial THz-TDS setup (Figure 7.1). In parallel to the terahertz measurements it was possible to film the crystallisation process using a small camera that was integrated into the setup.

The central part of the setup was the crystallisation cell that held a cuvette containing the solution during the measurements. The cuvette was manufactured by Hellma (Southend-on-Sea, UK). It was made of two pieces of z-cut quartz (each 1.5 mm thick to avoid etalon reflections) glued together using EP220 epoxy (Fiberdur, Aldenhoven, Germany) with an outlet on each side giving a pathway of solution. The channel was 24.5 mm long and 100 μm thick, and a schematic drawing is shown in Figure 7.2.

The quartz cuvette was held in a metal jacket which has been machined with channels to allow for water to circulate through the metal block in order to control the temperature of the quartz cuvette using a water bath and pump (Figure 7.3). A thermocouple was fitted to the block to allow for accurate temperature control. During the THz-TDS measurement, the assembled crystallisation cell was positioned at the focal position of the measurement chamber and the terahertz beam propagated through the centre of the cuvette with a beam width of about 2 mm.

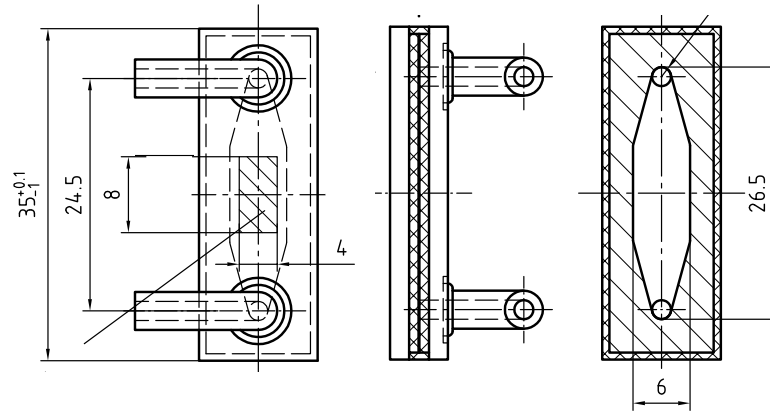


Figure 7.2. Three-view drawing of the cuvette. Left: view from the front, centre: view from the side, right: view from the bottom. Lengths are in mm.

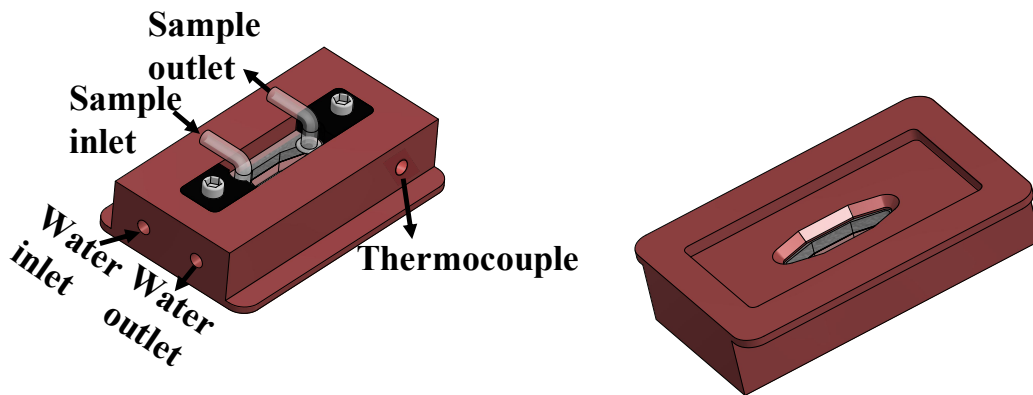


Figure 7.3. Renderings of the metal sample holder with cuvette inserted.

The temperature of the crystallisation cell was controlled by an external recirculating water bath that was connected to the inlet and outlet of the sample holder metal jacket. The pipes between water bath and crystallisation cell were insulated using foam pipe lagging, circulation of the coolant/ heating medium was performed using a pump (120s cased pump, Watson Marlow, Falmouth, UK), and the temperature was controlled by balancing variable heating with an in-built stirrer and PID controller (Anova Applied Electronics, San Francisco, CA, USA) against the near constant cooling from a surrounding ice bath.

Using this setup it was possible to vary the temperature set point by 0.1 °C intervals and to ramp the temperature over the course of a measurement. Using water and ice as the respective circulating and cooling media, the temperature of the crystallisation cell could be equilibrated between 4 °C to 90 °C without further adjustments. Crystallisation was triggered by slowly decreasing the temperature of the crystallisation cell.

In order to investigate the effect of continuous sample flow, a syringe pump (Aladdin Syringe ONE Programmable Syringe Pump AL-1000, World Precision Instruments, Hitchin, UK) was used to provide a steady flow of solution. At its lowest setting, the flowrate was 0.375 ml min⁻¹, which corresponded to a residence time of approximately 2.4 s within the sample cuvette when assuming plug flow. The syringe was contained by a metal tube which was wrapped with a heating coil (SRT051-040LSE, silicon rubber tape, Omega Engineering, Manchester, UK). This ensured that the heat provided by the heating coil was evenly distributed and single-use syringes could easily be replaced between measurements. Further heating coil was wrapped around the transfer tube all the way to the inlet of the crystallisation cell. This made it possible to control and keep the temperature constant both inside the syringe and the transfer tube.

The temperature at the syringe was measured with a thermocouple and controlled via a PID controller (P6100, West Control Solutions, Brighton, UK). The syringe was kept at an elevated temperature to avoid supersaturation and to minimise the chance of nucleation and crystallisation occurring in the solution before reaching the cell. Over the course of the experiment, the solution was pumped into the crystallisation cell. The temperature at the inlet of the cell was again measured with a thermocouple to assure that the temperature was

still high enough to avoid nucleation before the solution reached the cell. This thermocouple was not connected to the PID controller and has been added only to monitor the system. Once the solution had passed through the cell, it flowed through the outlet at the bottom side to a beaker that was placed within the sample compartment of the terahertz spectrometer to collect the solution that was purged.

An optical camera (CF-25, CrazyFire, China) was attached to the cell and focused on the liquid layer in order to acquire images every 2 s of the crystallisation process in addition to the terahertz spectra.

The temperature was monitored continuously throughout the crystallisation experiments using thermocouples located in the water bath, at the heater, and inside the flow cell, as well as at the inlet as mentioned above. Temperature data was acquired once every second.

Sample Preparation and Operation

The MgSO_4 water solution was prepared by dissolving $\text{MgSO}_4 \cdot 7\text{H}_2\text{O}$ (Sigma-Aldrich, Gillingham, UK) in Milli-Q water (IQ 7000, Merck, Darmstadt, Germany, resistivity $18.2 \text{ M}\Omega \cdot \text{cm}$) to the desired concentration in a beaker. The mixture was placed on a magnetic stirrer for constant stirring until the sample was fully dissolved. It was sometimes heated to a slightly higher temperature (in the range of 25°C to 35°C) when preparing solutions with high concentrations to facilitate dissolution. EDTA solution was used for cleaning and purging the crystallisation cell after each measurement. For the cleaning solution, commercial EDTA solution ($\text{pH} = 8$; Fisher Scientific, Loughborough, UK) was mixed with NaOH solution (Reagecon Diagnostics, Shannon, Ireland) to adjust the pH to 10, in which $\text{MgSO}_4 \cdot 7\text{H}_2\text{O}$ has a better solubility.

The temperature of the metal jacket around the crystallisation cell was equilibrated before injecting the solution. Once the sample was injected into the crystallisation cell the temperature was either kept stable and crystallisation was observed as a function of time or it was varied using the heater control in order to induce crystallisation or dissolution.

For static measurements, solution was injected outside the spectrometer to avoid spillage inside the sample chamber. Tubes were connected to the inlet and outlet of the cell and

solution was injected with a syringe from one end. Care was taken that no air bubbles remained within the crystallisation cell. Surplus solution purged from the cell was collected in a beaker and disposed of.

Previously it had been observed that crystals tend to form either at the inlet or outlet of the cell, or, if connected, at the end of tubes. To ensure higher reproducibility, the inlet and outlet tubes were truncated at a length of 3 cm and the ends were sealed with parafilm to avoid evaporation of the sample. It would also have been possible to do without tubes, however, due to the small size of the crystallisation cell and the need to seal the inlet and outlet, this often introduced air bubbles so that it was decided to use tubes of a constant length instead.

Following injection, the sample holder was immediately placed into the chamber and measurement acquisition was initiated no longer than 30 s after injecting the sample.

For the continuous flow measurements, a suitably large syringe was first fully filled with the prepared MgSO_4 solution, and placed into the metal tube that was kept at the set-point temperature. The syringe within the temperature controlled metal jacket was then fixed to the syringe pump and connected to the inlet tube before starting the measurements.

In either case, static or continuous flow, once the sample was injected into the crystallisation cell the temperature was either kept stable or varied using the circulating water bath, depending on the type of experiment performed.

To clean the flow cell and to remove remaining crystals after an experiment was completed, the cell was purged with the cleaning solution several times before and after each measurement, additionally with Milli-Q water as well. The spectrometer was used to confirm the absence of crystals after purging.

Terahertz Time-Domain Spectroscopy

A TeraPulse 4000 (Teraview, Cambridge, UK) spectrometer was used to perform the terahertz transmission measurements. The thickness of the z-cut quartz windows comprising the flow cell, as well as the need to use air as the reference, caused a relatively large optical delay between the reference pulse and the sample pulse for these measurements. Therefore, the

high-resolution mode was chosen, which allowed for acquiring a time-domain waveform of 45 ps duration.

Each spectrum was calculated from the co-average of 15 individual waveforms, resulting in the acquisition of one spectrum per 20 s. The spectral resolution set in the software was 0.94 cm^{-1} . Given the dynamic range of the spectrometer and the absorption of water in the terahertz region, high quality spectroscopic data were acquired in the frequency range of 0.3 THz to 2 THz.

7.1.3 Results and Discussion

Data Processing

During a THz-TDS measurement, the waveforms of reference and sample were recorded. The ratio of the Fourier transforms of reference and sample (the so-called power spectrum) yielded the complex transmission coefficient of the sample as a function of frequency.

In their paper from 1996 Duvillaret et al. described a reliable method to extract optical constants from THz-TDS measurements by taking the complex refractive indices of the surrounding media and sample into consideration, and solving the inverse problem of extracting the complex index of refraction iteratively from the measured transmission coefficient.³¹⁶

In this case however, the analysis was complicated by the fact that the surrounding media were not the same for the reference and sample measurement, as is demonstrated in Figure 7.4. To avoid the Fabry-Prot effect from internal reflections caused by the empty crystallisation cell, the reference measurements were performed in air without quartz windows.

This posed a challenge when attempting to calculate the complex optical constants using the method of Duvillaret et al. because their method assumed the surrounding media for the reference and sample measurement were the same.

The absorption of z-cut quartz windows in the terahertz region of interest is very low, with an extinction coefficient of approximately zero and the real part of the refractive index being approximately constant. Inserting windows into the beam path mostly lead to a longer time delay before detecting the pulse on the order of 20 ps for a window thickness of 3 mm.

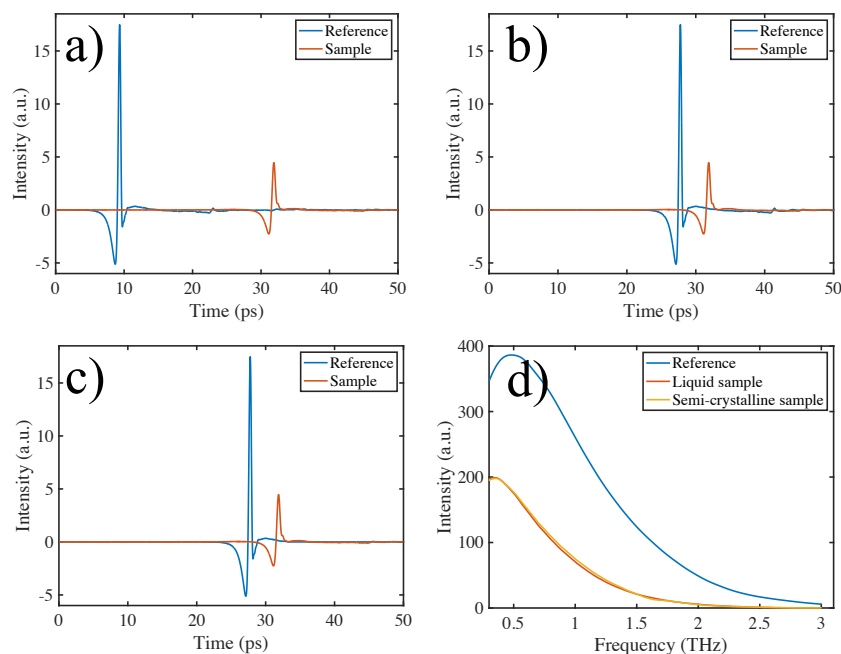


Figure 7.5. a)-c): Reference (blue) and sample (orange) waveforms. a): original case, b): after shifting the reference waveform, c): after shifting and zero-padding the reference waveform. d) Power spectra of reference (blue) and sample (red and yellow). In red, a liquid sample and in yellow after crystallisation.

Results and Discussion

When operated under stagnant condition the concentration of MgSO_4 in the solution within the cuvette was constant and crystallisation could be observed as a function of time, depending on the chosen temperature and concentration. At concentrations of 25 wt% to 29 wt% MgSO_4 crystallised into its heptahydrate form within minutes at temperatures between 4°C to 12°C .

In Figure 7.6, the crystallisation of a supersaturated MgSO_4 solution over time is shown while the sample was being kept at approximately 4°C . As expected, the spectrum of the MgSO_4 solution was completely featureless with a monotonously increasing baseline. Such spectral features are expected for aqueous solutions where no molecular order on the timescales of picoseconds is maintained and thus the molecules in solution are completely disordered in an amorphous phase. Over time the baseline dropped, and a peak emerged at 1.6 THz, evidencing the formation and existence of crystals.

Magnesium sulphate heptahydrate - water spectra containing crystalline features could

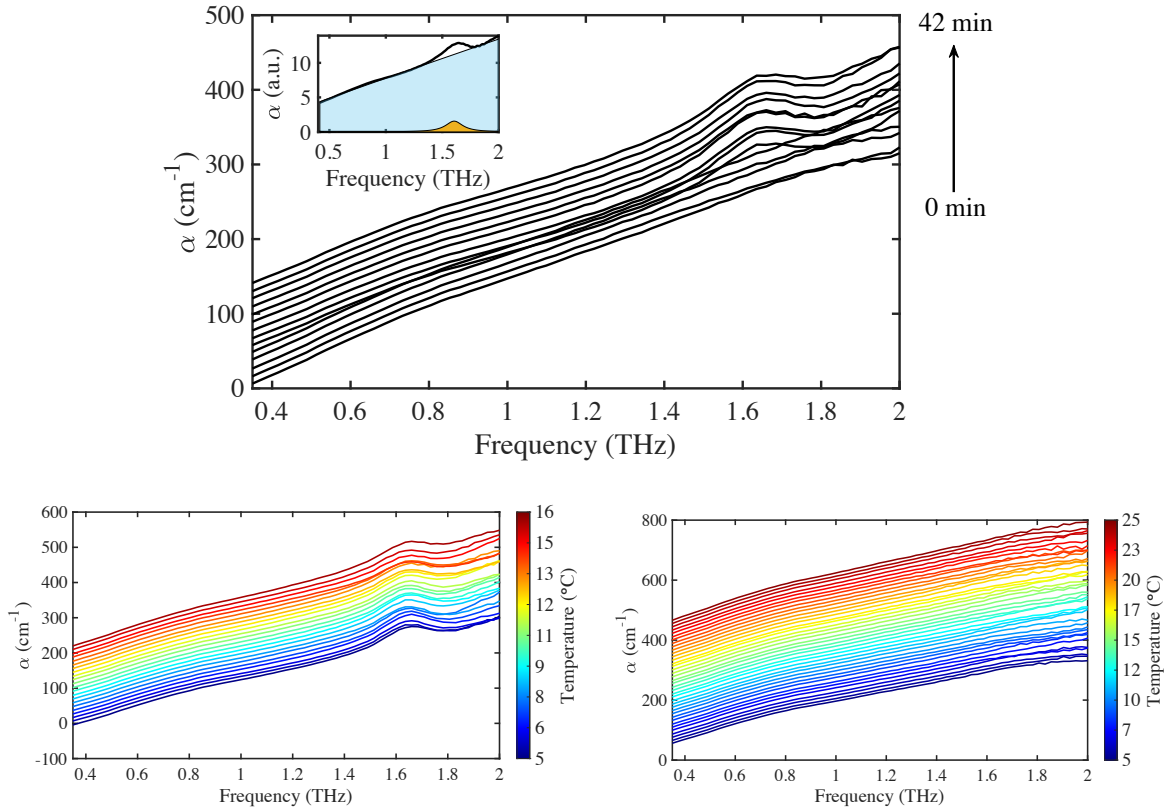


Figure 7.6. Top: Spectra recorded at different times throughout the process. Each subsequent spectrum is offset by 10 cm^{-1} . Inset: Typical spectrum of the crystalline system. It is depicted here as the sum of the amorphous background (blue) and the peak at 1.6 THz (orange). Bottom: Absorption spectra of MgSO_4 heptahydrate (left) and water (right) at different temperatures. Each subsequent spectrum is offset by 10 cm^{-1} .

hence be separated into the sum of the amorphous background and the peak at 1.6 THz, as shown in the inset in Figure 7.6 at the top.

Observed Clipping

When comparing the absorption of water with literature values^{89;317}, it was observed that the terahertz beam was clipped somewhat by the sample holder, resulting in a typical reduction of the measured absorption at lower frequencies compared to literature values. However, the clipping only affects the spectrum below approximately 1 THz (Figure 7.7). Furthermore, we were not interested in absolute values as of yet and because the geometry was constant throughout the measurements, relative changes in absorption are still valid and useful for

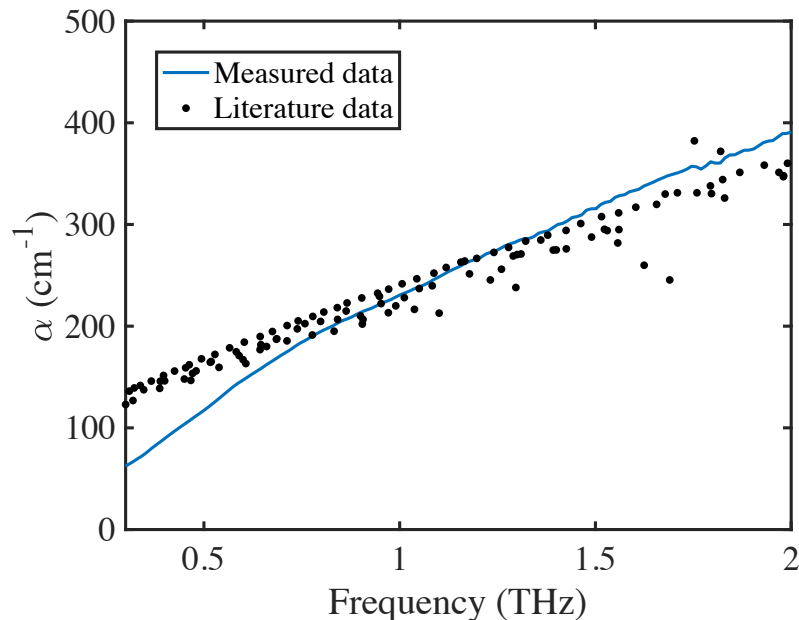


Figure 7.7. Absorption coefficient of water from literature (black dots)^{89;317} and measured in the crystallisation cell (blue line).

investigating sample properties.

7.1.4 Conclusions

A setup is reported in this section that can be used to observe crystallisation processes from aqueous and other organic solvents utilising terahertz time-domain spectroscopy in transmission geometry. Both static systems and systems under flow were investigated while either keeping the temperature constant or employing temperature ramping. Utilising the versatility of the setup, the magnesium sulphate heptahydrate system was studied at different temperatures before, during, and after crystals formed, thereby allowing the investigation of both crystals and the solvent at different levels of saturation.

The effects of temperature and concentration changes will be investigated further. The setup is designed for operating temperatures between 4 °C to 90 °C, which can be extended with minor adjustments. Therefore, it can be applied to a wide range of crystalline systems at various concentrations. Future work will focus on being able to trigger crystallisation

within the cell, allowing the observation of initial crystal nucleation and growth.

7.2 Measuring Solute Concentration with Terahertz Time-Domain Spectroscopy in Single and Multiphase Systems

7.2.1 Introduction

Terahertz time-domain spectroscopy (THz-TDS) is a useful far-infrared spectroscopy tool that is increasingly used in the field of solid state crystallography to complement X-ray diffraction methods to distinguish between polymorphs and other solid forms, as it probes collaborative motions in molecular systems that are largely influenced by the different crystalline packing.²³⁵ Its use can be extended to study crystallisation itself and it has been shown that even low amounts of crystallinity can be detected in semi-crystalline systems,²⁶ and we recently developed a setup that allows for the in-situ investigation of crystallisation from the liquid phase over a range of concentrations and temperatures.²⁴

Ultraviolet-visible (UV-Vis) spectroscopy has been widely applied for determining the concentration of a range of chemical species in a liquid, such as in the field of solution chemistry and water quality monitoring.³¹⁸ By measuring the absorption spectrum of the sample of interest, the identity of a known compound or molecule in solution can be confirmed and using a calibration curve, the concentration of the compound can be determined quantitatively.³¹⁹ However, despite its excellent sensitivity and ready availability some drawbacks of the method remain: the electronic transitions that give rise to the absorption in the UV-Vis are not very specific and often overlap and it is not always straightforward to utilise UV-Vis spectroscopy for measuring the concentration of chemicals in semi-crystalline systems, as the crystal particles will result in scattering losses and signal distortion.

In contrast, Raman spectroscopy can resolve the formation of crystals in the mid-infrared with much higher chemical specificity even in the presence of water, but it is inherently limited

to study the properties of the crystals in solution rather than capturing much information about the liquid phase.³²⁰ Other optical techniques such as second harmonic generation and polarized light microscopy can both detect the onset of the crystallisation, but are not ideally suited to infer detailed mechanistic insight into the nascent molecular structures.^{321;322}

The method that is proposed in this study is using THz-TDS to determine the concentration of the solute prior and during crystallisation. In contrast to UV-VIS spectroscopy the method does not require the presence of a chromophore but rather exploits the differences in relaxation dynamics of the dipole moments of the solvent molecules that strongly affect the absorption measured at terahertz frequencies. In analogy to the quantification by UV-Vis a calibration curve over a range of concentrations is required but for the THz-TDS method the sample temperature needs to be taken into account as well.

Using this method, it is possible to measure the concentration of solute in the liquid phase not just in the neat liquid but throughout phase changes such as during crystallisation. In liquid systems, the coupling of photons to the vibrational density of state (VDOS) forms the so-called microscopical peak, which is responsible for an increasing absorption coefficient with frequency observed in the terahertz region. In crystalline systems, the VDOS is depleted and instead spectral peaks are formed at discrete frequencies, thereby decreasing the baseline. Hence, terahertz spectroscopy can probe liquid relaxation dynamics as well as vibrational transitions in crystals simultaneously, represented by the baseline and the peaks on a spectrum, respectively. It is demonstrated at the example of the crystallisation of the model system magnesium sulphate heptahydrate.

7.2.2 Experimental Section

THz-TDS Measurements of Crystalline $\text{MgSO}_4 \cdot 7\text{H}_2\text{O}$ in the Solid State

A sample of $\text{MgSO}_4 \cdot 7\text{H}_2\text{O}$ (Sigma-Aldrich, Gillingham, UK) was ground using an agate mortar and a pestle, and then mixed with polyethylene (PE) powder to 2.5 w/w% by gentle mixing. The powder mixture was compressed into a pellet of 13 mm diameter using a hydraulic press (Specac Ltd., Kent, UK) at a load of 2 tons. A blank PE pellet was used as

a reference. A terahertz time-domain spectrometer TeraPulse 4000 (Teraview, Cambridge, UK) was equipped with a cryostat (Janis, Massachusetts, USA) and an attached heater and controller (Lakeshore 330, Ohio, USA). The setup was capable of performing temperature-variant transmission measurements. For each measurement, 1000 waveforms were acquired and averaged and a spectral resolution of 0.94 cm^{-1} was achieved per spectrum.

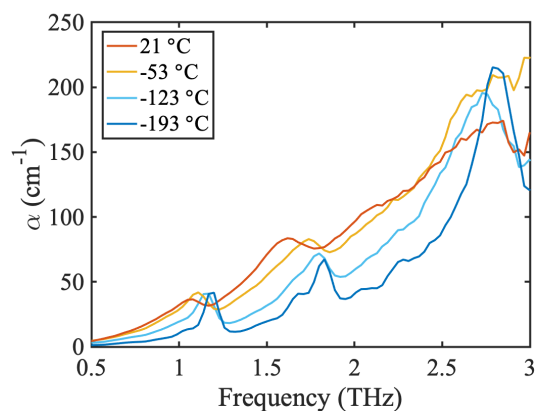
MgSO₄ Solution Measurements

Aqueous magnesium sulphate solutions were prepared to various defined concentrations from commercial MgSO₄·7H₂O (Sigma-Aldrich, Gillingham, UK). The experimental setup was described in detail in Section 7.1²⁴ and consisted of a liquid cell inserted into a hollow metal sample holder. The temperature was controlled by a recirculating water bath. The setup could be used either under stagnant conditions, i.e. the solution was inserted at the beginning of the measurement and the liquid cell was sealed, or in the continuous flow conformation, i.e. the solution was initially kept in a heated syringe that was fixed to a syringe pump, and was slowly injected into the cell.

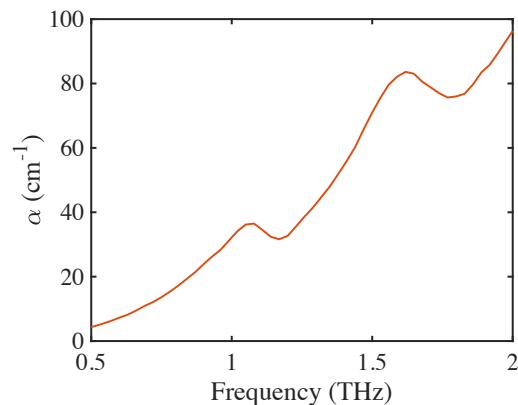
Once solution was injected into the liquid cell and the temperature had stabilised at the setpoint temperature (here $\sim 4\text{ }^{\circ}\text{C}$), the temperature of the cell was slowly increased at a rate of $1\text{ }^{\circ}\text{C min}^{-1}$ up to $25\text{ }^{\circ}\text{C}$. In the present study, calibration was therefore performed in the temperature range of $4\text{ }^{\circ}\text{C}$ to $25\text{ }^{\circ}\text{C}$ and the concentration region that was explored ranged from 0 (pure water) to 0.28 w/w % (MgSO₄ to water). The weight ratio/concentration is denoted as c (w/w %), which represents the concentration of solution.

Transmission spectra were acquired using a TeraPulse 4000 spectrometer (Teraview, Cambridge, UK) and images were acquired with an attached camera (CF-25, CrazyFire, China). Utilising the high-resolution mode of the spectrometer, time-domain waveforms of 45 ps duration with a spectral resolution of 0.94 cm^{-1} were recorded. Each spectrum was calculated from the average of 15 individual waveforms, resulting in the acquisition of one spectrum per 20 s and covering the frequency range from 0.35 THz to 2 THz.

Several thermocouples continuously monitored the temperature of the water bath, of the circulating water surrounding the crystallisation cell, of the syringe, and of the solution at



(a) Solid-state terahertz spectra of $\text{MgSO}_4 \cdot 7\text{H}_2\text{O}$ at various temperature at 0.5 THz to 3 THz.



(b) Solid-state terahertz spectra of $\text{MgSO}_4 \cdot 7\text{H}_2\text{O}$ at 21 °C at 0.5 THz to 2 THz.

Figure 7.8. Solid-state terahertz spectra of crystalline $\text{MgSO}_4 \cdot 7\text{H}_2\text{O}$.

the inlet of the cell.

7.2.3 Results and Discussion

Crystalline $\text{MgSO}_4 \cdot 7\text{H}_2\text{O}$

Reference terahertz spectra of crystalline $\text{MgSO}_4 \cdot 7\text{H}_2\text{O}$ in the solid state were acquired over a range of temperatures in order to characterise the vibrational features that are characteristic of the crystalline form. Three strong vibrational features were identified at 1.2, 1.6 and 2.8 THz in the spectral range that was accessible using the THz-TDS setup (Figure 7.8a). The measurement at temperatures below room temperature confirmed the presence of sharp vibrational features that underly each of the features observed at room temperature. Given that the subsequent crystallisation experiments were performed in the temperature range of 4 °C to 25 °C, and that the presence of the liquid flow cell limits the spectral bandwidth of the spectrometer to the range of 0.35 THz to 2 THz, the more intense feature at 1.6 THz at 21 °C was used to represent the behaviour of the crystalline phase (Figure 7.8b).

Concentration Calibration

The temperature-dependent behaviour of the liquid phase was characterised with terahertz spectroscopy for solutions over a range of concentrations c . For the measurement of solution at each concentration, the absorption at select frequencies was taken from the spectra and a linear fit was applied against temperature, as demonstrated in Figure 7.9.

$$\alpha(c, T, \nu) = a_1 \cdot T[\text{°C}] + b_1 \quad (7.1)$$

where α is the absorption extracted from the terahertz spectra of solution at a certain concentration c acquired in the temperature (T) range of 4 °C to 25 °C at a chosen frequency ν . a_1 and b_1 are the least square linear fitting parameters. Using this methodology, the parameters a_1 and b_1 for a range of concentrations are determined.

Based on the calibration methodology outlined above it is then possible to fit the change in absorption with concentration at a given temperature and frequency with a_2 and b_2 as the linear fit parameters.

$$\alpha_{\nu,T}(c) = a_2 \cdot c[\text{w/w \%}] + b_2 \quad (7.2)$$

Figure 7.10 shows the data that was derived for the case of MgSO_4 solution at the three chosen frequencies: 0.5 THz (lower bound), 1.0 THz (high signal to noise ratio), and 1.6 THz (centre of the crystalline peak) at a temperature of 5 °C. The measurements were performed under static as well as continuous flow, and no significant deviation was identified between the different conditions, as demonstrated by the red data points in Figure 7.10 which correspond to the continuous flow conditions.

The calibration procedure can thus be used to extract the concentration of the solute in the liquid phase based on the measured absorption at any given temperature within calibration range and for any frequency within the spectral bandwidth of the instrument.

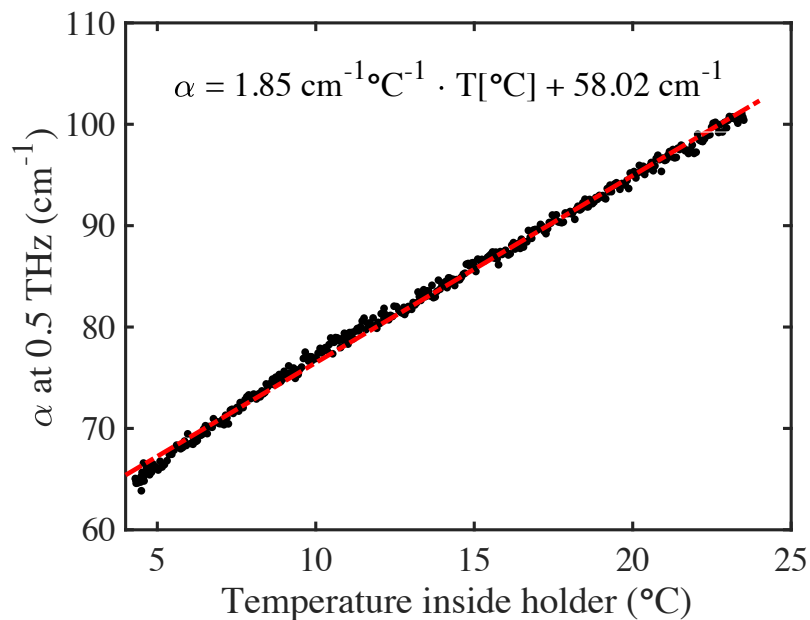


Figure 7.9. The linear fit of temperature (°C) and absorption at the example of a solution of MgSO₄ at a frequency of 0.5 THz and $c = 0.14$ w/w %.

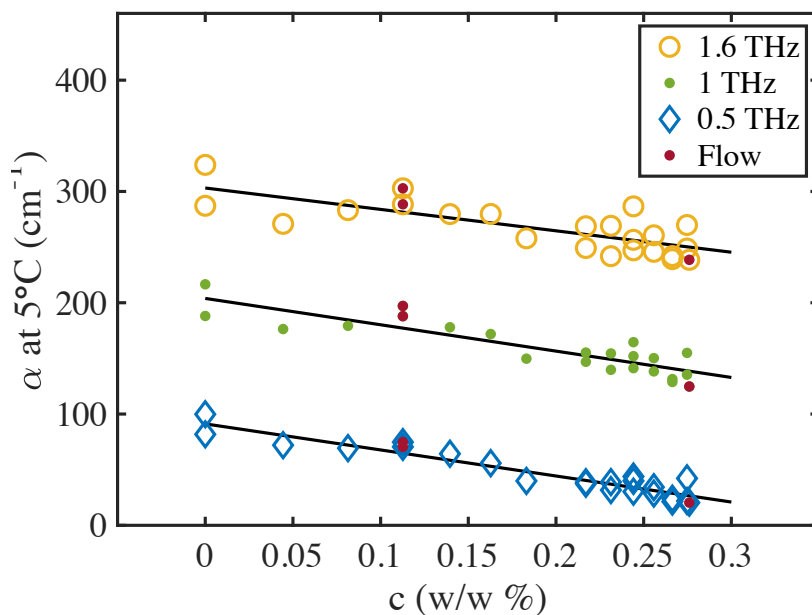


Figure 7.10. The calibration curve of MgSO₄·7H₂O at 5°C. The absorption at 0.5, 1.0, and 1.6 THz is represented by the yellow, green, and blue markers, respectively, and the red data points are the measurements using continuous flow.

Case Study of MgSO₄ Crystallisation

Applying the above method, it was possible to determine the local concentration of solute in the liquid phase during the crystallisation process. Compared to the case of measuring the solute concentration in the neat solution outlined above in the presence of a solid phase, i.e. the crystals, the total absorption (α) is the sum of the absorption from the liquid phase α_{liquid} and the solid phase α_{solid} , here crystalline MgSO₄ heptahydrate. To identify the local concentration in solution the contribution from α_{solid} can be minimised by measuring the absorption at the lower frequency end of the available bandwidth for the calibration curve. At a frequency of 0.5 THz the crystalline phase exhibits negligible absorption (Figure 7.8) and $\alpha \approx \alpha_{\text{liquid}}$. The vast majority of crystalline systems do not exhibit phonon modes at frequencies below a few hundred gigahertz and hence this method is not restricted to the MgSO₄ system but generally applicable as long as the spectral characteristics have been established by a simple transmission measurement of the crystalline phase. As a general rule it can be assumed that the higher the frequency that is chosen for the analysis the more likely it would be affected by the crystalline phase when calculating the equivalent concentration.

Figure 7.11(a) shows the absorption at 0.5 THz directly extracted from the terahertz spectra acquired throughout the crystallisation process, which was at the lower bound of the frequency window and no crystalline feature was expected.

With the information of frequency, temperature, and absorption, the corresponding concentration of the liquid phase was determined as shown in Figure 7.11(b) using the calibration curve in Figure 7.10. The concentration first decreased gradually due to the water depletion from the two ends of the flow cell. In the second region, the concentration increased drastically as crystals started to grow which resulted in relatively denser liquid in the area that was probed with THz-TDS. Afterwards, the concentration reduced again and slowly reached the same equilibrium point as in the beginning, which was assumed as the stable concentration at that temperature. In this way, the temperature-dependent absorption was converted to information that was independent of temperature.

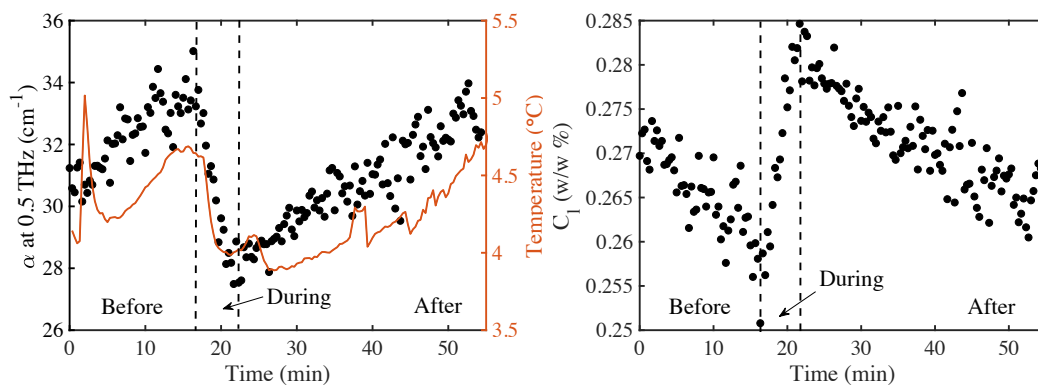


Figure 7.11. The absorption and calculated concentration c_l at 0.5 THz. (a) The change of absorption over time at 0.5 THz along with the temperature profile. (b) The calculated c_l during the crystallisation process.

7.2.4 Conclusions

The newly established set up, based on microfluidics and THz-TDS, has been applied to develop the proposed method of measuring solute concentration as well as the local concentration of semi-crystalline systems. By acquiring terahertz spectra of liquid samples with different concentrations at various temperatures, the calibration curve was determined by the extracted absorption at terahertz frequencies. This was then used to calculate the concentration of solutions. Furthermore, this method can also be applied to study local concentration of the liquid phase while crystallisation occurs. Using the absorption at lower frequencies is recommended in this case, since the complexity of entangled spectral features of liquid and crystalline phases at higher frequencies complicates the spectra. THz-TDS can hence be used as a complementary method for studying concentration changes in a variety of systems under different conditions.

7.3 In-Situ Observation of the Structure of Crystallising Magnesium Sulphate Heptahydrate Solutions with Terahertz Transmission Spectroscopy

7.3.1 Introduction

The crystallisation process has been used for centuries as a purification and separation step for various applications. Therefore, it is surprising that empirical models rather than fundamental understanding still govern the comprehension of crystallisation's underpinning mechanisms and kinetics. What is well established is that nucleation and crystal growth are the two main steps contributing to the crystallisation process. However, the microscopic mechanism of the formation of the nuclei and how they subsequently evolve into crystals is still unclear.^{311;323-325} Two widely popular models are used to describe the crystallisation process: classical nucleation theory and non-classical theory. The former states that density and order fluctuations in the solution cause the formation of crystal-like clusters, which in turn result in nuclei that gradually grow into the crystal form defined by the packing of the cluster.³²⁶ The non-classical theory proposes that the clusters first formed are liquid like, and crystalline order is only introduced later when they grow into nuclei.^{327;328}

One widely used model system for investigating crystallisation is the $\text{MgSO}_4\text{-H}_2\text{O}$ system. A variety of hydrate forms can crystallise depending on the temperature and concentrations in solution, but this system also recently received added attention because the presence of such sulphates and their hydrated forms are discussed as the origin of near-surface water content on Mars.³²⁹ A comprehensive understanding of the crystallisation mechanism is highly desirable to support further research into this topic.

A range of techniques are widely used to investigate the crystallisation process: Traditional crystallographic methods characterise crystalline structures, such as small-angle and wide-angle X-ray scattering, X-ray spectroscopy, and X-ray diffraction; spectroscopic techniques including nuclear magnetic resonance (NMR), Fourier-transform infrared spectroscopy

(FTIR), and Raman spectroscopy provide insight into the chemical structure and the shape of the molecules during crystallisation; ultraviolet-visible (UV-Vis) spectroscopy can measure the solute concentration but is of limited use when nascent particles result in scattering losses that cannot be distinguished from absorption^{311;318}; second-harmonic generation and polarised light microscopy are applied to detect the onset of crystallisation but are not very sensitive to the structure.^{321;322}

When investigating crystallisation in aqueous solutions, the strong absorption due to the presence of water makes it impossible to perform FTIR measurements in transmission. Instead, observations are restricted to surface measurements using attenuated total reflection (ATR). While Raman spectroscopy does not suffer from this restriction, the lack of interaction means that only very little information, if any, of the solvent molecules during the crystallisation process can be extracted.³²⁰

Terahertz time-domain spectroscopy (THz-TDS) offers a unique perspective to characterise the crystallisation process both in terms of information from the solvent as well as the emerging crystals. By measuring the amplitude and phase of single-cycle pulses of far-infrared radiation, in solution, THz-TDS can probe large-amplitude inter-molecular vibrations as well as high-frequency dielectric relaxation processes that correspond to relaxation times of less than 10 ps.²⁶ In solids, the technique can distinguish between different polymorphic forms, cocrystals, hydrates and solvates, as well as provide an excellent measure for overall crystallinity and defect density crystallinity since the long-range order in crystals results in well-defined spectral features (fingerprints) in the terahertz region. In contrast, in amorphous materials, the lack of long-range order results in the collapse of the well-defined peaks into a vibrational density of states (VDOS), which starts at a few hundred gigahertz and exceeds the entire spectral bandwidth of modern THz-TDS spectrometers (0.3 THz to 3 THz). It is characterised by a featureless, monotonously increasing absorption coefficient that typically peaks at frequencies beyond 3 THz.³³⁰

Studies of water and water/alcohol mixtures with THz-TDS suggested key concentration transition points that marked different stages of water and alcohol molecular interactions.⁸⁹ Other water mixtures and solutions also demonstrated the use of THz-TDS to probe water

molecules based on their mobilities and the behaviour of the hydration shell.^{109;110} As well as for characterising static structures, THz-TDS has also been found useful to probe reaction dynamics, such as solid-solid phase transitions, amorphous-solid transformations, and crystallisation.^{26;130;140;141}

Previously, terahertz spectroscopy has been applied to study the crystallisation of sugar and L-(+)-tartaric acid utilising attenuated total reflectance geometry and triggering the crystallisation process by the evaporation of water from the aqueous solution.^{140;141} During crystallisation the VDOS is depleted, resulting in the emergence of peaks and a dropping of the overall baseline given its nature as the flank of the VDOS. THz-TDS can therefore simultaneously probe amorphous and crystalline phases represented by the behaviour of the baseline and peaks, respectively. In addition, this suggests that the behaviour of liquid phase can be extracted explicitly from the baseline while crystallising, hence the solute concentration can be measured even in semi-crystalline samples.²⁵

MgSO₄ is chosen as a model system to demonstrate that THz-TDS is an option to complement the currently widely applied tools in the field of crystallisation. The versatile set-up based on THz-TDS in transmission geometry and the methodology described in detail in Section 7.1 and 7.2 are further used to observe the dissolution of crystals at elevated temperatures, calculate the equivalent local concentration, and can be extended to other systems of interest.

7.3.2 Methods

Solid-State Samples Measurements

Commercial samples of four different MgSO₄ hydrates were investigated. These crystalline samples were ground gently in an agate mortar with a pestle, and the polycrystalline samples were then mixed with polyethylene (Induchem, Volketswil, Switzerland) to a defined concentration that varied for different hydrates, as detailed in Table 7.1.

The well-mixed powder was compressed into a pellet of 13 mm diameter with a thickness of 2 mm to 3 mm using a hydraulic press (Specac Ltd., Kent, UK) at a load of 2 ton, and

Table 7.1. Concentration overview for different solid-state samples.

Sample	Concentration
anhydrous MgSO ₄ 97 % (Acros Organics)	7.5 % w/w
anhydrous MgSO ₄ 99.5 % (Alfa Aesar)	7.5 % w/w
MgSO ₄ monohydrate 97 % (Sigma-Aldrich)	6.3 % w/w
MgSO ₄ heptahydrate 98 % (Sigma-Aldrich)	2.5 % w/w
MgSO ₄ heptahydrate crystallised at room temperature from solution	2.5 % w/w

a blank polyethylene pellet prepared in the same way was used as a reference. During the THz-TDS transmission measurement, 1000 waveforms were acquired and averaged, with a resolution of 0.94 cm^{-1} .

Additionally, a supersaturated solution of MgSO₄ was prepared from MgSO₄ heptahydrate 98 % (Sigma-Aldrich, Gillingham, UK) dissolved in Milli-Q water (IQ 7000, Merck, Darmstadt, Germany, resistivity $18.2 \text{ M}\Omega \cdot \text{cm}$), and filled into a well-sealed petri dish. The petri dish was left in a fume hood at 20°C until crystals formed. This process was to mimic the crystallisation process in the crystallisation cell. Due to constraints of the set-up it was impossible to investigate crystals grown directly in the microfluidic cell at cryogenic temperatures. The crystals grown in the petri dish were made into pellets using the method described above and characterised at cryogenic temperatures with terahertz spectroscopy later to confirm their structure more accurately.

THz-TDS measurements were performed with a commercial spectrometer TeraPulse 4000 (TeraView Ltd., Cambridge, UK), and the measurement chamber was purged with nitrogen to eliminate the effect of water vapour. Variable-temperature measurements were facilitated by a cryostat (Janis, Massachusetts, USA) and the temperature was well-controlled with an attached temperature controller (Lakeshore 330, Ohio, USA). The sample pellets were first cooled down to 80 K and then heated up in steps to 300 K to examine the temperature-dependent behaviour of the spectral features. Measuring commercial samples at room temperatures allows the direct comparison of their spectra with those acquired during crystallisation experiments. However, acquiring spectra for crystalline samples at lower temperatures improves their quality since absorption in the terahertz region is highly affected by the temperature background, reflected in effects such as peak broadening and peak shifting.

Crystallisation Measurements

To investigate crystallisation, magnesium sulphate solutions were prepared to various concentrations using commercial MgSO_4 heptahydrate 98 % (Sigma-Aldrich, Gillingham, UK). The sample was dissolved in Milli-Q water in a beaker, which was then left on a magnetic stirrer until the crystals were fully dissolved. After several rounds of preliminary experiments, three concentrations (mass ratio of MgSO_4 heptahydrate to water) were chosen for further repeats: 1.41:1, 1.29:1, and 1.20:1. This was based on the time and temperature observed for crystallisation.

A detailed description of the crystallisation set up was given in an earlier paper²⁴ (also in Section 7.1). The set up consisted of a liquid cell that was held by a hollow metal sample holder inside of which water was circulated. The temperature of the circulating water was controlled via an external water bath, whose temperature was balanced between an electric heater and the surrounding ice bath with an accuracy of 0.1 °C. The operation temperature was in the range of 4 °C to 90 °C, and during the experiments described here it was operated between 4 °C to 25 °C.

Air was used as the reference, and the high-resolution mode of the spectrometer was utilised to extend the extent of acquired time-domain waveforms to 45 ps. Each spectrum was formed of the average of 15 individual waveforms with a spectral resolution of 0.94 cm^{-1} , resulting in an acquisition time of 20 s per spectrum. The valid frequency range was from 0.35 THz to 2 THz.

When monitoring the crystallisation process at a set temperature, the cell was first cooled down and kept constant at the target temperature until the system was stable. Afterwards, the MgSO_4 solution was injected into the flow cell with a syringe via a tube, and the outlets on both sides of the flow cell were sealed with parafilm. The sample holder including the cell was promptly placed at the centre of the measurement chamber and terahertz spectra and images were acquired. The time from injecting the solution to the start of the measurement was minimised to no more than 30 s, in case of triggering undesired nucleation. The temperature was kept as constant as possible during the whole crystallisation process, until crystals formed

across the cell in the view of the optical probe and the terahertz spectra did not exhibit further changes. The experiment was either terminated at this point, or the behaviour of the system during slow heating to room temperature was studied. In the latter case, the temperature was increased by $0.2\text{ }^{\circ}\text{C min}^{-1}$ up to $25\text{ }^{\circ}\text{C}$ in the flow cell. This was found to be an ideal heating rate to introduce a constant temperature change to the cell.

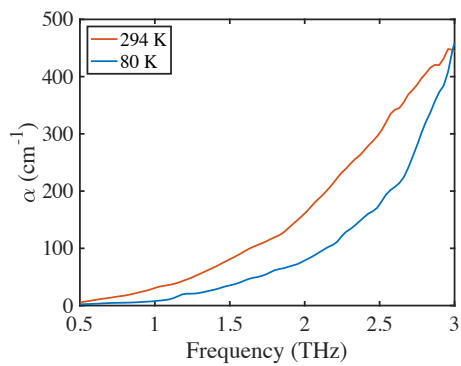
For all measurements, three thermocouples monitored the temperature at various positions: in the water bath, inside the metal sample holder, and at the inlet of the cell, and one data point was acquired per second. The optical probe used for image acquisition was set to acquire one photo every two seconds. After each crystallisation measurement, the liquid cell was thoroughly cleaned to remove grown crystals, contaminations, or seeds which could influence subsequent measurements. The cleaning solution was prepared from commercial EDTA solution ($\text{pH} = 8$; Fisher Scientific, Loughborough, UK) and NaOH solution (Reagecon Diagnostics, Shannon, Ireland) to adjust the pH to 10 in which MgSO_4 exhibits a higher solubility.

7.3.3 Results and Discussion

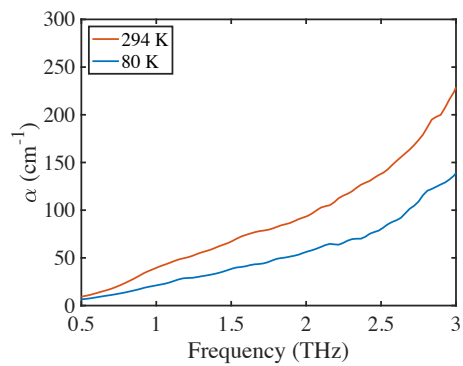
Terahertz Spectra of MgSO_4 Hydrates

The terahertz spectra of MgSO_4 anhydrous, monohydrate, heptahydrate, and the crystal grown in the lab from solution were acquired at different temperatures (Figure 7.12). Comparing the spectra of the three different hydrates, neither the anhydrous nor monohydrate forms of MgSO_4 showed pronounced peaks in the region of interest (0.3 THz to 3.0 THz), and only baseline dropping occurred upon cooling.

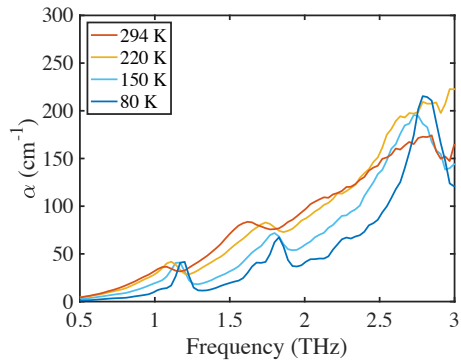
For the commercial heptahydrate sample, three pronounced bands were observed at 80 K : at 1.2 THz , 1.7 THz (double features), and 2.8 THz . These vibrations probably resulted from the interactions between MgSO_4 and water because they were not present in the anhydrous and monohydrate samples. As expected, the spectra exhibited peak broadening and shifting as well as an increase of the baseline upon heating to room temperature. This is due to the significant population of excited vibrational states at room temperature, which is a



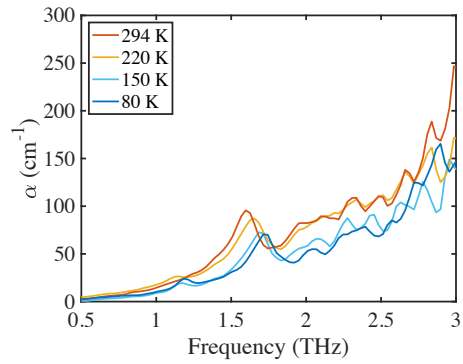
(a) Anhydrous MgSO_4 .



(b) MgSO_4 monohydrate.



(c) Commercial MgSO_4 heptahydrate.



(d) MgSO_4 heptahydrate grown in the lab from solution.

Figure 7.12. Crystalline MgSO_4 hydrates measured at different temperatures.

characteristic of the far-infrared where the energy gap between ground state and excited states is lower than in the infrared. In addition, the increased thermal vibration and emission contribute to this effect. At 294 K, which was close to the temperature of the crystallisation experiments, the high intensity peak at 2.8 THz diminished into the baseline and the two features at lower frequencies became weaker and broader while the double peak at 1.7 THz merged and shifted to a single feature at 1.6 THz.

The spectra of crystals grown under the conditions similar to the crystallisation in the flow cell exhibited less temperature-dependent behaviour. The feature at 1.2 THz was slightly more intense at low temperatures, while the peak at 1.7 THz was consistently observable in the whole temperature range. The latter shifted to 1.6 THz upon heating to room temperature, though as a single feature rather than a double one at temperatures above 80 K. The high similarity between the terahertz spectra of heptahydrate and grown crystals, especially at 294 K, confirmed that the crystals grown in the crystallisation cell were indeed MgSO_4 heptahydrate. The differences between the two could be accounted for by the different purity and defect density. In addition, the 1.1 THz peak became too weak to be observed at room temperature, so the feature at 1.6 THz was used in the following analysis to monitor the crystallisation process.

Crystallisation of $\text{MgSO}_4 \cdot 7\text{H}_2\text{O}$

As described in the method section, the flow cell was kept constant at the desired temperature for crystallisation, and the process was monitored with both terahertz spectroscopy and an optical probe. Confirmed by visual analysis, crystallisation was usually observed to start at either inlet or outlet (or both) of the crystallisation cell, followed by crystal growth across the cell to its other end. Acquired images were useful complimentary information to track the progress of crystal growth throughout the cell. After performing image edge detection and binarisation, crystals were represented by white pixels, and the amount of crystals in the field of view of the camera was quantified as demonstrated in Figure 7.13. In most measurements, it took approximately 4 min to 10 min for crystals to grow from one end of the cell to the other once crystal growth had initiated.

The spot of terahertz radiation probing the centre of the cell was about 2 mm in diameter (as highlighted in Figure 7.13b). Before the crystals had grown into the centre of the cell, the sample volume probed with terahertz radiation was entirely filled with liquid, and the terahertz spectra were hence completely featureless. However, as crystal growth continued toward the centre of the cell, the absorption below 1.6 THz decreased and a peak emerged at 1.6 THz. This indicated the existence of crystals in the field of view of the spectrometer (see Figure 7.13d). The peak at 1.6 THz correlated with the peak in the solid state heptahydrate samples measured previously and shown in Figure 7.12. The time by which crystals were detected by THz-TDS coincided well with the time expected from image analysis (also shown in Figure 7.13c).

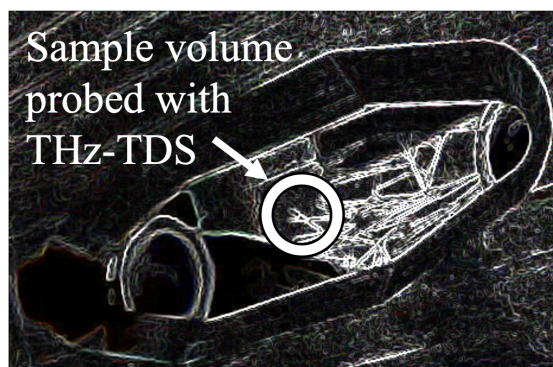
Three frequencies were chosen to illustrate the changes of the spectrum over the course of the experiment: 1.6 THz, i.e. the peak maximum, 1.0 THz, the frequency where the spectrometer has the highest signal to noise ratio, and 0.5 THz, which was a sufficiently low-frequency that it should not directly be influenced by the crystalline spectral feature. At each of those three frequencies, the absorption coefficient was extracted and plotted as a function of time, as illustrated in Figure 7.14.

An algorithm was used to differentiate reliably and reproducibly between three regions (before, during, and after crystal growth) by fitting three linear functions to the data and selecting the fits that minimised the sum of their root mean square error. The fits are shown in Figure 7.14. This allowed more information to be extracted at each stage of the crystallisation, and facilitated comparison between the subsequent measurements which were performed under a range of conditions.

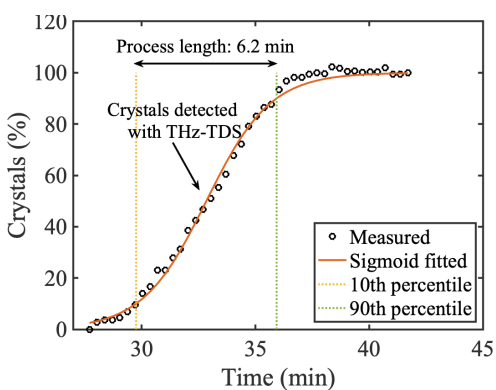
Crystallisation experiments and the analysis described above were performed for a range of different temperatures and concentrations. A measure for how fast the crystals covered the field of view was found by evaluating the time difference between the emergence of the peak and reaching the equilibrium afterwards. This time period was denoted as “second region”. The “first region” corresponded to the time before crystals appeared in the field of view, and the “third region” referred to the last part of the experiment after crystals had fully covered the field of view.



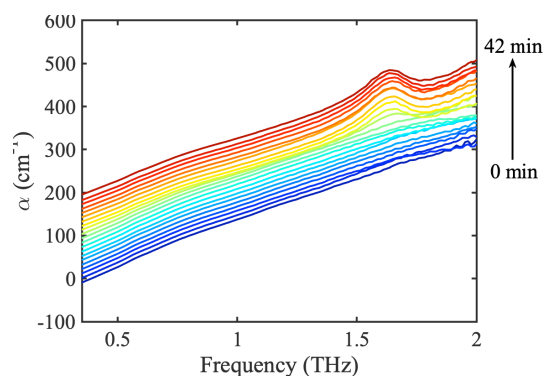
(a) Raw image recorded when the crystals grew into the middle of the cell and were detected by THz-TDS.



(b) 7.13a after edge detection and binarisation. The approximate sample volume probed with THz-TDS is highlighted.



(c) Percentage of area covered by crystals as observed with visual analysis plotted against time. In this case, the crystal growth through the cell occurred in about 6 min at around 4°C.



(d) Terahertz spectra acquired during crystallisation. Each subsequent spectrum is offset by 10 cm⁻¹.

Figure 7.13. Visual analysis of crystal growth.

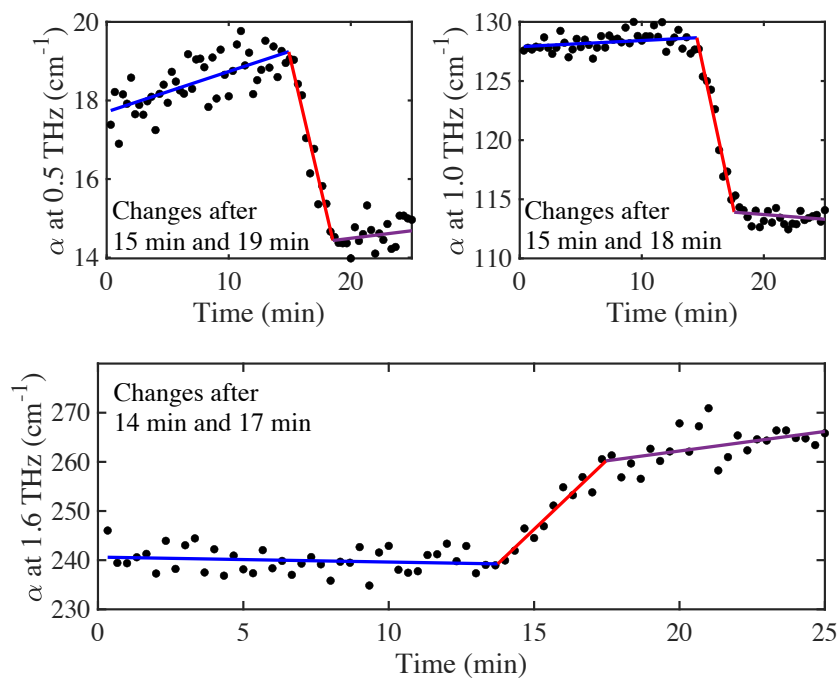


Figure 7.14. Absorption extracted at 0.5, 1, and 1.6 THz. This highlighted the different behaviour of the peak feature compared to the rest of the spectrum (i.e. the differences between crystalline and liquid phases). Whereas the absorption at 1.6 THz increased after 14 min, when crystallisation occurred, the absorption decreased at lower frequencies. Linear fits were performed before (first region, blue), during (second region, red), and after (third region, purple) crystal growth through the field of view.

During analysis, the slope of the linear fit to the data points in the second region was evaluated. In most experiments, the gradient of the linear fit was positive for 1.6 THz and negative at lower frequencies.

Figure 7.15a clearly shows the different behaviour of the absorption for the peak at 1.6 THz compared to other frequencies. While the absorption at 1.6 THz (triangles) increased during crystallisation, it decreased for lower frequencies (dots and diamonds). The spread was higher at higher concentrations, meaning that a faster crystallisation was more likely to result from more supersaturated solutions of MgSO_4 .

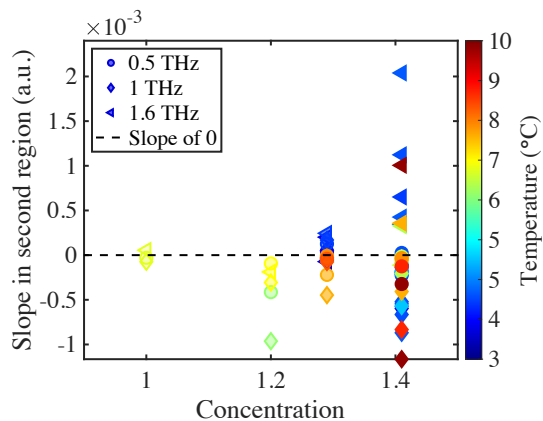
If less time was spent in the second region, i.e. the crystal growth rate was increased, the higher was the absolute gradient in that region at all frequencies. This was shown in Figure 7.15b. For better clarity, the slope during the phase at which the crystals grew into the field of view of the THz-TDS system was shown at only 1 THz, where the signal to noise ratio was largest. The slope in the second region of the data at 1 THz was plotted against the time the crystals took to fully cover the field of view of the spectrometer. The shown slope was negative because the absorption decreased at 1 THz when crystals appeared.

Figure 7.15c shows the relationship between the duration of the middle region with the temperature at which the experiments were performed. While crystal growth through the field of view of the spectrometer seemed to take around 4 min at temperatures between 3.5 °C to 5 °C, the spread was larger at temperatures above 6 °C. In one extreme case it took almost 40 min for the crystals to fully cover the field of view. In most other cases, it took between 2 min to 12 min, independent of concentration. At last, Figure 7.15d showed how much the absorption at 1.0 THz changed with time at different temperatures and concentrations.

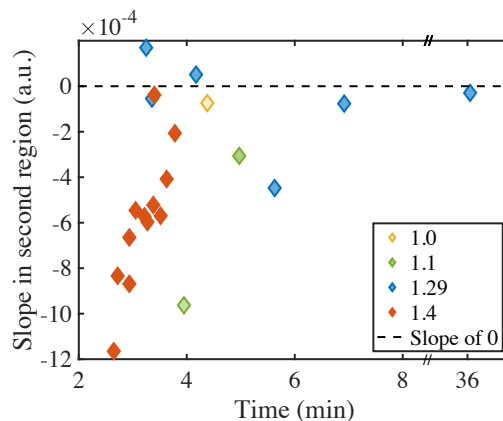
Combining Figure 7.15a and Figure 7.15c it was concluded that, based on the results from our experiments presented here, both a higher initial concentration and elevated temperature above 6 °C made the crystal growth more erratic indicated by a wider spread of the data.

Calibrated Local Concentration and Hydration Shell

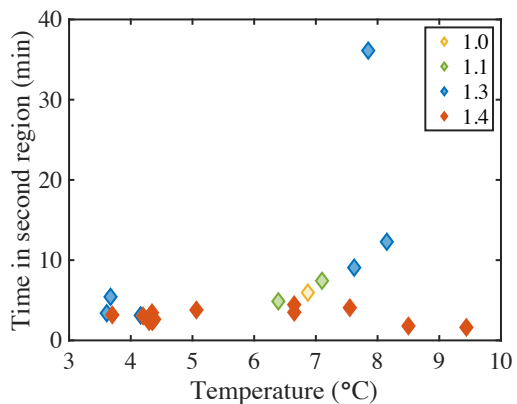
Terahertz spectra are inherently temperature dependent. As discussed above, both a decrease in MgSO_4 concentration and an increase in temperature yield a higher absorption coefficient.



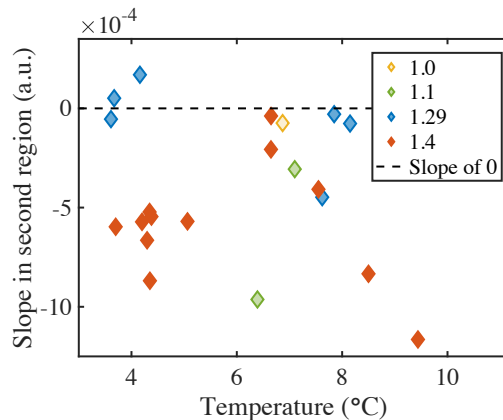
(a) Slope in the second region plotted against concentration, shown at 0.5 THz (dots), 1.0 THz (diamonds), and 1.6 THz (triangles). The colour denoted the temperature at which the system was kept during crystallisation.



(b) Gradient of the linear fit to the absorption at 1.0 THz in the second region plotted against time. The colour denoted the different initial concentrations.



(c) Time spent in the second region plotted against temperature. The data was extracted at 1.0 THz and different colours denoted different initial concentrations.



(d) Slope in the second region plotted against the temperature at which the experiments were performed, shown at 1.0 THz and different colours denoted different initial concentrations.

Figure 7.15. Analysis parameters during crystal growth plotted against concentration, time, and temperature. The concentrations were represented by the mass ratio of MgSO_4 heptahydrate to water.

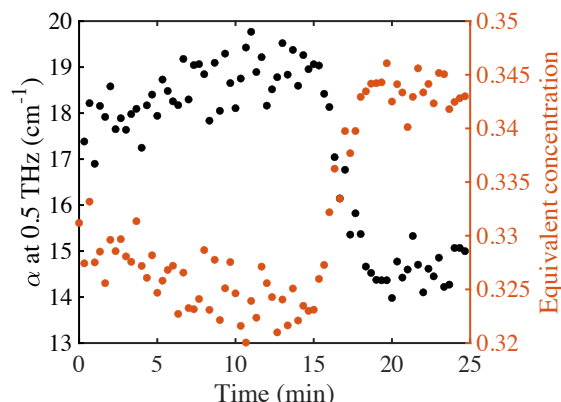
Therefore, if the data are corrected for temperature variations, all changes that are observed in the absorption coefficient are directly linked to structural changes of the probed sample volume.

To eliminate temperature effects, a calibration procedure previously established in Kölbel et al. was followed.²⁵ By measuring the absorption of liquid mixtures of varying concentrations at different temperatures, a calibration curve had previously been determined. This allowed the calculation of the concentration of a solution of unknown concentration at arbitrary temperatures. In purely liquid samples, the calibration procedure resulted in the actual concentration for solutions. However, the emergence of crystalline features affected the spectra and in this case, the liquid phase absorption was calculated at frequencies furthest away from the peak of the crystalline feature at 1.6 THz.

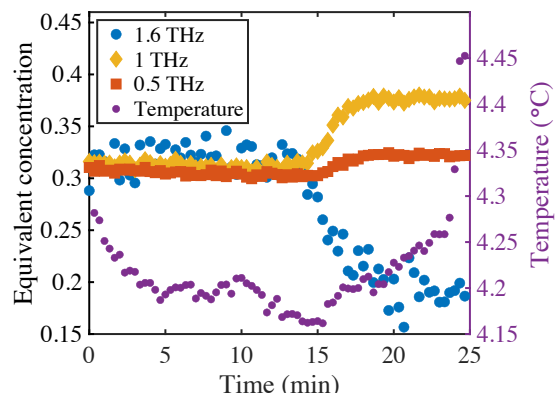
An example of converting temperature-dependent data into the temperature-independent equivalent concentration is shown in Figure 7.16. Instead of the slowly rising absorption before crystals reached the field of view that was observed in Figure 7.14, the concentration decreased. This complemented the information gained only by analysing the absorption coefficient and yielded an explanation of the changes in the spectra during crystallisation as follows.

At the beginning of the experiment, both the terahertz spectra and visual analysis confirmed the absence of MgSO_4 crystals located in the centre of the cell. Once nucleation occurred, typically not in the centre of the cuvette but near one end of the cell, a local increase in water concentration was observed in the terahertz spectra due to the increase in water concentration immediately adjacent to the growing crystals as magnesium and sulphate ions crystallised into the MgSO_4 heptahydrate form. This caused a slight increase of the absorption coefficient, corresponding to a lower MgSO_4 concentration measured in the centre of the cell.

MgSO_4 in solution is surrounded by a hydration shell whose absorption is markedly different from that of bulk water.¹¹³ This was demonstrated by calculating a theoretical absorption coefficient based on the known absorption coefficient of pure water (α_{water}) and that of anhydrous MgSO_4 and that of $\text{MgSO}_4 \cdot 7\text{H}_2\text{O}$ (α_{crystal}), neglecting the effect of a larger hydration



(a) Absorption α at 0.5 THz (black) and corresponding calculated liquid phase solute concentration over time (red).



(b) Liquid phase solute concentration calculated at 0.5 THz (red squares), 1.0 THz (orange diamonds), and 1.6 THz (blue dots). Right: The temperature throughout the measurement. It was stable and stayed within 0.1 °C of the set-point until the temperature control was turned off after crystallisation.

Figure 7.16. Illustration of using the calibration method to calculate liquid phase solute concentration based on measured absorption at various frequencies.

shell. A series of MgSO_4 aqueous solution with a range of concentrations were measured, and a difference between the measured (α_{solution}) and the calculated ($\alpha_{\text{ideal mixture}}$) absorption was consistently observed.

$$\alpha_{\text{ideal mixture}} = \alpha_{\text{crystal}} \cdot c_{\text{MgSO}_4} + \alpha_{\text{water}} \cdot c_{\text{water}} > \alpha_{\text{solution}} \quad (7.3)$$

This difference was calculated with Eqn. 7.3 for a number of measurements and is shown in Figure 7.17 for anhydrous MgSO_4 , where c_{MgSO_4} represents the molar concentration of anhydrous MgSO_4 or $\text{MgSO}_4 \cdot 7\text{H}_2\text{O}$ of the solutions in the corresponding case. Calculated values for both anhydrous MgSO_4 and MgSO_4 heptahydrate are shown in Table 7.2. Changes were subtle below 0.02 molar concentration and increased steadily above in both the case of anhydrous MgSO_4 and MgSO_4 heptahydrate.

The calculated theoretical absorption excluding the effect of the hydration shell was larger than that of the measured absorption, indicating that the hydration shell surrounding MgSO_4 had a lower absorption coefficient than the bulk water that it replaced which is in line

Table 7.2. Data for Figure 7.17.

Molar conc. (MgSO_4)	Relative abs. (cm^{-1})	Molar conc. ($\text{MgSO}_4 \cdot 7\text{H}_2\text{O}$)	Relative abs. (cm^{-1})
0.007	7.80	0.007	7.96
0.013	6.68	0.014	6.85
0.019	-1.21	0.021	-1.15
0.024	11.42	0.028	11.27
0.028	20.26	0.035	19.81
0.032	43.00	0.042	42.18
0.040	37.29	0.055	35.55
0.040	42.19	0.055	40.45
0.043	40.44	0.062	38.17
0.043	47.64	0.062	45.37
0.046	39.54	0.068	36.70
0.046	35.24	0.068	32.40
0.049	39.59	0.074	36.15
0.049	41.39	0.074	37.95
0.054	67.92	0.087	63.21

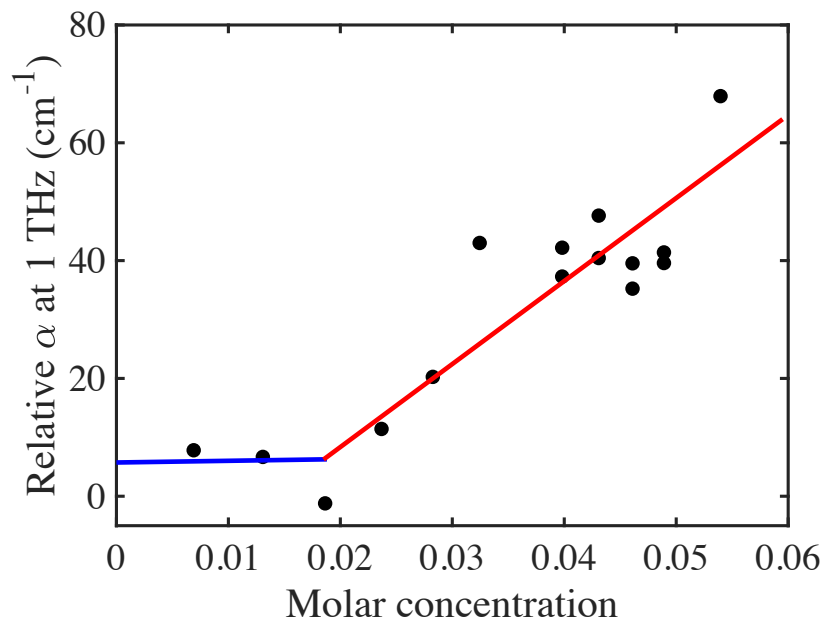


Figure 7.17. Relative absorption calculated and plotted against molar concentration of MgSO_4 . The experimental error is on the order of 4 cm^{-1} . The lines are drawn to guide the eye and are not intended to be indicative of a physical model.

with expectation as the dipoles in the hydration shell tend to exhibit slower relaxation behaviour. The results also inferred that the hydration shell encompassed more than the 7 water molecules that form part of the MgSO_4 heptahydrate crystal because of the observed difference between the measured and calculated absorption. This is in line with other observations that also found extended hydration shells when probing samples with THz-TDS.¹¹³

An increase of the overall absorption coefficient at 0.5 THz and 1.0 THz as seen in experiments when crystals grew hence corresponded to water being expelled from the hydration shells into the bulk phase when the crystals formed. The bulk aqueous phase was pushed toward the field of view sampled by THz-TDS during the growth of the crystals before the crystals themselves entered the field of view of the terahertz beam. Therefore, the growth of MgSO_4 heptahydrate, that started at one end of the cell, increased the local concentration of bulk water in the centre of the cell, where it was probed with THz-TDS. This explained the initial slight increase in absorption that was observed at both 0.5 THz and 1.0 THz, given that the absorption coefficient of bulk water is much higher than that of the solution mixed with MgSO_4 or the heptahydrate.

Once the crystals reached the centre of the cell, the absorption at 0.5 THz and 1 THz decreased (see Figure 7.14) as the probed sample became more ordered and thereby the VDOS was depleted, while the absorption at 1.6 THz increased as the peak emerged. On the other hand, the liquid phase concentration seemed to increase at 0.5 THz and 1.0 THz when crystals started to grow in the field of view of THz-TDS. This was in line with a decrease of the hydration shell size and a potentially denser liquid in the area of forming crystals that was probed with THz-TDS.³¹¹ The absorption coefficient at the peak at 1.6 THz clearly increased, and this effect was accompanied by a decrease in MgSO_4 concentration. Once the crystals covered the centre of the cell and the system reached an equilibrium state, the changes at all frequencies became subtle again.

However, the calculated liquid phase concentration was not quantitatively valid at frequencies close to crystal features, as no rigorous method has yet been developed to systematically account for peak effects to the baseline, and the calibration curve was determined from the experimental data of a series of samples in the liquid phase only.

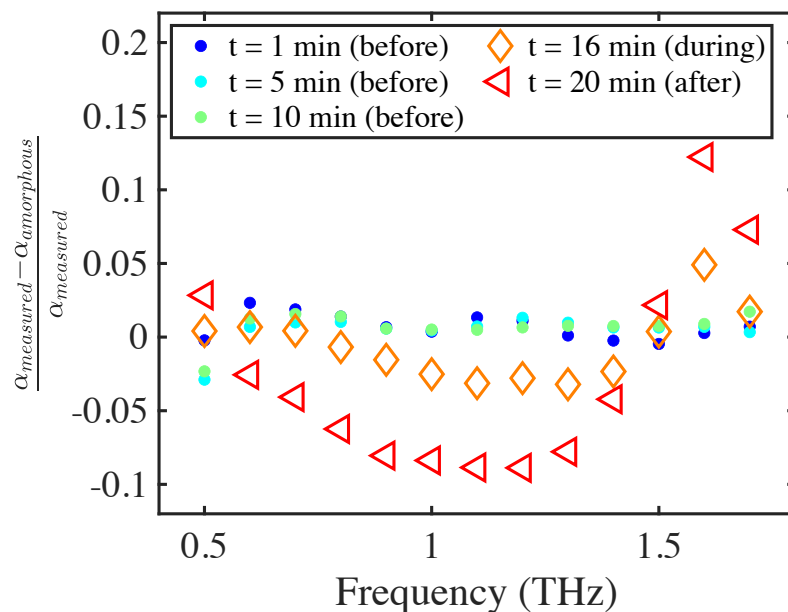


Figure 7.18. Relative changes in α when comparing the measured to the calculated purely liquid absorption before, during, and after crystallisation.

To examine further the influence of the crystalline feature to the data collected at other frequencies, the previous procedure for calculating concentration was applied inversely, i.e. the known and frequency-independent calculated concentration was used to calculate the equivalent absorption if it was fully liquid (α_{liquid}). Of the three frequencies described here, the data at 0.5 THz were the least affected by the crystalline feature, since that frequency was the furthest away from the feature at 1.6 THz. Therefore, the concentration calculated from it was being used as the basis to calculate α_{liquid} .

The relative difference compared to the measured absorption is plotted in Figure 7.18 for different experimental stages. Before crystals were observed in the field of view, the relative difference was close to zero for all frequencies. During crystal growth into the field of view however, the relative difference increased between 1.5 THz to 1.7 THz, and decreased between 0.6 THz to 1.4 THz. This effect became even stronger once crystallisation was complete. Maxima of the relative difference were found at 1 THz and 1.6 THz while the difference decreased toward lower frequencies. This showed that while the peak only seemed to impact a relatively narrow frequency range between 1.5 THz and 1.7 THz, the effects of crystallisation

are still strongly observed at 1.0 THz. The spectral change was directly visible: depletion of the VDOS below 1.5 THz and appearance of a peak above. It should be noted that while current results focus on crystal growth into field of view of the spectrometer, nucleation itself has not yet been observed directly. This will be the focus of future work, possibly by observing very subtle spectral changes.

Dissolution Observed

All the crystallisation experiments were performed and monitored at a constant temperature, and once both visual and spectral analysis confirmed that the crystallisation was completed, the system was slowly heated up. Meanwhile, it was also observed that crystals started to dissolve at elevated temperatures. Therefore, further measurements were carried out to study this phenomenon systematically.

With the well-controlled heating component, an experimental heating rate of $0.1\text{ }^{\circ}\text{C} / 30\text{ s}$ was determined to ensure a constant temperature change in the crystallisation cell. Faster heating might have led to a temperature difference between the circulating water and the inside of the cell, while slower heating rates (although possible) prolonged the experiment. With the chosen heating rate, crystal dissolution was observed within a reasonable experimental time frame. However, an accurate dissolution temperature was not measured because hysteresis effects related to kinetics of crystallisation and dissolution have to be taken into account.

The temperature profile over time is shown in Figure 7.19a, and the times when characteristic changes occurred in the spectra are highlighted with vertical lines. These agreed well with the times extracted from the images acquired by the camera. When the temperature was increased steadily once crystals grew completely, crystal dissolution was observed both visually as the percentage of crystals decreased drastically in the cell (Figure 7.19c), as well as with THz-TDS resulting in the disappearance of the crystalline feature at higher temperatures (Figure 7.19b). This was also investigated by utilising the calculation of liquid phase concentrations to remove the temperature effect from the spectra (Figure 7.19d).

The calculated concentration stayed mostly constant once crystals had formed until

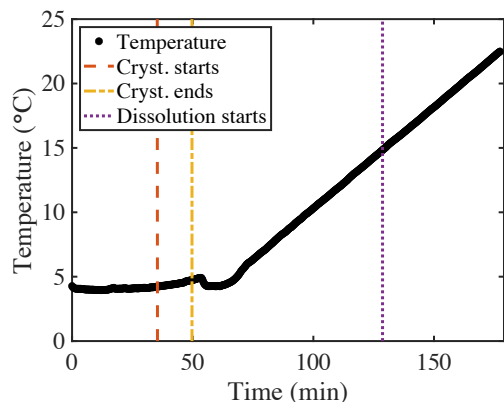
around 130 min after the beginning of the experiment, which coincided with the first observation of crystal dissolution in the camera images. Because heat was constantly being added to the system and the temperature increased steadily, the equilibrium concentration of MgSO_4 in the vicinity of the crystal features varied because the saturation point changed with temperature. Therefore, the crystals dissolved slowly while the surrounding liquid was approaching the point of local saturation upon increasing the temperature. Opposite to crystal growth, dissolution resulted in an enlargement of the hydration shells accompanied by an increase of the absorption at 0.5 THz and 1.0 THz and a decrease at 1.6 THz. The calculated concentration however decreased at 0.5 THz.

7.3.4 Conclusions

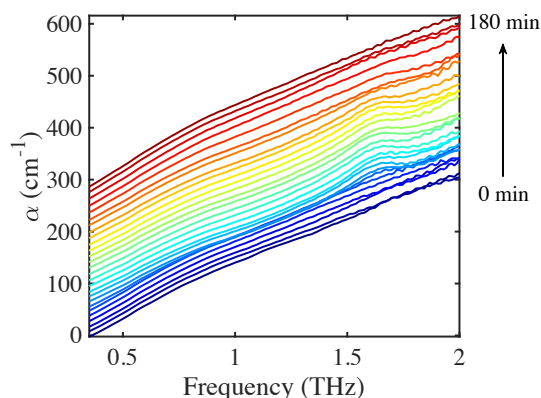
THz-TDS was used to study the crystallisation process of $\text{MgSO}_4 \cdot 7\text{H}_2\text{O}$. The emergence and disappearance of the spectral feature at 1.6 THz indicated the growth or dissolution of crystals in the field of view of the spectrometer (validated by image analysis), while the change of the baseline reflected the behaviour of solvent. This is useful for investigating solvation dynamics and the behaviour of molecular species at phase boundaries.

The absorption at three frequencies was investigated in particular, and the process clearly showed three stages. Experiments at three concentrations and in the temperature range of 4 °C to 9 °C suggested that both a higher initial concentration and elevated temperature above 6 °C were likely to result in a more erratic crystal growth. The faster the crystals grew through the field of view of the spectrometer, the higher was the change in absorption at all frequencies. The temperature effect on terahertz spectra was addressed as outlined previously in Section 7.2, leading to the calculation of an equivalent liquid phase concentration. In addition, changes in the absorption coefficient were correlated with the composition and size of the hydration shell surrounding the salt ions.

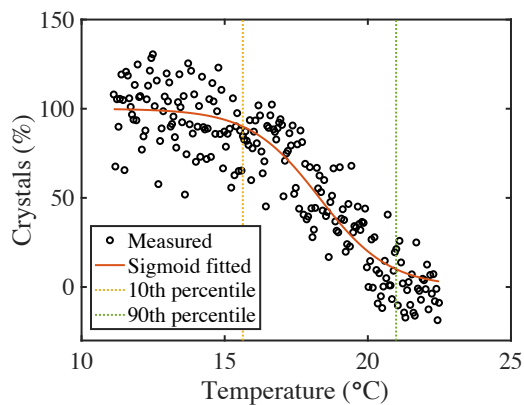
The results covered here are from experiments where the crystals grew into an area probed by terahertz radiation. Therefore, the onset of nucleation was not observed directly. The focus of on-going work is to trigger nucleation at desired locations (e.g. in the centre of



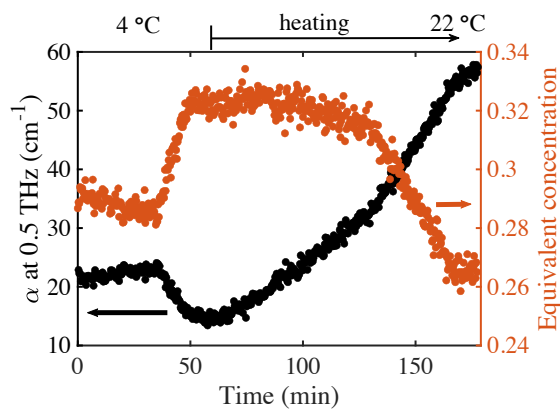
(a) Temperature profile during the experiment. Vertical lines denote changes in the spectra.



(b) Terahertz spectra acquired throughout the experiment (liquid - semi-crystalline - liquid). Subsequent spectra are offset by 10 cm^{-1} .



(c) Dissolution of crystals observed with visual analysis, which started at a temperature shortly below $16 \text{ }^\circ\text{C}$ and was completed just above $20 \text{ }^\circ\text{C}$. At a heating rate of $0.1^\circ / 30 \text{ s}$, this process took about 34 min to complete.



(d) α at 0.5 THz and corresponding calculated concentration over time. After initial crystallisation, the temperature was steadily increased up to room temperature.

Figure 7.19. Crystal dissolution analysis.

the cell) so that the investigation can be extended from that of crystal growth to that of nucleation. The current setup is designed for operating temperatures between 4 °C to 9 °C, and this range can be extended further with simple adjustments. Therefore, this technique can be applied to investigate a wide range of crystalline and semi-crystalline systems, thereby offering an interesting perspective of low-frequency motions of multiphase systems.

Chapter 8

Conclusions and Future Work

8.1 Porous Metal-Organic Frameworks

Porous metal-organic frameworks (MOFs) have been a popular class of novel materials known for their high surface area and flexibility and which can be applied to a wide range of applications, such as energy and gas storage, chemical separation, and catalysis amongst others. The combinations of various metals and organic linkers result in a number of structural possibilities of MOFs. In Section 4.1, one classic MOF material, ZIF-8 (Zn-based) and its analogue ZIF-67 were discussed. I specifically focused on the methyl groups that occupy the pores. ZIF-8 has only one type of functional group in the pores, which makes it an ideal candidate to study how the molecular dynamics within the pores can affect the adsorption process. By comparing the results with those from ZIF-67, which is Co-based rather than Zn-based, the study also demonstrates the influence of metal atoms to the properties of MOFs. This can help with the future design and screening of desired MOFs. Terahertz spectroscopy probes the collective motions falling in the low-frequency vibrational region in ZIF-8 and ZIF-67, including shearing, gate-opening, and methyl rotation. The DFT simulations complement the experimental results and offer an opportunity to isolate the three-fold rotation motion (0° to 120°) of methyl groups, and allow us to calculate the potential energy barriers of both ZIFs. The results prove that the methyl group rotation remains active even at very low

temperatures. The different metal atoms in the two ZIFs clearly affect the volume of the pores, which in turn results in a relatively higher energy barrier of ZIF-67 compared to that of ZIF-8. Additionally, the results were comparable with previously published studies that applied inelastic neutron scattering methods to investigate this effect.

The works presented in Section 4.2 builds on the results and methodology developed in Section 4.1. The study discussed the investigation of the elasticity of MOF-5. While this work was entirely computational, the results were compared to the published data as reported in the literature that were acquired by many other methods, both theoretically and experimentally. The results prove that, by using the meta-GGA density functional M06-2X, the accuracy of both the optimised structure and the predicted elastic constants is considerably improved, and yields results that are much more comparable with the experimental values compared to the calculations employing LDA or GGA functionals. This proved the feasibility of the general method. Even though performing calculations with a hybrid functional is more time-consuming, it can be a good choice if highly accurate results are required.

The studies of porous MOFs show that the combination of methodologies can offer a lot of insight into the molecular dynamics, flexibility, and a close investigation on certain functional groups and fragments. However, most studies are usually focused on certain MOFs as prototypical examples and there is no experimental database available containing reliable quantitative data (e.g. elastic constants), and the accuracy of available simulated results are currently not consistent. Therefore, it will be very helpful to develop more standardised computational methods in the future to obtain important properties that can be made available through large databases to aid the design of new materials.

Initially, the method could be tested on a list of chosen MOFs that are of particular interest in the chemistry community. The predicted values should be double checked with experimental measurements, such as THz-TDS, in an approach that is very similar to the current individual studies. Afterwards, the method could be adapted for a wider range of materials that will offer more information in the database to support the screening process for future applications.

8.2 Metal-Organic Perovskites

Metal-organic perovskites have a cation occupying the pore at the centre of the structure. Therefore, this type of material has very different potential applications to the porous MOFs covered in the last section. Based on the types of metal-organic perovskites, this type of material can be applied to solar cells, multiferroic materials and data storage. In Chapter 5, a series of Gua-MOF perovskites, which have interesting ferromagnetic properties, were discussed to investigate the effect of metal atoms on the low-frequency vibrational spectra. These materials naturally possess disorder that is readily evident from the unavoidable prediction of negative modes whenever the symmetry is maintained during computational lattice dynamics calculations. The computational results show that all the optimised structures of the seven systems that were studied here are slightly distorted from the published space groups in the crystallographic data. The high similarities of their structures are reflected in their comparable terahertz spectra, with similar active motions that are observed at relatively similar frequencies. Interestingly, in the case of Mn-MOF a significant blue shift in the spectral features is observed compared to other systems given that the outer electronic shell in Mn^{2+} is only and just half filled.

Calculations were performed on selected perovskites of different magnetism. This offers a new way to study the influence of spin configuration on the low-frequency vibrations. The results also predict the most likely configuration, which is that of the lowest energy among the proposed structures with the same metal atoms. The prediction matches with the experimental data that were published in previous studies.

Further simulations can be carried out to calculate the polarisability of the series of molecules, which is also of great importance for potential applications. In addition, the combined methodologies can be applied to study the properties of other perovskites based on the desired application, such as charge mobilities. If this project will attract attention, it may help stimulate discussions in the physics and chemistry community to see how to better use terahertz spectroscopy to gain more insight into the field of MOF perovskites.

8.3 Small Organic Molecules

Small organic molecules have been widely studied and are used in a number of applications, yet a range of phenomena in these materials are not fully understood, such as the exact mechanism of their phase transitions and the properties of polymorphic forms in general and crystalline disorder in particular. In Chapter 6, two well-known small organic molecular crystals that are widely used as pharmaceutical drugs, aspirin and theophylline, were explored with terahertz spectroscopy and DFT simulations as examples to investigate the role of disorder in crystalline systems. In both cases, the combined methodologies show advantages for identifying polymorphs and distinguishing complex and disordered crystalline structures.

In Section 6.1, the study was focused on gaining further insight into the crystallographic disorder in aspirin forms I and II. These two polymorphs are widely known for their structural similarities, which makes them ideal candidates to test the sensitivity of the combined methodologies and also to verify hypotheses of the influence of defects on polymorphs. Experimental terahertz spectra of the two forms resulted in minor differences. Therefore, very strict computational settings were applied for all the calculations to provide accurate results for further examining the differences between the two forms. Experimental spectra were fitted with Lorentzian and power law functions to extract quantitative information regarding the level of disorder and to explore evidence that the two forms are intergrown rather than completely pure. However, this study did not provide an effective way to fully quantify the disorder.

Due to the high similarities of the structure of FI and FII, the only difference being a half cell length shift between every other layer, it is hypothesised that the phase transition/intergrowth between the polymorphs originates from local defects during the crystal growth. Such defects could be the mispositioning of few molecules or unexpected vacancies in the crystal lattice. As a result, the molecules surrounding the defects have to move around to find new positions to achieve local stability, which results in one polymorphic form or the other. Computationally, this concept could be explored by a combination of DFT and AIMD simulations. However, in reality, the defects will have a very low concentration, otherwise

the whole system would be too unstable from the beginning. A supercell structure must be applied to the calculations in order to create a large background for inserting defects. This makes it highly time consuming and requires a large amount of computational resources. Preliminary work was performed on CRYSTAL17 using the keyword “ghost” to remove a dimer from the original packing of form I that only deleted atoms but kept the basis sets. The structure was stable and shrank as expected. Due to the limited computational resources, the geometry optimisation calculations did not converge, and it was not possible to continue subsequent AIMD calculations. If the following steps can be achieved, it will provide valuable results to the mechanical properties and plastic deformation of small organic molecules. Similar studies can also be potentially applied to recently discovered aspirin polymorphs and other materials of interest, such as benzocaine and caffeine.

In Section 6.2, the metastability of theophylline FIII was closely investigated along with the phase transitions involving the other two polymorphs FM→FIII→FII. The existence of FIII has been previously discussed, yet its structure had not been reported. Results of mid- and low-frequency Raman spectroscopy and terahertz spectroscopy both showed distinct spectra for FM, FIII and FII. TGA also provided evidence of discernible weight loss after FM being dehydrated. The dehydration experiments of FM were monitored both on pure samples and samples mixed with PE. After purging under N₂ overnight or under vacuuming for a long time, the pronounced peak features of FM terahertz spectra all disappeared. Unclear spectral features of FIII, after the dehydration of FM, reflect that its structure is highly disordered, and also explains why it was not easy to be determined via traditional X-ray diffraction. However, the lattice parameters are comparable with those of FM. Therefore, the hypothesis was that the FIII structure is very similar to that of FM but with the water molecules removed. DFT simulations were then applied to explore the idea. Two possible structures were proposed: One as FM without water but fixed cell length; the other with only the restriction of symmetry. Comparing the simulated and experimental spectra, the second structure is more promising with no clear features below 3 THz, which supported the hypothesised structure of FIII. In addition, the sample pellets were remeasured after being kept at around 20 °C and 40 % relative humidity. The terahertz spectra changed again from

the very disordered crystals to the well-organised FII. This observation completed the phase transitions process discussed in the literature. In this project, the combination of THz-TDS and DFT simulations provided definitive evidence of the disordered structure of FIII, and this combination of methods is an effective complementary tool to XRD to characterise the crystallographic structure of ordered crystals.

I was limited by the available computational resources and therefore the symmetry was kept constrained when performing the geometry optimisations. However, it would be worth trying to re-simulate the structure for a fully relaxed system. This will result in a FIII structure that should be closer to the real structure, and which in turn could provide more information of how disordered the metastable state actually is. Additionally, one main assumption of the DFT method is that all calculations correspond to a temperature of 0 K, which means no extra energy can be provided to the system. In contrast, all the phase transitions investigated here happen at much higher temperatures, around room temperature, and the system will need extra energy to support the molecular mobility that leads to a more stable conformation. In order to investigate the whole phase transitions between theophylline polymorphs, it is worthwhile to carry out simulations based on ab initio molecular dynamics, which can provide the trajectories of molecules. This also needs a large amount of computational time and powerful computational facilities.

8.4 In-Situ Observation of Crystallisation with THz-TDS

A versatile setup was developed that can be applied to characterise solutions and monitor crystallisation process with terahertz spectroscopy in transmission geometry. It was built up based on a customised flow cell with additional components to allow for a wide range of temperature whilst maintaining precise control and stability of the temperature. As parts of the terahertz beam were slightly clipped by the sample holder, it will be useful to adjust it for future work. The set up was firstly applied to study pure solutions (e.g. $\text{MgSO}_4 \cdot 7\text{H}_2\text{O}$

in water) over a range of concentrations, resulting in the concentration calibration curves. Therefore, by acquiring a terahertz spectrum of a solution of unknown concentration, the solute concentration can be determined from the calibration curve with the absorption at a certain frequency and temperature. The method was then extended to multi-phase solutions, i.e. the change of the solute concentration while crystallising. In this case, an absorption at the low-frequency end is recommended for the solute concentration measurement since it is less likely to be affected by the crystalline features.

The crystallisation process of magnesium sulphate heptahydrate was studied in detail using this setup as well as the concentration measurement method. Crystalline $\text{MgSO}_4 \cdot 7\text{H}_2\text{O}$ possesses an intense feature at 1.6 THz, in the region of interest, which clearly reflected the growth of crystals. In addition, the baseline dropping was a characteristic signature of the occurrence of crystallisation as well. Other than crystal formation, the dissolution of crystal was also observed while heating up the setup slowly. However, for all the measurements the crystals started to grow from the two ends of the flow cell, therefore terahertz spectroscopy could only capture the behaviour when they reached the centre of the cell. It will be more informative if the crystallisation can be triggered at chosen positions, so the onset of nucleation can also be studied. Future work on other crystallisation systems is also of interest to expand the possible applications of the developed methodologies.

Bibliography

- [1] O. Mitrofanov, T. Siegrist, D. V. Lang, C. Kloc, W.-Y. So, M. A. Sergent, and A. P. Ramirez. Defects in Organic Molecular Crystals: Spectroscopy and Effects on Electronic and Optical Properties. In *2007 IEEE International Reliability Physics Symposium Proceedings. 45th Annual*, pages 240–242, 2007.
- [2] K. Müllen. Molecular Defects in Organic Materials. *Nature Reviews Materials*, 1:15013, 2016.
- [3] J. Spitaler and S. K. Estreicher. Perspectives on the Theory of Defects. *Frontiers in Materials*, 5:70, 2018.
- [4] B. Civalleri, F. Napoli, Y. Noël, C. Roetti, and R. Dovesi. Ab-Initio Prediction of Materials Properties with CRYSTAL: MOF-5 as a Case Study. *CrystEngComm*, 8(5):364–371, 2006.
- [5] D. Fairen-Jimenez, R. Galvelis, A. Torrisi, A. D. Gellan, M. T. Wharmby, P. A. Wright, C. Mellot-Draznieks, and T. Düren. Flexibility and Swing Effect on the Adsorption of Energy-Related Gases on ZIF-8: Combined Experimental and Simulation Study. *Dalton Transactions*, 41(35):10752–10762, 2012.
- [6] P. Z. Moghadam, S. M.J. Rogge, A. Li, C.-M. Chow, J. Wieme, N. Moharrami, M. Aragonés-Anglada, G. Conduit, D. A. Gomez-Gualdrón, V. Van Speybroeck, and D. Fairen-Jimenez. Structure-Mechanical Stability Relations of Metal-Organic Frameworks via Machine Learning. *Matter*, 1(1):219–234, 2019.

- [7] H. Furukawa, K. E. Cordova, M. O’keeffe, and O. M. Yaghi. The Chemistry and Applications of Metal–Organic Frameworks. *Science*, 341(6149):1230444, 2013.
- [8] B. R. Pimentel, A. Parulkar, E. Zhou, N. A. Brunelli, and R. P. Lively. Zeolitic Imidazolate Frameworks: Next–Generation Materials for Energy–Efficient Gas Separations. *Chemistry–Sustainability–Energy–Materials*, 7(12):3202–3240, 2014.
- [9] M. H. Teplensky, M. Fantham, P. Li, T. C. Wang, J. P. Mehta, L. J. Young, P. Z. Moghadam, J. T. Hupp, O. K. Farha, C. F. Kaminski, and D. Fairen–Jimenez. Temperature Treatment of Highly Porous Zirconium–Containing Metal–Organic Frameworks Extends Drug Delivery Release. *Journal of the American Chemical Society*, 139(22):7522–7532, 2017.
- [10] Q. Li, A. J. Zaczek, T. M. Korter, J. A. Zeitler, and M. T. Ruggiero. Methyl–Rotation Dynamics in Metal–Organic Frameworks Probed with Terahertz Spectroscopy. *Chemical Communications*, 341:123–444, 2018.
- [11] K.-L. Hu, M. Kurmoo, Z. Wang, and S. Gao. Metal–Organic Perovskites: Synthesis, Structures, and Magnetic Properties of $[\text{C}(\text{NH}_2)_3][\text{M}^{\text{II}}(\text{HCOO})_3]$ (M=Mn, Fe, Co, Ni, Cu, and Zn; $\text{C}(\text{NH}_2)_3$ = Guanidinium). *Chemistry – A European Journal*, 15(44):12050–12064, 2009.
- [12] K. L. Svane and A. Walsh. Quantifying Thermal Disorder in Metal–Organic Frameworks: Lattice Dynamics and Molecular Dynamics Simulations of Hybrid Formate Perovskites. *The Journal of Physical Chemistry C*, 121(1):421–429, 2017.
- [13] M. Guo, H.-L. Cai, and R.-G. Xiong. Ferroelectric Metal Organic Framework (MOF). *Inorganic Chemistry Communications*, 13(12):1590–1598, 2010.
- [14] W. Li, Z. Zhang, E. G. Bithell, A. S. Batsanov, P. T. Barton, P. J. Saines, P. Jain Jain, C. J. Howard, M. A. Carpenter, and A. K. Cheetham. Ferroelasticity in a Metal–Organic Framework Perovskite; Towards a New Class of Multiferroics. *Acta Materialia*, 61(13):4928–4938, 2013.

- [15] M. Shen, Y. Zhang, H. Xu, and H. Ma. MOFs Based on the Application and Challenges of Perovskite Solar Cells. *iScience*, 24(9):103069, 2021.
- [16] D. Y. Heo, H. H. Do, S. H. Ahn, and S. Y. Kim. Metal–Organic Framework Materials for Perovskite Solar Cells. *Polymers*, 12(9):2061, 2020.
- [17] C.-C. Chueh, C.-I. Chen, Y.-A. Su, H. Konnerth, Y.-J. Gu, C.-W. Kung, and K. C.-W. Wu. Harnessing MOF Materials in Photovoltaic Devices: Recent Advances, Challenges, and Perspectives. *Journal of Materials Chemistry A*, 7:17079–17095, 2019.
- [18] Y. Roggo, P. Chalus, L. Maurer, C. Lema-Martinez, A. Edmond, and N. Jent. A Review of Near Infrared Spectroscopy and Chemometrics in Pharmaceutical Technologies. *Journal of Pharmaceutical and Biomedical Analysis*, 44(3):683–700, 2007.
- [19] S. Gaisford and A. B. M. Buanz. Pharmaceutical Physical Form Characterisation with Fast ($> 200 \text{ C min}^{-1}$) DSC heating rates. *Journal of Thermal Analysis and Calorimetry*, 106(1):221–226, 2011.
- [20] A. D. Bond. Pharmaceutical Crystallography: Is There a Devil in the Details? *CrytEngComm*, 14:2363–2366, 2012.
- [21] P. Bawuah and J. A. Zeitler. Advances in Terahertz Time-Domain Spectroscopy of Pharmaceutical Solids: A Review. *TrAC Trends in Analytical Chemistry*, 139:116272, 2021.
- [22] Q. Li, A. D. Bond, T. M. Korter, and J. A. Zeitler. New Insights into the Crystallographic Disorder in the Polymorphic Forms of Aspirin from Low-Frequency Vibrational Analysis. *Molecular Pharmaceutics*, 19(1):227–234, 2022.
- [23] E. M. Paiva, Q. Li, A. J. Zaczek, C. F. Pereira, J. J. R. Rohwedder, and J. A. Zeitler. Understanding the Metastability of Theophylline FIII by Means of Low-Frequency Vibrational Spectroscopy. *Molecular Pharmaceutics*, 18(9):3578–3587, 2021.

- [24] Q. Li, J. Kölbl, T. Threlfall, and J. A. Zeitler. Flow Cell to Study Crystallisation Processes In-Situ Using Terahertz Time-Domain Spectroscopy. *IEEE Transactions on Terahertz Science and Technology*, pages 1–1, 2021.
- [25] J. Kölbl, Q. Li, T. L. Threlfall, and J. A. Zeitler. Measuring Solute Concentration with Terahertz Time-Domain Spectroscopy in Single and Multiphase Systems. *Analytical Chemistry*, 94(3):1713–1716, 2022.
- [26] J. Sibik, M. J. Sargent, M. Franklin, and J. A. Zeitler. Crystallization and Phase Changes in Paracetamol from the Amorphous Solid to the Liquid Phase. *Molecular Pharmaceutics*, 11(4):1326–1334, 2014.
- [27] BRUKER. Terahertz Spectroscopy. <https://www.bruker.com/products/infrared-near-infrared-and-raman-spectroscopy/terahertz.html> (Accessed: 08/06/2018).
- [28] E. P. J. Parrott and J. A. Zeitler. Terahertz Time-Domain and Low-Frequency Raman Spectroscopy of Organic Materials. *Applied Spectroscopy*, 69(1):1–25, 2015.
- [29] J. A. Zeitler, D. A. Newnham, P. F. Taday, T. L. Threlfall, R. W. Lancaster, R. W. Berg, C. J. Strachan, M. Pepper, K. C. Gordon, and T. Rades. Characterization of Temperature-Induced Phase Transitions in Five Polymorphic Forms of Sulfathiazole by Terahertz Pulsed Spectroscopy and Differential Scanning Calorimetry. *Journal of Pharmaceutical Sciences*, 95(11):2486–2498, 2006.
- [30] J. A. Zeitler, K. Kogermann, J. Rantanen, T. Rades, P. F. Taday, M. Pepper, J. Aaltonen, and C. J. Strachan. Drug Hydrate Systems and Dehydration Processes Studied by Terahertz Pulsed Spectroscopy. *International Journal of Pharmaceutics*, 334(1):78–84, 2007.
- [31] A. R. Pallipurath, F. Civati, J. Sibik, C. Crowley, J. A. Zeitler, P. McArdle, and A. Erxleben. A Comprehensive Spectroscopic Study of the Polymorphs of Diflunisal

- and Their Phase Transformations. *International Journal of Pharmaceutics*, 528(1):312–321, 2017.
- [32] Y. C. Shen, T. Lo, P. F. Taday, B. E. Cole, W. R. Tribe, and M. C. Kemp. Detection and Identification of Explosives Using Terahertz Pulsed Spectroscopic Imaging. *Applied Physics Letters*, 86(24):241116, 2005.
- [33] D. G. Allis, D. A. Prokhorova, and T. M. Korter. Solid-State Modeling of the Terahertz Spectrum of the High Explosive HMX. *The Journal of Physical Chemistry A*, 110(5):1951–1959, 2006.
- [34] E. M. Kleist, C. L. K. Dandolo, J.-P. Guillet, P. Mounaix, and T. M. Korter. Terahertz Spectroscopy and Quantum Mechanical Simulations of Crystalline Copper-Containing Historical Pigments. *The Journal of Physical Chemistry A*, 123(6):1225–1232, 2019.
- [35] J. E. Lee, H. Lee, J. Kim, T. S. Jung, J. H. Kim, J. Kim, N. Y. Baek, Y. N. Song, H. H. Lee, and J. H. Kim. Terahertz Spectroscopic Analysis of the Vermilion Pigment in Free-Standing and Polyethylene-Mixed Forms. *ACS Omega*, 6(21):13802–13806, 2021.
- [36] R. Ulbricht, E. Hendry, J. Shan, T. F. Heinz, and M. Bonn. Carrier Dynamics in Semiconductors Studied with Time-Resolved Terahertz Spectroscopy. *Reviews of Modern Physics*, 83:543–586, 2011.
- [37] G. Schweicher, G. D’Avino, M. T. Ruggiero, D. J. Harkin, K. Broch, D. Venkateshvaran, G. Liu, A. Richard, C. Ruzié, J. Armstrong, A. R. Kennedy, K. Shankland, K. Takimiya, Y. H. Geerts, J. A. Zeitler, S. Fratini, and H. Sirringhaus. Chasing the “Killer” Phonon Mode for the Rational Design of Low-Disorder, High-Mobility Molecular Semiconductors. *Advanced Materials*, 31(43):1902407, 2019.
- [38] T. Ikeda, A. Matsushita, M. Tatsuno, Y. Minami, M. Yamaguchi, K. Yamamoto, M. Tani, and M. Hangyo. Investigation of Inflammable Liquids by Terahertz Spectroscopy. *Applied Physics Letters*, 87(3):034105, 2005.

- [39] M. Batens, T. A. Shmool, J. Massant, J. A. Zeitler, and G. Van den Mooter. Advancing Predictions of Protein Stability in the Solid State. *Physical Chemistry Chemical Physics*, 22:17247–17254, 2020.
- [40] H. Lindley-Hatcher, R. I. Stantchev, X. Chen, A. I. Hernandez-Serrano, J. Hardwicke, and E. Pickwell-MacPherson. Real Time THz Imaging—Opportunities and Challenges for Skin Cancer Detection. *Applied Physics Letters*, 118(23):230501, 2021.
- [41] T. A. Shmool, P.J. Woodhams, M. Leutzsch, A. D. Stephens, M. U. Gaimann, M. D. Mantle, G. S. Kaminski Schierle, C. F. van der Walle, and J. A. Zeitler. Observation of High-Temperature Macromolecular Confinement in Lyophilised Protein Formulations Using Terahertz Spectroscopy. *International Journal of Pharmaceutics: X*, 1:100022, 2019.
- [42] T. Y. Chang, T. J. Bridges, and E. G. Burkhardt. cw Submillimeter Laser Action in Optically Pumped Methyl Fluoride, Methyl Alcohol, and Vinyl Chloride Gases. *Applied Physics Letters*, 17(6):249–251, 1970.
- [43] P. Chevalier, A. Amirzhan, F. Wang, M. Piccardo, S. G. Johnson, F. Capasso, and H. O. Everitt. Widely Tunable Compact Terahertz Gas Lasers. *Science*, 366(6467):856–860, 2019.
- [44] P. R. Griffiths and C. Homes. Instrumentation for Far-infrared Spectroscopy. https://infrared.phy.bnl.gov/pdf/homes/homes_01ins.pdf(Accessed: 27/12/2021).
- [45] 4. Detection of Far-Infrared Radiation. In L. C. Robinson, editor, *Physical Principles of Far-Infrared Radiation*, volume 10 of *Methods in Experimental Physics*, pages 157–228. Academic Press, 1973.
- [46] THz Detectors. *Progress in Quantum Electronics*, 34(5):278–347, 2010.
- [47] D. H. Auston, K. P. Cheung, and P. R. Smith. Picosecond Photoconducting Hertzian Dipoles. *Applied Physics Letters*, 45(3):284, 1998.

- [48] D. H. Auston, K. P. Cheung, J. A. Valdmanis, and D. A. Kleinman. Cherenkov Radiation from Femtosecond Optical Pulses in Electro-Optic Media. *Physical Review Letters*, 53(16):1555–1558, 1984.
- [49] P. R. Smith, D. H. Auston, and M. C. Nuss. Subpicosecond Photoconducting Dipole Antennas. *IEEE Journal of Quantum Electronics*, 24(2):255–260, 1988.
- [50] Ch. Fattinger and D. Grischkowsky. Point Source Terahertz Optics. *Applied Physics Letters*, 53(16):1480, 1998.
- [51] K. E. Peiponen, J. A. Zeitler, and M. Kuwata-Gonokami. *Terahertz Spectroscopy and Imaging*. Springer Series in Optical Sciences. 2013.
- [52] C. A. Schmuttenmaer. Exploring Dynamics in the Far-Infrared with Terahertz Spectroscopy. *Chemical Reviews*, 104(4):1759–1780, 2004.
- [53] D. You, R. R. Jones, P. H. Bucksbaum, and D. R. Dykaar. Generation of High-Power Sub-Single-Cycle 500-fs Electromagnetic Pulses. *Optical Letters*, 18(4):290–292, 1993.
- [54] T. Löffler, F. Jacob, and H. G. Roskos. Generation of Terahertz Pulses by Photoionization of Electrically Biased Air. *Applied Physics Letters*, 77(3):453–455, 2000.
- [55] D. J. Cook and R. M. Hochstrasser. Intense Rerahertz Pulses by Four-Wave Rectification in Air. *Optical Letters*, 25(16):1210–1212, 2000.
- [56] K.-J. Kim and A. Sessler. Free-Electron Lasers: Present Status and Future Prospects. *Science*, 250(4977):88–93, 1990.
- [57] G. Scalari, C. Walther, M. Fischer, R. Terazzi, H. Beere, D. Ritchie, and J. Faist. THz and Sub-THz Quantum Cascade Lasers. *Laser & Photonics Reviews*, 3(1-2):45–66, 2009.
- [58] H. Hertz. *Eletric Waves*. Dover, New York, 1962.

- [59] G. Mourou, C. V. Stancampiano, A. Antonetti, and A. Orszag. Picosecond Microwave Pulses Generated with a Subpicosecond Laser-Driven Semiconductor Switch. *Applied Physics Letters*, 39(4):295, 1998.
- [60] J. Karin, P. Downey, and R. J. Martin. Radiation from Picosecond Photoconductors in Microstrip Transmission Lines. *IEEE Journal of Quantum Electronics*, 22(5):677–681, 1986.
- [61] A. P. DeFonzo and C. R. Lutz. Optoelectronic Transmission and Reception of Ultra-short Electrical Pulses. *Applied Physics Letters*, 51(4):212, 1998.
- [62] Ch. Fattinger and D. Grischkowsky. Terahertz Beams. *Applied Physics Letters*, 54(6):490, 1998.
- [63] N. M. Burford and M. El-Shenawee. Review of Terahertz Photoconductive Antenna Technology. *Optical Engineering*, 56(1):010901–010901, 2017.
- [64] P. U. Jepsen, D. G. Cooke, and M. Koch. Terahertz Spectroscopy and Imaging—Modern Techniques and Applications. *Laser & Photonics Reviews*, 5(1):124–166, 2011.
- [65] I. S. Gregory, C. Baker, W. R. Tribe, M. J. Evans, H. E. Beere, E. H. Linfield, A. G. Davies, and M. Missous. High Resistivity Annealed Low-Temperature GaAs with 100 fs Lifetimes. *Applied Physics Letters*, 83(20):4199–4201, 2003.
- [66] A. C. Warren, J. M. Woodall, J. L. Freeouf, D. Grischkowsky, D. T. McInturff, M. R. Melloch, and N. Otsuka. Arsenic Precipitates and the Semi-Insulating Properties of GaAs Buffer Layers Grown by Low-Temperature Molecular Beam Epitaxy. *Applied Physics Letters*, 57(13):1331–1333, 1990.
- [67] Y. Kostoulas, L. J. Waxer, I. A. Walmsley, G. W. Wicks, and P. M. Fauchet. Femtosecond Carrier Dynamics in Low-Temperature-Grown Indium Phosphide. *Applied Physics Letters*, 66(14):1821–1823, 1995.

- [68] I. Wilke, R. Ascazubi, H. Lu, and W. J. Schaff. Terahertz Emission from Silicon and Magnesium Doped Indium Nitride. *Applied Physics Letters*, 93(22):221113, 2008.
- [69] M. van Exter, Ch. Fattinger, and D. Grischkowsky. High-Brightness Terahertz Beams Characterized with an Ultrafast Detector. *Applied Physics Letters*, 55(4):337–339, 1989.
- [70] H. Harde and D. Grischkowsky. Coherent Transients Excited by Subpicosecond Pulses of Terahertz Radiation. *Journal of the Optical of America B*, 8(8):1642–1651, 1991.
- [71] X.-C. Zhang. Generation and Detection of Terahertz Electromagnetic Pulses from Semiconductors with Femtosecond Optics. *Journal of Luminescence*, 66–67:488–492, 1995.
- [72] M. Tani, S. Matsuura, K. Sakai, and S. Nakashima. Emission Characteristics of Photoconductive Antennas Based on Low-Temperature-Grown GaAs and Semi-Insulating GaAs. *Applied Optics*, 36(30):7853–7859, 1997.
- [73] BATOP optoelectronics. PCA-Photoconductive Antenna. https://www.batop.de/information/PCA_infos.html(Accessed: 27/12/2021).
- [74] M. Bass, P. A. Franken, J. F. Ward, and G. Weinreich. Optical Rectification. *Physical Review Letters*, 9(11):446, 1962.
- [75] D.H. Auston and M.C. Nuss. Electrooptical Generation and Detection of Femtosecond Electrical Transients. *IEEE Journal of Quantum Electronics*, 24(2):184–197, 1988.
- [76] G. Gallot, J. Zhang, R. W. McGowan, T.-I. Jeon, and D. Grischkowsky. Measurements of the THz Absorption and Dispersion of ZnTe and Their Relevance to the Electro-Optic Detection of THz Radiation. *Applied Physics Letters*, 74(23):3450–3452, 1999.
- [77] T. J. Carrig, G. Rodriguez, T. S. Clement, A. J. Taylor, and K. R. Stewart. Scaling of Terahertz Radiation via Optical Rectification in Electro-Optic Crystals. *Applied Physics Letters*, 66(2):121–123, 1995.

- [78] A. Rice, Y. Jin, X. F. Ma, X.C. Zhang, D. Bliss, J. Larkin, and M. Alexander. Terahertz Optical Rectification from $\langle 110 \rangle$ Zinc-Blende Crystals. *Applied Physics Letters*, 64(11):1324–1326, 1994.
- [79] P. Y. Han, M. Tani, F. Pan, and X.-C. Zhang. Use of the Organic Crystal DAST for Terahertz Beam Applications. *Optical Letters*, 25(9):675–677, 2000.
- [80] L. Xu, X.C. Zhang, and D. H. Auston. Terahertz Beam Generation by Femtosecond Optical Pulses in Electro-Optic Materials. *Applied Physics Letters*, 61(15):1784–1786, 1992.
- [81] Q. Chen and X.-C. Zhang. Polarization Modulation in Optoelectronic Generation and Detection of Terahertz Beams. *Applied Physics Letters*, 74(23):3435–3437, 1999.
- [82] J. Li and J. Li. Terahertz (THz) Generator and Detection. *Electrical Science & Engineering*, 02(01):11–25, 2020.
- [83] J. A. Zeitler, P. F. Taday, D. A. Newnham, M. Pepper, K. C. Gordon, and T. Rades. Terahertz Pulsed Spectroscopy and Imaging in the Pharmaceutical Setting—A Review. *Journal of Pharmacy and Pharmacology*, 59(2):209–223, 2010.
- [84] J. Sibik, S. R. Elliott, and J. A. Zeitler. Thermal Decoupling of Molecular-Relaxation Processes from the Vibrational Density of States at Terahertz Frequencies in Supercooled Hydrogen-Bonded Liquids. *The Journal of Physical Chemistry Letters*, 5(11):1968–1972, 2014.
- [85] R. de L. Kronig. On the Theory of Dispersion of X-Rays. *Journal of the Optical Society of America*, 12(6):547–557, 1926.
- [86] Rotation and Vibration of Diatomic Molecules. http://www.iiserpune.ac.in/~bhasbapat/phy420_files/Demtroeder_rotovibrazioni.pdf (Accessed: 01/08/2021).

- [87] E. B. Wilson, J. C. Decius, and P. C. Cross. *Molecular Vibrations: The Theory of Infrared and Raman Vibrational Spectra*. Dover Publications, New York, 1980.
- [88] T. Theophanides. *Fourier Transform Infrared Spectroscopy: Industrial Chemical and Biochemical Applications*. D.Reidel Publishing Company, 1984.
- [89] R. Li, C. D’Agostino, J. McGregor, M. D. Mantle, J. A. Zeitler, and L. F. Gladden. Mesoscopic Structuring and Dynamics of Alcohol/Water Solutions Probed by Terahertz Time-Domain Spectroscopy and Pulsed Field Gradient Nuclear Magnetic Resonance. *The Journal of Physical Chemistry B*, 118(34):10156–10166, 2014.
- [90] J. P. Poley. Microwave Dispersion of Some Polar Liquids. *Applied Scientific Research, Section A*, 4(1):337–387, 1955.
- [91] G. P. Johari. Molecular Inertial effects in Liquids: Poley Absorption, Collision-Induced Absorption, Low-Frequency Raman Spectrum and Boson Peaks. *Journal of Non-Crystalline Solids*, 307–310:114–127, 2002.
- [92] D. A. Turton, J. Hunger, A. Stoppa, A. Thoman, M. Candelaresi, G. Hefter, M. Walther, R. Buchner, and K. Wynne. Rattling the Rage: Micro- to Mesoscopic Structure in Liquids as Simple as Argon and as Complicated as Water. *Journal of Molecular Liquids*, 159(1):2–8, 2011.
- [93] G. W. Chantry and H. A. Gebbie. Sub-Millimetre Wave Spectra of Polar Liquids. *Nature*, 208(5008):378–378, 1965.
- [94] U. Strom, J. R. Hendrickson, R. J. Wagner, and P. C. Taylor. Disorder-Induced Far Infrared Absorption in Amorphous Materials. *Solid State Communications*, 15(11):1871–1875, 1974.
- [95] C. J. Reid and M. W. Evans. Dielectric and Far Infrared Study of Solutions in the Glassy State from 100 Hz to 10 THz: Discovery and Characterization of the Universal γ Process. *The Journal of Chemical Physics*, 76(5):2576–2584, 1982.

- [96] B. Ruta, G. Baldi, V. M. Giordano, L. Orsingher, S. Rols, F. Scarponi, and G. Monaco. Communication: High-Frequency Acoustic Excitations and Boson Peak in Glasses: A Study of Their Temperature Dependence. *The Journal of Chemical Physics*, 133(4):041101, 2010.
- [97] J. Sibik and J. A. Zeitler. Direct Measurement of Molecular Mobility and Crystallisation of Amorphous Pharmaceuticals Using Terahertz Spectroscopy. *Advanced Drug Delivery Reviews*, 100:147–157, 2016.
- [98] A. Cavagna. Supercooled Liquids for Pedestrians. *Physics Reports*, 476(4):51–124, 2009.
- [99] A. I. McIntosh, B. Yang, S. M. Goldup, M. Watkinson, and R. S. Donnan. Crystallization of Amorphous Lactose at High Humidity Studied by Terahertz Time-Domain Spectroscopy. *Chemical Physics Letters*, 558:104–108, 2013.
- [100] S. N. Taraskin, S. I. Simdyankin, S. R. Elliott, J. R. Neilson, and T. Lo. Universal Features of Terahertz Absorption in Disordered Materials. *Physical Review Letters*, 97(5):055504, 2006.
- [101] J. A. Zeitler, P. F. Taday, M. Pepper, and T. Rades. Relaxation and Crystallization of Amorphous Carbamazepine Studied by Terahertz Pulsed Spectroscopy. *Journal of Pharmaceutical Sciences*, 96(10):2703–2709, 2007.
- [102] W. Götze. *Complex Dynamics of Glass-Forming Liquids a Mode-Coupling Theory*. Oxford University Press, Oxford; New York, 2009.
- [103] S. Kalepu and V. Nekkanti. Insoluble Drug Delivery Strategies: Review of Recent Advances and Business Prospects. *Acta Pharmaceutica Sinica B*, 5(5):442–453, 2015.
- [104] J. Sibik, K. Löbmann, T. Rades, and J. A. Zeitler. Predicting Crystallization of Amorphous Drugs with Terahertz Spectroscopy. *Molecular Pharmaceutics*, 12(8):3062–3068, 2015.

- [105] C. Ronne, L. Thrane, P.-O. Astrand, A. Wallqvist, K. V. Mikkelsen, and S. R. Keiding. Investigation of the Temperature Dependence of Dielectric Relaxation in Liquid Water by THz Reflection Spectroscopy and Molecular Dynamics Simulation. *The Journal of Chemical Physics*, 107(14):5319–5331, 1997.
- [106] D. S. Venables and C. A. Schmuttenmaer. Spectroscopy and Dynamics of Mixtures of Water with Acetone, Acetonitrile, and Methanol. *The Journal of Chemical Physics*, 113(24):11222–11236, 2000.
- [107] H. Yada, M. Nagai, and K. Tanaka. Origin of the Fast Relaxation Component of Water and Heavy Water Revealed by Terahertz Time-Domain Attenuated Total Reflection Spectroscopy. *Chemical Physics Letters*, 464(4):166–170, 2008.
- [108] H. Yada, M. Nagai, and K. Tanaka. The Intermolecular Stretching Vibration Mode in Water Isotopes Investigated with Broadband Terahertz Time-Domain Spectroscopy. *Chemical Physics Letters*, 473(4):279–283, 2009.
- [109] K. J. Tielrooij, D. Paparo, L. Piatkowski, H. J. Bakker, and M. Bonn. Dielectric Relaxation Dynamics of Water in Model Membranes Probed by Terahertz Spectroscopy. *Biophysical Journal*, 97(9):2484–2492, 2009.
- [110] K.-J. Tielrooij, J. Hunger, R. Buchner, M. Bonn, and H. J. Bakker. Influence of Concentration and Temperature on the Dynamics of Water in the Hydrophobic Hydration Shell of Tetramethylurea. *Journal of the American Chemical Society*, 132(44):15671–15678, 2010.
- [111] N. Y. Tan, R. Li, P. Bräuer, C. D’Agostino, L. F. Gladden, and J. A. Zeitler. Probing Hydrogen-Bonding in Binary Liquid Mixtures with Terahertz Time-Domain Spectroscopy: A Comparison of Debye and Absorption Analysis. *Physical Chemistry Chemical Physics*, 17:5999–6008, 2015.
- [112] U. Heugen, G. Schwaab, E. Bründermann, M. Heyden, X. Yu, D. M. Leitner, and M. Havenith. Solute-Induced Retardation of Water Dynamics Probed Directly by Ter-

- ahertz Spectroscopy. *Proceedings of the National Academy of Sciences*, 103(33):12301–12306, 2006.
- [113] D. M. Leitner, M. Gruebele, and M. Havenith. Solvation Dynamics of Biomolecules: Modeling and Terahertz Experiments. *HFSP Journal*, 2(6):314–323, 2008.
- [114] J. Sun, G. Niehues, H. Forbert, D. Decka, G. Schwaab, D. Marx, and M. Havenith. Understanding THz Spectra of Aqueous Solutions: Glycine in Light and Heavy Water. *Journal of the American Chemical Society*, 136(13):5031–5038, 2014.
- [115] S. Funkner, G. Niehues, D. A. Schmidt, M. Heyden, G. Schwaab, K. M. Callahan, D. J. Tobias, and M. Havenith. Watching the Low-Frequency Motions in Aqueous Salt Solutions: The Terahertz Vibrational Signatures of Hydrated Ions. *Journal of the American Chemical Society*, 134(2):1030–1035, 2012.
- [116] M. R. Ryder, B. Civalleri, T. D. Bennett, S. Henke, S. Rudić, G. Cinque, F. Fernandez-Alonso, and J. C. Tan. Identifying the Role of Terahertz Vibrations in Metal–Organic Frameworks: From Gate–Opening Phenomenon to Shear–Driven Structural Destabilization. *Physical Review Letters*, 113(21):215–502, 2014.
- [117] N. Y. Tan, M. T. Ruggiero, C. Orellana-Tavra, T. Tian, A. D. Bond, T. M. Korter, D. Fairen-Jimenez, and J. A. Zeitler. Investigation of the Terahertz Vibrational Modes of ZIF-8 and ZIF-90 with Terahertz Time-Domain Spectroscopy. *Chemical Communications*, 51(89):16037–16040, 2015.
- [118] K. Kawase, Y. Ogawa, Y. Watanabe, and H. Inoue. Non-Destructive Terahertz Imaging of Illicit Drugs Using Spectral Fingerprints. *Optics Express*, 11(20):2549–2554, 2003.
- [119] S.-Y. Lin. An Overview of Famotidine Polymorphs: Solid-State Characteristics, Thermodynamics, Polymorphic Transformation and Quality Control. *Pharmaceutical Research*, 31(7):1619–1631, 2014.

- [120] M. J. Turner, S. P. Thomas, M. W. Shi, D. Jayatilaka, and M. A. Spackman. Energy Frameworks: Insights into Interaction Anisotropy and the Mechanical Properties of Molecular Crystals. *Chemical Communications*, 51(18):3735–3738, 2015.
- [121] M. Walther, B. Fischer, M. Schall, H. Helm, and P. U. Jepsen. Far-Infrared Vibrational Spectra of All-Trans, 9-Cis and 13-Cis Retinal Measured by THz Time-Domain Spectroscopy. *Chemical Physics Letters*, 332(3):389–395, 2000.
- [122] M. Walther, B. M. Fischer, and P. U. Jepsen. Noncovalent Intermolecular Forces in Polycrystalline and Amorphous Saccharides in the Far Infrared. *Chemical Physics*, 288(2):261–268, 2003.
- [123] P. F. Taday, I. V. Bradley, D. D. Arnone, and M. Pepper. Using Terahertz Pulse Spectroscopy to Study the Crystalline Structure of a Drug: A Case Study of the Polymorphs of Ranitidine Hydrochloride. *Journal of Pharmaceutical Sciences*, 92(4):831–838, 2003.
- [124] P. F. Taday. Applications of Terahertz Spectroscopy to Pharmaceutical Sciences. *Philosophical Transactions. Series A, Mathematical, Physical, and Engineering Sciences*, 362(1815):351–63– discussion 363–4, 2004.
- [125] C. J. Strachan, P. F. Taday, D. A. Newnham, K. C. Gordon, J. A. Zeitler, M. Pepper, and T. Rades. Using Terahertz Pulsed Spectroscopy to Quantify Pharmaceutical Polymorphism and Crystallinity. *Journal of Pharmaceutical Sciences*, 94(4):837–846, 2005.
- [126] H.-B. Liu and X.-C. Zhang. Dehydration Kinetics of D-Glucose Monohydrate Studied Using THz Time-Domain Spectroscopy. *Chemical Physics Letters*, 429(1):229–233, 2006.
- [127] M. T. Ruggiero, T. Bardon, M. Strlič, P. F. Taday, and T. M. Korter. Assignment of the Terahertz Spectra of Crystalline Copper Sulfate and its Hydrates via Solid-State Density Functional Theory. *The Journal of Physical Chemistry A*, 118(43):10101–10108, 2014.

- [128] M. T. Ruggiero, T. Bardon, M. Strlič, P. F. Taday, and T. M. Korter. The Role of Terahertz Polariton Absorption in the Characterization of Crystalline Iron Sulfate Hydrates. *Physical Chemistry Chemical Physics*, 17:9326–9334, 2015.
- [129] L. Chen, G. Ren, L. Liu, P. Guo, E. Wang, L. Zhou, Z. Zhu, J. Zhang, B. Yang, W. Zhang, Y. Li, W. Zhang, Y. Gao, H. Zhao, and J. Han. Terahertz Signatures of Hydrate Formation in Alkali Halide Solutions. *The Journal of Physical Chemistry Letters*, 11(17):7146–7152, 2020.
- [130] J. A. Zeitler, D. A. Newnham, P. F. Taday, C. J. Strachan, M. Pepper, K. C. Gordon, and T. Rades. Temperature Dependent Terahertz Pulsed Spectroscopy of Carbamazepine. *Thermochimica Acta*, 436(1):71–77, 2005.
- [131] P. C. Upadhyaya, K. L. Nguyen, Y. C. Shen, J. Obradovic, K. Fukushige, R. Griffiths, L. F. Gladden, A. G. Davies, and E. H. Linfield. Characterization of Crystalline Phase-Transformations in Theophylline by Time-Domain Terahertz Spectroscopy. *Spectroscopy Letters*, 39(3):215–224, 2006.
- [132] M. T. Ruggiero, J. A. Zeitler, and T. M. Korter. Concomitant Polymorphism and the Martensitic-Like Transformation of an Organic Crystal. *Physical Chemistry Chemical Physics*, 19:28502–28506, 2017.
- [133] M. T. Ruggiero, J. J. Sutton, S. J. Fraser-Miller, A. J. Zaczek, T. M. Korter, K. C. Gordon, and J. A. Zeitler. Revisiting the Thermodynamic Stability of Indomethacin Polymorphs with Low-Frequency Vibrational Spectroscopy and Quantum Mechanical Simulations. *Crystal Growth & Design*, 18(11):6513–6520, 2018.
- [134] M. T. Ruggiero, W. Zhang, A. D. Bond, D. M. Mittleman, and J. A. Zeitler. Uncovering the Connection Between Low-Frequency Dynamics and Phase Transformation Phenomena in Molecular Solids. *Physical Review Letters*, 120:196002, 2018.
- [135] R. Li, J. A. Zeitler, D. Tomerini, E. P. J. Parrott, L. F. Gladden, and G. M. Day. A Study into the Effect of Subtle Structural Details and Disorder on the Terahertz

- Spectrum of Crystalline Benzoic Acid. *Physical Chemistry Chemical Physics*, 12:5329–5340, 2010.
- [136] S. P. Delaney, D. Pan, M. Galella, S. X. Yin, and T. M. Korter. Understanding the Origins of Conformational Disorder in the Crystalline Polymorphs of Irbesartan. *Crystal Growth & Design*, 12(10):5017–5024, 2012.
- [137] D. V. Nickel, S. P. Delaney, H. Bian, J. Zheng, T. M. Korter, and D. M. Mittleman. Terahertz Vibrational Modes of the Rigid Crystal Phase of Succinonitrile. *The Journal of Physical Chemistry A*, 118(13):2442–2446, 2014.
- [138] D. V. Nickel, M. T. Ruggiero, T. M. Korter, and D. M. Mittleman. Terahertz Disorder–Localized Rotational Modes and Lattice Vibrational Modes in the Orientationally–Disordered and Ordered Phases of Camphor. *Physical Chemistry Chemical Physics*, 17:6734–6740, 2015.
- [139] F. Zhang, H.-W. Wang, K. Tominaga, M. Hayashi, and T. Sasaki. Terahertz Fingerprints of Short–Range Correlations of Disordered Atoms in Diflunisal. *The Journal of Physical Chemistry A*, 123(21):4555–4564, 2019.
- [140] R. May and P. F. Taday. Crystallization of Sucrose Monitored by Terahertz Pulsed Spectroscopy. In *2013 38th International Conference on Infrared, Millimeter, and Terahertz Waves (IRMMW-THz)*, pages 1–1, 2013.
- [141] A. Soltani, D. Gebauer, L. Duscheck, B. M. Fischer, H. Cölfen, and M. Koch. Crystallization Caught in the Act with Terahertz Spectroscopy: Non-Classical Pathway for l-(+)-Tartaric Acid. *Chemistry*, 23(57):14128–14132, 2017.
- [142] K. L. Nguyen, T. Frišćić, G. M. Day, L. F. Gladden, and W. Jones. Terahertz Time–Domain Spectroscopy and the Quantitative Monitoring of Mechanochemical Cocrystal Formation. *Nature Materials*, 6:206–209, 2007.
- [143] E. P. J. Parrott, J. A. Zeitler, T. Frii, M. Pepper, W. Jones, G. M. Day, and L. F. Gladden. Testing the Sensitivity of Terahertz Spectroscopy to Changes in Molecular

- and Supramolecular Structure: A Study of Structurally Similar Cocrystals. *Crystal Growth & Design*, 9(3):1452–1460, 2009.
- [144] S. P. Delaney and T. M. Korter. Terahertz Spectroscopy and Computational Investigation of the Flufenamic Acid/Nicotinamide Cocrystal. *The Journal of Physical Chemistry A*, 119(13):3269–3276, 2015.
- [145] M. P. Davis, M. Mohara, K. Shimura, and T. M. Korter. Simulation and Assignment of the Terahertz Vibrational Spectra of Enalapril Maleate Cocrystal Polymorphs. *The Journal of Physical Chemistry A*, 124(47):9793–9800, 2020.
- [146] Y. Han, Y. Pan, J. Lv, W. Guo, and J. Wang. Powder Grinding Preparation of Co-amorphous β -Azelnidipine and Maleic Acid Combination: Molecular Interactions and Physicochemical Properties. *Powder Technology*, 291:110–120, 2016.
- [147] R. Tanaka, S. Ishihara, T. Sasaki, Y. Hattori, and M. Otsuka. Injection-Molded Coamorphous Tablets: Analysis of Intermolecular Interaction and Crystallization Propensity. *Journal of Pharmaceutical Sciences*, 110(9):3289–3297, 2021.
- [148] T. Tanno, Y. Watanabe, K. Umeno, A. Matsuoka, H. Matsumura, M. Odaka, and N. Ogawa. In Situ Observation of Gas Adsorption onto ZIF-8 Using Terahertz Waves. *Journal of Physical Chemistry C*, 121(33):17921–17924, 2017.
- [149] W Zhang, J. Maul, D. Vulpe, P. Z. Moghadam, D. Fairen-Jimenez, D. M. Mittleman, J. A. Zeitler, A. Erba, and M. T. Ruggiero. Probing the Mechanochemistry of Metal–Organic Frameworks with Low–Frequency Vibrational Spectroscopy. *The Journal of Physical Chemistry C*, 122(48):27442–27450, 2018.
- [150] K. Schröck, F. Schröder, M. Heyden, R. A. Fischer, and M. Havenith. Characterization of Interfacial Water in MOF-5 ($\text{Zn}_4(\text{O})(\text{BDC})_3$)—A Combined Spectroscopic and Theoretical Study. *Physical Chemistry Chemical Physics*, 10:4732–4739, 2008.
- [151] B. Pattengale, J. Neu, S. Ostresh, G. Hu, J. A. Spies, R. Okabe, G. W. Brudvig, and C. A. Schmuttenmaer. Metal–Organic Framework Photoconductivity via

- Time-Resolved Terahertz Spectroscopy. *Journal of the American Chemical Society*, 141(25):9793–9797, 2019.
- [152] J. A. Spies, J. Neu, U. T. Tayvah, M. D. Capobianco, B. Pattengale, S. Ostresh, and C. A. Schmuttenmaer. Terahertz Spectroscopy of Emerging Materials. *The Journal of Physical Chemistry C*, 124(41):22335–22346, 2020.
- [153] G. J. O. Beran. Modelling Polymorphic Molecular Crystals with Electronic Structure Theory. *Chemical Reviews*, 116(9):5567–5613, 2016.
- [154] D. C. Rapaport. *The Art of Molecular Dynamics Simulation*. Cambridge University Press, 2nd edition, 2004.
- [155] S. J. Clark, M. D. Segall, C. J. Pickard, P. J. Hasnip, M. J. Probert, K. Refson, and M. C. Payne. First Principles Methods Using CASTEP. *Zeitschrift für Kristallographie*, 220(5-6):567–570, 2005.
- [156] G. Kresse and J. Furthmüller. Efficient Iterative Schemes for Ab Initio Total-Energy Calculations Using a Plane-Wave Basis Set. *Physical Review B*, 54:11169–11186, 1996.
- [157] M. J. Frisch, G. W. Trucks, H. B. Schlegel, G. E. Scuseria, M. A. Robb, J. R. Cheeseman, G. Scalmani, V. Barone, G. A. Petersson, H. Nakatsuji, X. Li, M. Caricato, A. V. Marenich, J. Bloino, B. G. Janesko, R. Gomperts, B. Mennucci, H. P. Hratchian, J. V. Ortiz, A. F. Izmaylov, J. L. Sonnenberg, D. Williams-Young, F. Ding, F. Lipparini, F. Egidi, J. Goings, B. Peng, A. Petrone, T. Henderson, D. Ranasinghe, V. G. Zakrzewski, J. Gao, N. Rega, G. Zheng, W. Liang, M. Hada, M. Ehara, K. Toyota, R. Fukuda, J. Hasegawa, M. Ishida, T. Nakajima, Y. Honda, O. Kitao, H. Nakai, T. Vreven, K. Throssell, J. A. Montgomery, J. E. Peralta, F. Ogliaro, M. J. Bearpark, J. J. Heyd, E. N. Brothers, K. N. Kudin, V. N. Staroverov, T. A. Keith, R. Kobayashi, J. Normand, K. Raghavachari, A. P. Rendell, J. C. Burant, S. S. Iyengar, J. Tomasi, M. Cossi, J. M. Millam, M. Klene, C. Adamo, R. Cammi, J. W. Ochterski, R. L. Mar-

- tin, K. Morokuma, O. Farkas, J. B. Foresman, and D. J. Fox. Gaussian16 Revision C.01, 2016. Gaussian Inc. Wallingford CT.
- [158] T. D. Kühne, M. Iannuzzi, M. Del Ben, V. V. Rybkin, P. Seewald, F. Stein, T. Laino, R. Z. Khaliullin, O. Schütt, F. Schiffmann, D. Golze, J. Wilhelm, S. Chulkov, M. H. Bani-Hashemian, V. Weber, U. Bortnik, M. Taillefumier, A. S. Jakobovits, A. Lazzaro, H. Pabst, T. Müller, R. Schade, M. Guidon, S. Andermatt, N. Holmberg, G. K. Schenter, A. Hehn, A. Bussy, F. Belleflamme, G. Tabacchi, A. Glöβ, M. Lass, I. Bethune, C. J. Mundy, C. Plessl, M. Watkins, J. VandeVondele, M. Krack, and J. Hutter. CP2K: An Electronic Structure and Molecular Dynamics Software Package—Quickstep: Efficient and Accurate Electronic Structure Calculations. *The Journal of Chemical Physics*, 152(19):194103, 2020.
- [159] R. Dovesi, A. Erba, R. Orlando, C. M. Zicovich Wilson, B. Civalleri, L. Maschio, M. Rérat, S. Casassa, J. Baima, S. Salustro, and B. Kirtman. Quantum–Mechanical Condensed Matter Simulations with CRYSTAL. *WIREs Computational Molecular Science*, 110(39):e1360, 2018.
- [160] D. Morin. Introduction to Quantum Mechanics. https://scholar.harvard.edu/files/david-morin/files/waves_quantum.pdf(Accessed: 04/01/2022).
- [161] L. De Broglie. The Reinterpretation of Wave Mechanics. *Foundations of Physics*, 1(1):5–15, 1970.
- [162] W. Heisenberg. Mehrkörperproblem und Resonanz in der Quantenmechanik. *Zeitschrift für Physik*, 38, 1926.
- [163] E. Schrödinger. An Undulatory Theory of the Mechanics of Atoms and Molecules. *Physical Review*, 28(6):1049, 1926.
- [164] R. M. Martin. *Electronic Structure: Basic Theory and Practical Methods*. Cambridge University Press, UK, 2004.

- [165] M. Born and R. Oppenheimer. Zur Quantentheorie der Moleküle. *Annalen der Physik*, 389(20):457–484, 1927.
- [166] N. S. Ostlund and A. Szabo. *Modern Quantum Chemistry: Introduction to Advanced Electronic Structure Theory*. Dover Publications, 1996.
- [167] I. Ekeland. On the Variational Principle. *Journal of Mathematical Analysis and Applications*, 47(2):324–353, 1974.
- [168] D. S. Sholl and N.J. Hoboken. *Density Functional Theory a Practical Introduction*. Wiley, 2009.
- [169] W. Pauli. Über den Zusammenhang des Abschlusses der Elektronengruppen im Atom mit der Komplexstruktur der Spektren. *Zeitschrift für Physik*, 31:765–783, 1925.
- [170] D. R. Hartree. The Wave Mechanics of an Atom with a Non-Coulomb Central Field. Part II. Some Results and Discussion. *Mathematical Proceedings of the Cambridge Philosophical Society*, 24(1):111–132, 1928.
- [171] V. Fock. Näherungsmethode zur Lösung des Quantenmechanischen Mehrkörperproblems. *Zeitschrift für Physik*, 61, 1930.
- [172] V. Fock. “Selfconsistent Field” mit Austausch für Natrium. *Zeitschrift für Physik*, 62(11):795–805, 1930.
- [173] D. R. Hartree and W. Hartree. Self-Consistent Field, with Exchange, for Beryllium. *Proceedings of the Royal Society of London. Series A – Mathematical and Physical Sciences*, 150(869):9–33, 1935.
- [174] L. H. Thomas. The Calculation of Atomic Fields. *Mathematical Proceedings of the Cambridge Philosophical Society*, 23(5):542–548, 1927.
- [175] E. Fermi. Un Metodo Statistico per La Determinazione di Alcune Priorietà Dell’atomo. *Endiconti: Accademia Nazinale del Lincei*, 6:602–607, 1927.

- [176] P. A. M. Dirac. Note on Exchange Phenomena in the Thomas Atom. *Mathematical Proceedings of the Cambridge Philosophical Society*, 26(3):376–385, 1930.
- [177] E. Teller. On the Stability of Molecules in the Thomas-Fermi Theory. *Reviews of Modern Physics*, 34(4):627–631, 1962.
- [178] P. Hohenberg and W. Kohn. Inhomogeneous Electron Gas. *Physical Review*, 136(3B):B864, 1964.
- [179] W. Kohn and L. J. Sham. Self-Consistent Equations Including Exchange and Correlation Effects. *Physical Review*, 140(4A):A1133–A1138, 1965.
- [180] J. P. Perdew and Y. Wang. Accurate and Simple Analytic Representation of the Electron-Gas Correlation Energy. *Physical Review B*, 45(23):13244, 1992.
- [181] J. P. Perdew, K. Burke, and M. Ernzerhof. Generalized Gradient Approximation Made Simple. *Physical Review Letters*, 77(18):3865–3868, 1996.
- [182] J. Tao, J. P. Perdew, V. N. Staroverov, and G. E. Scuseria. Climbing the Density Functional Ladder: Nonempirical Meta-Generalized Gradient Approximation Designed for Molecules and Solids. *Physical Review Letters*, 91:146401, 2003.
- [183] Y. Zhao and D. G. Truhlar. The M06 Suite of Density Functionals for Main group Thermochemistry, Thermochemical Kinetics, Noncovalent Interactions, Excited States, and Transition Elements: Two New Functionals and Systematic Testing of Four M06-Class Functionals and 12 Other Functionals. *Theoretical Chemistry Accounts*, 120(1-3):215–241, 2007.
- [184] A. D. Becke. Density-Functional Exchange-Energy Approximation with Correct Asymptotic Behavior. *Physical Review A*, 38(6):3098, 1988.
- [185] C. Lee, W. Yang, and R. G. Parr. Development of the Colle-Salvetti Correlation-Energy Formula into A Functional of the Electron Density. *Physical Review B*, 37(2):785, 1988.

- [186] P. J. Stephens, F. J. Devlin, C. F. Chabalowski, and M. J. Frisch. Ab Initio Calculation of Vibrational Absorption and Circular Dichroism Spectra Using Density Functional Force Fields. *The Journal of Physical Chemistry*, 98(45):11623–11627, 1994.
- [187] J. P. Perdew, A. Ruzsinszky, J. Tao, V. N. Staroverov, G. E. Scuseria, and G. I. Csonka. Prescription for the Design and Selection of Density Functional Approximations: More Constraint Satisfaction with Fewer Fits. *The Journal of Chemical Physics*, 123(6):062201, 2005.
- [188] S. Grimme, J. Antony, S. Ehrlich, and H. Krieg. A Consistent and Accurate Ab Initio Parametrization of Density Functional Dispersion Correction (DFT-D) for the 94 Elements H-Pu. *The Journal of Chemical Physics*, 132(15):154104, 2010.
- [189] S. Grimme, S. Ehrlich, and L. Goerigk. Effect of the Damping Function in Dispersion Corrected Density Functional Theory. *Journal of Computational Chemistry*, 32(7):1456–1465, 2011.
- [190] W. J. Hehre, R. F. Stewart, and J. A. Pople. Self-Consistent Molecular-Orbital Methods. I. Use of Gaussian Expansions of Slater-Type Atomic Orbitals. *The Journal of Chemical Physics*, 51(6):2657–2664, 1969.
- [191] R. Ditchfield, W. J. Hehre, and J. A. Pople. Self-Consistent Molecular-Orbital Methods. IX. An Extended Gaussian-Type Basis for Molecular-Orbital Studies of Organic Molecules. *The Journal of Chemical Physics*, 54(2):724–728, 1971.
- [192] W. J. Hehre, R. Ditchfield, and J. A. Pople. Self-Consistent Molecular Orbital Methods. XII. Further Extensions of Gaussian-Type Basis Sets for Use in Molecular Orbital Studies of Organic Molecules. *The Journal of Chemical Physics*, 56(5):2257–2261, 1972.
- [193] P. C. Hariharan and J. A. Pople. The Influence of Polarization Functions on Molecular Orbital Hydrogenation Energies. *Theoretica Chimica Acta*, 28(3):213–222, 1973.

- [194] G. A. Petersson, A. Bennett, T. G. Tensfeldt, M. A. Al-Laham, W. A. Shirley, and J. Mantzaris. A Complete Basis Set Model Chemistry. I. The Total Energies of Closed-Shell Atoms and Hydrides of the First-Row Elements. *The Journal of Chemical Physics*, 89(4):2193–2218, 1988.
- [195] G. A. Petersson and M. A. Al-Laham. A Complete Basis Set Model Chemistry. II. Open-Shell Systems and the Total Energies of the First-Row Atoms. *The Journal of Chemical Physics*, 94(9):6081–6090, 1991.
- [196] A. Schäfer, H. Horn, and R. Ahlrichs. Fully Optimized Contracted Gaussian Basis Sets for Atoms Li to Kr. *The Journal of Chemical Physics*, 97(4):2571–2577, 1992.
- [197] A. Schäfer, C. Huber, and R. Ahlrichs. Fully Optimized Contracted Gaussian Basis Sets of Triple Zeta Valence Quality for Atoms Li to Kr. *The Journal of Chemical Physics*, 100(8):5829–5835, 1994.
- [198] F. Weigend and R. Ahlrichs. Balanced Basis Sets of Split Valence, Triple Zeta Valence and Quadruple Zeta Valence Quality for H to Rn: Design and Assessment of Accuracy. *Physical Chemistry Chemical Physics*, 7:3297–3305, 2005.
- [199] F. Weigend. Accurate Coulomb-Fitting Basis Sets for H to Rn. *Physical Chemistry Chemical Physics*, 8:1057–1065, 2006.
- [200] M. van Exter, Ch. Fattering, and D. Grischkowsky. Terahertz Time-Domain Spectroscopy of Water Vapor. *Optics Letters*, 14(20):1128–1130, 1989.
- [201] B. M. Fischer and P. U. Jepsen. Dynamic Range in Terahertz Time-Domain Transmission and Reflection Spectroscopy. *Optics Letters*, 30(1):29–31, 2005.
- [202] N. W. Ashcroft. *Solid State Physics*. Harvard University Press, Tokyo, 1976.
- [203] F. Bloch. Über die Quantenmechanik der Elektronen in Kristallgittern. *Zeitschrift für Physik*, 52(7):555–600, 1929.

- [204] J. C. Slater and G. F. Koster. Simplified LCAO Method for the Periodic Potential Problem. *Physical Review*, 94(6):1498, 1954.
- [205] C. R. Groom, I. J. Bruno, M. P. Lightfoot, and S. C. Ward. The Cambridge Structural Database. *Acta Crystallographica Section B: Structural Science, Crystal Engineering and Materials*, 72(2):171–179, 2016.
- [206] S. M. Blinder. Basic Concepts of Self-Consistent-Field Theory. *American Journal of Physics*, 33(6):431–443, 1965.
- [207] H. J. Monkhorst and J. D. Pack. Special Points for Brillouin-Zone Integrations. *Physical Review B*, 13(12):5188–5192, 1976.
- [208] S. F. Boys and F. Bernardi. The Calculation of Small Molecular Interactions by the Differences of Separate Total Energies. Some Procedures with Reduced Errors. *Molecular Physics*, 19(4):553–566, 1970.
- [209] V. F. Scalfani, A. J. Williams, V. Tkachenko, K. Karapetyan, A. Pshenichnov, R. M. Hanson, J. M. Liddie, and J. E. Bara. Programmatic Conversion of Crystal Structures into 3D Printable Files Using Jmol. *Journal of Cheminformatics*, 8(1):1174, 2016.
- [210] F. Pascale, C. M. Zicovich-Wilson, F. L. Gejo, B. Civalleri, R. Orlando, and R. Dovesi. The Calculation of the Vibrational Frequencies of Crystalline Compounds and its Implementation in the CRYSTAL Code. *Journal of Computational Chemistry*, 25(6):888–897, 2004.
- [211] Y. Noel, C. M. Zicovich-Wilson, B. Civalleri, P. D’Arco, and R. Dovesi. Polarization Properties of ZnO and BeO: An Ab Initio Study through the Berry Phase and Wannier Functions Approaches. *Physical Review B*, 65(1):14–111, 2001.
- [212] L. Maschio, B. Kirtman, M. Rérat, R. Orlando, and R. Dovesi. Ab Initio Analytical Raman Intensities for Periodic Systems through a Coupled Perturbed Hartree-Fock/Kohn-Sham Method in an Atomic Orbital Basis. I. Theory. *The Journal of Chemical Physics*, 139(16):164101, 2013.

- [213] L. Maschio, B. Kirtman, M. Rérat, R. Orlando, and R. Dovesi. Ab Initio Analytical Raman Intensities for Periodic Systems through a Coupled Perturbed Hartree–Fock/Kohn–Sham Method in an Atomic Orbital Basis. II. Validation and Comparison with Experiments. *The Journal of Chemical Physics*, 139(16):164102, 2013.
- [214] D. G. M. Anderson. Iterative Procedures for Nonlinear Integral Equations. *Journal of the Association for Computing Machinery*, 12(4):547–560, 1965.
- [215] W. F. Perger, J. Criswell, B. Civalleri, and R. Dovesi. Ab–Initio Calculation of Elastic Constants of Crystalline Systems with the CRYSTAL Code. *Computer Physics Communications*, 180(10):1753–1759, 2009.
- [216] J. F. Nye. *Physical Properties of Crystals*. Dover Publications, New York, 1986.
- [217] A. Erba, M. Shahrokhi, R. Moradian, and R. Dovesi. On How Differently the Quasi–Harmonic Approximation Works for Two Isostructural Crystals: Thermal Properties of Periclase and Lime. *The Journal of Chemical Physics*, 142(4):044114, 2015.
- [218] H. C. Zhou, J. R. Long, and O. M. Yaghi. Introduction to Metal–Organic Frameworks. *Chemical Reviews*, 112(2):673–674, 2012.
- [219] B. Chen, Z. Yang, Y. Zhu, and Y. Xia. Zeolitic Imidazolate Framework Materials: Recent Progress in Synthesis and Applications. *Journal of Materials Chemistry A*, 2(40):16811–16831, 2014.
- [220] A. Schneemann, V. Bon, I. Schwedler, I. Senkowska, S. Kaskel, and R. A. Fischer. Flexible Metal–Organic Frameworks. *Chemical Society Reviews*, 43(16):6062–6096, 2014.
- [221] P. Z. Moghadam, A. Li, S. B. Wiggin, A. Tao, A. G. P. Maloney, P. A. Wood, S. C. Ward, and D. Fairen-Jimenez. Development of a Cambridge Structural Database subset: A Collection of Metal–Organic Frameworks for Past, Present, and Future. *Chemistry of Materials*, 29(7):2618–2625, 2017.

- [222] B. J. Sikora, R. Winnegar, D. M. Proserpio, and R. Q. Snurr. Textural Properties of a Large Collection of Computationally Constructed MOFs and Zeolites. *Microporous Mesoporous Materials*, 186:207–213, 2014.
- [223] J. T. A. Jones, T. Hasell, X. Wu, J. Bacsá, K. E. Jelfs, M. Schmidtman, S. Y. Chong, D. J. Adams, A. Trewin, F. Schiffman, F. Cora, Ben S., A. Steiner, G. M. Day, and A. I. Cooper. Modular and Predictable Assembly of Porous Organic Molecular Crystals. *Nature Communications*, 474(7351):367–371, 2011.
- [224] D. Nazarian, J. S. Camp, and D. S. Sholl. A Comprehensive Set of High-Quality Point Charges for Simulations of Metal–Organic Frameworks. *Chemistry of Materials*, 28(3):785–793, 2016.
- [225] A. U. Ortiz, A. Boutin, A. H. Fuchs, and F. Coudert. Investigating the Pressure-Induced Amorphization of Zeolitic Imidazolate Framework ZIF-8: Mechanical Instability due to Shear Mode Softening. *Journal of Physical Chemistry Letters*, 4(11):1861–1865, 2013.
- [226] N. Lock, M. Christensen, Y. Wu, V. K. Peterson, M. K. Thomsen, R. O. Piltz, A. J. Ramirez-cuesta, G. J. McIntyre, K. Norén, R. Kutteh, C. J. Kepert, G. J. Kearley, and B. B. Iversen. Scrutinizing Negative Thermal Expansion in MOF-5 by Scattering Techniques and Ab Initio Calculations. *Dalton Transactions*, 42(6):1996–2007, 2013.
- [227] X. Wang, R. Guo, D. Xu, J. Chung, M. Kaviani, and B. Huang. Anisotropic Lattice Thermal Conductivity and Suppressed Acoustic Phonons in MOF-74 from First Principles. *Journal of Physical Chemistry C*, 119(46):26000–26008, 2015.
- [228] L. Mu, B. Liu, H. Liu, Y. Yang, C. Sun, and G. Chen. A Novel Method to Improve the Gas Storage Capacity of ZIF-8. *Journal of Materials Chemistry*, 22(24):12246–12252, 2012.
- [229] I. B. Vasconcelos, T. G. Da Silva, G. C. G. Militão, T. A. Soares, N. M. Rodrigues, M. O. Rodrigues, N. B. Da Costa, R. O. Freire, and S. A. Junior. Cytotoxicity and Slow

- Release of the Anti-Cancer Drug Doxorubicin from ZIF-8. *RSC Advances*, 2(25):9437–9442, 2012.
- [230] W. Zhou, H. Wu, T. J. Udovic, J. J. Rush, and T. Yildirim. Quasi-Free Methyl Rotation in Zeolitic Imidazolate Framework-8. *The Journal of Physical Chemistry A*, 112(49):12602–12606, 2008.
- [231] J. Qian, F. Sun, and L. Qin. Hydrothermal Synthesis of Zeolitic Imidazolate Framework-67 (ZIF-67) Nanocrystals. *Materials Letters*, 82:220–223, 2012.
- [232] Q. Shi, Z. Chen, Z. Song, J. Li, and J. Dong. Synthesis of ZIF-8 and ZIF-67 by Steam-Assisted Conversion and an Investigation of Their Tribological Behaviors. *Angewandte Chemie*, 50(3):672–675, 2011.
- [233] A. J. Zaczek and T. M. Korter. Polymorphism in Cis-Trans Muconic Acid Crystals and the Role of C-H...O Hydrogen Bonds. *Crystal Growth & Design*, 17:4458–4466, 2017.
- [234] M. R. C. Williams, D. J. Aschaffenburg, B. K. Ofori-okai, and C. A. Schmuttenmaer. Intermolecular Vibrations in Hydrophobic Amino Acid Crystals: Experiments and Calculations. *Journal of Physical Chemistry B*, 117(36):10444–10461, 2013.
- [235] M. T. Ruggiero, J. Sibik, J. A. Zeitler, and T. M. Korter. Examination of l-Glutamic Acid Polymorphs by Solid-State Density Functional Theory and Terahertz Spectroscopy. *Journal of Physical Chemistry A*, 120(38):7490–7495, 2016.
- [236] M. T. Ruggiero, J. Sibik, A. Erba, J. A. Zeitler, and T. M. Korter. Quantification of Cation–Anion Interactions in Crystalline Monopotassium and Monosodium Glutamate Salts. *Physical Chemistry Chemical Physics*, 19(42):28647–28652, 2017.
- [237] M. T. Ruggiero, M. Krynski, E. O. Kissi, J. Sibik, D. Markl, N. Y. Tan, D. Arslanov, W. van der Zande, B. Redlich, T. M. Korter, H. Grohgan, K. Löbmann, T. Rades, S. R. Elliott, and J. A. Zeitler. The Significance of the Amorphous Potential Energy Landscape for Dictating Glassy Dynamics and Driving Solid-State Crystallisation. *Physical Chemistry Chemical Physics*, 19(44):30039–30047, 2017.

- [238] M. T. Ruggiero, J. A. Zeitler, and A. Erba. Intermolecular Anharmonicity in Molecular Crystals: Interplay Between Experimental Low-Frequency Dynamics and Quantum Quasi-Harmonic Simulations of Solid Purine. *Chemical Communications*, 53(26):3781–3784, 2017.
- [239] J. P. Perdew, A. Ruzsinszky, G. I. Csonka, O. A. Vydrov, G. E. Scuseria, L. A. Constantin, X. Zhou, and K. Burke. Restoring the Density-Gradient Expansion for Exchange in Solids and Surfaces. *Physical Review Letters*, 100(13):136–406, 2008.
- [240] S. Grimme. Semi-empirical GGA-Type Density Functional Constructed with a Long-Range Dispersion Correction. *Journal of Computational Chemistry*, 27(15):1787–1799, 2006.
- [241] S. Khazaei and D. Sebastiani. Tunnelling of Coupled Methyl Quantum Rotors in 4-Methylpyridine: Single Rotor Potential versus Coupling Interaction. *The Journal of Chemical Physics*, 147(19):194–303, 2017.
- [242] P. C. Hariharan and J. A. Pople. Accuracy of AH n Equilibrium Geometries by Single Determinant Molecular Orbital Theory. *Molecular Physics*, 27(1):209–214, 2006.
- [243] J. D. Lewis, T. B. Malloy, T. H. Chao, and J. Laane. Periodic Potential Functions for Pseudorotation and Internal Rotation. *Journal of Molecular Structure*, 12(3):427–449, 1972.
- [244] D. F. Bahr, J. A. Reid, W. M. Mook, C. A. Bauer, R. Stumpf, A. J. Skulan, N. R. Moody, B. A. Simmons, M. M. Shindel, and M. D. Allendorf. Mechanical Properties of Cubic Zinc Carboxylate IRMOF-1 Metal-Organic Framework Crystals. *Physical Review B*, 76(18):184–106, 2007.
- [245] J. J. Vlassak and W. D. Nix. Measuring the Elastic Properties of Anisotropic Materials by Means of Indentation Experiments. *Journal of the Mechanics and Physics of Solids*, 42(8):1223–1245, 1994.

- [246] A. Samanta, T. Furuta, and J. Li. Theoretical Assessment of the Elastic Constants and Hydrogen Storage Capacity of Some Metal-Organic Framework Materials. *The Journal of Chemical Physics*, 125(8):084714, 2006.
- [247] L. A. Samoska. An Overview of Solid-State Integrated Circuit Amplifiers in the Submillimeter-Wave and THz Regime. *IEEE Transactions on Terahertz Science and Technology*, 1(1):9–24, 2011.
- [248] N. L. Rosi, J. Eckert, M. Eddaoudi, D. T. Vodak, J. Kim, M. O’Keeffe, and O. M. Yaghi. Hydrogen Storage in Microporous Metal–Organic Frameworks. *Science*, 300(5622):1127–1129, 2003.
- [249] N. Lock, Y. Wu, M. Christensen, L. J. Cameron, V. K. Peterson, A. J. Bridgeman, C. J. Kepert, and B. B. Iversen. Elucidating Negative Thermal Expansion in MOF–5. *Journal of Physical Chemistry C*, 114(39):16181–16186, 2010.
- [250] T. Yildirim and M. R. Hartman. Direct Observation of Hydrogen Adsorption Sites and Nanocage Formation in Metal-Organic Frameworks. *Physical Review Letters*, 95(21):215–504, 2005.
- [251] R. Gaillac, P. Pullumbi, and F. Coudert. ELATE: An Open-Source Online Application for Analysis and Visualization of Elastic Tensors. *Journal of Physics: Condensed Matter*, 28(27):275–201, 2016.
- [252] H. Schmid. Multi-Ferroic Magnetolectrics. *Ferroelectrics*, 162(1):317–338, 1994.
- [253] W. Eerenstein, N. D. Mathur, and J. F. Scott. Multiferroic and Magnetoelectric Materials. *Nature*, 442:759–765, 2006.
- [254] T. Kimura, T. Goto, H. Shintani, K. Ishizaka, T. Arima, and Y. Tokura. Magnetic Control of Ferroelectric Polarization. *Nature*, 426(6962):55–58, 2003.
- [255] J. Wang, J. B. Neaton, H. Zheng, V. Nagarajan, S. B. Ogale, B. Liu, D. Viehland, V. Vaithyanathan, D. G. Schlom, U. V. Waghmare, N. A. Spaldin, K. M. Rabe,

- M. Wuttig, and R. Ramesh. Epitaxial BiFeO₃ Multiferroic Thin Film Heterostructures. *Science*, 299(5613):1719–1722, 2003.
- [256] H. Liu and X. Yang. A Brief Review on Perovskite Multiferroics. *Ferroelectrics*, 507(1):69–85, 2017.
- [257] D. T. Sun, L. Peng, W. S. Reeder, S. M. Moosavi, D. Tiana, D. K. Britt, E. Oveisi, and W. L. Queen. Rapid, Selective Heavy Metal Removal from Water by a Metal–Organic Framework/Polydopamine Composite. *ACS Central Science*, 4(3):349–356, 2018.
- [258] A. Stroppa, P. Jain, P. Barone, M. Marsman, J. M. P. Mato, A. K. Cheetham, H. W. Kroto, and S. Picozzi. Electric Control of Magnetization and Interplay between Orbital Ordering and Ferroelectricity in a Multiferroic Metal–Organic Framework. *Angewandte Chemie International Edition*, 50(26):5847–5850, 2011.
- [259] A. Stroppa, P. Barone, P. Jain, J. M. P. Mato, and S. Picozzi. Hybrid Improper Ferroelectricity in a Multiferroic and Magnetoelectric Metal–Organic Framework. *Advanced Materials*, 25(16):2284–2290, 2013.
- [260] M. Sánchez-Andújar, S. Presedo, S. Yáñez-Vilar, S. Castro-García, J. Shamir, and M. A. Señarís-Rodríguez. Characterization of the Order–Disorder Dielectric Transition in the Hybrid Organic–Inorganic Perovskite-Like Formate Mn(HCOO)₃[(CH₃)₂NH₂]. *Inorganic Chemistry*, 49(4):1510–1516, 2010.
- [261] C. S. Ponseca Jr. and V. Sundström. Revealing the Ultrafast Charge Carrier Dynamics in Organo Metal Halide Perovskite Solar Cell Materials Using Time Resolved THz Spectroscopy. *Nanoscale*, 8:6249–6257, 2016.
- [262] X. Zheng, T. R. Hopper, A. Gorodetsky, M. Maimaris, W. Xu, B. A. A. Martin, J. M. Frost, and A. A. Bakulin. Multipulse Terahertz Spectroscopy Unveils Hot Polaron Photoconductivity Dynamics in Metal-Halide Perovskites. *The Journal of Physical Chemistry Letters*, 12(36):8732–8739, 2021.

- [263] M. T. Ruggiero, J. J. Sutton, S. J. Fraser-Miller, A. J. Zaczek, T. M. Korter, K. C. Gordon, and J. A. Zeitler. Revisiting the Thermodynamic Stability of Indomethacin Polymorphs with Low-Frequency Vibrational Spectroscopy and Quantum Mechanical Simulations. *Crystal Growth & Design*, 18(11):6513–6520, 2018.
- [264] C. M. Zicovich-Wilson, F. Pascale, C. Roetti, V. R. Saunders, R. Orlando, and R. Dovesi. Calculation of the Vibration Frequencies of Alpha-Quartz: The Effect of Hamiltonian and Basis Set. *Journal of Computational Chemistry*, 25(15):1873–1881, 2004.
- [265] P. J. Wheatley. The Crystal and Molecular Structure of Aspirin. *Journal of the Chemical Society*, pages 6036–6048, 1964.
- [266] P. Vishweshwar, J. A. McMahon, M. Oliveira, M. L. Peterson, and M. J. Zaworotko. The Predictably Elusive Form II of Aspirin. *Journal of the American Chemical Society*, 127(48):16802–16803, 2005.
- [267] C. Ouvrard and S. L. Price. Toward Crystal Structure Prediction for Conformationally Flexible Molecules: The Headaches Illustrated by Aspirin. *Crystal Growth & Design*, 4(6):1119–1127, 2004.
- [268] A.D. Bond, R. Boese, and G.R. Desiraju. On the Polymorphism of Aspirin. *Angewandte Chemie International Edition*, 46(4):615–617, 2007.
- [269] A.D. Bond, R. Boese, and G.R. Desiraju. On the Polymorphism of Aspirin: Crystalline Aspirin as Intergrowths of Two “Polymorphic” Domains. *Angewandte Chemie International Edition*, 46(4):618–622, 2007.
- [270] A. D. Bond, K. A. Solanko, S. Parsons, and S. Redder. Single Crystals of Aspirin Form II: Crystallisation and Stability. *CrystEngComm*, 13:399–401, 2011.
- [271] E. L. Crowell, Z. A. Dreger, and Y. M. Gupta. High-Pressure Polymorphism of Acetylsalicylic Acid (Aspirin): Raman Spectroscopy. *Journal of Molecular Structure*, 1082:29–37, 2015.

- [272] A. G. Shtukenberg, C. T. Hu, Q. Zhu, M. U. Schmidt, W. Xu, M. Tan, and B. Kahr. The Third Ambient Aspirin Polymorph. *Crystal Growth & Design*, 17:3562–3566, 2017.
- [273] Polytypism. Online Dictionary of Crystallography. <http://precog.iitd.edu.in/people/anupama> (Accessed: 07/08/2021).
- [274] S. Wen and G. J. O. Beran. Accidental Degeneracy in Crystalline Aspirin: New Insights from High-Level Ab Initio Calculations. *Crystal Growth & Design*, 12(5):2169–2172, 2012.
- [275] A. M. Reilly and A. Tkatchenko. Role of Dispersion Interactions in the Polymorphism and Entropic Stabilization of the Aspirin Crystal. *Physical Review Letters*, 113:055701, 2014.
- [276] Y. Vaksler, A. Idrissi, V.V. Urzhuntseva, and S. V. Shishkina. Quantum Chemical Modeling of Mechanical Properties of Aspirin Polymorphic Modifications. *Crystal Growth & Design*, 21(4):2176–2186, 2021.
- [277] M. J. Turner, S. P. Thomas, M. W. Shi, D. Jayatilaka, and M. A. Spackman. Energy Frameworks: Insights into Interaction Anisotropy and the Mechanical Properties of Molecular Crystals. *Chemical Communications*, 51:3735–3738, 2015.
- [278] E. J. Chan, T. R. Welberry, A. P. Heerdegen, and D. J. Goossens. Diffuse Scattering Study of Aspirin Forms (I) and (II). *Acta Crystallographica Section B*, 66(6):696–707, 2010.
- [279] N. Chieng, T. Rades, and J. Aaltonen. An Overview of Recent Studies on the Analysis of Pharmaceutical Polymorphs. *Journal of Pharmaceutical and Biomedical Analysis*, 55(4):618–644, 2011.
- [280] M. D. King, W. D. Buchanan, and T. M. Korter. Identification and Quantification of Polymorphism in the Pharmaceutical Compound Diclofenac Acid by Terahertz Spectroscopy and Solid-State Density Functional Theory. *Analytical Chemistry*, 83(10):3786–3792, 2011.

- [281] M. D. King, W. D. Buchanan, and T. M. Korter. Understanding the Terahertz Spectra of Crystalline Pharmaceuticals: Terahertz Spectroscopy and Solid-State Density Functional Theory Study of (S)-(+)-Ibuprofen and (RS)-Ibuprofen. *Journal of Pharmaceutical Sciences*, 100(3):1116–1129, 2011.
- [282] N. Laman, S. S. Harsha and D. Grischkowsky. Narrow-Line Waveguide Terahertz Time-Domain Spectroscopy of Aspirin and Aspirin Precursors. *Applied Spectroscopy*, 62(3):319–326, 2008.
- [283] C. C. Wilson. Interesting Proton Behaviour in Molecular Structures. Variable Temperature Neutron Diffraction and Ab Initio Study of Acetylsalicylic Acid: Characterising Librational Motions and Comparing Protons in Different Hydrogen Bonding Potentials. *New Journal of Chemistry*, 26:1733–1739, 2002.
- [284] L. Donà, J. G. Brandenburg, I. J. Bush, and B. Civalleri. Cost-Effective Composite Methods for Large-Scale Solid-State Calculations. *Faraday Discussions*, 224:292–308, 2020.
- [285] N. Y. Tan and J. A. Zeitler. Probing Phase Transitions in Simvastatin with Terahertz Time-Domain Spectroscopy. *Molecular Pharmaceutics*, 12(3):810–815, 2015.
- [286] D. Khamar, I. J. Bradshaw, G. A. Hutcheon, and L. Seton. Solid State Transformations Mediated by a Kinetically Stable Form. *Crystal Growth & Design*, 12(1):109–118, 2012.
- [287] M. D. Eddleston, K. E. Hejczyk, E. G. Bithell, G. M. Day, and W. Jones. Determination of the Crystal Structure of a New Polymorph of Theophylline. *Chemistry – A European Journal*, 19(24):7883–7888, 2013.
- [288] C. Sun, D. Zhou, D. J. W. Grant, and V. G. Young. Theophylline Monohydrate. *Acta Crystallographica Section E*, 58(4):o368–o370, 2002.
- [289] A. C. Pinon, A. J. Rossini, C. M. Widdifield, D. Gajan, and L. Emsley. Polymorphs of Theophylline Characterized by DNP Enhanced Solid-State NMR. *Molecular Pharmaceutics*, 12(11):4146–4153, 2015.

- [290] U. J. Griesser. *The Importance of Solvates*. John Wiley & Sons, Ltd, 2006.
- [291] S. Airaksinen, M. Karjalainen, E. Räsänen, J. Rantanen, and J. Yliruusi. Comparison of the Effects of Two Drying Methods on Polymorphism of Theophylline. *International Journal of Pharmaceutics*, 276(1–2):129–141, 2004.
- [292] N. V. Phadnis and R. Suryanarayanan. Polymorphism in Anhydrous Theophylline—Implications on the Dissolution Rate of Theophylline Tablets. *Journal of Pharmaceutical Sciences*, 86(11):1256–1263, 1997.
- [293] K. Matsuo and M. Matsuoka. Solid-State Polymorphic Transition of Theophylline Anhydrate and Humidity Effect. *Crystal Growth & Design*, 7(2):411–415, 2007.
- [294] A. M. Amado, M. M. Nolasco, and P. J. A. Ribeiro-Claro. Probing Pseudopolymorphic Transitions in Pharmaceutical Solids Using Raman Spectroscopy: Hydration and Dehydration of Theophylline. *Journal of Pharmaceutical Sciences*, 96(5):1366–1379, 2007.
- [295] M. Karjalainen, S. Airaksinen, J. Rantanen, J. Aaltonen, and J. Yliruusi. Characterization of Polymorphic Solid–State Changes Using Variable Temperature X–Ray Powder Diffraction. *Journal of Pharmaceutical and Biomedical Analysis*, 39(1–2):27–32, 2005.
- [296] K. Fücke, G. J. McIntyre, C. Wilkinson, M. Henry, J. A. K. Howard, and J. W. Steed. New Insights into an Old Molecule: Interaction Energies of Theophylline Crystal Forms. *Crystal Growth & Design*, 12(3):1395–1401, 2012.
- [297] C. Robert, S. J. Fraser-Miller, K. Bērziš, P. O. Okeyo, J. Rantanen, T. Rades, and K. C. Gordon. Monitoring the Isothermal Dehydration of Crystalline Hydrates Using Low–Frequency Raman Spectroscopy. *Molecular Pharmaceutics*, 18(3):1264–1276, 2021.
- [298] P. J. Larkin, M. Dabros, B. Sarsfield, E. Chan, J. T. Carriere, and B. C. Smith. Polymorph Characterization of Active Pharmaceutical Ingredients (APIs) Using Low–Frequency Raman Spectroscopy. *Applied Spectroscopy*, 68(7):758–776, 2014.

- [299] A. C. Jørgensen, C. J. Strachan, K. H. Pöllänen, V. Koradia, F. Tian, and J. Rantanen. An Insight into Water of Crystallization during Processing Using Vibrational Spectroscopy. *Journal of Pharmaceutical Sciences*, 98(11):3903–3932, 2009.
- [300] H.-B. Liu, Y. Chen, and X.-C. Zhang. Characterization of Anhydrous and Hydrated Pharmaceutical Materials with THz Time–Domain Spectroscopy. *Journal of Pharmaceutical Sciences*, 96(4):927–934.
- [301] J. Hisazumi, T. Suzuki, H. Nakagami, and K. Terada. Quantification of Pharmaceutical Polymorphs and Prediction of Dissolution Rate Using Theophylline Tablet by Terahertz Spectroscopy. *Chemical & Pharmaceutical Bulletin*, 59(4):442–446, 2011.
- [302] C. Nunes, A. Mahendrasingam, and R. Suryanarayanan. Investigation of the Multi–Step Dehydration Reaction of Theophylline Monohydrate Using 2–Dimensional Powder X–Ray Diffractometry. *Pharmaceutical Research*, 23(10):2393–2404, 2006.
- [303] K. L. Vora, G. Buckton, and D. Clapham. The Use of Dynamic Vapour Sorption and Near Infra–Red Spectroscopy (DVS–NIR) to Study the Crystal Transitions of Theophylline and the Report of a New Solid–State Transition. *European Journal of Pharmaceutical Sciences*, 22(2–3):97–105, 2004.
- [304] A. S. Larsen, M. A. Olsen, H. Moustafa, F. H. Larsen, S. P. A. Sauer, J. Rantanen, and A. Madsen. Determining Short–Lived Solid Forms During Phase Transformations Using Molecular Dynamics. *CrystEngComm*, 21(27):4020–4024, 2019.
- [305] G. M. Day, J. A. Zeitler, W. Jones, T. Rades, and P. F. Taday. Understanding the Influence of Polymorphism on Phonon Spectra: Lattice Dynamics Calculations and Terahertz Spectroscopy of Carbamazepine. *The Journal of Physical Chemistry B*, 110(1):447–456, 2006.
- [306] E. M. Paiva, R. L. Ribessi, C. F. Pereira, and J. J. R. Rohwedder. Low–Frequency Raman Spectrophotometer with Wide Laser Illumination on the Sample: A Tool for Phar-

- maceutical Analytical Analysis. *Spectrochimica Acta. Part A, Molecular and Biomolecular Spectroscopy*, 228:117798, 2020.
- [307] F. S. Vieira and C. Pasquini. Determination of Cellulose Crystallinity by Terahertz–Time Domain Spectroscopy. *Analytical Chemistry*, 86(8):3780–3786, 2014.
- [308] V. H. da Silva, F. S. Vieira, J. J. R. Rohwedder, C. Pasquini, and C. F. Pereira. Multivariate Quantification of Mebendazole Polymorphs by Terahertz Time–Domain Spectroscopy (THZ–TDS). *Analyst*, 142:1519–1524, 2017.
- [309] M. D. King, W. D. Buchanan, and T. M. Korter. Investigating the Anharmonicity of Lattice Vibrations in Water-Containing Molecular Crystals through the Terahertz Spectroscopy of l-Serine Monohydrate. *The Journal of Physical Chemistry A*, 114(35):9570–9578, 2010.
- [310] J. Hulliger. Chemistry and Crystal Growth. *Angewandte Chemie International Edition*, 33(2):143–162, 1994.
- [311] R. J. Davey, S. L. M. Schroeder, and J. H. ter Horst. Nucleation of Organic Crystals—A Molecular Perspective. *Angewandte Chemie International Edition*, 52(8):2166–2179, 2013.
- [312] S. Alfihed, J. F. Holzman, and I. G. Foulds. Developments in the Integration and Application of Terahertz Spectroscopy with Microfluidics. *Biosensors and Bioelectronics*, page 112393, 2020.
- [313] M. Nagel, P. Haring Boilvar, M. Brucherseifer, H. Kurz, A. Bosserhoff, and R. Büttner. Integrated THz Technology for Label-Free Genetic Diagnostics. *Applied Physics Letters*, 80(1):154–156, 2002.
- [314] D. S. Venables and C. A. Schmuttenmaer. Far-Infrared Spectra and Associated Dynamics in Acetonitrile–Water Mixtures Measured with Femtosecond THz Pulse Spectroscopy. *The Journal of Chemical Physics*, 108(12):4935–4944, 1998.

- [315] T. M. Duncan and J. A. Reimer. *Chemical Engineering Design and Analysis: An Introduction*. Cambridge University Press, Cambridge, 2019.
- [316] L. Duvillaret, F. Garet, and J.-L. Coutaz. A Reliable Method for Extraction of Material Parameters in Terahertz Time-Domain Spectroscopy. *IEEE Journal of selected topics in quantum electronics*, 2(3):739–746, 1996.
- [317] J. Xu, K. W. Plaxco, and S. J. Allen. Absorption Spectra of Liquid Water and Aqueous Buffers between 0.3 and 3.72 THz. *The Journal of Chemical Physics*, 124(3):036101, 2006.
- [318] C. B. Ojeda and F. S. Rojas. Process Analytical Chemistry: Applications of Ultraviolet/Visible Spectrometry in Environmental Analysis: An Overview. *Applied Spectroscopy Reviews*, 44(3):245–265, 2009.
- [319] G. D. Brabson. *Ultraviolet/Visible Absorption Spectroscopy in: ASM Handbook, Volume 10.: Materials Characterization*. ASM International, 1986.
- [320] N. Rodríguez-Hornedo, S. J. Nehm, K. F. Seefeldt, Y. Pagan-Torres, and C. J. Falkiewicz. Reaction Crystallization of Pharmaceutical Molecular Complexes. *Molecular Pharmaceutics*, 3(3):362–367, 2006.
- [321] C. Correa-Soto, N. S. Trasi, P. D. Schmitt, Y. Su, Z. Liu, E. Miller, N. Variankaval, P. J. Marsac, G. J. Simpson, and L. S. Taylor. Second Harmonic Generation Microscopy as a Tool for the Early Detection of Crystallization in Spray Dried Dispersions. *Journal of Pharmaceutical and Biomedical Analysis*, 146:86–95, 2017.
- [322] R. C. Basso, A. P. B. Ribeiro, M. H. Masuchi, L. A. Gioielli, L. A. G. Gonçalves, A. O. dos Santos, L. P. Cardoso, and R. Grimaldi. Tripalmitin and Monoacylglycerols as Modifiers in the Crystallisation of Palm Oil. *Food Chemistry*, 122(4):1185–1192, 2010.
- [323] J. J. De Yoreo, P. U. P. A. Gilbert, N. A. J. M. Sommerdijk, R. Lee Penn, S. Whitlam, D. Joester, H. Zhang, J. D. Rimer, A. Navrotsky, J. F. Banfield, A. F. Wallace,

- F. M. Michel, F. C. Meldrum, H. Cölfen, and P. M. Dove. Crystallization by Particle Attachment in Synthetic, Biogenic, and Geologic Environments. *Science*, 349(6247), 2015.
- [324] G. R. Desiraju. Crystal Engineering: From Molecule to Crystal. *Journal of the American Chemical Society*, 135(27):9952–9967, 2013.
- [325] M. Svärd, K. R. Devi, D. Khamar, D. Mealey, D. Cheuk, J. Zeglinski, and Å. C. Rasmuson. Solute Clustering in Undersaturated Solutions—Systematic Dependence on Time, Temperature and Concentration. *Physical Chemistry Chemical Physics*, 20(22):15550–15559, 2018.
- [326] M. Volmer. *Kinetics of Phase Formation*. Leipzig, 1939.
- [327] P. G. Vekilov. Nucleation. *Crystal Growth Design*, 10(12):5007–5019, 2010.
- [328] D. Gebauer and H. Cölfen. Prenucleation Clusters and Non-Classical Nucleation. *Nano Today*, 6(6):564–584, 2011.
- [329] D. T. Vaniman, D. L. Bish, S. J. Chipera, C. I. Fialips, J. W. Carey, and W. C. Feldman. Magnesium Sulphate Salts and the History of Water on Mars. *Nature*, 431(7009):663–665, 2004.
- [330] J. Sibik, E. Y. Shalaev, and J. A. Zeitler. Glassy Dynamics of Sorbitol Solutions at Terahertz Frequencies. *Physical Chemistry Chemical Physics*, 15(28):11931–11942, 2013.